

CRACK-DEPENDENT RESPONSE OF STRUCTURAL STEEL MEMBERS REPAIRED
WITH CFRP

A Dissertation
Submitted to the Graduate Faculty
of the
North Dakota State University
of Agriculture and Applied Science

By

Amer Hmidan

In Partial Fulfillment
for the Degree of
DOCTOR OF PHILOSOPHY

Major Department:
Civil Engineering

April 2014

Fargo, North Dakota

Title

Crack-Dependent Response of Structural Steel Members Repaired with CFRP

By

Amer Hmidan

The Supervisory Committee certifies that this *disquisition* complies with North Dakota State University's regulations and meets the accepted standards for the degree of

DOCTOR OF PHILOSOPHY

SUPERVISORY COMMITTEE:

Dr. Jimmy Kim

Co-Chair

Dr. Frank Yazdani

Co-Chair

Dr. Magdy Abdelrahman

Dr. Jerry Gao

Approved:

April 21, 2014

Date

Dr. Dinesh Katti

Department Chair

ABSTRACT

Cracking of the lower flange in steel-girder bridges is a critical consideration because it will influence flexural behavior such as load-carrying capacity. Timely rehabilitation will save long-term repair costs and warrant sustainable performance. Carbon-fiber-reinforced polymer (CFRP) is a promising material to repair damaged steel members. This non-metallic reinforcement provides a number of benefits when compared to traditional repair materials (e.g., welded steel plates) for deteriorated steel girders: for example, a favorable strength-to-weight ratio, resistance to corrosion and fatigue, rapid installation in practice, and reduced long-term maintenance expenses.

Although applying CFRP to steel members has recently attracted the rehabilitation community, its contribution to the behavior of repaired members is not fully understood. Very limited information about the interaction between the level of initial damage in steel girders and CFRP-repair is available, and also, scant research about the long-term performance and environmental durability for such repaired members has been done. This study addresses these identified research gaps based on a two-phase experimental program. The first phase focuses on CFRP-repaired steel beams having various levels of initial damage (representing multiple stages of fatigue crack propagation). The second phase is focused on testing the repaired beams when subjected to various levels of sustained intensity and cold temperature.

A three-dimensional non-linear finite element (FE) model is developed to predict the flexural behavior of CFRP-repaired beams, including CFRP debonding and crack propagation across the critical section of the repaired beams. Also, the FE method is used and regression equations are proposed to predict the static strength of standard steel W Shapes repaired with CFRP, taking into consideration the material and geometric properties.

ACKNOWLEDGMENTS

I would like to thank my advisers, Dr. Jimmy Kim and Dr. Frank Yazdani, for giving me the opportunity to complete my degree. Through your support, guidance, advice, and wisdom, you have helped me fulfill a lifetime dream. I would like to thank the other members of my committee, Dr. Magdy Abdelrahman and Dr. Jerry Gao, for their time, thoughtful advice, and revisions.

I gratefully thank the Department of Civil Engineering at North Dakota State University (NDSU) for its financial support. My thanks also go to Dr. Dinesh Katti and Dr. Magdy Abdelrahman in NDSU's Department of Civil Engineering and to their graduate students for allowing and helping me to use their testing equipment to conduct part of the experimental work needed for this research. Dr. Ghodrat Karami and Mr. Curt Doetkott, thank you so very much for all your help.

I would like to acknowledge and offer my sincere thanks to Dean and Sandra Eggermont for all the help and support they provided to make this accomplishment possible.

Finally, I am thankful for the unconditional love, support, patience, and encouragement from my family, in general, and my parents, in particular. I never would have made it here without you.

DEDICATION

To my parents

TABLE OF CONTENTS

ABSTRACT.....	iii
ACKNOWLEDGMENT.....	iv
DEDICATION.....	v
LIST OF TABLES	xiii
LIST OF FIGURES	xiv
LIST OF ABBREVIATION.....	xx
LIST OF SYMBOLS	xxi
LIST OF APPENDIX TABLES	xxvi
LIST OF APPENDIX FIGURES.....	xxvii
CHAPTER 1. INTROCUATION	1
1.1. General.....	1
1.2. Problem Statement.....	2
1.2.1. Crack-Dependent Behavior of Steel Members Strengthened with CFRP ...	2
1.2.2. Behavior of Notched Steel Beams Strengthened With CFRP	3
1.2.3. Durability Of CFRP-Strengthened Steel Beams.....	4
1.2.4. Fracture Response of CFRP-Strengthened Cracked Steel I-Beams	5
1.3. Objective of the Dissertation	6
1.4. Scope of the Dissertation	6
1.5. Dissertation Organization	7
CHAPTER 2. LITERATURE REVIEW	9
2.1. Background.....	9
2.2. Conventional Strengthening Techniques of Metallic Structures	9
2.3. Strengthening of Steel Structures Using FRP Composite Materials	11

2.3.1.	Introduction.....	11
2.3.2.	Carbon-Fiber-Reinforced Polymer (CFRP).....	12
2.3.3.	Flexural Response of Steel Beams Reinforced with CFRP Materials.....	15
2.3.3.1.	Cracked steel beams strengthened with CFRP	16
2.3.3.2.	Other cases of strengthening steel beams with CFRP	24
2.3.4.	Bond Characteristics and Force Transfer Between CFRP and Steel	24
2.4.	Durability of Metallic Structures Strengthened with FRP Composites	31
2.4.1.	Introduction.....	31
2.4.2.	Effect of Temperature and Environment	32
2.4.2.1.	Durability of the joint interface	33
2.4.2.2.	Durability of the composite materials.....	38
2.4.3.	Surface Preparation and Bond Durability	41
2.4.4.	Fatigue and Creep Effects.....	42
2.4.5.	Galvanic Corrosion	47
2.5.	Analysis and Design	51
2.5.1.	CFRP-to-Steel Bonded joint	51
2.5.2.	Steel Beams Reinforced with FRP Bonded Composites	55
2.6.	Failure Modes in Steel-CFRP System	56
2.7.	Cracks and Fracture	58
2.7.1.	Stress Concentrations.....	58
2.7.2.	Fracture Mechanics.....	59
2.7.2.1.	Damage tolerance	60
2.7.2.2.	Fracture and failure criteria.....	62
2.7.2.3.	Crack-tip plasticity.....	67

2.7.2.4. The stress intensity factor (SIF).....	68
2.7.2.5. The J contour integral	70
2.7.3. Fracture-Based Approach for Strengthening with CFRP Composites	73
2.8. Finite Element Analysis (FEA).....	76
2.8.1. Background.....	76
2.8.2. Finite Element Method (FEM) Procedure	77
2.8.2.1. General.....	77
2.8.2.2. Appropriate element selection	80
2.8.2.3. Linear and nonlinear response	80
2.8.2.4. Mesh design	81
2.9. Field Applications of CFRP Reinforcement	83
CHAPTER 3. CRACK-DEPENDENT RESPONSE OF STEEL ELEMENTS	
STRENGTHENED WITH CFRP SHEETS	87
3.1. Abstract.....	87
3.2. Research Significance.....	87
3.3. Computational Modeling	88
3.3.1. Specimen Details	88
3.3.2. Constitutive Material Modeling.....	90
3.3.3. Elements and Boundary Conditions.....	91
3.3.4. Validation of the Proposed Modeling Approach	93
3.3.4.1. Interfacial response	93
3.3.4.2. Unstrengthened steel member in axial tension	93
3.3.4.3. Strengthened steel member in axial tension	94
3.3.5. Summary of the Validation.....	95

3.4.	Analysis of the Results.....	96
3.4.1.	Load-Carrying Capacity and Failure Mode	96
3.4.2.	Crack Mouth Opening Displacement.....	97
3.4.3.	Crack Propagation.....	98
3.4.4.	Strain Profile	100
3.4.5.	Fracture Properties	103
3.5.	Summary and Conclusions	106
CHAPTER 4. CFRP-REPAIR OF STEEL BEAMS HAVING VARIOUS INITIAL CRACK CONFIGURATIONS		
4.1.	Abstract	109
4.2.	Research Significance	109
4.3.	Experimental Program	110
4.3.1.	Beam Details	110
4.3.2.	Surface Preparation and Micro-Topography	112
4.3.3.	Test Set-Up and Instrumentation	114
4.4.	Proposed Model	114
4.4.1.	Constitutive Modeling	114
4.4.2.	Element Description and Boundary Condition	115
4.4.3.	Validation of Interface Modeling Approach.....	117
4.4.3.1.	Single-edge notched specimen in axial tension	117
4.4.3.2.	Double-lap steel joint bonded with CFRP sheets	117
4.5.	Test Results and Analysis	118
4.5.1.	Failure Mode	118
4.5.2.	Load-Deflection	120
4.5.3.	Crack Mouth Opening Displacement.....	122

4.5.4.	Crack Propagation Up the Web	124
4.5.5.	Debonding Behavior	124
4.5.6.	Fracture Characteristics	128
4.6.	Summary and Conclusions	131
CHAPTER 5. EFFECT OF SUSTAINED LOAD COMBINED WITH COLD		
TEMPERATURE ON FLEXURE OF DAMAGED STEEL BEAMS		
REPAIRED WITH CFRP SHEETS		
5.1.	Abstract	133
5.2.	Research Significance	134
5.3.	Experimental Program	134
5.3.1.	Test Beams and Materials	135
5.3.2.	Sustained Load and Temperature Exposure	136
5.3.3.	Test Set-Up and Instrumentation	138
5.4.	Test Results and Discussion.....	139
5.4.1.	Load-Carrying Capacity.....	139
5.4.2.	Load-Deflection Behavior	142
5.4.3.	Energy Dissipation.....	145
5.4.4.	Crack Mouth Opening Displacement.....	146
5.4.5.	Failure Mode	148
5.4.6.	Behavior of CFRP-Steel Interface	149
5.4.6.1.	Strain distribution along CFRP sheet.....	149
5.4.6.2.	Bond stress-slip response	151
5.5.	Summary and Conclusions	154

CHAPTER 6. STRESS INTENSITY FACTORS FOR STRUCTURAL STEEL I-BEAMS STRENGTHENED WITH CFRP SHEETS	156
6.1. Abstract	156
6.2. Research Significance	156
6.3. Beam Details and Parameters for Cracked I-Beams	158
6.4. Equations for the Stress Intensity Factor	159
6.4.1. Flange-to-Web Area Ratio Parameter	161
6.4.2. Remote Stress: the Uncracked Section Extreme Tensile Fiber Stress	165
6.5. Finite Element Model Development	167
6.5.1. Element Types and Boundary Conditions	167
6.5.2. Crack-Tip Quadrilateral Element	168
6.5.3. Mesh Design for Crack-Tip Region	169
6.6. Results and Discussion	172
6.6.1. Experimental Evidence and Approach Validation	172
6.6.1.1. Overview of the experimental program and test results	172
6.6.1.2. SIF and approach validation	175
6.6.1.3. Correction factors including a parametric analysis	180
6.6.2. SIF for Cracked W Shapes with λ Ranging from 0.91 to 2.01	186
6.6.2.1. Correction factors for unrepaired beams	187
6.6.2.2. Correction factors for repaired beams	188
6.7. Summary and Conclusions	195
CHAPTER 7. CONCLUSIONS AND RECOMMENDATIONS	199
7.1. Introduction	199
7.2. Summary and Conclusions	199
7.2.1. Steel Elements Strengthened with CFRP	199

7.2.2. CFRP-Repair of Steel Beams.....	200
7.2.3. Durability of the CFRP-Repair of Steel Beams	201
7.2.4. SIF for Structural Steel I-Beams Strengthened with CFRP	202
7.3. Recommendations for Future Research	203
REFERENCES	206
APPENDIX A. CALCULATED CORRECTION FACTORS.....	221
APPENDIX B. REGRESSION DIAGNOSTICS FOR THE CORRECTION FACTORS.....	229

LIST OF TABLES

<u>Table</u>	<u>Page</u>
2.1 Bridges around the world strengthened using CFRP composites.....	86
3.1 Specimen details	89
3.2 Material properties from manufacturer	91
4.1 Material properties from manufacturer	111
4.2 Test matrix	112
5.1 Material properties from manufacturer	135
5.2 Beam details.....	138
6.1 Matrix of W Shapes employed in Finite Element Analysis.....	162
6.2 Coefficients for regression equations for correction factor for beams with λ ranging from 0.91 to 2.01.....	196

LIST OF FIGURES

<u>Figure</u>	<u>Page</u>
2.1. Typical strengthening of steel girder with steel plates (Tilly et al. 2008)	10
2.2. Pultrusion scheme (Cui 2013).....	13
2.3. Typical stress-strain curves for steel, GFRP, and three grades of CFRP (Shaat 2007).....	14
2.4. Process of converting PAN precursor fibers to carbon fibers (Agarwal et al. 2006)	15
2.5. Some available forms/shapes of carbon fibers (Great Planes 2014).....	15
2.6. Repair of steel girders with CFRP (Liu et al. 2001)	17
2.7. Rehabilitation of damaged steel-concrete composite beams with CFRP (Tavakkolizadeh and Saadatmanesh 2003b).....	19
2.8. Strengthening of cracked steel-concrete composite girders using CFRP material (Shaat and Fam 2008)	21
2.9. Fatigue strength of steel girders strengthened with CFRP patch (Tavakkolizadeh and Saadatmanesh 2003a).....	23
2.10. Repair of a steel bridge girders with CFRP plates (Miller et al. 2000)	26
2.11. Dog-bone shaped steel plates bonded with CFRP (Al-Emrani et al. 2005).....	27
2.12. Steel-CFRP pull-off test specimen and set-up (Xia and Teng 2005).....	28
2.13. Steel-CFRP composite lap joints (Fawzia et al. 2013)	30
2.14. Effective bond length of CFRP strips bonded to fatigued steel bridge I-girders (Nozaka et al. 2005).....	31
2.15. Schematic for van der Waals forces at the adhesive-adherend interface (SpecialChem 2013).....	34
2.16. Schematic representation of ASTM D 3762 wedge test.....	36
2.17. Determination of bond durability (Kharbania and Shully 1995).....	37
2.18. Schematic for double-lap shear joint configuration (Albat and Romilly 1999)	52

2.19.	Schematic view of likely failure modes in CFRP-steel system (Zhao and Zhang 2007).....	57
2.20.	Stress concentrations due to geometric changes (Boresi and Schmidt 2003).....	59
2.21.	Damage tolerance analysis (Broek 1989)	61
2.22.	The traditional strength approach versus the fracture mechanics approach (Anderson 2005)	64
2.23.	Stresses in an element near the crack of an elastic material	66
2.24.	Plastic zone ahead of crack tip.....	68
2.25.	The three basic modes of loading	69
2.26.	K_I solutions for two of the common test specimens (Zehnder 2007)	69
2.27.	Arbitrary closed contour around the tip of a crack	72
2.28.	Typical J - R curve for a ductile material	73
2.29.	Cracked steel members reinforced by prestressed CFRP patch (Colombi et al. 2003)	75
2.30.	The process of FEA (Bathe 1996)	79
2.31.	Some typical elements used in FEA	80
2.32.	Typical linear and nonlinear material responses and iteration approach for the numerical solution.....	82
2.33.	Element degeneration at the crack tip.....	83
2.34.	Installation procedure of CFRP to steel-girder bridges (Phares et al. 2003)	85
3.1.	Specimen details	89
3.2.	Constitutive behavior: (a) steel; (b) CFRP sheet; (c) CFRP-steel interface; (d) crack opening of steel	90
3.3.	FEA model constructed.....	92
3.4.	Validation of the proposed modeling approach: (a) interfacial response; (b) unstrengthened steel member (Specimen D25 in Hollstein et al. 1983); (c) strengthened steel member (Specimen SN80 in Fawzia et al. 2006); (d) strain distribution along Specimen SN80 in Fawzia et al. (2006)	95

3.5.	Load-displacement response: (a) unstrengthened specimens; (b) strengthened specimens with one layer of CFRP; (c) strengthened specimens with three layers of CFRP; (d) comparison of various CFRP reinforcement ratios for specimens with $a_0/h = 0.6$	97
3.6.	Crack mouth opening displacement: (a) unstrengthened specimens; (b) strengthened specimens with one layer of CFRP; (c) strengthened specimens with three layers of CFRP; (d) comparison of CMOD-compliance per specimen thickness	99
3.7.	Crack propagation: (a) unstrengthened specimens; (b) strengthened specimens with one layer of CFRP; (c) effect of CFRP strengthening for specimens with $a_0/h = 0.1$; (d) effect of CFRP strengthening for specimens with $a_0/h = 0.6$	100
3.8.	Strain profile along the specimen: (a) $a_0/h = 0.1$ with one layer of CFRP; (b) $a_0/h = 0.3$ with one layer of CFRP; (c) $a_0/h = 0.6$ with one layer of CFRP; (d) comparison of various a_0/h ratios	102
3.9.	CFRP-strain profiles across the specimen at notched location (circle = tip of notch): (a) specimen having $a_0/h = 0.1$ strengthened with one layer of CFRP; (b) comparison of specimens having various a_0/h ratios strengthened with three layers of CFRP	103
3.10.	Work done per specimen thickness: (a) unstrengthened; (b) strengthened with 1 layer of CFRP; (c) strengthened with 3 layers of CFRP; (d) comparison at a displacement of 2.0 mm	105
3.11.	J integral of the specimens.....	106
4.1.	Beam details and test set-up (unit: mm)	111
4.2.	Micro-topography of steel surface: (a) surface preparation; (b) laser scanning; (c) details of laser scanner; (d) unprepared surface; (e) prepared surface.....	113
4.3.	Constitutive modeling: (a) steel beam; (b) CFRP sheet; (c) crack-opening displacement of steel section; (d) CFRP-steel interface	115
4.4.	Proposed modeling approach: (a) constructed model; (b) crack propagation model across steel section; (c) debonding propagation model along CFRP-steel interface	116
4.5.	Validation of interface modeling: (a) single-edge notched steel coupon; (b) element response of CFRP-steel interface; (c) steel coupon bonded with CFRP; (d) strain distribution along CFRP bonded to steel substrate	118
4.6.	Failure mode: (a) unrepaired experimental beam; (b) unrepaired predicted beam; (c) CFRP-debonding propagated along the interface; (d) CFRP-rupture at notch location..	119

4.7.	Load-deflection of beams: (a) beams with $a_0/h = 0.1$; (b) beams with $a_0/h = 0.3$; (c) beams with $a_0/h = 0.5$; (d) comparison of ultimate load.....	121
4.8.	Effect of initial damage: (a) increase of ultimate load after repair; (b) increase of elastic stiffness after repair	122
4.9.	Load-crack mouth opening displacement: (a) beams with $a_0/h = 0.1$; (b) beams with $a_0/h = 0.3$; (c) beams with $a_0/h = 0.5$; (d) effect of CFRP-repair on crack control.....	123
4.10.	Load-crack propagation measured from top of the notch (distance above notch): (a) beams with $a_0/h = 0.1$; (b) beams with $a_0/h = 0.3$; (c) beams with $a_0/h = 0.5$	125
4.11.	Measured strains along the CFRP: (a) beam with $a_0/h = 0.1$; (b) beam with $a_0/h = 0.3$; (c) beam with $a_0/h = 0.5$	127
4.12.	Predicted CFRP strains of beam with $a_0/h = 0.1$: (a) within service range; (b) beyond service range	128
4.13.	Variation of fracture energy up to peak load	129
4.14.	Energy dissipated from steel beams (hollow = experiment; solid = FEA): (a) unrepaired; (b) repaired with CFRP.....	130
4.15.	Variation of J-Integral for unrepaired and repaired beams.....	131
5.1.	Test beam and notch detail	136
5.2.	Applying sustained load: (a) schematic view; (b) loading frame; (c) environmental chamber.....	137
5.3.	Set-up for residual test	139
5.4.	Comparison of flexural behavior with respect to temperature exposure: (a) ultimate load; (b) loss of load-carrying capacity on average; (c) elastic stiffness; (d) loss of elastic stiffness on average.....	141
5.5.	Load-deflection behavior of beams: (a) effect of strengthening; (b) effect of sustained load without cold temperature; (c) subject to $+25^{\circ}\text{C}$; (d) subject to -20°C ; (e) subject to -30°C	144
5.6.	Variation of energy in test beams: (a) energy dissipated up to peak load; (f) loss of energy dissipated.....	146
5.7.	Load-crack mouth opening displacement: (a) effect of sustained load; (b) subject to $+25^{\circ}\text{C}$; (c) subject to -20°C ; (d) subject to -30°C ; (e) CMOD at ultimate load; (f) CMOD decrease ratio compared to reference beam.....	147

5.8.	Failure mode	148
5.9.	Measured strains along the CFRP: (a) 40% F_u at 25°C; (b) 60% F_u at 25°C; (c) 40% F_u at - 20°C; (d) 60% F_u at -20°C; (e) 40% F_u at -30°C; (f) 60% F_u at -30°C	150
5.10.	Effect of long-term load on CFRP-strain development at 25% P_u of the reference beam S+25+0: (a) without cold temperature exposure; (b) with cold temperature exposure	151
5.11.	Development of CFRP slip: (a) S1+25+40; (b) S1-30+40	152
5.12.	Local shear stress-slip of CFRP-steel interface: (a) reference beam (S+25+0); (b) beam subjected to 40% F_u without cold temperature exposure (S1+25+40); (c) beam subjected to 60% F_u with cold temperature exposure (S1-30+60)	153
6.1.	Beam details showing the three geometries: (a) beam geometry; (b) cross-section for Control (unrepaired) beam; (c) cross-section for repaired Full-Flange beam; (d) cross-section for repaired Half-Flange beam	161
6.2.	Correlation between λ and ϕ for all W Shapes in AISC	164
6.3.	Effect of λ on the correction factor	165
6.4.	The transformed-section method (uncracked cross-section)	166
6.5.	Proposed modeling approach: (a) constructed FEA model; (b) degeneration of the quadrilateral element into a triangle at the crack tip; (c) crack-tip region showing spider-web configuration	170
6.6.	Comparison of SIFs calculated from FEA and handbooks for edge crack in beam in bending.....	171
6.7.	Fine mesh mapping near the crack tip region at different crack lengths: (a) $a/h \leq 0.5$; (b) $a/h > 0.5$	172
6.8.	Experimental behavior of test beams [Hmidan et al. 2011]: (a) load-deflection response at midspan of beams (faint = unrepaired; dark = repaired); (b) comparison of ultimate load; (c) increase of ultimate load after repair; (d) measured strains along the CFRP.....	174
6.9.	Correlations between SIF and crack length for W4 × 13 beams under different bending moments: (a) unrepaired beams; (b) repaired beams; (c) decrease in SIF after repair.....	177

6.10.	Comparison between the numerical prediction of the critical load (P_{cr}) using the proposed SIF solutions and other loads determined experimentally in Hmidan et al. (2011) : (a) loads for unrepaired beams; (b) loads for repaired beams; (c) % difference in loads for unrepaired beams; (d) % difference in loads for repaired beams	179
6.11.	Effect of repair on stress intensity correction factors for W4 × 13 beams ($\psi = 0.005$ and $\eta = 1.135$): (a) comparison between unrepaired and repaired beams; (b) decrease of Y after repair	181
6.12.	Effect of crack length on strain distribution along the uncracked ligament: (a) cracked beam repaired with CFRP under bending; (b) strain distribution when $a_o/h \leq 0.5$; (c) strain distribution when $a_o/h > 0.5$	184
6.13.	Correction factors for CFRP-repaired W4 × 13 beams at various ψ values: (a) $\eta = 0.75$; (b) $\eta = 1.135$; (c) $\eta = 1.5$; (d) decrease of Y after repair at different η (faint for $\psi = 0.005$; dark for $\psi = 0.025$).....	186
6.14.	Correction factors for CFRP-repaired W4 × 13 beams.....	187
6.15.	Correction factors for unrepaired beams: (a) 2-D plot; (b) 3-D plot	188
6.16.	Correction factors for repaired beams under Full-Flange geometry: (a) $\eta = 0.75$; (b) $\eta = 1.125$; (c) $\eta = 1.5$	190
6.17.	Comparison for decrease of Y after repair under Full-Flange geometry (faint for $\psi = 0.002$; dark for $\psi = 0.010$): (a) effect of elastic modulus of CFRP ($\lambda = 0.91$); (b) effect of flange-to-web area ratio ($\eta = 1.125$).....	191
6.18.	Correction factors for repaired beams under Half-Flange geometry: (a) $\eta = 0.75$; (b) $\eta = 1.125$; (c) $\eta = 1.5$	193
6.19.	Comparison for decrease of Y after repair under Half-Flange geometry (faint for $\psi = 0.001$; dark for $\psi = 0.005$): (a) effect of elastic modulus of CFRP ($\lambda = 0.91$); (b) effect of flange-to-web area ratio ($\eta = 1.125$)	194
6.20.	Comparison of correction factors for repaired beams under Full and Half-Flange geometries for $\eta = 1.125$: (a) correction factors for Full-Flange at $\psi = 0.004$ (2 layers) and Half-Flange at $\psi = 0.002$ (2 layers) and 0.004 (4 layers) (b) decrease of Y after repair for beams with $\lambda = 0.91$	195

LIST OF ABBREVIATIONS

ACI.....	American Concrete Institute
AISC	American Institute of Steel Construction
ASCE	American Society of Civil Engineers
ASTM	American Society of Testing and Materials
CFRP.....	Carbon-Fiber-Reinforced Polymer
CMOD.....	Crack Mouth Opening Displacement
CTE.....	Coefficient of Thermal Expansion
CVN	Charpy V-Notch
EPFM.....	Elastic-Plastic Fracture Mechanics
FHWA.....	Federal Highway Administration
FE.....	Finite Element
FEA.....	Finite Element Analysis
FEM	Finite Element Method
FRP	Fiber-Reinforced Polymer
GFRP.....	Glass-Fiber-Reinforced Polymer
LEFM.....	Linear-Elastic Fracture Mechanics
NDSU.....	North Dakota State University
PAN.....	Polyacrylonitrile
SAS	Statistical Analysis System
SIF.....	Stress Intensity Factor
SSY	Small-Scale Yielding
USDOT.....	United States Department of Transportation

LIST OF SYMBOLS

A	cross-sectional area of each composite part in an area
A_c	cross-sectional area of CFRP reinforcement
A_f	area of the flange of I-beam
A_s	cross-sectional area of steel I-beam
A_w	area of the web of I-beam
a	crack or notch size
a_o	initial crack or notch size
a_f	critical crack size
B	specimen thickness
c	curve-fitting coefficients
d	height of I-beam including the flange thickness
d_o	perpendicular distance between the centroidal axis and the parallel axis
ds	length increment along Γ path
E	elastic modulus of the material
E_c	elastic modulus of CFRP
E_d	energy dissipation
E_s	elastic modulus of steel
F	work done by external forces
F_u	ultimate load of strengthened beam without sustained load
f	safety factor
f_{ta}	tensile strength of the adhesive
G	energy release rate
G_a	shear modulus of the adhesive

G_c toughness of the material
 G_f fracture energy
 H time for safe operation of cracked element
 h specimen or beam height
 I moment of inertia for the transformed uncracked-strengthened I-beam
 \bar{I} moment of inertia for each composite part in an area
 I' moment of inertial of the uncracked cross section of I-beam
 J nonlinear energy release rate
 J_{Ic} elastic-plastic fracture toughness of the material
 K tangent stiffness matrix
 K_I mode I stress intensity factor
 K_{II} mode II stress intensity factor
 K_{III} mode III stress intensity factor
 K_{Ic} fracture toughness of the material
 K_{FEA} stress intensity factor calculated by FEA
 K_{LIT} stress intensity factor computed from formulas found in literature
 l length of crack-tip element
 M bending moment
 P applied load
 P_{ci} crack initiation load
 P^e external loads
 P^i internal forces
 P_{res} residual load

P_s highest anticipated service load
 P_u ultimate load
 P_y yield load
 R^2 coefficient of determination
 r remaining safety factor
 r_o radial distance from the crack tip
 r_y radius of the plastic zone ahead of the crack tip
 T_g glass transition temperature
 t traction vector
 t_a thickness of the adhesive
 t_c thickness of the CFRP
 t_f thickness of the flange of I-beam
 t_w thickness of the web of I-beam
 U absorbed energy
 U_o elastic energy content of the loaded uncracked plate
 U_a change in elastic strain energy
 U_p potential energy
 U_γ change in elastic surface energy
 u_a surface free energies of the adhesive
 u_{al} surface free energies of the adhesive in the presence of liquid
 u_i displacement vector components
 u_s surface free energies of the substrate
 u_{sl} surface free energies of the substrate in the presence of liquid

u_{as}	interfacial free energy
Δu	displacement increments
W_A	work of adhesion in an inert medium
W_{Al}	work of adhesion in the presence of liquid
W_u	energy dissipated up to peak load
W	strain energy density
X	side length of the square region surrounding the crack tip
x	direction parallel to the crack line
x_p	displacement at the peak load
Y	correction factor
y	direction normal to the crack line
y'	position of the neutral axis for the uncracked-unstrengthened I-beam
\tilde{y}	algebraic distance for the centroid of each composite part
\bar{y}	position of the neutral axis for the uncracked-strengthened I-beam
σ	remote tensile stress
σ_1	maximum principal stress
σ_f	critical stress
σ_{xx}	normal stress component acting on an element parallel to the x-axis
σ_{ys}	yield strength of the material
σ_{yy}	normal stress component acting on an element parallel to the y-axis
σ'	maximum normal stress of the joint
$\bar{\sigma}$	strength of the adhesive determined experimentally
τ_{xy}	shear stress component acting on an element in x-y plane

θ polar angle between an element and the crack tip
 Γ curve/path that surrounds the crack tip
 ρ_{CFRP} CFRP-reinforcement ratio
 δ_l slip value at the peak stress
 δ_f slip value at zero stress
 Ω angular displacement at midspan
 λ flange-to-web area ratio of I-beam
 ζ normalized crack length of I-beam
 ψ CFRP-to-steel area ratio of I-beam
 η CFRP-to-steel stiffness ratios of I-beam
 ϕ depth-to-width ratio of I-beam
 $\varepsilon_{\text{rupture}}$ rupture strain of CFRP
 τ maximum shear stress of the joint
 τ_f local bond strength that is $0.8f_{ta}$

LIST OF APPENDIX TABLES

<u>Table</u>	<u>Page</u>
A.1. Correction factors for repaired W4 × 13 beams.....	221
A.2. Correction factors for unrepaired (control) beams.....	222
A.3. Correction factors for repaired Full-Flange beams ($\eta = 0.75$).....	223
A.4. Correction factors for repaired Full-Flange beams ($\eta = 1.125$).....	224
A.5. Correction factors for repaired Full-Flange beams ($\eta = 1.5$).....	225
A.6. Correction factors for repaired Half-Flange beams ($\eta = 0.75$).....	226
A.7. Correction factors for repaired Half-Flange beams ($\eta = 1.125$).....	227
A.8. Correction factors for repaired Half-Flange beams ($\eta = 1.5$).....	228

LIST OF APPENDIX FIGURES

<u>Figure</u>	<u>Page</u>
B.1. Fit diagnostics panel of the correction factor for repaired W4 × 13 beams	229
B.2. Fit diagnostics panel of the correction factor for unrepaired (control) beams.....	230
B.3. Fit diagnostics panel of the correction factor for Full-Flange geometry ($\eta = 0.75$)	231
B.4. Fit diagnostics panel of the correction factor for Full-Flange geometry ($\eta = 1.125$)	232
B.5. Fit diagnostics panel of the correction factor for Full-Flange geometry ($\eta = 1.5$)	233
B.6. Fit diagnostics panel of the correction factor for Half-Flange geometry ($\eta = 0.75$).....	234
B.7. Fit diagnostics panel of the correction factor for Half-Flange geometry ($\eta = 1.125$).....	235
B.8. Fit diagnostics panel of the correction factor for Half-Flange geometry ($\eta = 1.5$).....	236

CHAPTER 1. INTRODUCTION

1.1. General

Infrastructure needs particular attention and improvement. The impact of deteriorated infrastructure is significant on the economy and safety. According to the American Society of Civil Engineers (ASCE 2013), over 20% of the 607,380 bridges in the United States are classified as structurally deficient or functionally obsolete, while the average age for all bridges is 42 years. The deficiency rate of these bridges in urban areas has been almost constant for over a decade without noticeable enhancement (USDOT 2008). According to the Federal Highway Administration, \$20.5 billion are needed annually to eliminate deficiencies in the nation's bridges over the next 15 years (FHWA 2013). Of interest are steel-girder bridges because of their susceptibility to corrosion and fatigue damage (Kim and Harries 2011). Over 50% of the structurally deficient or functionally obsolete bridges in the United States are made of steel (Deng and Lee 2009). Repairing damaged members is generally recommended rather than costly replacement. Traditional repair methods, such as steel-plating to existing steel girders, merely provide a short-term solution because repair materials are not durable (i.e., repaired members are still vulnerable to environmental, corrosion, and fatigue damage). The need for sustainable materials as well as cost-effective repair methods is, therefore, emerging.

Composite materials may be adhesively bonded to the tensile soffit of a deteriorated member to enhance structural performance: load-carrying capacity and serviceability (Kim et al. 2007, 2010a). Such a chemical bond method will not induce residual stresses and fatigue-crack problems that frequently accompany welded steel plates. Carbon fiber reinforced polymer (CFRP) composites have demonstrated significant potential as an alternative to conventional repair materials (Bakis et al. 2002; Lopez and Nanni 2006; Kim et al. 2010b). CFRP provides

favorable strength-to-density ratios, strong resistance to fatigue and environmental damage including corrosion, and easy implementation on site (Teng et al. 2003; Kim and Heffernan 2008). The high initial material cost of CFRP can be offset with reduced long-term maintenance expenses. In fact, the portion of material costs in the overall budget for a rehabilitation project is not significant (Hollaway and Cadei 2002). Noticeable advancement has been made with CFRP applications for civil structures over the last two decades; most improvements are concerned with concrete members (Teng et al. 2002). Recent studies exhibit the efficacy of CFRP repair for deteriorated steel structures (Zhao and Zhang 2007; Harries and El-Tawil 2008); however, extant knowledge is still incomplete to understand the behavior of such applications.

1.2. Problem Statement

1.2.1. Crack-Dependent Behavior of Steel Members Strengthened with CFRP

Recent research reports that CFRP strengthening can noticeably increase the load-carrying capacity of damaged steel beams (Tavakkolizadeh and Saadatmanesh 2003; Shaat and Fam 2008) and can enhance the stability of axial steel members (Harries et al. 2009; Zhao and Al-Mahaidi 2009). It is, however, not fully understood how externally bonded CFRP sheets interact with damaged steel members.

Of particular interest are the bond behavior and fracture characteristics of CFRP sheets bonded to a steel surface. Although such an investigation is crucial to understand the failure mechanism of a CFRP strengthening system for damaged steel members (e.g., fatigue cracks in bridge girders), there has been no research on the interaction between CFRP sheets and notched steel elements. It is, therefore, necessary to study the local response of CFRP sheets when associated with various crack properties. Such an investigation will eventually be used to understand the global behavior of damaged flexural steel members strengthened with CFRP

sheets. Contrary to reinforced/prestressed concrete applications that have design standards and guidelines (ACI 2007), virtually no design guidelines are available for steel applications of CFRP composites. Significant research efforts are, thus, required to warrant adequate usage of CFRP materials to rehabilitate steel structures.

1.2.2. Behavior of Notched Steel Beams Strengthened with CFRP

Previous research has shown that the load-carrying capacity of steel beams is significantly improved by applying CFRP materials (Rizkalla et al. 2008; Shaat and Fam 2008). Some experimental study reports that CFRP can enhance the flexural stiffness of repaired members (Sen et al. 2001). To simulate structural damage in laboratory-scale investigations, part of the tension flange is cut, or a web is notched (Al-Saidy et al. 2004; Shaat and Fam 2008). CFRP-repaired steel beams typically fail by either debonding or rupture of the CFRP (Shaat and Fam 2008). Nozaka et al. (2005) reported an experimental study regarding the effective bond length of the CFRP bonded to steel girders. The contribution of a bonding agent was highlighted in terms of redistributing bond stresses along the CFRP-steel interface. Lenwari et al. (2006) carried out a parametric study to examine the effect of various CFRP-repair schemes on the debonding strength of the CFRP bonded to steel beams. Linghoff et al. (2009) suggested a tapered CFRP laminate to reduce the peeling stress of the CFRP-steel interface. Harries and Webb (2009) conducted a simple four-point fracture mechanics test to assess the strain energy release rate of CFRP-repaired steel plates. Modeling efforts have been made to predict the behavior of steel beams bonded with CFRP. Colombi and Poggi (2006) proposed a simple two-dimensional finite element (FE) model for a steel beam strengthened with CFRP. The beam was simplified using a line element, and rigid links were employed to connect the beam and CFRP.

Haedir et al. (2010) suggested a model to predict the flexure of a tubular steel beam wrapped with CFRP sheets; the model was based on a conventional sectional analysis.

All existing modeling approaches assume a perfect connection between CFRP and steel, thus ideal strain compatibility across a beam section is observed (Fam et al. 2009; Pellegrino et al. 2009). While the efficacy of CFRP-repair for steel beams has been discussed through experimental and numerical studies, the primary interests are concerned with strength gain, failure mode, and interfacial stresses between the CFRP and steel. None of them addresses a relationship between the level of initial damage for steel beams and CFRP-repair.

1.2.3. Durability of CFRP-Strengthened Steel Beams

Steel-girder bridges are susceptible to corrosion and fatigue damage. Such a concern may increase for bridges situated in cold regions due to frequent use of de-icing salt, the transition of temperature-dependent material characteristics, and thermally induced stresses. Although CFRP repair has been increasingly accepted by the infrastructure community (Hollaway and Cadei 2002; Shaat et al. 2004; Rizkalla et al. 2008), scant information is available on the long-term performance and environmental durability. Currently available test results in this area include fatigue (Kim and Harries 2011) and wet-dry durability (Dawood and Rizkalla 2010). Very limited research has been conducted about the creep-induced distress of CFRP-repaired steel structures. Cold-region durability of such members is another area to explore (Kim et al. 2012).

While little work has been completed to examine the effect of sustained load and low temperature on the behavior of CFRP-repaired concrete members, the combined effect of sustained loading and low-temperature exposure has not been reported in the literature for the CFRP-repair of steel members. The lack of understanding about the environmental durability of the bond in a CFRP-steel strengthening system, such as the long-term exposure to low

temperatures in conjunction with the sustained loading, is one of the main reasons for the drawbacks of using CFRP materials in retrofitting metallic civil infrastructure.

1.2.4. Fracture Response of CFRP-Strengthened Cracked Steel I-Beams

As previously discussed, results for cracked steel members repaired with CFRP sheets illustrated the need for a failure criterion to predict the critical loads and to ensure the safety of the repaired members. Because the failure of such members ultimately involves crack propagation assisted by local stress intensities, some researchers examined the fracture mechanics' path to the problem by utilizing the elastic and fracture-material properties. A number of studies investigated the behavior of simple cracked steel plates reinforced with CFRP laminates by evaluating the stress intensity factors (SIFs) at the tip of the crack using finite element analysis (FEA) (Colombi et al. 2003; Lam et al. 2010; Yu et al. 2012; Wu et al. 2013). The proposed solutions indicated that the SIF at the crack tip of the CFRP-reinforced steel plates was affected by the CFRP repair.

The SIF, which defines the amplitude of the stress field ahead of the crack tip, for the CFRP-strengthened cracked beams cannot be overlooked. In the design against fracture and according to the fundamental theory of fracture mechanics, the applied SIF of mode I (K_I) must not exceed the material's fracture toughness (K_{Ic}) to preclude crack propagation. Although a number of studies proposed SIF solutions for cracked I-beams (Dunn et al. 1997; Albrecht et al. 2008; Ghafoori and Motavalli 2011), SIF evaluation for structural cracked steel I-beams repaired with CFRP composites has not been reported in the literature for the CFRP repair of steel members.

1.3. Objective of the Dissertation

This research is done to better understand and provide answers for the problems mentioned in the previous section. Although recent studies exhibit the efficacy of CFRP repair for deteriorated steel structures, extant knowledge is still incomplete to understand the behavior of such applications. The specific objectives of the study can be summarized as follows:

- To study the flexural behavior of cracked steel beams repaired with carbon fiber reinforced polymer (CFRP) sheets.
- To examine the interaction between the level of initial damage (i.e., crack size) and the CFRP repair.
- To examine the residual behavior of damaged steel beams strengthened with CFRP sheets subjected to a sustained load in conjunction with cold temperatures. Emphasis is given to flexural responses, including the performance of the CFRP-steel interface.
- To develop a reliable computational model to predict the flexural behavior of test beams, including CFRP debonding and crack propagation across the critical section of the repaired beams.
- To evaluate the fracture characteristics of cracked steel I-beams repaired with CFRP as well as to develop accurate and reliable solutions to predict the critical loads.

1.4. Scope of the Dissertation

The scope of this study consists of experimental investigations as well as intensive computational modeling. The primary focus of this research is to investigate the flexural behavior of cracked steel I-beams strengthened with CFRP composites, as mentioned in the previous sections.

The experimental program includes two phases. Phase I examines the behavior of steel beams with various damage properties that are repaired with CFRP sheets. Of interest is the interaction between the damage level and CFRP repair (i.e., the influence of initial damage, such as crack depth, on the behavior of a CFRP-repaired beam). A total of 6 beams have been tested in four-point bending configurations. Phase II of the experimental program examines the behavior of damaged steel beams repaired with CFRP sheets that are subjected to a sustained load in conjunction with cold temperatures. In this phase, a total of 12 beams have been tested in three-point bending configurations.

Two numerical models have been developed for cracked steel I-beams that are strengthened with CFRP and subjected to bending loads. The first model is a three-dimensional non-linear finite element (FE) model that is developed to predict the flexural behavior of the beams tested in Phase I. The proposed model is unique because it simultaneously considers crack propagation across the critical section of a steel beam repaired with CFRP and the debonding progression of the CFRP. The second numerical FE model is also a three-dimensional, developed to predict the effect of the CFRP material and geometry on the fracture response of the repaired beams. Then, a comprehensive parametric study is done and introduces predictive equations for structural cracked steel I-beams (i.e., W Shapes) repaired with CFRP. Both models are verified against experimental results.

1.5. Dissertation Organization

This dissertation is written in manuscript format and is divided into seven chapters. The following section is a brief description of the content of each chapter:

- **Chapter 1** contains an Introduction which includes the background of this research, problem statement and research justification, research objectives, research scope and methodology, and Dissertation Organization.
- **Chapter 2** presents a review of literature that is relevant to the research topic.
- **Chapter 3** presents a numerical investigation of the crack-dependent behavior for steel elements strengthened with CFRP sheets subjected to axial tension, which is a critical issue to elucidate the flexural behavior of CFRP-strengthened steel members with fatigue cracks.
- **Chapter 4** presents an experimental investigation and numerical prediction for using CFRP sheets to strengthen steel beams with various notch sizes.
- **Chapter 5** presents an experimental program to examine the long-term durability of damaged steel beams that are strengthened with CFRP sheets and are subjected to a sustained load in conjunction with cold temperatures.
- **Chapter 6** introduces a numerical method to evaluate the fracture response for structural cracked steel I-beams (i.e., cracked W Shapes) that are repaired with CFRP composites and are subjected to bending loads.
- **Chapter 7** provides the dissertation's summary and conclusions as well as recommendations for future research.

CHAPTER 2. LITERATURE REVIEW

2.1. Background

Metal as a structural material began with cast iron in the late 1770s, with a number of cast-iron bridges, mostly arched-shaped, constructed during the period from 1780-1820. In the 1940s, wrought iron replaced cast iron as the primary metal in construction. However, hot rolled steel is the most versatile material that can be used in bridge construction and it began replacing iron in the late 1800s.

Deterioration and structural deficiencies are among the major problems that threaten the nation's infrastructure. Of particular interest are steel-girder bridges. Over 43% of United States bridges are made of steel (Tavakkolizadeh and Saadatmanesh 2003). Steel-girder bridges are vulnerable to deterioration and deficiencies mainly due to the repeated live load (i.e., fatigue damage) and corrosion. The Federal Highway Administration (FHWA) became actively involved in monitoring the condition of bridges after the Silver Bridge collapsed into the Ohio River in 1967. They instituted a program that scheduled biennial inspections of bridges with the intent to determine and monitor developing problems. The FHWA reports that 31.3% of the girder bridges in the United States are deficient (FHWA 2009). In most cases, repairing the damaged members, rather than costly replacement, is recommended.

2.2. Conventional Strengthening Techniques of Metallic Structures

Structural strengthening, reinforcing, and improving capacity are of primary importance in bridge repair. Structural strengthening is used to increase the load capacity for structural members, supporting increased loads that were not accounted for in the original design, to allow for correction of errors occurred during design or construction, or to return a structure to its original designated load capacity. For steel-girder bridges, deterioration of the structural

capacity over time is usually due to impact damage, corrosion, and/or fatigue cracking (Hollaway et al. 2002; Schnerch et al. 2005).

The traditional rehabilitation methods for restoring the strength of steel structures typically involve bolting or welding steel plates to the structural member. This technique increases the effective cross-sectional area or the buckling resistance of the repaired structure (Bakht et al. 1979). Figure 2.1 shows the typical strengthening of a structural steel girder by welding and bolting steel plates to the existing structure.

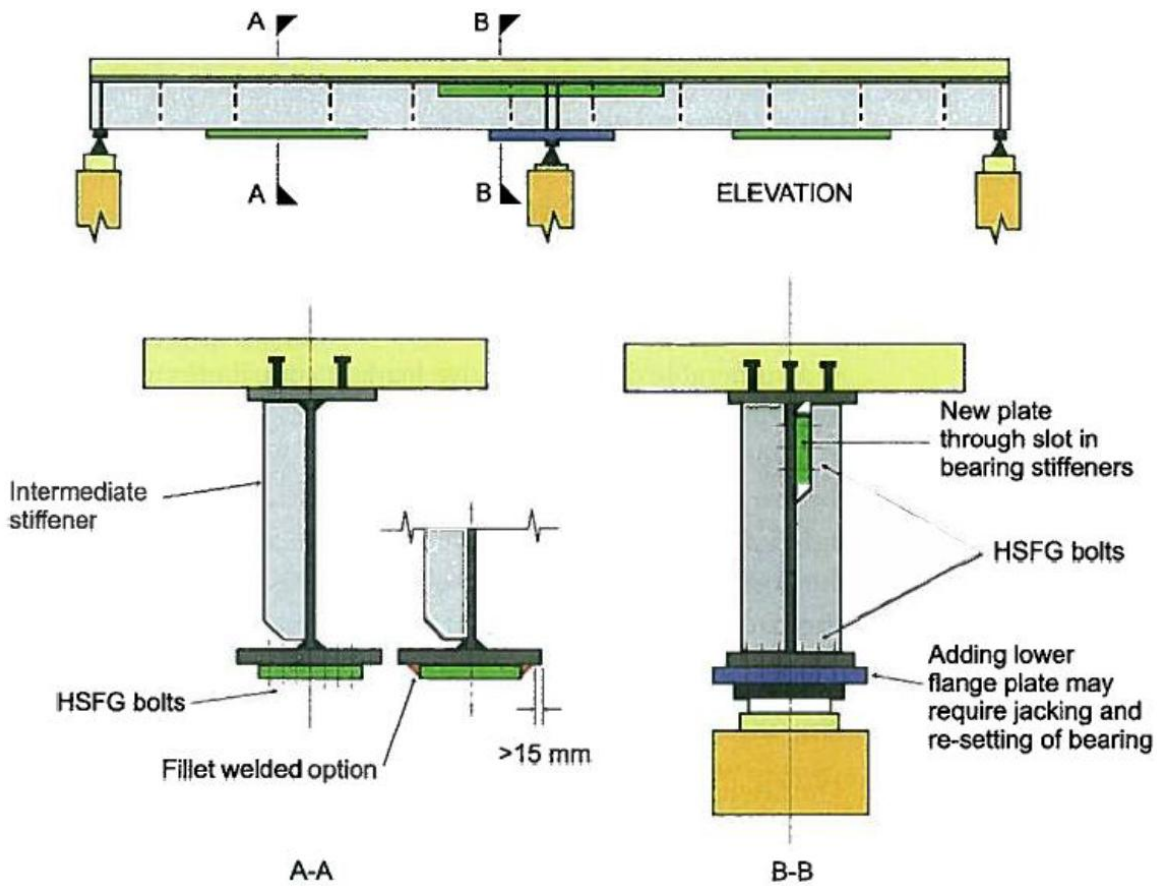


Fig. 2.1. Typical strengthening of steel girder with steel plates (Tilly et al. 2008)

To upgrade steel bridges, Bakht et al. (1979) recommended the following action:

- Welding cover plates to the critical flange areas of the bridge's floor beams.

- When flange material is added, the existing bolt system may become insufficient, which would be corrected by adding more bolts or substituting larger bolts.
- Reinforcing bearing stiffeners by bolting or welding angles or plates.
- If the web was not originally spliced to resist moment, splice webs to resist moment by adding plates.

These conventional methods for strengthening steel bridges have some constructability and durability drawbacks. Welding is not a desirable solution because it induces thermal stress in the steel member, leading to a reduction in its fatigue resistance (Kulak and Grondin 2002; Manteghi and Maddox 2006). Although mechanical connections (i.e., bolted connections) have better fatigue life, drilling holes results in a cross-sectional loss of the existing member, which reduces the efficiency of this retrofit technique. Not only are these steel plates heavy and may add considerable load to the structure, they are also susceptible to fatigue and corrosion that could lead to increased future maintenance costs (Colombi et al. 2003). Moreover, field drilling and aligning the bolt holes require highly skilled professionals and are time-consuming processes.

2.3. Strengthening the Steel Structures Using FRP Composite Materials

2.3.1. Introduction

Although traditional rehabilitation methods are still suitable and preferred in some structural steel elements, such as the gusset plates used to connect various elements of the bridge, there is a need to look for alternatives and to adopt a cost-effective and durable strengthening technique to overcome the limitations of conventional rehabilitation methods for steel members, as discussed in the previous section. Fiber reinforced polymer (FRP) composites, in the form of sheets or laminates, can be used to reinforce damaged structures by bonding them to the tensile

soffit of a damaged structural member using epoxy adhesives to enhance structural performance (Teng et al. 2003; Kim and Heffernan 2008). The advantages of FRP composites for structural rehabilitation are favorable strength-to-density ratios, durability, fatigue resistance, prompt execution on site, and reduced long-term maintenance costs (Teng et al. 2003; Kim et al. 2006, 2008a). The high initial material cost for FRPs can be offset with reduced long-term maintenance expenses. In fact, the portion of material costs in the overall budget of a rehabilitation project is not significant (Hollaway and Cadei 2002).

Application of FRP composite materials in the aerospace field and the marine industry is a well-established practice where composites are utilized as crack arrestors when repairing damaged metallic components and stiffening steel plates (Myhre and Beck 1979; Hutchinson 1992). The FRP materials have been increasingly used for civil engineering applications since the 1950s; the FRPs are utilized as a rehabilitation material for old buildings and semi-permanent structures (Wu 2006). Noticeable advancement has been made with FRP applications for civil structures over the last two decades, most of which are concerned with concrete members. The successful use of FRP composites as a strengthening material in various fields has recently attracted the rehabilitation community to study using this material to strengthen steel structures in civil applications.

2.3.2. Carbon-Fiber-Reinforced Polymer (CFRP)

FRPs are composite materials consist of fiber reinforcement such as aramid, glass, or carbon materials embedded in matrix (resin) material to form fibrous composites. While the fibers provide increased strength and stiffness, the resin matrix transfers loads to the fiber, bind the fibers together in place, and protects them against environmental attack. The most common matrices used in composites are polyesters, epoxies, and vinyl esters. Due to the fact that fibrous

composites are capable of achieving high strengths, they have become the most important class of composite materials (Agarwal et al. 2006).

FRP composite materials are usually manufactured by one of the three common processes: pultrusion, lay-up, and filament winding. Pultrusion is a continuous manufacturing process for producing long FRPs with a nearly constant profile. Figure 2.2 shows a schematic diagram for this process. Continuous fibers are drawn from a creel stands and saturated gradually in a resin bath where fibers are impregnated; then, excess resin is removed by pre-former, and then into a heated die. The desired length is then cut after the FRP enters the pulling system. The hand lay-up technique is the simplest and most commonly used method. Fiber reinforcements and resin are manually placed against a mold surface. The desired sheet thickness and shape are controlled by the layers of materials placed against the mold. This technique, however, is a low-volume and labor-intensive process. The filament winding technique can be automated to wrap resin-wetted fibers around a mandrel for the manufacture of surfaces of revolution such as tubes and pipes.

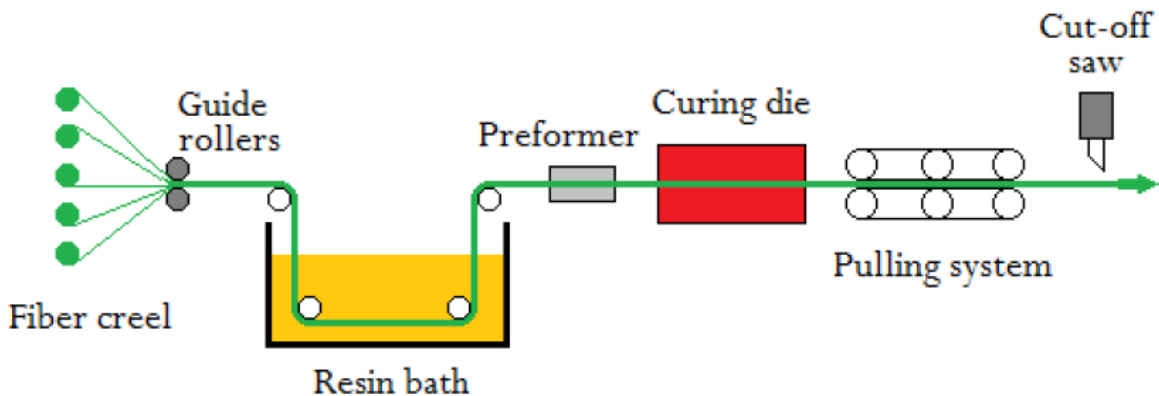


Fig. 2.2. Pultrusion scheme (Cui 2013)

Although carbon FRP (CFRP) and glass FRP (GFRP) composites are available to strengthen damaged structural members, CFRP is dominantly used because of its higher tensile

strength and modulus (ACI 2007). Figure 2.3 shows the stress-strain behavior comparison for steel and commercially available FRPs.

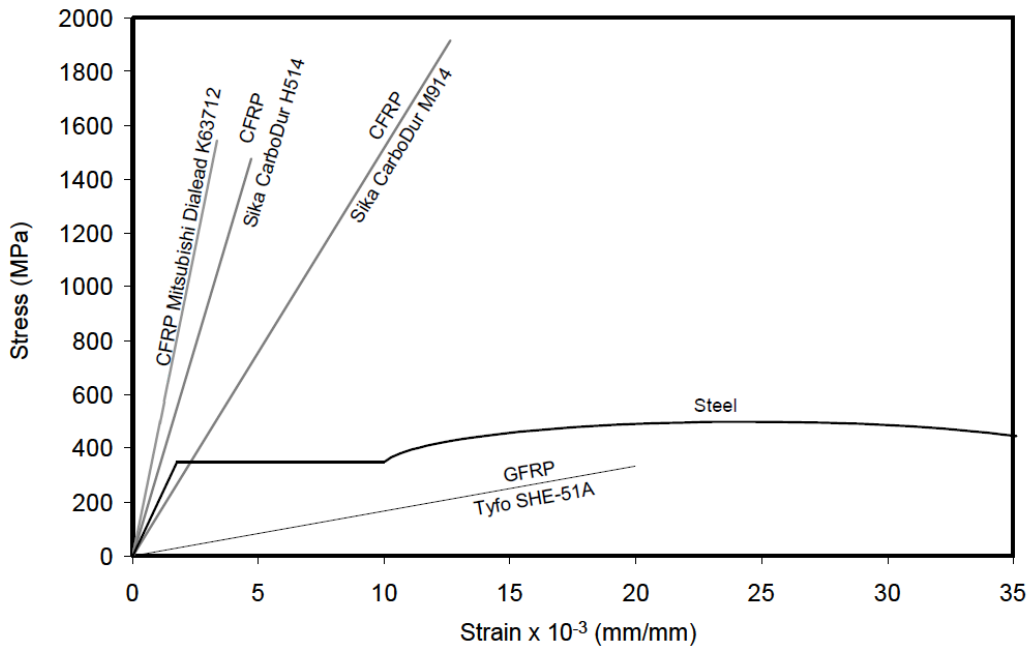


Fig. 2.3. Typical stress-strain curves for steel, GFRP, and three grades of CFRP (Shaat 2007)

Carbon or graphite fibers are considered the dominant high-strength, high-modulus reinforcement used in the fabrication of high-performance polymer-matrix composites. The technology for producing carbon fiber generally centers on the thermal decomposition for one of the three organic precursors: polyacrylonitrile (PAN), rayon, and pitch. Each precursor produces a carbon fiber with distinct advantages and disadvantages in terms of cost and properties. Figure 2.4 summarizes the five-step process by which the PAN precursor is converted into carbon fibers.

Property combinations of carbon fibers can be changed easily due to the ease of controlling their structure through the heat-treatment during the manufacturing process. Carbon fibers are in various forms: chopped, mat, woven, continuous, and fabric. Figure 2.5 shows some of the available carbon fiber products, such as sheets, rods, tubes, and strips.

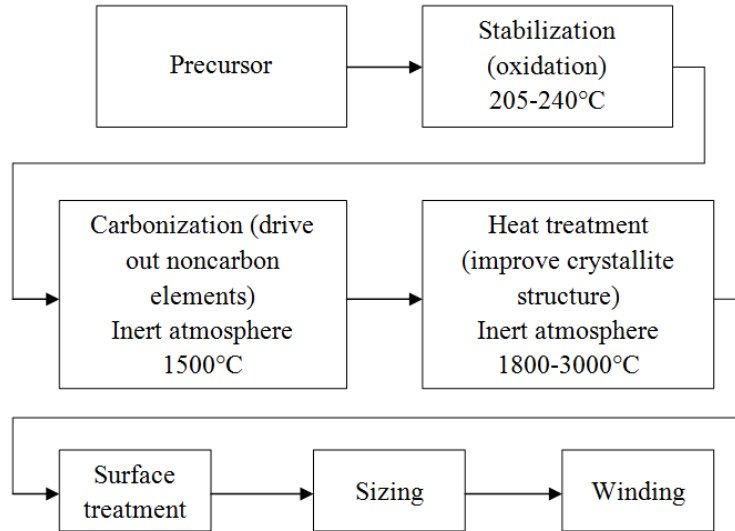


Fig. 2.4. Process of converting PAN precursor fibers to carbon fibers (Agarwal et al. 2006)

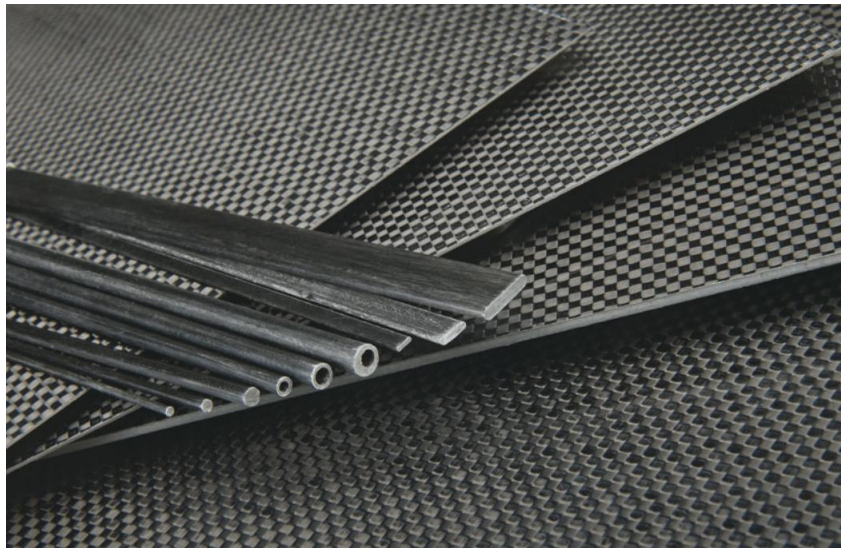


Fig. 2.5. Some available forms/shapes of carbon fibers (Great Planes 2014)

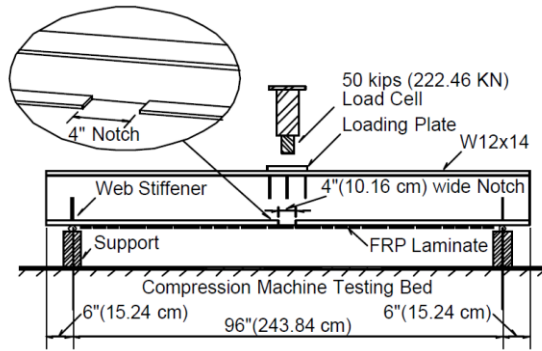
2.3.3. Flexural Response of Steel Beams Reinforced with CFRP Materials

Structural steel and CFRP materials have tensile modulus that are comparable. This means that CFRP materials are an ideal candidate for strengthening deteriorated steel members. Previous research has shown that CFRP can enhance the flexural stiffness of repaired members.

A number of experimental, analytical, and numerical studies were performed to evaluate the effectiveness of CFRP materials for strengthening steel members. The following section is a summary of recent test programs evaluating the effectiveness of CFRP-strengthened steel beams.

2.3.3.1. Cracked steel beams strengthened with CFRP

Steel beams were frequently notched to simulate structural damage such as corrosion and fatigue cracks prior to applying CFRP sheets. Liu et al. (2001) conducted a study to develop competitive techniques capable of retrofitting corroded steel members by testing artificially damaged steel beams that were retrofitted with CFRP laminates. Four W 310 x 21 steel beams were tested under three-point bending [Fig. 2.6(a)]. One beam (unit 1) was left intact (undamaged) to serve as a control specimen where the tension flanges of the three beams were completely cut at the midspan to simulate damage. The beam from unit 2 was not given the CFRP repair so that it could be used as a damaged control beam. All of the other beams had repairs that completed with the CFRP, as shown in Fig. 2.6(b). The bond length was examined by applying the CFRP plate for the entire length of unit 3's beam and only on one-quarter of the length in unit 4. To prevent local buckling, all beams were braced laterally. The failure mode for both unrepaired beams was lateral torsional buckling of the compression flange. Units 3 and 4 showed debonding of CFRP. In unit 3 this was a gradual process while unit 4's debonding was abrupt. Figure 2.6(c) shows the load-deflection responses at the midspan for all beams. Although none of the repaired beams reached the full strength of the intact control beam (unit 1), 56% and 41% of the load-carrying capacity were recovered for the unit 3 and unit 4 beams, respectively. Based on the experimental results, it was clear that increased in stiffness and plastic load for the corroded steel members can be achieved from the application of CFRP laminates to the tension flange of corroded steel members.

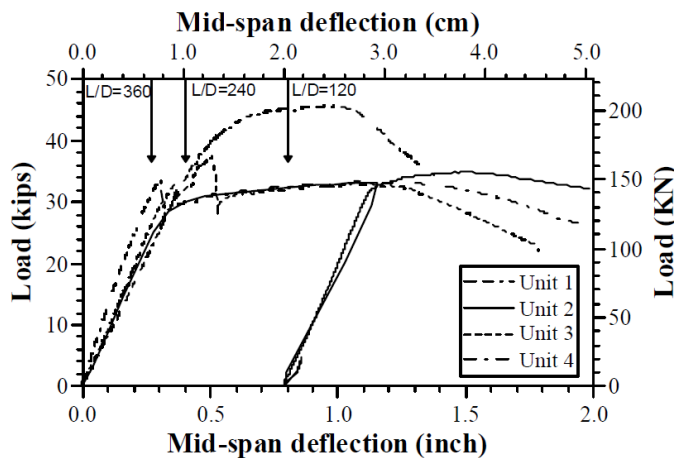


(a) Test set-up

Test Unit	Retrofit	Notch
Unit 1	none	none
Unit 2	none	c
Unit 3	a	c
Unit 4	b	c

a - Full length retrofit with 3.94 in. (100 mm) wide CFRP laminate.
 b - Quarter length retrofit with 3.94 in. (100 mm) wide CFRP laminate.
 c - 4 in. (10.16 cm) wide notch at the mid-span of the tension (bottom) flange.

(b) Test matrix



(c) load-midspan deflections

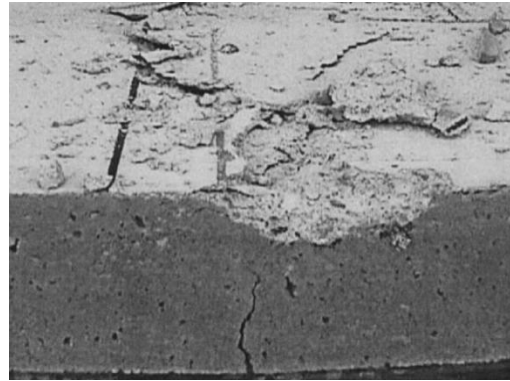
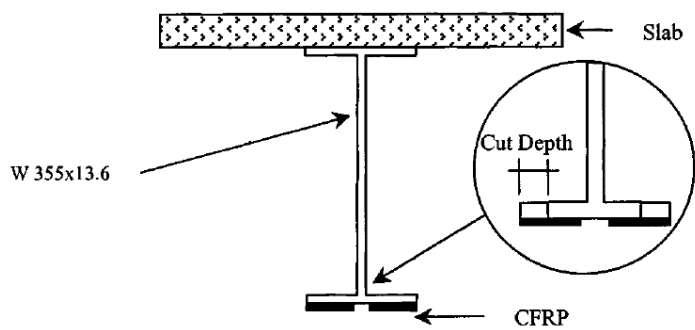
Fig. 2.6. Repair of steel girders with CFRP (Liu et al. 2001)

Sen et al. (2001) evaluated the flexural behavior of concrete-topped steel beams where CFRP laminates were used as the strengthening material. The objectives of the experimental program were to develop a procedure of CFRP-strengthening for steel beams and to assess the potential for this strengthening method. To simulate severe deterioration, the composite beams were preloaded to yielding of the tension flange. The strengthened beams showed an increased load-carrying capacity, up to 52% when compared to an unstrengthened beam while the stiffness improvement was insignificant.

Tavakkolizadeh and Saadatmanesh (2003b) tested steel-composite girders that had been repaired with CFRP laminates to determine their flexural behavior. A total of three large-scale

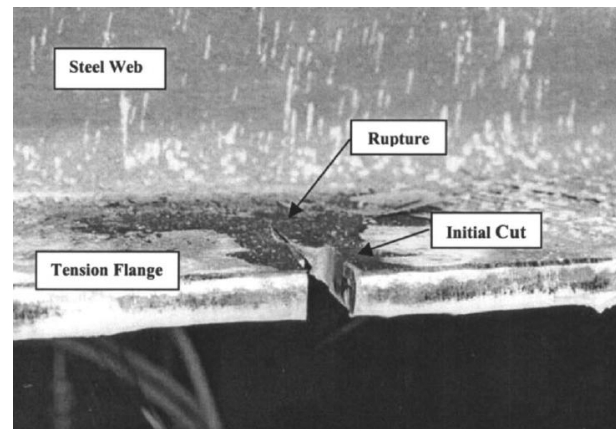
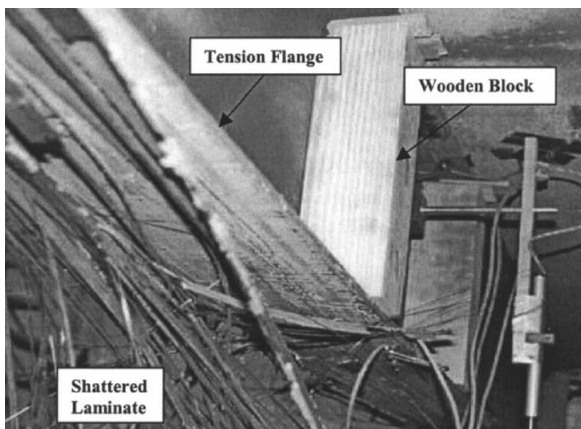
structural steel sections (W355x13.6) with concrete flange of 910mm wide x 75mm thick tested under static loading. Differing amounts of damage to the bottom flange (25%, 50%, and 100%) were simulated by cutting the tension flanges of the beams 43mm, 86mm, and 171mm, respectively [Fig. 2.7(a)]. Then, epoxy-bonded CFRP in 1, 3, and 5 layers was used to repair the damaged girder. CFRP overall length was identical for all girders and covered over 80% of the span length. The repairs were tested and the results revealed that the CFRP repair did restore the load capacity and also went beyond that with an increase of 20%, 80%, and 10% for the 25%, 50%, and 100% damaged girders, respectively, when compared to the capacity of the control (intact) beam that was calculated theoretically. Also, CFRP repair nearly restored the elastic stiffness of the girders to 91%, 102%, and 86% for the 25%, 50%, and 100% damaged girders, respectively, compared to the control beam. Three forms of failure conditions were looked for on the test beams: rupture of CFRP laminate, crushing of concrete, and complete debonding of CFRP for beams with 25%, 50%, and 100% loss of the bottom flange, respectively, as shown in Fig. 2.7(b) through (d). The study concluded that epoxy-bonded CFRP laminate is a very promising strengthening technique for damaged steel-concrete composite girders.

Following a similar approach, Al-Saidy et al. (2004) evaluated the potential of CFRP-strengthening for steel beams using a numerical model combined with a test program. A simple sectional-analysis model was advanced to attempt to forecast the flexure of CFRP-strengthened steel beams, based on force equilibrium and displacement compatibility. The bottom flange of the steel beams (W200 x 22) was partially removed introducing a 50% and 75% loss of the bottom flanges to represent a damaged condition. The developed model showed good agreement with experimental load-deflection responses. The flexural strength and stiffness of the damaged

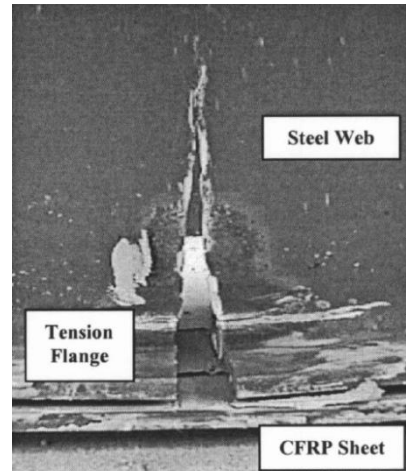
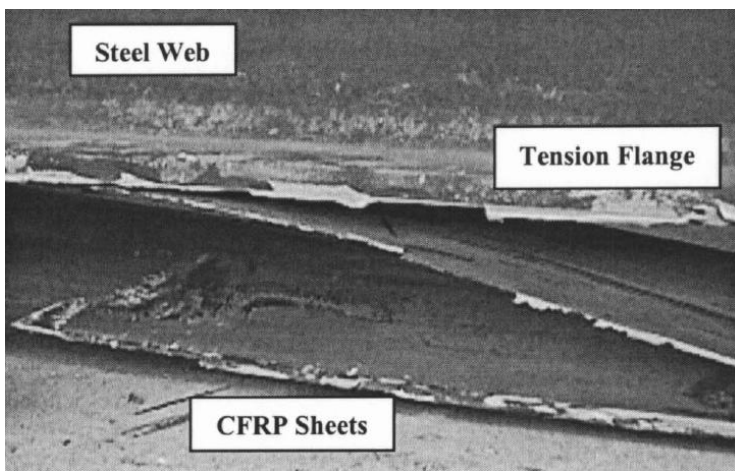


(a) Schematic of beams cross-section at the midspan

(b) Concrete crushing for a beam had a 50% reduction in tension flange



(c) CFRP rupture followed by flange rupture for a beam with a 25% reduction in tension flange




(d) CFRP debonding followed by web rupture for beam with 100% loss in tension flange

Fig. 2.7. Rehabilitation of damaged steel-concrete composite beams with CFRP (Tavakkolizadeh and Saadatmanesh 2003b)

beams were improved by CFRP strengthening, whereas the ductility of such beams decreased. No bond failure was observed for the strengthened beams.

Shaat and Fam (2008) utilized a test program to evaluate the flexural behavior of steel-concrete composite beams repaired with CFRP. Eleven 2,000 mm long, steel beams (W150 x 22 topped with a concrete slab of 465 mm x 75 mm) were notched at the midspan to simulate structural damage and were tested under bending. Test parameters included the type of CFRP sheets (standard and high CFRP modulus), and various strengthening schemes (CFRP was applied on either one side or both sides of the cracked flange with different lengths [Fig. 2.8(a)]. Examining the results showed that CFRP repair recovered the load-carrying capacity of the damaged beams to different levels and, for a number of beams, exceeded the capacity of the undamaged state. Additionally, test results showed that the bonded CFRP length affected the level of strength increase. For example, the increase in the strength for beams repaired with CFRP bonded to 8% to 97% of the span, ranged from 46% to 116% of the control (intact) beam, respectively, while the stiffness increases were 86% to 126% of the control beam [Fig. 28(b)]. Two failure modes were observed for test beams: debonding and rupture of the CFRP. Beams repaired with standard modulus CFRP failed by debonding, whereas rupture of CFRP was observed for beams repaired with CFRP with high modulus [Fig. 2.8(c)]. Results from the study indicated that bonding the CFRP sheet on both sides of the tension flange had an insignificant influence compared to beams repaired with the CFRP bonded to the external side of the tension flange.

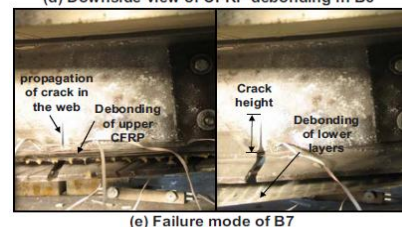
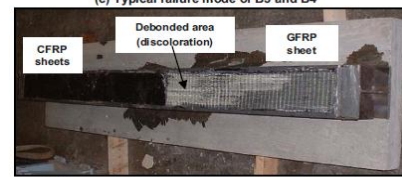
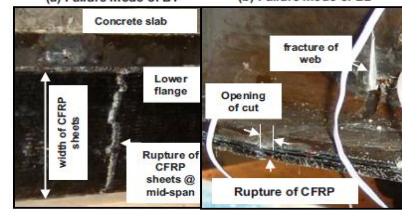
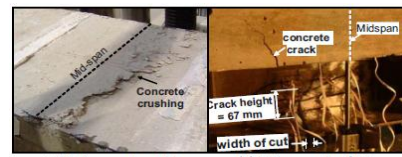
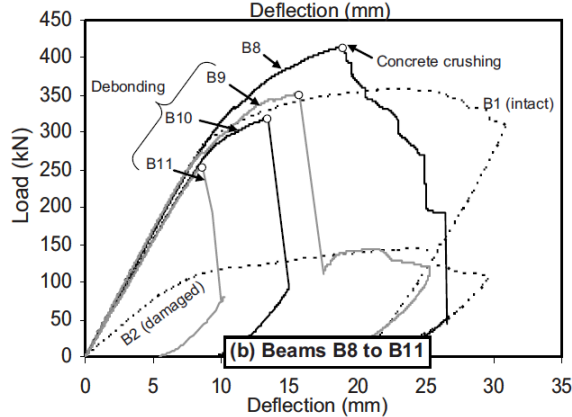
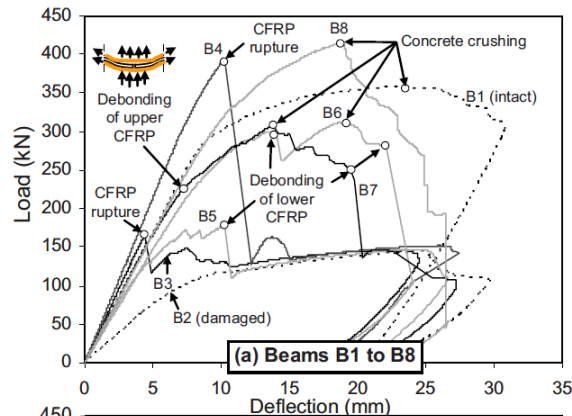
The influence of fatigue loading on the effectiveness of CFRP materials to strengthen cracked steel members has been reported through a number of studies. The CFRP repair of steel beams subjected to fatigue loading was investigated and was proven to be effective and

Specimen I.D.	Type of CFRP	Area of CFRP (mm ²)	ω^a % age	Bonded sides of the tension flange	Configurations of FRP layers [Σ (number of layers \times width \times length)]		
					GFRP base layer	CFRP layers 	
B1	Intact (control 1)						
B2	Damaged (control 2)						
B3	C1	648	87	Lower	1 \times 150 \times 1900	1 \times 150 \times 1900 + 2 \times 150 \times 1850 + 2 \times 150 \times 1800 + 2 \times 150 \times 1750 + 1 \times 150 \times 1700	
B4	C1	1134	152	Lower	1 \times 150 \times 1900	1 \times 150 \times 1900 + 2 \times 150 \times 1850 + 2 \times 150 \times 1800 + 2 \times 150 \times 1750 + 2 \times 150 \times 1700 + 2 \times 150 \times 1650 + 2 \times 150 \times 1600 + 1 \times 150 \times 1550	
B5 ^b	C2	668	198	Lower	1 \times 150 \times 1900	1 \times 150 \times 1900 + 2 \times 150 \times 1850 + 2 \times 150 \times 1800	
B6	C3	744	193	Lower	1 \times 134 \times 1900	1 \times 134 \times 1900 + 2 \times 134 \times 1850 + 2 \times 134 \times 1800	
B7	C3	716	185	Lower	1 \times 128 \times 1900	1 \times 128 \times 1900 + 1 \times 104 \times 1850 + 1 \times 87 \times 1850	
				Upper	2 \times 64 \times 1900	2 \times 64 \times 1900 + 2 \times 46 \times 1850 + 2 \times 35 \times 1850	
B8	C3	813	210	Lower	1 \times 128 \times 1900	1 \times 128 \times 1900 + 1 \times 128 \times 1850 + 1 \times 128 \times 1850	
				Upper	2 \times 64 \times 1900	2 \times 64 \times 1900 + 2 \times 64 \times 1850 + 2 \times 46 \times 1850	
B9	C3	813	210	Lower	1 \times 128 \times 1000	1 \times 128 \times 1000 + 1 \times 128 \times 950 + 1 \times 128 \times 950	
				Upper	2 \times 64 \times 1000	2 \times 64 \times 1000 + 2 \times 64 \times 950 + 2 \times 46 \times 950	
B10	C3	813	210	Lower	1 \times 128 \times 250	1 \times 128 \times 250 + 1 \times 128 \times 200 + 1 \times 128 \times 200	
				Upper	2 \times 64 \times 250	2 \times 64 \times 250 + 2 \times 64 \times 200 + 2 \times 46 \times 200	
B11	C3	813	210	Lower	1 \times 128 \times 150	1 \times 128 \times 150 + 1 \times 128 \times 145 + 1 \times 128 \times 145	
				Upper	2 \times 64 \times 150	2 \times 64 \times 150 + 2 \times 64 \times 145 + 2 \times 46 \times 145	

^aForce equivalence index.

^bLate application of FRP.

(a) Test matrix



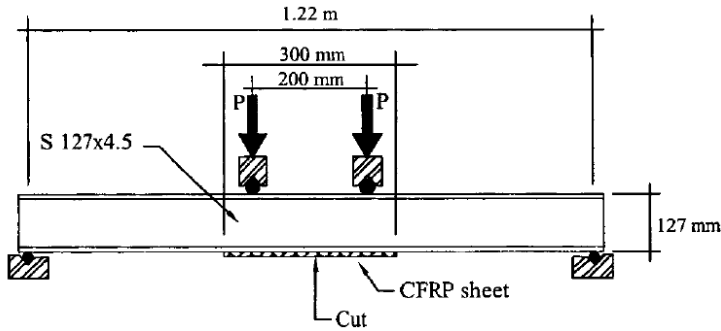
(b) Load-deflection behavior

(c) Failure modes

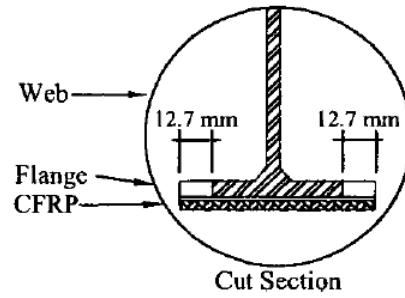
Fig. 2.8. Strengthening of cracked steel-concrete composite girders using CFRP material (Shaath and Fam 2008)

promising in prolonging the fatigue life of damaged beams. Tavakkolizadeh and Saadatmanesh (2003a) carried out an experimental program to investigate the fatigue behavior of damaged small-scale steel beams (S127 x 4.5) retrofitted with a CFRP patch under medium cyclic loading. A total of 21 beams were examined and tested under bending loading with stress ranges from 69 MPa to 379 MPa [Fig. 2.9(a)]. Fatigue sensitive details were approximated by making cuts on both sides of the tension flanges [Fig. 2.9(b)]. All beams were repaired with CFRP sheets that have identical lengths and thicknesses. S-N curves were developed to predict the fatigue life of the repaired beams. The repairs were successful in that the fatigue life was increased by a factor of 2.6 to 3.4 for stress ranges of 345 MPa to 207 MPa, respectively, compared to unrepaired beams. It was reported that retrofitting with CFRP decreased the crack-growth rate by 65% compared to the unretrofitted beams. Additionally, test results show that the average number of cycles to the ultimate strength after the onset of the crack for CFRP-strengthened beams was 3.5 times higher than the one for the unstrengthened counterparts [Fig. 2.9(c) and (d)]. Also, it was reported that, under lower stresses, the strengthened beams were able to withstand additional cyclic loading even after a complete cracking of the tension flange. The study concluded that CFRP retrofitting of damaged steel beams was a very promising practice to increase the fatigue life.

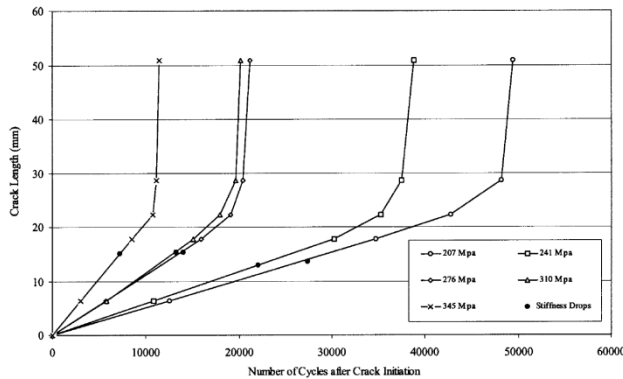
Kim and Harries (2011) also conducted tests that evaluated the flexural behavior of steel beams that had been purposely damaged and then strengthened with CFRP strips under static and fatigue loading. The primary foci of the investigation were the local plasticity near the damage location and the CFRP-steel interface. A total of six W150 x 18 steel beams were tested in three-point bending configuration. The beams were artificially damaged by cutting the tension flange



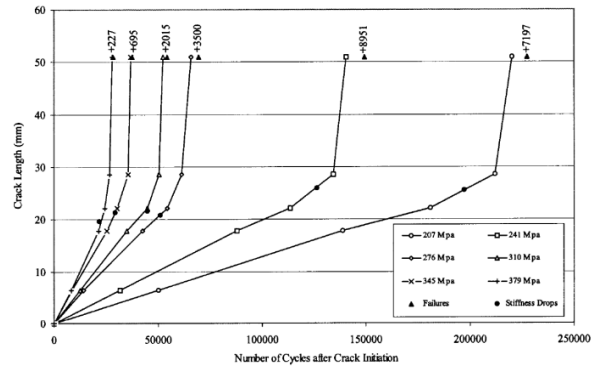
(a) Schematic of test set-up



(b) Schematic of cuts in the tension flange



(c) Change in the crack length for unretrofitted beams



(d) Change in the crack length for retrofitted beams

Fig. 2.9. Fatigue strength of steel girders strengthened with CFRP patch (Tavakkolizadeh and Saadatmanesh 2003a)

entirely at a location of 152mm offset with respect to the midspan, leaving a control beam undamaged. The initial notch in the tension flange was made to cause crack propagation from the beam flange to the web and to the initial CFRP debonding toward the closer support. Three beams were monotonically loaded while the remaining three beams were put under cyclic loading with stress ranging between 81 MPa and 274 MPa. The study reported that the static load-carrying capacity of CFRP-repaired beams was significantly improved compared to the intact (undamaged) beam. This influence of the CFRP repair did not proportionally affect the local plasticity near the damage. The stress range at the damage location significantly influenced the fatigue life of repaired beams and affected the rate of crack propagation. Brittle web fracture

of the repaired beams was observed when approximately 50% of the fatigue life was reached, while insignificant fatigue-crack growth was noticed during the first half of the fatigue life.

2.3.3.2. Other cases of strengthening steel beams with CFRP

Research efforts to investigate the effectiveness of strengthening steel girders using CFRP composites have not only focused on damaged or cracked beams (as discussed above), but also included the strengthening of plain or intact steel beams (Edberg et al. 1996; Gillespie et al. 1996b; El Damatty et al. 2003; Tavakkolizadeh and Saadatmanesh 2003a; Schnerch 2005; Dawood 2005; Colombi and Poggi 2006; Al-Saidy et al. 2007; Linghoff et al. 2006; Deng and Lee 2007), strengthening of naturally corroded or naturally deteriorated beams (Gillespie et al. 1996a), and strengthening of beams with tubular cross-sections (Schnerch et al. 2004; Seica et al. 2006; Photiou et al. 2006a). The findings from these studies consistently indicated that the presence of CFRP can help increase the strength and stiffness of the repaired beams, hence attracting the rehabilitation community to further study the potential adoption of CFRP composites for strengthening steel structures in civil applications.

2.3.4. Bond Characteristics and Force Transfer Between CFRP and Steel

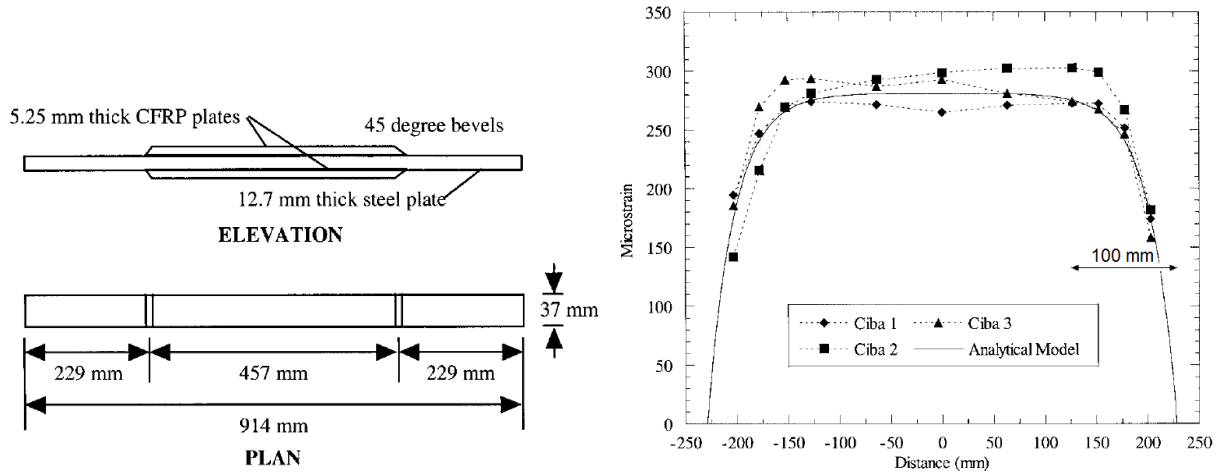
Existing knowledge illustrates the feasibility of using CFRP materials to retrofit steel beams. The bond at the steel-FRP interface is the dominant factor that controls the force transfer and the overall composite behavior of the system. Upon initiation of CFRP debonding, the stress transfer from the host beam to the CFRP is reduced. Unlike the FRP-to-concrete bonded joint where the concrete is the weak link, the adhesive bonding was confirmed to be the weakest link in the FRP-to-metal bonded joint due to the high stress concentration (Smith and Teng 2004). This can be clearly seen from the common debonding (steel-adhesive interface) failure mode that was most observed when testing strengthened steel members with FRP materials. Due to the

brittle nature of the debonding failure which is a very important aspect and concern regarding the safety and effectiveness of FRP-to-steel bonded structures, a number of studies have been conducted to understand the behavior of the bonded joints. Previous studies investigated the FRP-to-steel bonded joints, and a number of such as the surface preparation of the steel, thicknesses of FRP laminate and adhesive, resin and the fiber properties, environmental exposure, bond length, adhesive curing temperature, and the type of mechanical loading, were found to influence the bond performance (Bourban et al. 1994; Schnerch 2005; Shaat and Fam 2008; Nguyen et al. 2012). Different bond-testing methods and several approaches were adopted to investigate and predict the bond strength and behavior for FRP-strengthened steel structures.

A number of experimental studies were conducted to evaluate the CFRP-to-steel bonded joint behavior using single-lap and double-lap shear joint tests. Miller et al. (2000) investigated the behavior of a CFRP-to-steel bonded joint system by testing six double-lap shear joints [Fig. 2.10(a)]. The double-lap specimen consisted of two CFRP plates (457mm long x 37mm wide) bonded to both side of the steel specimen (914 mm long x 37 mm wide). Three types of adhesive were used in this study (Ciba 1, 2, and 3; Fig. 2.10(b)). Test results showed that nearly 98% of the applied load transferred to the CFRP plates along the first 100 mm of the end of the bonded plate [Fig. 2.10(b)].

Lam et al. (2004) also used the double-lap testing configuration to study the tensile strength of the steel-CFRP bond. It was concluded from the study that the increase in bond length had an insignificant influence for increasing the bond strength; however, the ductility of the bonded steel-CFRP joint was affected by the increase in bond length. Additionally, test results show that the tensile strength for the bonded joint improved significantly by increasing

axial stiffness of CFRP plate. The study reported that debonding of CFRP was the typical failure mode for all lap lengths.



(a) Schematic of the bond-test specimen (b) Measured and calculated strain along the plate

Fig. 2.10. Repair of a steel bridge girders with CFRP plates (Miller et al. 2000)

Al-Emrani et al. (2005) ran an experimental program to study the response of composite steel-CFRP elements, mainly in the post-yielding stage. The double-lap shear test specimens consisted of dog-bone shaped steel plates with CFRP strips bonded on each side [Fig. 2.11]. The selected shape of the test specimen (dog-bone) aimed at allowing the yielding of steel prior to CFRP failure. A variety of adhesives and CFRP laminates were utilized so that their effect on the behavior of the treated elements could be determined. The study reported that the behavior of test specimens varied widely. Test results showed that the increase in strength ranged from 12% to 80%. Also, it was reported that the degree of ductility for the bonded coupons varied from brittle to very ductile failure. Using standard modulus CFRP (155 MPa to 175 MPa) resulted in the highest gain for strength and ductility. However, debonding took place long after the steel underwent significant yielding at the mid-section. Also, specimens bonded with higher CFRP modulus (362 MPa to 383 MPa) resulted in an increased yield strength but experienced sudden rupture of CFRP at low strains.

Xia and Teng (2005) adopted a single-shear pull-off test to understand and model the debonding failure in CFRP-strengthened steel beams [Fig. 2.12]. A series of pull-off test specimens was studied to investigate the interface region between the CFRP and the steel joint, and to develop stress-slip curves that help understand the debonding mechanisms for such joints. As a result of the study and from the measured stress-slip responses of test specimens, a bi-linear bond-slip model was proposed to predict the ultimate load and effective bond length for the pull-off test specimen. The predicted bond strength was found to be dependent on elastic modulus, thickness, and width of the CFRP. Additionally, the study reported that the thickness of the adhesive layer significantly affected the failure mode. When a thick adhesive layer is used, debonding by plate delimitation, which is a brittle failure mode, was observed, whereas ductile debonding within the adhesive layer (i.e., cohesive failure) took place when a think adhesive layer was used.

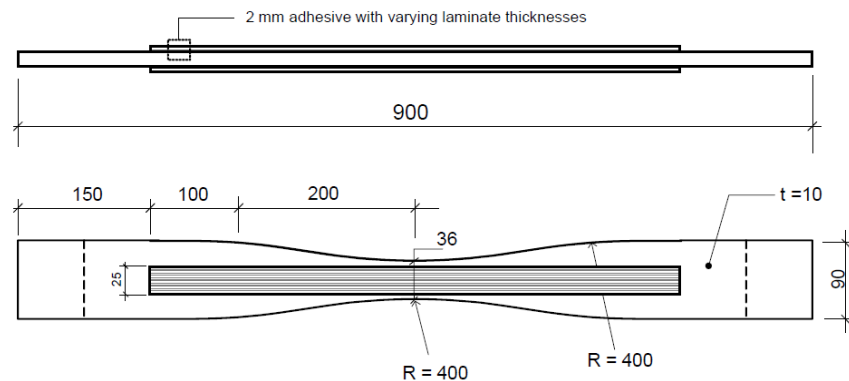


Fig. 2.11. Dog-bone shaped steel plates bonded with CFRP (Al-Emrani et al. 2005)

Fawzia et al. (2006) studied the behavior of CFRP-bonded steel elements. A double-lap joint specimen, consisting of two steel strips (210mm long \times 5mm thick \times 50mm wide) bonded with CFRP sheets (LCFRP = 80mm), was monotonically loaded in axial tension until failure took place. The CFRP sheet had a thickness of 0.176 mm with a tensile modulus of 215 GPa while the adhesive included a tensile strength of 32 MPa and a modulus of 1.9 GPa with a layer

thickness of 0.224 mm. It was reported that the dominant failure mode for normal modulus CRPP sheets (240 GPa) was the bond failure. Also, it was reported that additional increase in bond length beyond the effective bond length has an insignificant influence on the load-carrying capacity of the bonded specimen.

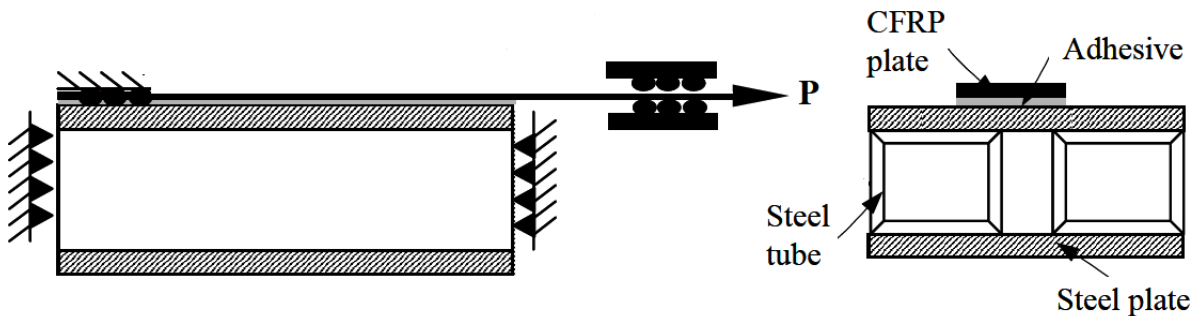


Fig. 2.12. Steel-CFRP pull-off test specimen and set-up (Xia and Teng 2005)

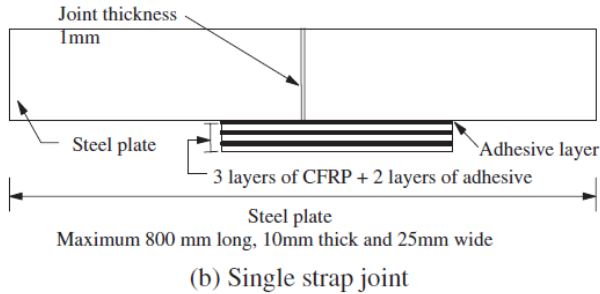
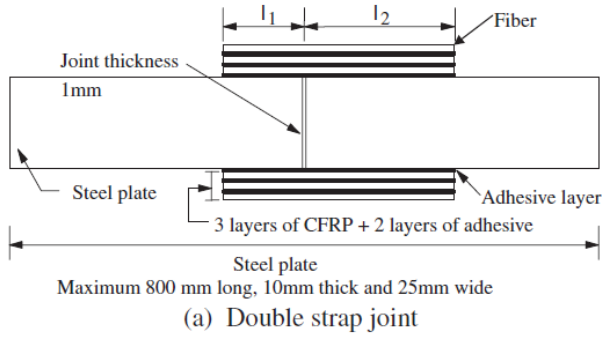
Bocciarelli et al. (2009) experimentally investigated the fatigue behavior of steel tension coupons bonded with CFRP. The bond-test specimen is similar to the one shown in Fig. 2.10(a). S-N curves for the strengthening system were developed by testing the coupons under a variety of stress ranges. Test results showed that debonding of the CFRP plates initiated at the plate ends (areas with high stress concentration) and then spread through the interfacial region between the adhesive and steel. It was reported that a degradation in stiffness precedes total failure of the bonded plate. It was noted that a reduction in stiffness of 85% of the original value indicated that debonding propagated from the end of plate to midspan of specimen. It was concluded that the fatigue resistance of a steel-CFRP bonded specimen is comparable to that of welded cover plates.

Wu et al. (2012) studied the bonding behaviors between steel and ultra high modulus CFRP laminates. Thirteen double strap steel joints were brought up and tested in tension. The investigators studied one kind of CFRP laminate that had an elastic modulus of 460 GPa and two kinds of adhesives. Test results showed that adhesive properties influenced both the strength as well as the failure mode of test specimens. Results also showed that the failure mode for

specimens bonded with adhesives with lower modulus altered from CFRP delimitation to CFRP rupture with the increase in bond length, which resulted in an increase in ultimate loads.

However, cohesive failure was consistently noticed for specimens bonded with a high adhesive modulus. The study reported that the effective bond length for the bonded specimens ranged from 70 mm to 110 mm.

Fawzia et al. (2013) led another experimental study to examine and compare the bond characteristics of a steel-CFRP joint in single- and double-strap configurations loaded in tension [Fig. 2.13(a)]. The primary objective was to study the load-carrying capacity, effective length, and failure mode for both joint types. Test results reported that adhesive-interface debonding was consistently observed as the failure mode for both the single- and double-strap joint [Fig. 2.13(b)]. It was concluded that the single-strap joint was efficient in regard to the bond length required to achieve an equivalent capacity as for the double strap joint. Only an additional 20% of the double-bond length was needed for the single-strap joint to achieve an equivalent load-carrying capacity. It was also reported that both joint types have a bilinear, shear stress-slip response that includes a linear elastic stage followed by softening and then debonding. The experimental studies discussed above used lap-joint tension specimens where the interface region between the steel and CFRP is only subjected to shear stresses. Other testing methods were conducted to better simulate the adhesive peel stresses that are generated by flexural loads. Nozaka et al. (2005) reported an experimental study regarding the effective bond length for steel girders bonded with CFRP laminate. The contribution of a bonding agent was highlighted in terms of redistributing the bond stresses along the CFRP-steel interface. A special test setup was developed in this study where the CFRP sheet was adhesively applied to the steel plates that



(a) Schematic of the strap joints

(b) Failure mode

Fig. 2.13. Steel-CFRP composite lap joints (Fawzia et al. 2013)

were bolted to the bottom flange of a steel girder (W360 x 101), as shown in Fig. 2.14. The study suggested that the adhesive in this setup was subjected to both shear and peeling stresses. The intent from the large hole in the web and the slit in the tension flange at midspan was to isolate the tensile force in the CFRP laminate. Five types of adhesive and two types of CFRP (elastic modulus 157 GPa and 114 GPa) were used to prepare 27 test specimens. It was reported that adhesives with higher ductility assisted in maximizing the strain for the CFRP laminate, resulting in a better redistribution of the stresses within the adhesive layer. Test results indicated that increased capacity of the bonded joint was observed as the number of CFRP increased. It was also indicated that any increase in bond length beyond the effective length had an insignificant influence on the increased strength of the bonded joint.

2.4. Durability of Metallic Structures Strengthened with FRP Composites

2.4.1. Introduction

Existing research and studies have confirmed that aged or deteriorated structural steel members can be effectively strengthened with FRP composite materials where stiffness and the ultimate strength of the enhanced members can be satisfactorily upgraded and nearly restored in some instances. However, inconclusive predictions regarding the long-term durability and performance aspects of the FRP-steel system remain a concern and an obstacle for the rapid expansion of utilizing FRP materials to retrofit steel structures. The lack of confidence among practicing engineers and designers to recommend this strengthening technique results as a factor of the unclear potential degradation of the steel-FRP system, which may be affected by the long-term exposure to the environment and the applied stresses, as well as the possibility of galvanic corrosion between carbon and steel.

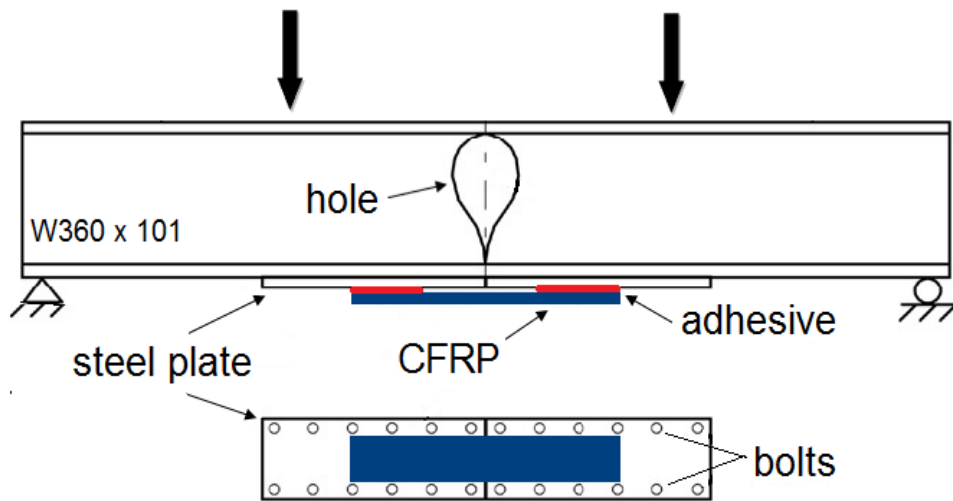


Fig. 2.14. Effective bond length of CFRP strips bonded to fatigued steel bridge I-girders (Nozaka et al. 2005)

Based on the available research, numerous factors which may influence the adhesive, adherent, or the interfacial region and, as a result, may affect the durability of the adhesively

bonded joints have been identified. Environmental exposure (e.g., temperature, water, salt, or radiation), physical exposure (i.e., stresses), adhesive and adherent types, the fiber type (in the case of FRP composites), and surface treatment all affect durability. The mechanical performance of adhesively bonded structures may improve, degrade, or stay unaffected by exposure to one or any combination of these factors. The discussions below highlight the factors that are seen as the most significant and their influence on durability of adhesively bonded joints.

2.4.2. Effects of Temperature and Environment

Civil infrastructure, particularly bridges, is typically exposed to various weathering conditions. In essence, it is vital to investigate and understand the environmental durability of the bonded system to ensure adequate long-term performance. Exposure to various environmental conditions, such as water, temperature, humidity, and other corrosive environments, may influence the bonded FRP system, not only by degrading each individual constituent, but also with the loss of interaction between them. Degradation of the retrofitting composite materials may result in structural instability which, ultimately, causes the failure of the bonded FRP-steel system. Regardless of the substrate material to which composites are applied, several factors influence the degradation of FRP composites such as stress corrosion that cause loss of strength of fibers, chemical degradation of matrix material, degradation in the fiber-matrix interface bond, time and temperature dependence of the matrix strength and modulus, and accelerated degradation due to the combined effect of chemical and temperature exposure (Karbhari et al. 2000; Agarwal et al. 2006).

Although using adhesives to bond metallic surfaces is common occurrence in marine, aerospace, and other manufacturing industries and the available durability data can be directly used in some instances, the bonded FRP-steel system is a relatively new practice for civil

infrastructure rehabilitation where durability of the bonded joints needs to be further investigated due to the different nature of civil engineering applications.

2.4.2.1. Durability of the joint interface

Environmental durability of the adhesive joints in general, and the FRP-steel bonded joints, in particular, has been studied by several researchers who concluded that a wet environment is a major determinant for the degradation and strength reduction of the adhesively bonded joints due to the pervasive nature of water combined with its ability of penetration. Kinloch (1983) indicated that the largest problem facing the adhesive scientists and technologists is the long-term durability of structural adhesive joints exposed to environments where the concentration of liquid water, or water vapor, is high; in these circumstances, the ingress of water is becoming the primary concern.

Water can penetrate the bonded joints by one or more of the following mechanisms: diffusion through the adhesive from the exposed edges, transport along the adhesive/substrate interface especially where wetting of the substrate is incomplete, capillary action associated with voids and micro-cracking that are mainly found in elderly joints or absorption through the porous adherent. Having penetrated into the joint, water may negatively affect not only the physical and chemical properties of the adhesive and the joint, but also the nature of the interface between the adhesive and the adherent by one or combined effects of the following processes: altering the properties of the adhesive, adhesive plasticization, causing swelling and residual stresses in the joint, attacking the interface between the adhesive and the adherent (Hartshorn 1986; Minford 1991; Bowditch 1996; Pizzi and Mittal 2003). The breakdown of adhesively bonded joints can be characterized into two types: a cohesive failure that results from deterioration within the

adhesive itself, and an adhesive failure which results due to a compromise at the interface between the adhesive and one of the substrates (Schnerch 2005). In related research, Hashim (1999) highlighted the main two mechanisms that contribute to strength reduction in bonded steel joints in wet environments: degradation of adhesive strength due to plasticization and corrosion of adherents, and interfacial attack to displace the adhesive from the adherent. It was noted that the latter mechanism is the most influential one.

According to the adhesion's physical absorption theory, adhesive bonds are attributable to secondary van der Waals forces (the weakest among all intermolecular forces) which develop between the molecules of the two different materials across their interface [Fig. 2.15]. The theory defines the thermodynamic work of adhesion between two materials to be the energy required to separate the bonded interface into two separate surfaces.

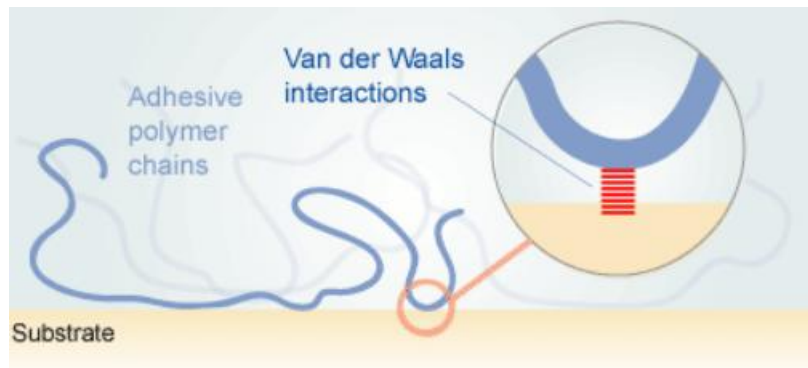


Fig. 2.15. Schematic for van der Waals forces at the adhesive-adherend interface (SpecialChem 2013)

In the presence of water, this energy becomes negative, indicating an unstable bond. That is to say, in wet environments, the force between the two adherents becomes repulsive which may lead to automatic debonding (Owens 1970; O'Brien 2003). Davis (1991) reported that, when water penetrates the adhesively bonded joint, the failure mode switches from cohesive failures that occur in the adhesive itself to the interface between the substrate and the adhesive. A

factor in this change could be the fact that metal oxide and polar surfaces are agents that assist in attracting water molecules that invariably interfere with the van der waals bonds across the substrate adhesive interface. Thermodynamically, this disruption in the bonds caused by wet environments can be seen by the work of adhesion in a chemically inactive medium, W_A , which can be defined as:

$$W_A = u_a + u_s - u_{as} \quad (2.1)$$

where u_a and u_s in Eqn. 2.1 are the surface free energies of the adhesive and substrate, respectively, and u_{as} is the interfacial free energy. In the existence of liquid, such as water, the work of adhesion, W_{Al} , becomes:

$$W_{Al} = u_{al} + u_{sl} - u_{as} \quad (2.2)$$

where u_{al} and u_{sl} in Eqn. 2.2 are now the interfacial free energies of the adhesive/liquid and substrate/liquid interfaces, respectively. In a static environment, the work of adhesion for a system that is bonded will be positive which would signal a stable interface. However, W_A could possibly become negative if there is moisture in the form of water. This would mean that the interface is no longer stable and may disconnect [Davis 1991].

The estimated long-term durability of adhesively bonded systems is most often determined by accelerated ageing environmental testing. The wedge crack test method, based on the concept of fracture mechanics, is evident to be highly dependable in determining and predicting the environmental durability of the adhesively bonded joints at the adhesive-adherent interface (Davis 1993). ASTM D 3762 is a commonly used wedge-crack propagation test where a wedge is driven between the adherents, cracking the adhesive at one end of the double-cantilever test specimen [Fig. 2.16]. Following this, the crack propagation under the combined effect of peel stresses and the desired environment (e.g. water, humidity, salt spray, heat, etc.) is

periodically recorded as a function of time. Finally, results are compared against determinant values and failure analysis is performed to provide understanding of the mechanism of crack propagation and bond durability (Marceau and Thrall 1985; Davis 1993).



Fig. 2.16. Schematic representation of ASTM D 3762 wedge test

Due to the great sensitivity of the wedge test to the environmental attacks on the bond between materials, Kharbania and Shully (1995) employed this method to investigate the environmental durability of the bond between the steel and composites. Steel surface of the test specimens was appropriately treated before the application of the composite. Since FRP composite was formed in situ, the resin itself acted as the adhesive to the steel surface. Under a room-temperature curing epoxy, five different types of fibers were used: three carbon fibers and two glass fibers [Fig. 2.17(a)]. Following to fabrication, specimens were exposed (for three weeks) to one of six different environments; water (at 65°C, 25°C, or -18°C), ambient, artificial sea water at 25°C, or freeze-thaw at 12 hr cycle between -18°C and 25°C. The study concluded that hot-water environment was the most aggressive one due to the deterioration at the interface as a result of prompt formation of oxides, whereas specimens subjected to freezing environment exhibited the most durable bonds [Fig. 2.17(b) through (d)]. Additionally, the type of fiber was found to play a role in affecting the environmental durability of the bond.

Hollaway and Cadei (2002) reported that the FRP-steel system is subjected to accelerated degradation when exposed to freeze-thaw cycles where development of drying and swelling caused by moisture can conceivably result in debonding of the laminates either on the steel side or the FRP plate. In a research program conducted to evaluate the environmental durability of the

bond of CFRP strengthening system to steel surfaces, Dawood and Rizkalla (2010) exposed CFRP-steel double-lap specimens to accelerated severe environmental conditions that included wet/dry cycles in a 5% NaCl solution at a temperature of 38°C for a time period up to six months. The findings concluded that the degradation at the interface between the adhesive and the steel was the primary reason behind the bonds loss of strength.

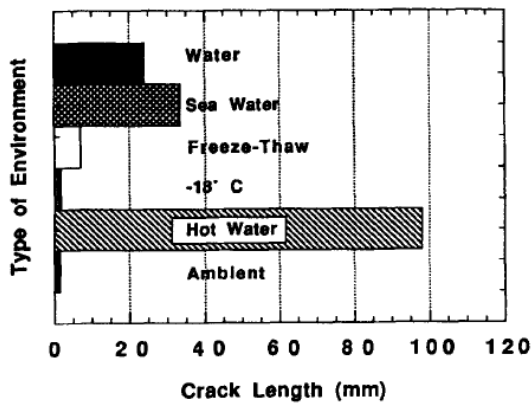
Fiber type (1)	Environment					
	Ambient (%) (2)	Hot water (%) (3)	-18°C (%) (4)	Freeze- thaw (%) (5)	Room- tempera- ture water (%) (6)	Salt water (%) (7)
C1-20	100	33.52	100	0	17.51	78.64
C1-30	100	13.96	100	0	14.74	22.71
C5-30	100	Broken	0	0	24.43	34.38
CE-30	100	47.35	0	0	10.88	23.33
GT-30	100	70.81	0	0	23.65	23.45

(a) Unimpregnated fiber properties

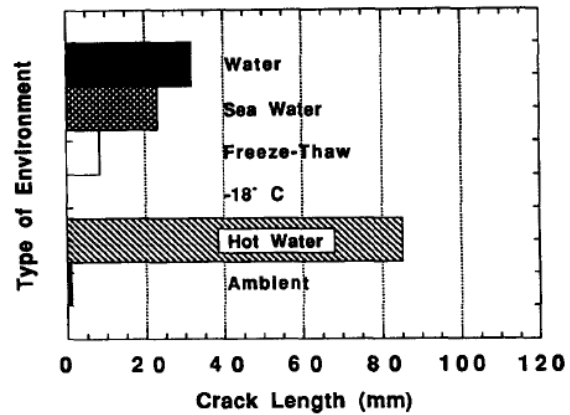
Fiber type (1)	Environment					
	Ambient (2)	Hot water (3)	-18°C (4)	Freeze- thaw (5)	Room- tempera- ture water (6)	Salt water (7)
C1-20	5	4	3	2	1	3
C1-30	4	3	5	3	4	4
C5-30	3	5	2	4	5	2
CE-30	2	2	1	5	2	5
GT-30	1	1	4	1	3	1

Note: 1 = Smallest crack extension and 5 = greatest crack extension.

(b) Evaluating and ranking of durability



(c) Durability of GT-30-based system



(d) Durability of C1-20-based system

Fig. 2.17. Determination of bond durability (Kharbania and Shully 1995)

In a study conducted by Colombi et al. (2005) to evaluate the effectiveness of CFRP composites in retrofitting steel structures in civil infrastructure, steel-CFRP double-lap shear coupons were exposed to different combinations of salt water spray and thermal cycles. Test results indicated a significant decrease in the ductility of the bonded joints between the steel surface and CFRP materials reached up to 50% of the unconditioned specimens. Nguyen et al.

(2012) conducted a study to evaluate the mechanical performance of steel/CFRP double strap joints subjected to harsh environments which included simulated sea-water at 20°C and 50°C, constant temperature at 50°C with 90% relative humidity, and cyclic temperature between 20°C and 50°C with constant relative humidity of 90%. Test results revealed that after one year of immersion in sea-water, significant reduction in joint strength and stiffness occurred; in particular specimens exposed to the higher temperature (50°C) exhibited loss in strength and stiffness of 26 and 55 percent, respectively, while CFRP composite showed unchanged mechanical properties under the same environmental condition. Additionally, test result indicated that a degradation of less than 10 percent in both strength and stiffness was reported in joint and bulk adhesive specimens exposed to the other two environments.

2.4.2.2. Durability of the composite materials

As indicated earlier, the second main mechanism, besides the interfacial attack, that contributes to strength reduction in adhesively bonded joints is the effect of the environment on the durability of composite materials, in particular the alteration in the properties of the adhesive itself. Changes in temperature and moisture content are the most commonly detected conditions that influence the properties of adhesives where exposure to such environments affects the distribution of the temperature and moisture concentration inside the material as a function of both position and time. These distributions, in return, influence the performance of the material (Agarwal et al. 2006).

A large number of researchers investigated the effect of environment on adhesives and composite materials. Water is a common environmental agent that affects the durability of adhesively bonded joints by changing the properties of adhesives through a reversible process such as plasticization or irreversible processes such as crazing, cracking, and hydrolysis (Moy

and Karaz 1980; Comyn 1987). The effect of water at different temperatures on the mechanical properties of aluminum lap-joints bonded with epoxy adhesive has been investigated by Brewis et al. (1983). The study reported that, under the combined effect of a wet environment and elevated temperature, the adhesive strength and modulus were reduced due to water ingress which significantly influenced the overall joint strength. Hand et al. (1991) studied the performance of several epoxy adhesives exposed to an adverse environment including exposure to different levels of humidity and submersion in water at room temperature. Test results revealed that all the adhesives investigated gained the bulk of their water uptake within 48 hours. Due to water submergence for 16 days, weight increase as a result of water absorption ranged from 2% to 7% compared to the dry weight. It was also reported that moisture absorption reduced the ultimate strength of the adhesives by 30% to 70%. Additionally, specimens that were subjected to a fixed strain level while exposed to moisture exhibited 50% to 90% stress relaxation. The effect of moisture ingress was evaluated via fracture analysis and stress relaxation. Analysis through fracture toughness suggested that ductility decreased with increased exposure duration while stress-relaxation results showed that some epoxy adhesives could retain about half their original dry strengths at equilibrium moisture strain.

Crasto and Kim (1996) conducted a study to evaluate the effect of moisture at different temperatures on the failure strength of CFRP double-lap shear coupons adhesively bonded with epoxy. Test results showed that saturated specimens under high temperature exposure exhibited a lower failure strength when compared to unconditioned specimens. This reduction of strength was explained by the reduction in glass transition temperature caused by the effect of water at elevated temperatures. Conversely, test results indicated that saturated specimens at low

temperatures exhibited higher failure strength than dry specimens. This increase in the measured strength was explained by the toughening of the epoxy adhesives caused by plasticization.

Bowditch (1999) indicated that it is imperative to consider the effect of water on the adhesive itself when investigating the durability of adhesive joints. Bowditch studied the durability of two bulk epoxy-based adhesives that each contained a different kind of inorganic fillers: calcium-carbonate filler particles and aluminum filler particles. After 2000 hours of immersion in 50°C water, the study showed that, when compared to unexposed specimen, the failure stress was reduced by approximately 85% and 78%, respectively. It was suggested that the presence of water significantly affected the strength; primarily due to either plasticization (in the case of the carbonate filler) or as a result of both plasticization and some interfacial adhesion force reduction (with the aluminum filler). Bowditch also indicated that to study the effect of water, careful emphasis needs to be on the temperature and the time that elapses because both factors may significantly influence the observed results.

In a study conducted to investigate the residual strength for an adhesive exposed to a wet marine environment, epoxy adhesives were bonded to steel lap-shear specimens (Hashim 1999). Following to curing, specimens were coated with epoxy paint to abase corrosion. Then, specimens were exposed to splash-zone conditions while under tensile loading of 10% of the initial failure load. After 5 years of exposure, a shear strength reduction of approximately 50% was observed.

Lapique and Redford (2002) studied the behavior of epoxy adhesives after being exposed to a 40°C temperature and water vapor with 90% to 100% relative humidity. Test results showed a weight increase for the epoxy specimen due to the increase water content with the exposure time. As a result, it was reported that the absorbed water worked as a plasticizer that caused

softening of the adhesive and a lowering of the failure strength while increasing the total deformation at failure.

2.4.3. Surface Preparation and Bond Durability

Taking the previously discussed findings into consideration, one can clearly ascertain the significance of the adherent surface to impact the quality of adhesively bonded joints. A considerable amount of research effort has focused on studying the effects of the substrates surface treatment and how this correlates to its performance, in particular the long-term durability of adhesively bonded joints. In a study conducted by Davis and Bond (1999) to investigate the basic principles essential for the yielding of strong and durable adhesive bonded structural joints, it was pointed out that poor processes during fabrication with a lack of quality surface preparation were considered to be the most significant deficiency that leads to the origination of most adhesive-bond failures. The study indicated that surface preparation for metallic substances is not exclusive to a clean exterior that is free of contamination, a chemically active superficial layer which enables the formation of chemical links between the adhesive and the adherent surface atoms is also important to achieve a bonded interface with longer-term environmental durability. Furthermore, the surface can be chemically modified to improve the hydration insusceptibility of the interface. Mays and Hutchinson (1992) claimed that cleaning before and after removing the weak layers is essential to produce a chemically active metallic surface that is free from contamination.

A common method to remove surface contamination from steel surfaces in civil infrastructure applications is through solvent degreasing such as acetone. Exposing a chemically active surface that is essential for any adhesive bonding process can be achieved by etching/abrasion of the metallic surface. An abrasion mechanism that is proven to be successful

in producing a high-energy steel surface is grit blasting (Davis and Bond 1999; Hollaway and Cadei 2002; Schnerch et al. 2005). However, performing grit blasting on a steel surface is typically insufficient to achieve an environmentally durable interface due to the potential exposure to contaminants or environmental conditions prior to applying the composite materials. As a result, the bond durability of the steel-epoxy interface for an infrastructure application can be improved by applying a primer such as the silane coupling agent immediately following grit blasting of the steel surface (Walker 1991; Mertz and Gillespie 1996; Cadei et al. 2004). In the study that was conducted by Dawood and Rizkalla (2010), a number of steel specimens were pretreated by brushing the surface with a silane coupling agent (γ -glycidoxypropyltrimethoxysilane) to study the primer's influence on the environmental durability of the interface. After analyzing the failure surface of a specimen that was pretreated with the silane, it was concluded that the presence of the silane obstructed the ingress of moisture into the interfacial layer and further enhanced the environmental durability of the bond. Additionally, it was suggested that the average measured bond strength increased by 20% due to the application of the silane adhesion promoter. Using primers, such as silanes, as adhesion promoters has been studied by other researchers and it was concluded that using such materials as part of the pretreatment of metallic adherents enhances the strength and long-term durability of adhesively bonded joints (Schrader and Cardamone 1978; Kinlock 1987; Tod et al. 1992).

2.4.4. Fatigue and Creep Effects

Adhesively bonded joints are expected to perform satisfactorily under service conditions which include, in addition to hostile environments, physical exposure such as static or dynamic stresses. Durability under sustained or cycle loading in combination with other environmental factors, such as moisture and elevated temperature, is a major concern when using FRP

composites to retrofit metallic structures due to the potential influence of such exposure on a reduction in the properties and durability of the bonded joints. Therefore, it is vital to understand the behavior of adhesively bonded joints under different loading and environmental conditions as well as any combination of the two so that the remarkable stiffness and strength of the retrofiting materials (i.e., composite materials) can be used with full advantage in structural applications.

The influence of stresses due to external loads on the durability of adhesively bonded joints can be evaluated by determining the residual joint strength after imposing a constant level of stress for a certain time, or by determining the time to failure at a given load. In a study conducted by Thrall and Shannon (1985), it was reported that the bonded joints degrade at a faster rate when cyclic stresses are applied in comparison to applying constant stresses. On the other hand, adhesive swelling, shrinkage, or thermal expansion disparity between the adhesive and the adherent (and/or between the fibers and the polymer matrix) may affect the durability of adhesively bonded joints by creating internal stresses. Hence, the long-term durability of adhesively bonded joints may be influenced significantly by the application of external stresses (e.g., fatigue or creep loading) in the presence of aggressive environments. Kinloch (1987) noted that application of stress accelerates the degrading effect of water; by either reducing the residual strength of the bonded joint or by decreasing its lifetime. It has also been observed that a critical stress level exists below which the degradation of the bonded joint does not occur or is not accelerated (Ripling et al. 1971; Cherry and Thompson 1977).

Number of studied investigated the combined effect of hostile environment and fatigue loading on the behavior of adhesively bonded joints. Su et al. (1992) conducted a durability program on double lap shear joints to study the effects of ageing and environmental exposure on

the fatigue life of mild steel joints bonded with adhesives that typically used in civil engineering applications. After 8 years of exposure to a variety of loading and environmental conditions, it was observed that adhesives cured with polyamide hardeners and had high initial strength and modulus exhibited excellent durability and that the fatigue life of some specimens actually improved with age. Conversely, other adhesives were adversely affected by the environment, particularly high humidity or exposure to the natural environment. It was concluded that the durability performance of the adhesive bore a close relation to the effects of moisture uptake in the adhesives.

Additional studies investigated the effect of high humidity exposure on fatigue performance of structural adhesive joints. Abel et al. (2006) used an accelerated test method based upon cyclic-fatigue testing to study the durability of adhesively bonded joints in two environments; dry environment of $25 \pm 2^\circ\text{C}$ with relative humidity of $55 \pm 5\%$, and wet environment where the joints were fully immersed in distilled water at $28 \pm 2^\circ\text{C}$. Test result concluded an existence of a critical humidity, somewhere between 55-80% RH, below which there is no significant effect of moisture upon the joint and that there would be no significant loss in joint performance upon exposure to relatively dry environments with humidity below 55% RH for prolonged periods. A similar decrease in fatigue life with increasing humidity was observed using aluminum-alloy substrates bonded using toughened epoxy structural adhesives (Fernando et al. 1996).

Harries and Fay (1992) reported a decrease in the fatigue life of steel-epoxy single lap shear joints as the test temperature increased. Test results also indicated that thinner adhesive layers result in stronger and more fatigue-resistance joints. It was also recommended that the glass transition temperature (T_g) of the adhesive should be above the maximum temperature

expected in service. Such degradation in the fatigue performance of structural adhesive joints as the temperature increased was also reported by Chen et al. (1990) and Ashcroft et al. (2001).

In recent past, Datla et al. (2011) conducted a study to investigate the effects of the temperature and humidity on the fatigue threshold and crack growth behavior of adhesively bonded aluminum asymmetric double cantilever beam specimens. It was reported that increasing the temperature to 80°C under dry condition have minor effect on the fatigue threshold, but caused an increase in the crack propagation rate. At lower temperatures, 40°C, fatigue behavior was noticed to be insensitive to moisture at higher crack growth rates, but became sensitive to moisture level in the test environment as crack growth rates slowed to the threshold. Additionally, degrading effect was also observed under hot-wet environment; the joint fatigue performance was degraded only due to the increased temperature at high crack growth rates, whereas degradation of the fatigue performance was primarily caused by elevated moisture at lower crack growth rate.

Similar to fatigue, limited amount of data have been reported regarding the environmental creep resistance of adhesively bonded joints. Small and Fay (1990) investigated the creep behavior, over three years period, of mild steel-epoxy lap joints under the effect of two environmental exposures; hot-wet (45°C and relative humidity of 95%) and hot (70°C) environments. Test results revealed that the effect humid environment on the failure time was more significant than the effect of dry conditions at 70°C as a factor of 10 times. Failure of specimens exposed to dry conditions was explained by the fact that such environmental exposure combined with loading caused the adhesive to creep and peel at the interface between the adhesive and the adherent. Such failure that included creep of the adhesive and peeling at the interface was accelerated due to exposure to high humidity.

Horton et al. (1992) investigated the durability of adhesively bonded aluminum joints under the combined effect of sustained load and environmental exposure, including submersion in distilled water and dilute solutions of sodium chloride. The test results indicated that the combined effect of stress and environmental exposure was more detrimental to the durability of the bond than environmental exposure alone. It was also found that the combined effect of stress and diluted solution of sodium chloride was more damaging to the bond durability than stress combined with distilled water. Such bond deterioration was explained by two possible mechanisms; interface instability and/or corrosion of the substrate material.

Dawood (2008) examined the effect of static loading on the environmental durability of CFRP-steel double-lap shear specimens. Test specimens were exposed to severe environments consisting of one week wet / one week dry cycles for a period up to six months. Submersion in 5% NaCl solution at a temperature of 38°C represented the wet portion of the cycle; whereas the dry cycle included exposure to ambient out-door temperatures (-9°C, 40°C, and 16°C). To study the effect of sustained load on the environmental durability, in addition to the accelerated environmental exposure, other double-lap shear specimens were subjected to a sustained load that represented 35% of the ultimate strength of the specimen that did not undergo the sustained load and environmental exposure trials. Both categories, loaded and unloaded specimens, were tested monotonically to failure, in tension, to appraise their residual bond strength. Test results revealed that degradation in the bond strength of approximately 60% was measured due to environmental exposure alone (unloaded specimens). For specimens subjected to both sustained loading and environment (loaded specimens), it was reported that a slight decrease in the measured strength was recorded compared with unloaded specimens. A conclusion was drawn from this study stated that the bond durability of tested specimens was not significantly affected

by the application of the sustained load. Meanwhile, it was indicated that not applying sufficient level of sustained loading that may have caused cracking and distress of the bond is a possible reason for such minor effect on bond durability.

2.4.5. Galvanic Corrosion

The possibility of galvanic corrosion between steel and carbon fiber becomes a major concern as it is also considered a primary mechanism of environmental degradation of adhesively bonded joints that ultimately affect the long-term durability. Unless the environmental exposure is actively corrosive towards the steel, loss of strength in adhesively bonded steel joints due to corrosion is not a concern. Theoretically, galvanic cell will not be generated as long as no contact between the two materials. However, both steel and carbon fibers possess metallic characteristics, hence initiating corrosion cells become highly possible. Number of conditions is necessary before bimetallic (galvanic) corrosion can take place; the two metals (electrodes) must have potential difference under direct electrical contact while immersed in an electrolyte solution (i.e. sea water). Due to the different natural potential between the two metals in the electrolyte, a current will flow from the more electronegative metal (anode) to the one with more electropositive (cathode), which will cause the anode to experience more corrosion (Francis 2000). Therefore, loss of bond strength due to galvanic corrosion becomes a major issue when using CFRP materials in strengthening steel structure, particularly in the presence of corrosive electrolytic environments. In civil infrastructure applications, electrically conductive liquids are very likely to be generated with the presence of moisture, deicing chemicals, salt, and other materials which may cause galvanic corrosion.

Tucker and Brown (1989) conducted an experimental study to investigate the possibility of galvanic corrosion for CFRP/epoxy (214mm long x 13mm wide x 6.4mm thick specimens)

and CFRP/vinylester (203mm long x 13mm wide x 9.5mm thick specimens) composites when directly coupled with mild steel in natural seawater environment. The study reported that formation of blisters (voids filled with solution) on the CFRP surface of the vinyl-ester based CFRP was significant, unlike the epoxy-based CFRP that did not exhibit such blistering. Although the study indicated that the cause of blister formation and the nature of the blisters remain uncertain, possible mechanisms for the formation of such solution-filled voids were suggested. Firstly, chemical composition of the resin material may have played a role in formation of blisters as it was noticed in the vinyl ester and not in the epoxy. Also, since blisters occurred in a regular pattern that coincided with the transverse fiberglass tows used to hold the carbon fiber in place, moisture diffusion into the composite and migration of water soluble molecules within the glass fiber may have been the reason for the blistering process by creating environments favorable for the buildup of a strong osmotic pressure within the composite. Lastly, it was suggested that poor consolidation of the composite materials during fabrication may have trapped voids in the CFRP that may have filled with fluid during the exposure to seawater.

Bellucci (1991) investigated the effect of metal and temperature on the galvanic corrosion induced by CFRP composites coupled with two different metallic materials (aluminum and steel) in neutral and air-saturated aqueous 3.5% NaCl solutions. The behavior of galvanic corrosion was studied by measuring the galvanic current, weight loss, and potentiostatic polarization curves. The experimental results revealed that the degree of galvanic corrosion is different from one metal to another where both steel and aluminum exhibited significant galvanic corrosion when coupled to CFRP composites. Also, test results concluded that galvanic corrosion can be increased by increasing the ambient temperature. In the second part of this study, Bellucci

(1992), the effect of CFRP-to-metal area ratio on the galvanic corrosion under the same environmental exposure as in the previous year was investigated. Test results indicated that the galvanic current is directly proportional to the cathodic area (CFRP) when coupled with steel or aluminum alloys and its independent on the anodic area (metal). As a result of this, the study suggested that the rate of dissolution of the metal may increase (i.e. increase of the corrosion rate) in the case of any CFRP exposure that may result from any loss of adhesions. The effect of cathode area on galvanic corrosion was also reported from a previous study (Evans and Race 1958) where it was concluded that a greater galvanic current is generated as the cathode area available for oxidation reduction increases.

Tavakkolizadeh and Saadatmneesh (2001) presented the results of an experimental study conducted to investigate the galvanic corrosion between CFRP laminates and steel and to evaluate the corrosion rate under two simulated aggressive environments; seawater and deicing solution. In addition to the two different environments, the study considered the effect of two more parameters on the corrosion rate of CFRP-steel system; the amount of epoxy coating of carbon fibers and the type of solvents used to remove sizing agents from the surface of loose carbon fibers. To investigate the corrosion properties, two tests were carried out; potentiodynamic polarization and galvanic corrosion. Test results indicated the presence of the galvanic corrosion is exist when there is a direct contact between the steel and CFRP. Also, test results showed that galvanic rate is highly proportional to the thickness of epoxy coating; the thicker the epoxy coating the less galvanic corrosion rate. On that matter, it was reported that galvanic corrosion rate in seawater and deicing salt reduced by 21% and 23%, respectively, when 0.25 mm of epoxy coating was applied. Additionally, it was concluded that the effect of deicing salt on galvanic corrosion rate is higher than the effect of seawater; such difference was more

noticeable for carbon fibers without epoxy coating. Regarding the effect of sizing agent, test results revealed that acetone was the most effective solvent in decreasing the galvanic corrosion rate. Finally, the use of nonconductive layer such as applying an isolating epoxy film on the surface of steel or using a fabric sheet between the carbon and steel was suggested as preventative alternatives for galvanic corrosion.

Considerable number of studies focused on the obstruction of galvanic corrosion phenomenon. Evans and Race (1958) suggested that insulating the two different metals from one another or applying coating with a water resistant sealant can prevent the galvanic action from happening. Trawinski et al. (1984) studied the effect of number of coatings on the joint durability of steel using wedge specimens. The study reported that specimens coated with zinc-phosphate exhibited optimum durability.

Although the use of FRP layer, such as GFRP, as an insulation layer between the steel and CFRP was suggested as a method to prevent galvanic corrosion (Hollaway and Cadei 2002), relying on such technique may be misleading due to the fact that GFRP material may be less durable than the adhesives and therefore it requires more attention (Choqueuse et al. 1997). In a related study conducted to investigate the long-term environmental degradation of composite materials in seawater, Sloan and Talbot (1992) indicated that after a few years of exposure to environmental conditions, only few materials can reserve their insulating properties due to number of factors such as chemical disruption, wear, or/and absorption of the electrolyte solution.

2.5. Analysis and Design

2.5.1. CFRP-to-Steel Bonded Joint

Finite element analysis (FEA) and analytical studies have also been used to evaluate stresses in bonded steel-CFRP joints. In fact, many of the experimental studies discussed above used the FEA method to make a comparison with the results obtained from proposed analytical models. FEA models have been developed to evaluate the bond stresses of the bonded steel-CFRP joints taking advantage of the powerfulness of this technique in studying variety of joint configurations and the effect of materials constitutive properties and geometry on the behavior of the bonded joints.

Based on Hart-Smith's one dimensional model, Albat and Romilly (1999) brought forth a basic one dimensional linear elastic analytical model for double lap shear joint and double sided reinforcements so that the adhesive shear stress distribution and normal stress distribution along the bonded length could be studied. This experiential model included a correction factor to allow for the shear lag in the adherends. Although the expression for the normal stresses was not presented, the one addressing the stresses in the outer adherend was presented. This expression is important because the stresses can be directly compared to the one measured experimentally through bonding strain gages to the outer adherend. The proposed model was experimentally verified by number of researchers (Miller et al. 2001; Matta et al. 2005; Schnerch et al. 2006; Colombi and Poggi 2006a). Eqn. 2.3 presents the longitudinal stress in the cover plate (i.e., outer adherend), σ_o , along the bond length $0 < y < \ell$ which is symmetric about the z -axis:

$$\sigma_o = \frac{1}{2} \left[\frac{P}{E_o t_o} - 2(\alpha_i - \alpha_o) \Delta T \right] \left[\cosh(\lambda y) - \frac{\sinh(\lambda y)}{\tanh(\lambda \ell)} \right] + \left[\frac{P}{E_i t_i} + (\alpha_i - \alpha_o) \Delta T \right] \left[1 - \frac{\sinh(\lambda y)}{\tanh(\lambda \ell)} \right] \quad (2.3)$$

where

$$\lambda = \left(\frac{\frac{1}{E_o t_o} + \frac{2}{E_i t_i}}{\frac{t_i}{4G_i} + \frac{t_a}{G_a} + \frac{3t_o}{8G_o}} \right)^{1/2}$$

E is the tensile modulus, G is the shear modulus, α is the coefficient of thermal expansion, ΔT is the change in temperature, subscripts i and o refer to inner and outer adherents, respectively, and a refers to the adhesive. All remaining parameters in Eqn. 2.3 are defined in Fig. 2.18.

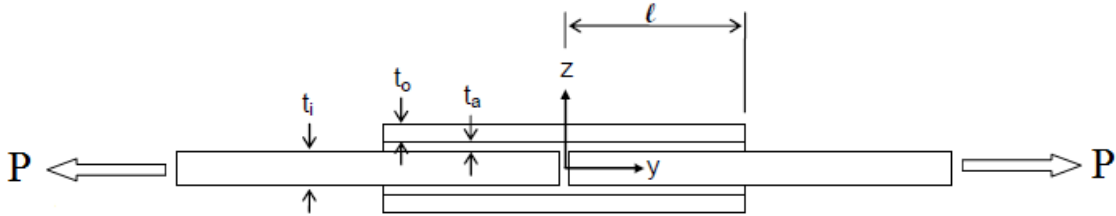


Fig. 2.18. Schematic for double-lap shear joint configuration (Albat and Romilly 1999)

The above analytical model assumes uniform stresses through the thickness of the adhesive. Consequently, Diaz et al. (2009) proposed an analytical model where the double-lap joint was considered as stacking of Reissner-Mindlin plates. The adhesive layer included two interfaces which result in two different stresses to be calculated at each of the adherent-adhesive interfaces.

Typically, the capacity of adhesively bonded joints is governed by the properties and strength of the adhesive material. Cadei et al. (2004) suggested that when both shear and peel

stresses are applied to the adhesive joint, the maximum principal stress, σ_1 , can characterize the failure of the adhesive layer, as follows:

$$\sigma_1 = \frac{\sigma'}{2} + \sqrt{\left(\frac{\sigma'}{2}\right)^2 + \tau^2} \leq \bar{\sigma} \quad (2.4)$$

where σ' and τ in Eqn. 2.4 are the maximum normal and shear stress of the joint, respectively, and $\bar{\sigma}$ is the strength of the adhesive that can be found experimentally.

Number of studies focused on developing predictive models to help anticipate strength degradation and life expectancy of adhesively bonded joints exposed to hostile environments. Such predictive modeling methodology is becoming more popular when studying adhesively bonded structures as it assists to minimize the uncertainty of the residual strength after extended service. Fick's law of moisture diffusion (Crank 1975) is widely used in developing analytical solutions for modeling the degradation in adhesively bonded structures. However, degradation in adhesively bonded joints mostly occurs at the adhesive/adherent interface.

Number of researchers has employed finite element analysis (FEA) to develop prediction durability models based on progressive failure analysis. Crocombe (1997) proposed a general framework, included both interfacial and cohesive (within the adhesive) weakening to form the basis of predictive modeling of the structural integrity of adhesively bonded structures in which service life or residual strength of the joint can be predicted.

Based on the framework proposed by Crocombe, Loh et al. (2002) employed a fracture mechanics approach to measure and characterize interfacial fracture of an adhesive/steel interface for a range of environmental exposure conditions. The study showed that the combination of experimental (e.g. moisture uptake data and/or moisture-dependent mechanical

properties of the adhesive), Scanning electron microscopy (to characterize the nature of the failure surface), and FEA (to measure critical loading to cause interfacial fracture) can be successfully used to investigate the adhesive/adherent interface and pointed out the crucial effect that the interface region plays on the behavior of adhesively bonded joints. A similar approach was presented by Wahab et al. (2002) where coupled diffusion-stress analyses using FEA have satisfactorily produced understanding of the degradation mechanisms of adhesively bonded joints (namely, single and butt joint) aged in hot/wet environment.

Another study based on the cohesive zone approach, environmental degradation of adhesive lap joints was demonstrated using a predictive modeling methodology (Crocombe et al. 2006). A mixed-mode interfacial rupture element was developed with a traction-separation law to model the moisture dependent progressive crack propagation using FEA. The predicted joint residual strengths agreed well with the corresponding experimental data for a range of aging environments.

Hua et al. (2008) proposed a displacement-based continuum damage model, using a coupled diffusion-mechanical FEA, to predict environmental degradation of adhesively bonded aluminum and composite single-lap joints bonded with epoxy adhesive. The study claimed that such a damage model not only has a higher potential to predict cohesive failure in ductile-bonded joints, but also it is mesh independent; which derives from a damage parameter that is defined in terms of the equivalent plastic displacement, rather than existing strain-based failure models.

Bordes et al. (2009) performed a numerical analysis using FEA to examine and predict the long-term behavior of adhesively bonded steel joints (both traditional and a new modified Acran double-lap shear specimens) aged in sea water. A coupled analysis, based on experimentally determined correlation between water content and adhesive property loss and a

diffusion model has been used to analyze the stress state in the specimens during aging. The study showed that the long-term response of aged structure in water can be predicted by using such coupled analysis.

Frantzis (2009) proposed a model for predicting the durability of butt mild steel adhesive joints subjected to static stresses in the presence of water at 25°C. Both test specimens geometry and the test method used allowed a fracture mechanics approach to be adopted for analyzing the results. The accelerated aging test equipment used allowed a constant load to be applied in a tensile manner in the presence of water, giving fracture data in the form of fracture stress against failure time. The proposed model was reasonably successful in predicting the environmental lifetimes of the butt adhesive joints independent of the detailed butt joint geometry and included the effect of crack tip blunting that occurred in the adhesives.

Nguyen et al. (2012) developed an analytical model to predict the degradation in the mechanical performance of steel/CFRP double strap joints subjected to harsh environments. The model was established to relate the moisture uptake with the mechanical degradation of the adhesive (included modeling strength and stiffness degradation of the bulk adhesive specimens) and then it was incorporated into a classical model developed by Hart-Smith (1973) to predict the strength and stiffness of the joints. The study reported that the experimental results obtained from the same study agreed well with the model prediction of strength and stiffness degradation of the steel/CFRP joints.

2.5.2. Steel Beams Reinforced with FRP Bonded Composites

The behavior of FRP-repaired steel beams is widely modeled by using the fundamental principle of mechanics which involves equilibrium and strain compatibility. Using this approach can result in predicting the behavior of strengthened beams such as the load-deflection and the

moment-curvature responses (Tavakkolizadeh and Saadatmanesh 2003a; Colombi and Poggi 2005; Schnerch 2005; Shaat and Fam 2008). In this approach, generally the beam's cross section (FRP, steel, and concrete in the case of composites steel-concrete section) is divided into layers. After locating the position of the neutral axis of the section, equilibrium of external loads, internal forces, and strain compatibility is applied. This procedure is repeated for various strain values until the complete response of the section is determined. Typically, failure of the critical section is assumed when the rupture strain of FRP is reached, or when concrete is crushed in compression in the case of FRP applied to steel-concrete composite section.

Modeling efforts using FEA have been made to predict the behavior of CFRP-repaired steel beams (Colombi et al. 2003a and 2003b; El Damatty et al. 2003; Deng et al. 2004; Sebastian 2003 and 2006, Colombi and Poggi 2006; Haedir et al. 2010). Colombi and Poggi (2006) proposed a simple two-dimensional finite element (FE) model for a steel beam repaired with CFRP. A line element was used to represent the beam and rigid links were employed to connect the beam and CFRP. Another model was suggested by Haedir et al. (2010) to predict the flexure of a tubular steel beam wrapped with CFRP sheets, based on a conventional sectional analysis. Most, if not all, existing modeling approaches assume a perfect connection between CFRP and steel and thus ideal strain compatibility across a beam section is observed (Fam et al. 2009; Pellegrino et al. 2009).

2.6. Failure Modes in Steel-CFRP System

The failure mode in adhesively bonded CFRP to steel members can be affected by the aspects of the three materials involved in such rehabilitation technique; steel, CFRP, and the adhesive. Zhoa and Zhang (2007) identified all possible failure modes associate to CFPR-steel bonded joint subjected to tensile force as follows [Fig. 2.19]:

- (a) adhesion failure at the interface between the adhesive and steel;
- (b) cohesion failure in the adhesive layer;
- (c) adhesive failure at the interface between the adhesive and CFRP;
- (d) delamination in CFRP laminate;
- (e) CFRP rupture;
- (f) yielding of steel.

In particular, the failure mode of the CFRP-steel bonded system is mainly influenced by the elastic modulus of CFRP (Jones and Civjan 2003; Fawzia et al. 2005) and the thickness and type of the adhesive material (Xia and Teng 2005). Typically, a combination of failure modes (a) and (d) is observed when normal modulus (100 to 250 MPa) CFRP is used, whereas CFRP rupture (failure mode (e)) is likely when using higher modulus CFRP sheets [Zhoa and Zhang 2007]. When the adhesive layer or when the quality of the adhesive used is low, cohesion failure (failure mode (b)) is likely to occur, whereas thick adhesive layer changes the failure mode to CFRP delamination (failure mode (d)). The adhesive failure between the steel and adhesive (failure mode (a)) is primarily related to poor surface treatment of the steel. Failure mode (f) is unlikely to occur as long as the thickness of the steel plate is sufficient.

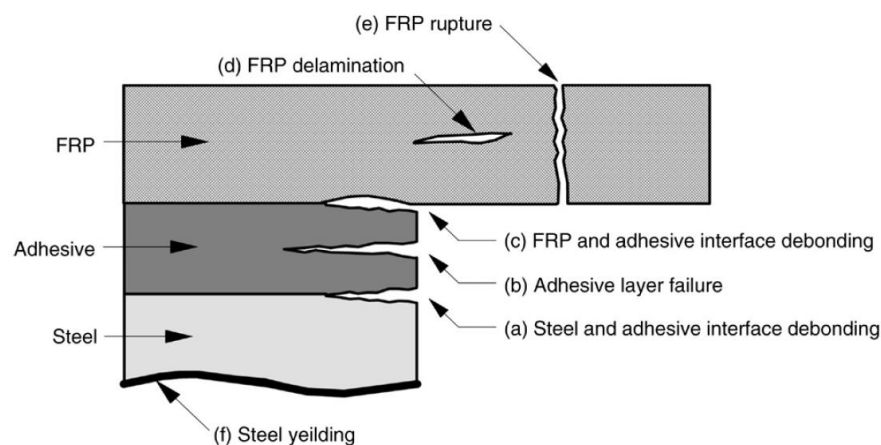


Fig. 2.19. Schematic view of likely failure modes in CFRP-steel system (Zhao and Zhang 2007)

2.7. Cracks and Fracture

2.7.1. Stress Concentrations

In many cases, it is inaccurate to assume that the distribution of stresses on a section of a member, such as a beam, can be expressed by relatively simple laws. Boresi and Schmidt (2003) indicated that the situations that may cause the stress at a point in a member to be greatly different from the value found from simple formulas include effects such as:

- sudden variations in section such as a plate or beam containing a hole;
- contact stress at the area of application of loads;
- material discontinuities such as steel with crystalline grain or nonmetallic inclusions;
- existing stresses in a member that may have resulted, for example, from residual stresses due to welding operation;
- cracks or notches that exist in the member.

These conditions that cause the stresses in a member to be radically higher than those calculated from the ordinary stress equations of mechanics of materials are called stress raisers or discontinuities. The very large stresses caused by stress raisers and are developed in only small portion of the member are called stress concentrations. Fig. 2.20 shows stress nonuniformities resulted from change in specimen geometry (holes or notches). The ration between the local maximum stress (σ_{\max}), resulted from the nonuniformity in stress distribution, and the nominal remote stress ($\sigma = P/A$) is called the stress concentration factor. The stress concentration factor becomes larger as the degree of the cross sectional abruption increases. That is, as a general rule, blunt notches produce lower local stresses, sharp notches cause higher local stresses. These large stresses (σ_{\max}) are usually highly localized and an ordinary mathematical analysis is challenging or impractical. Then, numerical, experimental, or mechanical methods of stress analysis are used.

2.7.2. Fracture Mechanics

The existence of cracks-like flaws in any engineering structure cannot be averted. Meanwhile, the high demands for energy and material conservation (high material costs) are dictating that man-made structures to be very critically designed. Consequently, accurate quantitative estimates of the damage tolerance of structures are the concerted effort by engineers, designers, inspectors, and metallurgists to ensure safe operations without catastrophic fracture in load-bearing components of the structure.

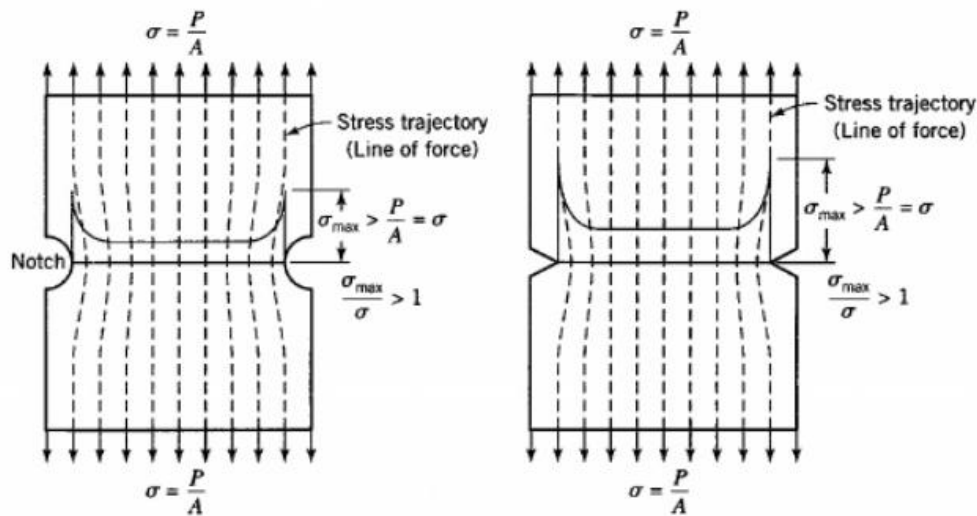


Fig. 2.20. Stress concentrations due to geometric changes (Boresi and Schmidt 2003)

The concept of fracture mechanics has played a significant role in the design of structural components that contain cracks-like defects and the evaluation of their safe continual service. The field of fracture mechanics is highly broad. It primarily draws upon the disciplines of applied mechanics (that expands into the theories of elasticity and plasticity) and materials science (such as crack propagations and failure criteria). Fracture mechanics, in its most basic form, can be applied to relate the maximum allowable loads acting upon a structural component to the size and location of a crack in the component. Thus, its concept is suitable for assessing

the integrity of the existing structural components that contain cracks-like flaws that are currently in service.

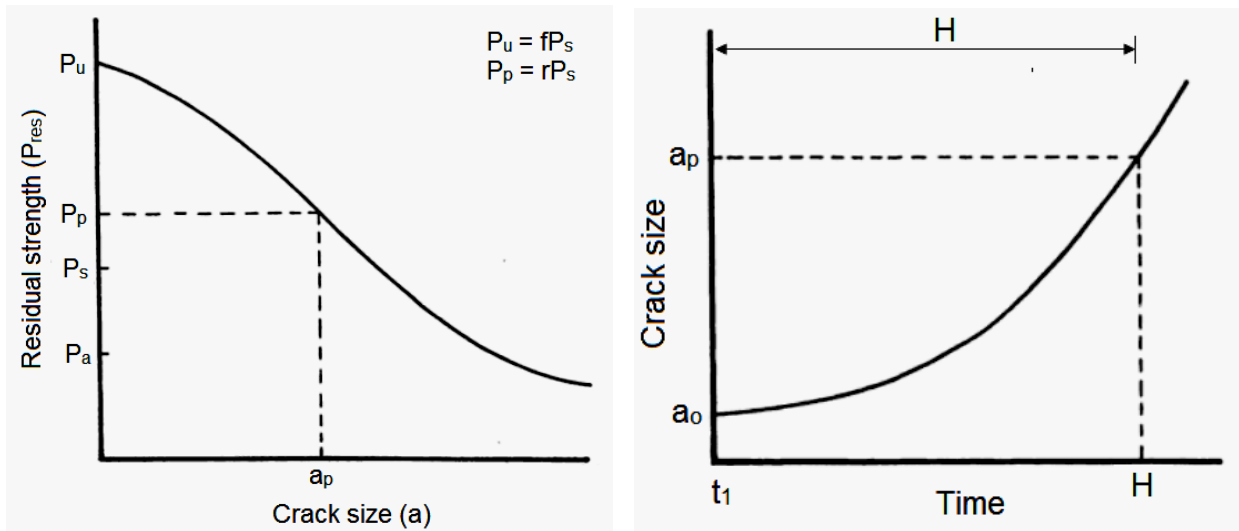
2.7.2.1. Damage tolerance

Fracture mechanics is the keystone for the damage tolerance assessment procedures. The presence of cracks in structural components does not necessarily mean that the component reached its useful service life. The cost of repair or replacement of a structural components that contain cracks-like flaws can be therefore balanced against the possibility that continued service could lead to failure (Kanninen and Popelar 1985). The concept of damage tolerance has been developed to provide quantitative guidance for this purpose. Determining the effect of cracks on the strength of the structural component and the rate of crack growth are the main two objectives of the damage tolerance analysis. These two objectives were discussed by Broek (1989) as explained below.

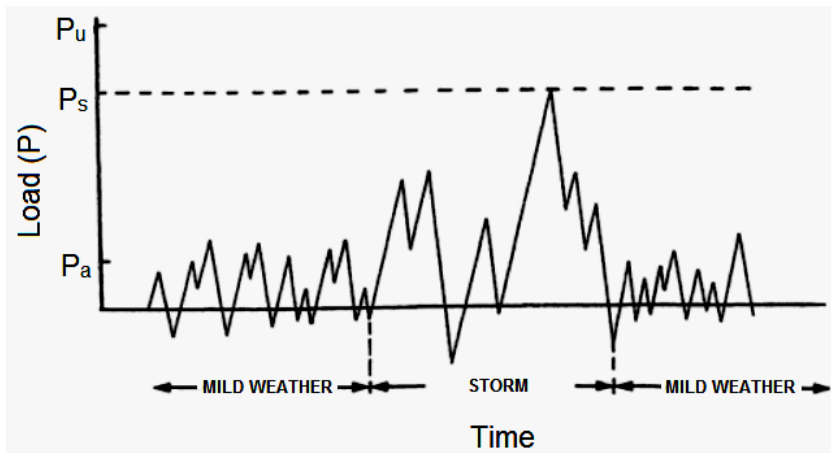
Figure 2.21 shows the correlation between the strength and crack depth, diagrammatically. In this discussion, the strength is expressed by the load, P , the structural member can withstand prior the occurrence of fracture, while the crack size is denoted by a . The strength of a new structure is the ultimate design strength, P_u , if one assumes that the new structure has no significant defects (i.e., $a = 0$), [Fig. 2.21(a)]. It should be noted that if the structure is not over-designed, it must fracture/fail when the applied load reaches P_u , and the probability of this occurring is non-zero.

In the case of presence of cracks in the structure, the strength is no longer the ultimate strength P_u . This remaining strength under the presence of cracks is generally referred to as the residual strength (P_{res}). Therefore, and due to cracks, the safety factor changes from f ($f = P_u / P_s$, where P_s is the highest expected service load) to a smaller safety factor $f = P_{res} / P_s$. Consequently,

the probability of fracture has become higher. Now, fracture is anticipated when the applied load P reaches P_{res} . Initially, a slow and stable fracture process is anticipated and eventually it develops into unstable process and the structure suddenly fractures. The switch from stable crack growth to unstable could take place in seconds. If the applied service loads continue to be at or below the residual strength of the cracked structure ($P < P_{res}$), the crack will propagate by cracking mechanisms such as fatigue or creep.



(a) Residual strength in the presence of cracks (b) Schematic crack growth curve



(c) Schematic for typical loading of offshore structures

Fig. 2.21. Damage tolerance analysis (Broek 1989)

As the crack continues to grow (i.e., crack size increases), the residual strength decreases, a lower safety factor, hence, the probability of fracture becomes higher. If the structure remains in service and nothing is done to the growing crack, the residual strength, P_{res} , ultimately will become equal to the maximum anticipated service load, P_s , or even lower to become closer to the average service load, P_a (Fig. 2.21(c) shows an example of a load history). This means that the safety factor is reduced to one or less than one and the fracture will occur at a load level equal to the highest service load, P_s , or even at a lower load level like P_a . This is what must be obstructed and avoided. Hence, the structural component must be replaced or the crack must be identified and repaired before such time.

The above discussion suggests that the lower limit for the residual strength of cracked structural component should be set somewhat above the maximum anticipated service load, P_s . For instance, the limit may be suggested to not be less than a minimum permissible residual strength P_p ($P_p = rP_s$; where r is the remaining safety factor). Once the residual strength diagram is known [Fig. 2.21(a)] (which is different for each structural component and crack location), the corresponding maximum allowable crack size, a_p , can be determined.

The other primary objective of the damage tolerance analysis is the development of the crack growth curve, as shown in Fig. 2.21(b). In other word, determining the time H of safe operation in which the flaw grows from its initial size to the maximum allowable size (the time when the critical crack, a_p , might be reached). It is important that the inspection interval must be less than the time H if the initial defect (i.e., a_0) is to be determined by inspection (Broek 1989).

2.7.2.2. Fracture and failure criteria

Strength failures of a structural system are usually based on the dominant failure mode and can be either of yielding-dominant (primarily by excessive deflection) or fracture-dominant

types. Several types of fracture-dominant failure may be considered. For instance, sudden fracture of brittle materials at normal temperatures or structural steel at low temperatures may occur suddenly, brittle fracture for structural component contains cracks-like flaw, fracture through fatigue, or fracture may occur in the form of creep rupture over time at high temperatures.

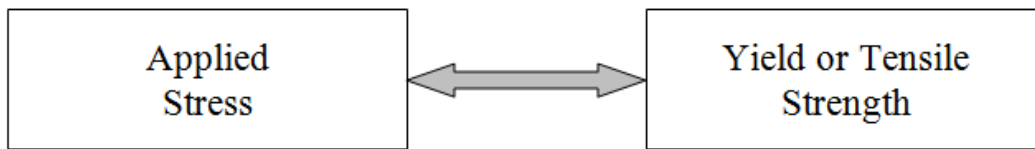
In general, material defects are important in all types of failures. However, defects that are significant for fracture differ from those influencing yielding and the resistance to plastic flow. Significant defects in yielding-dominant failure are those tend to interrupt crystal lattice planes, thus interfere with easy slide glide of dislocations and providing resistance to plastic flow. Examples of such significant defects that control the resistance to plastic flow are grain boundaries, precipitates, interstitials, and dislocation networks. These defects generally provide resistance to yielding that is important to the strength of high strength metals. Other defects, such as small cracks, porosity, or inclusions, provide little resistance to plastic flow (yielding).

For fracture-dominant failures (fracture before excessive yielding of the section), the size scale significant defects depend primarily on the notch toughness of the material. Notch toughness is a measure of the material's capability to deform and to absorb energy in the process before fracture. Fracture-dominant failures do not involve general plasticity (as in the case of yielding-dominant failure) but only the local stress-strain fields associated to the defects.

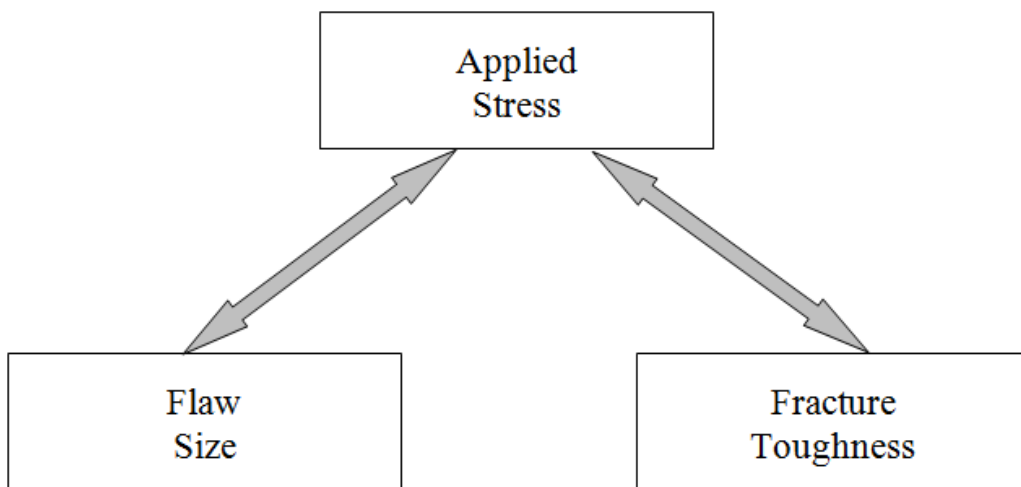
Fracture mechanics, of interest in this study, is concerned almost fully with fracture-dominant failure. Figure 2.22 compares between the traditional approach and fracture mechanics approach for the structural design and material selection. In traditional design approach, it is assumed that the design or material is adequate if the applied stress is less than the strength of the material, as summarized in two variables shown in Fig. 2.22(a). Whereas in the case of fracture

mechanics approach [Fig. 2.22(b)], three variables are included: applied stress, flaw size, and fracture toughness replacing the strength of the material in traditional approach as a material property. The critical combinations between these three variables are quantified by the fracture mechanics approach (Anderson 2005).

Although A. A. Griffith led the introduction of the energy concept of fracture mechanics in 1920, fracture mechanics was approved as an engineering science only in the middle 1950s as Irwin introduced the stress intensity approach and showed that it is equivalent to the energy approach, in terms of how fracture occurs when critical stresses ahead of the crack tip are reached. Therefore, the energy criteria and the stress intensity are the two alternative approaches for fracture analysis.



(a) The strength of materials approach



(b) The fracture mechanics approach

Fig. 2.22.The traditional strength approach versus the fracture mechanics approach (Anderson 2005)

2.7.2.2.1. The energy criteria

The energy method states that fracture (i.e., crack propagation) takes place when there is enough available energy to overcome the material's resistance. As the crack propagates in a structural component, the external applied loads and the strain energy stored in the component before fracture provide energy to the crack. The mechanisms of energy dissipation associated to crack propagation (fracture) in metals may include surface energy or plastic deformation in the vicinity of the crack tip. The energy release rate for a through-thickness crack in an infinite plate under a remote tensile stress, σ , can be given by

$$G = \frac{\pi \sigma^2 a}{E} \quad (2.5)$$

where G is the energy release rate (the available elastic energy per unit new crack surface area), and E is the elastic modulus. The fracture criteria for this approach can be given as

$$G \geq G_c \quad (2.6)$$

where G_c is the toughness of the materials, or energy per area required to propagate a crack. In other words, at fracture (failure), the critical combinations of crack size (a_f) and stress (σ_f) can be related as follow

$$G_c = \frac{\pi \sigma_f^2 a_f}{E} \quad (2.7)$$

It should be noted that for a constant G_c , the failure applied remote stress varies with $1/\sqrt{a}$.

2.7.2.2.2. The stress-intensity approach

Figure 2.23 schematically shows a crack tip and an element located within a cylindrical polar coordinates r_o and θ with respect to the crack tip in an elastic material, along with the in-plane stresses on this element. One can note that the constant K_I is common in all stress components; namely σ_{xx} , σ_{yy} , and τ_{xy} . Therefore, stress distributions at and near the crack

tip can be calculated once K_I is determined. This constant, K_I , is called the stress-intensity factor (SIF). K_I fully characterizes the conditions of the crack-tip in a linear elastic material. Hence, the critical combinations of strain and stresses that cause the material to fail/fracture locally must occur at a critical K_I , which is called the critical SIF, K_{Ic} , or the fracture toughness.

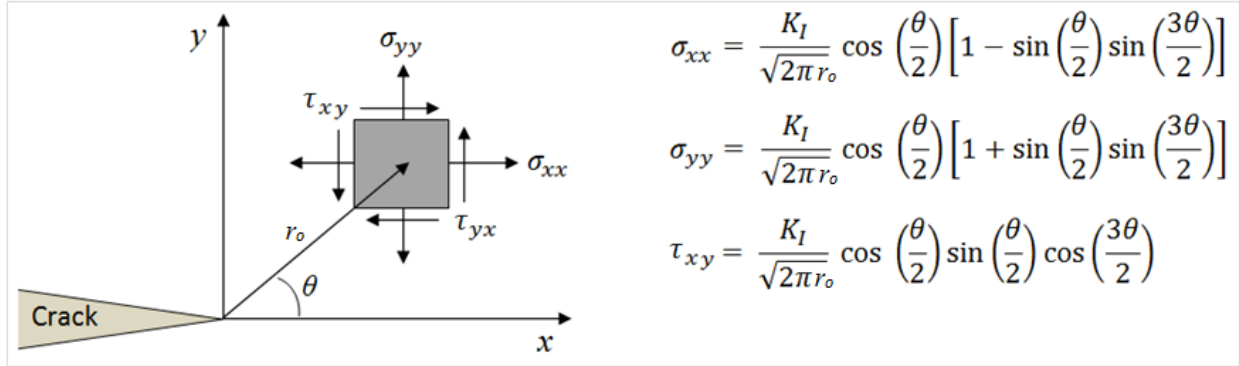


Fig. 2.23. Stresses in an element near the crack of an elastic material

For example, the SIF for a through-thickness crack in an infinite plate under a remote tensile stress, σ , can be given by

$$K_I = \sigma\sqrt{\pi a} \quad (2.8)$$

In small-scale yielding (SSY), the crack tip deformation and failure is driven solely by the SIF, K_I . Fracture or failure occurs (the crack will grow) when the applied load is such that

$$K_I \geq K_{Ic} \quad (2.9)$$

In SSY, the energy release rate, G , and the SIF, K_I , are related. Comparing Eqn. 2.5 and Eqn. 2.8 results in a relationship between G and K_I :

$$G = \frac{K_I^2}{E} \quad (2.10)$$

It should be noted that Eqn. 2.8 also holds for G_c and K_{Ic} . Thus, in fracture mechanics and for SSY, the energy and stress-intensity approaches are equivalent.

2.7.2.3. Crack-tip plasticity

The elastic stresses distribution ahead of the crack tip, and as shown in the equations in Fig. 2.23, predicts infinite stresses when r is zero. In other words, there is a stress singularity at the crack tip. However, stresses at the crack tip, in a real structural material, are finite because the radius of the tip of the crack must be finite. Thus, plastic deformation will occur so that the stresses cannot increase much further after yielding begins, and there will be a plastic zone surrounding the tip of the crack (Broek 1989).

Irwin approach evaluates the extent (or the size) of the crack-tip plastic deformation (i.e., crack-tip-yielding zone) where the elastic-plastic boundary is estimated by using elastic stress analysis. The radius of the plastic region ahead of the crack tip, r_y , was calculated to be the distance along a horizontal line where the stress would equal the yield strength of the material (σ_{ys}), as shown in Fig. 2.24, with

$$r_y = \frac{1}{2\pi} \left(\frac{K_I}{\sigma_{YS}} \right)^2 \quad (2.11)$$

If the size of the plastic zone near the tip of the crack in which inelastic deformation occurs is small compared to the physical length of the crack and other structural geometry of the cracked body, the stresses outside of this zone will be well approximated by the equations shown in Fig. 2.23. In fracture, this is so called SSY and linear elastic fracture mechanics (LEFM) apply. However, if this is not the case and more extensive yielding occurs (i.e., bigger plastic zone), then the problem has to be treated by elastic-plastic fracture mechanics (EPFM) that considers the nonlinear behavior of the material. Both LEFM (focusing on the stress- intensity factor) and EPFM (focusing on the J contour integral) are briefly discussed in the following sections.

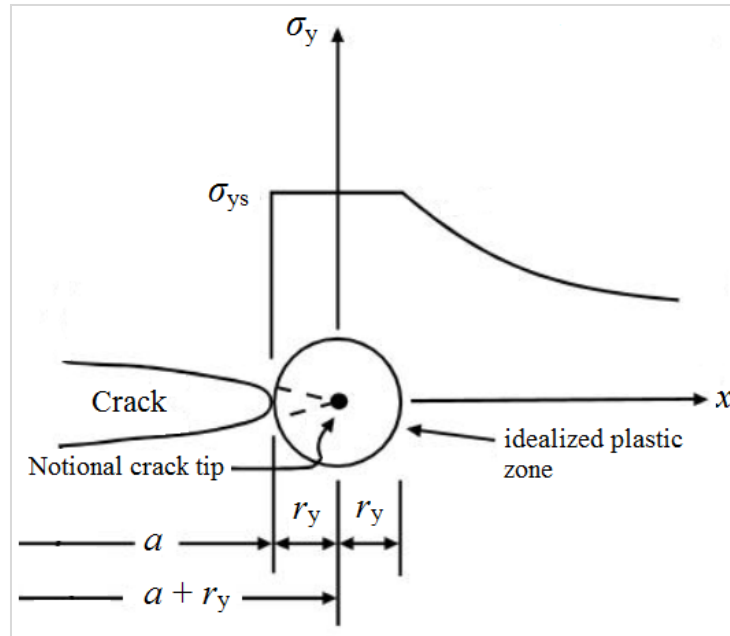


Fig. 2.24. Plastic zone ahead of crack tip

2.7.2.4. The stress intensity factor (SIF)

The SIF, K , which was introduced previously, defines the magnitude of the local stress field ahead of the crack tip. Additionally, it can associate the crack growth and propagation, and the fracture behavior of the cracked material provided that stress field surrounding the crack remains principally elastic. This correlating capability of the SIF makes it a critical and important parameter in the field of fracture mechanics.

The three load types that a crack may experience are: Mode I is the tensile (opening) mode, Mode II is the in-plane shear (sliding) mode, and Mode III is the out-of-plane shear (tearing) mode, as shown in Fig. 2.25. Correspondingly, the SIF is usually given a subscript to designate the mode of loading (i.e., K_I , K_{II} , and K_{III}). Figure 2.26 lists K_I solutions for several common fracture test specimens. Several handbooks are available and devoted solely to SIF solutions for common configurations.

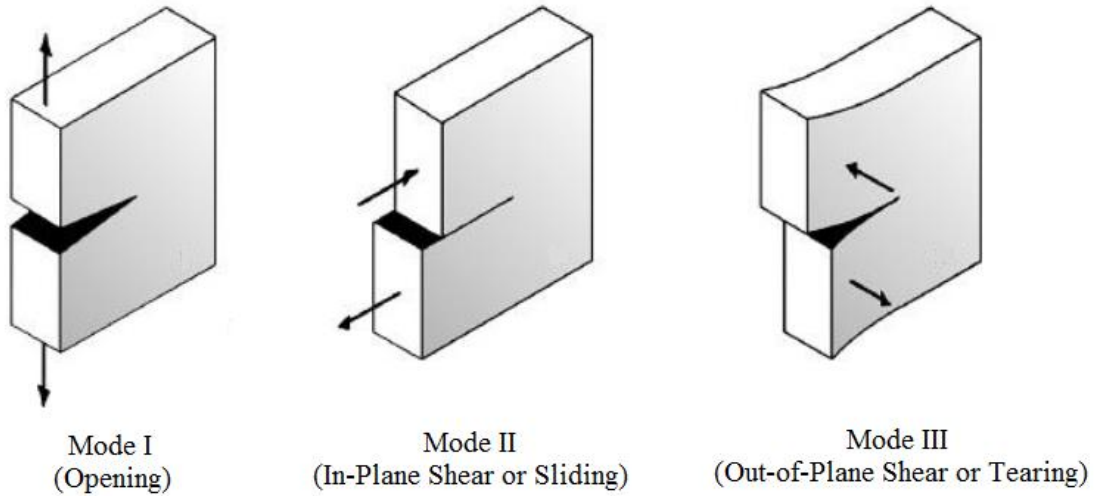


Fig. 2.25. The three basic modes of loading

The solutions for the SIF are given in many forms. However, K can always be related to the through-thickness crack through the relevant correction factor:

$$K_{(I,II,III)} = Y \sigma \sqrt{\pi a} \quad (2.12)$$

where σ is the remote applied stress, a is the crack size, and Y is the correction factor which is a function of the specimen, crack geometry, and loading mode.

	<p>Single Edge Notch Tension (SENT)</p> <p>$h/W > 1$</p> <p>$K_I = \sigma \sqrt{\pi a} F(a/W)$</p> <p>$F(a/W) = 0.265(1 - a/W)^4 + \frac{.857 + .265a/W}{(1 - a/W)^{3/2}}$</p>
	<p>Center Cracked Tension (CCT)</p> <p>$h/W > 3$</p> <p>$K_I = \sigma \sqrt{\pi a} F(a/W)$</p> <p>$F(a/W) = \sqrt{\sec \frac{\pi a}{2W} [1 - .025(a/W)^2 + .06(a/W)^4]}$</p>

Fig. 2.26. K_I solutions for two of the common test specimens (Zehnder 2007)

2.7.2.5. The J contour integral

For materials that exhibit time-dependent, nonlinear behavior, plastic deformations will usually occur before fracture. Therefore, LEFM, that applies only when the deformation is limited to a confined area around the crack tip, is not applicable. In other words, the plastic zone surrounding the crack tip is simply too large. For these cases, EPFM must be used. The J contour integral, introduced by Rice, is an elastic-plastic parameter used when the plastic deformations must be taken into account. This parameter characterizes the nonlinear material behavior ahead of the crack tip.

Rice (1968) employed deformation plasticity to the crack analysis in a material that behaves nonlinearly. Under the restriction of no unloading, nonlinear elastic behavior can be used, and valid, for an elastic-plastic material. This is what known as the deformation theory of plasticity, and is equivalent to nonlinear elasticity, which correlates total strains to stresses. Thus, Rice was able to extend the concept of energy release rate to materials with nonlinear behavior. Rice proved that the nonlinear energy release rate, which he called J -integral, can be expressed as a path-independent contour line. Also, Hutchinson (1968), and Rice and Rosengren (1968) conducted crack tip characterization studies in which J -integral was correlated to crack tip stresses and strains in nonlinear materials, which is known as HRR solution. Such analyses indicated that the J integral can be considered as a nonlinear energy as well as stress intensity parameter.

The J -integral concept is based on the energy balance approach. Therefore, the energy balance equations for linear elastic material behavior will be valid for nonlinear behavior as long as it remains elastic.

In the energy balance approach, the instability condition for crack growth to occur is given by:

$$\frac{d}{da}(F - U_a) \geq \frac{dU_\gamma}{da} \quad (2.13)$$

where F is the work from the external forces (dF/da is the energy produced by the external work F per unit new crack), U_a is the change in strain energy induced by formation the crack in the plate (dU_a/da is the increment of energy owing to the external work), U_γ is the change in surface energy induced by the extension of the crack surface (dU_γ/da is the surface energy of the crack surface, which is the energy required for the crack to grow (i.e., the resistance of the crack)), and a is the crack area. The equivalent nonlinear elastic parameter, J , can be defined as:

$$J = \frac{d}{da}(F - U_a) \quad (2.14)$$

In other words, J is the energy available for unit fracture surface area of the crack in a nonlinear material. The potential energy, U_p , is given by:

$$U_p = U_o + U_a - F \quad (2.15)$$

where U_o is the amount of energy of the uncracked loaded plate. Because U_o is constant, then

$$\frac{dU_p}{da} = \frac{d}{da}(U_a - F) = -\frac{d}{da}(F - U_a) \quad (2.16)$$

From Eqn. 2.14, it is seen that by definition:

$$J = -\frac{dU_p}{da} \quad (2.17)$$

where dU_p/da represents the change in stored energy. Thus, a reduction in stored energy, $-U_p/da$, means a release of crack driving energy, J , in order to provide the energy, dU_γ/da , for an increase in crack surface by da (Ewalds and Wanhill 1984).

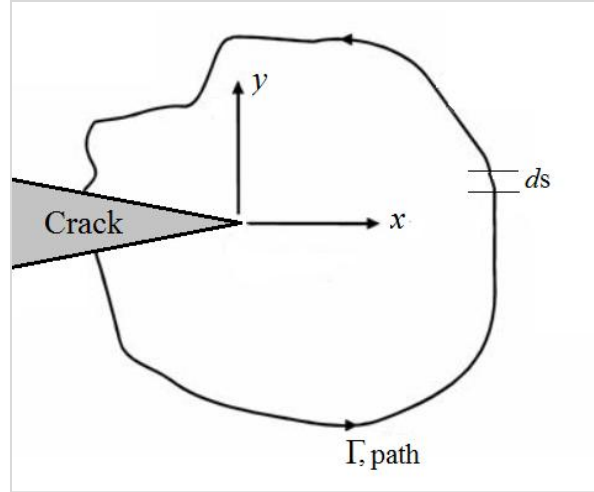


Fig. 2.27. Arbitrary closed contour around the tip of a crack

The basic relationship that Rice (1968) introduced for the path-independent J -integral is [Fig. 2.27]:

$$J = \int_{\Gamma} \left(w dy - t \frac{\partial u_i}{\partial x} ds \right) \quad (2.18)$$

where w is the strain energy density and the y direction is taken perpendicular to the crack line, Γ is a curve/path that surrounds the tip of the crack, t is component of the traction vector, ds is the increment of length along Γ path, and u_i is the displacement vector components. Of most importance is that, for deformation plasticity (i.e., nonlinear elastic behavior), the J -integral around the crack is independent of the path integration. In other words, J -integral will have the same value for any choice of Γ .

Under certain restrictions, as discussed earlier, J -integral may be considered as an elastic-plastic energy release rate. Therefore, there should be a critical value of J -integral that predicts the onset of crack extension. This value is J_{Ic} which is the fracture toughness of the material (i.e., characteristic of the material). The exact point at which cracks begins to propagate is usually not precisely defined, as in the case of defining the yield point for tensile testing. Consequently, the

determination of J_{Ic} stays difficult, and estimated to be at an offset of 0.2% of the yield strength. Figure 2.28 shows a typical J -integral resistance curve for materials that exhibit ductility which gives a relatively complete description of the fracture behavior.

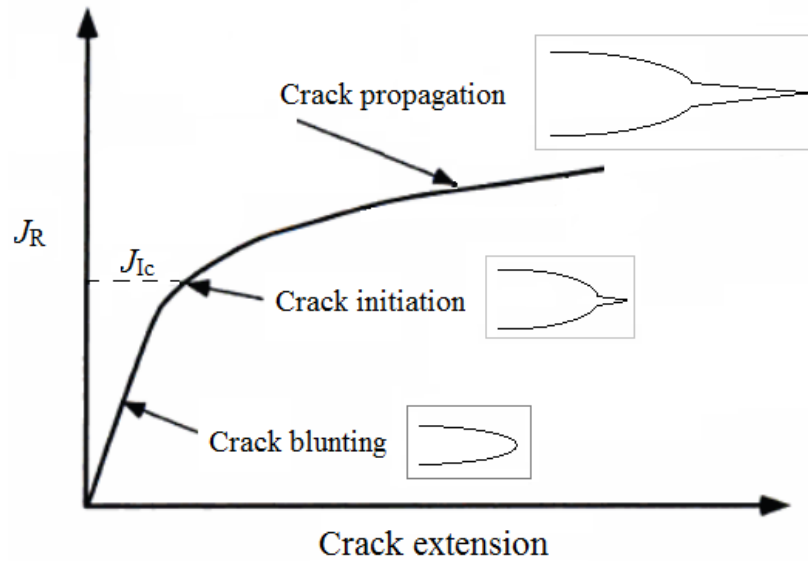


Fig. 2.28. Typical J - R curve for a ductile material

2.7.3. Fracture-Based Approach for Strengthening with CFRP Composites

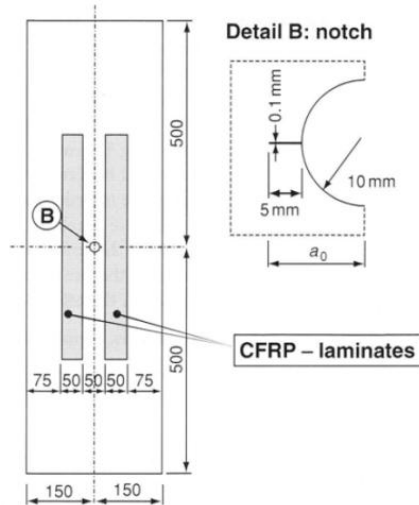
The experimental results for cracked steel members repaired with CFRP sheets, which was discussed previously, illustrated the need for a failure criterion to predict the critical loads and to ensure the safety of the repaired members. Because the failure of such members ultimately involves crack propagation assisted by local stress intensities, some researchers examined the fracture mechanics path to the problem by utilizing the elastic and fracture-material properties.

Colombi et al. (2003) investigated the fatigue response of center-cracked steel plates reinforced with CFRP laminates by evaluating mode I SIFs at the crack tip [Fig. 2.29]. A parametric study using 2-D finite element method was conducted to examine the sensitivity of the SIF levels to different geometries, material properties, and stress levels. SIF reduction was evident for the CFRP-reinforced plates compared to their unstrengthened counterparts. For

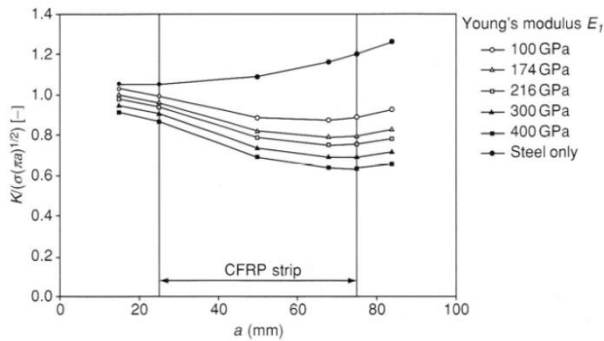
example, the study indicated that the effectiveness of CFRP repair was more pronounced when it was applied to plates with longer cracks. In other words, the corresponding SIF for CFRP-repaired steel plates with longer cracks was lower compared to the one for shorter cracks. This effect of CFRP on lowering the SIF for longer cracks was observed even with applying prestress loads, while such effect was negligible for shorter cracks. Also, the study reported that both CFRP modulus and thickness decreased the stress intensity factor as shown in Figs. 2.29(b) and (c), respectively. Additionally, the study concluded that prestressing the CFRP strip before bonding it to the steel plate promotes crack closure which ultimately reduced the SIF at the crack tip, and prevents further crack growth. Likewise, Lam et al. (2010) ran an experimental program to investigate the strain distribution around the crack region of a cracked steel plate that had been repaired with CFRP. The influence of several test parameters (e.g., CFRP thickness, CFRP dimensions, and CFRP stiffness) on the effectiveness of the CFRP repair for the cracked steel plates was examined through the SIF evaluation. The study reported that the CFRP width and length had a negligible effect on the SIF, whereas the influence for the increased CFRP thickness (i.e., number of layers) and modulus to decrease the SIF of the repaired plates was more noticeable.

Wu et al. (2013) introduced a modified SIF formula for CFRP-reinforced central cracked tensile steel plates based on the classical solutions for mode I SIF with the same configuration considering the effect of geometry and mechanical properties of CFRP composites. Yu et al. (2012) proposed a SIF formula for a CFRP-strengthened center cracked steel plate to predict and understand the influence of the CFRP repair. Such a formula was developed based on classical SIF solutions by applying the James-Anderson method. The proposed solution indicated that the

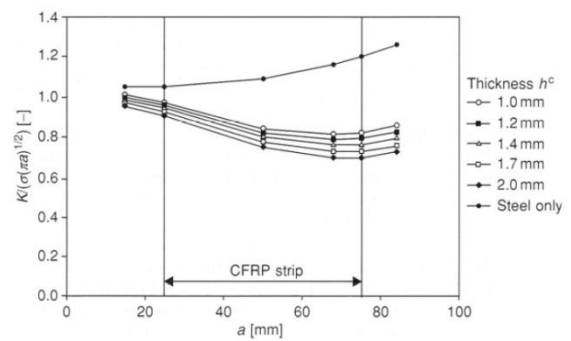
SIF for the CFRP-reinforced steel plate was affected by the CFRP patch and the degree of initial fatigue damage.



(a) Notched center-cracked steel plate reinforced with CFRP



(b) Sensitivity of SIF CFRP modulus



(c) Sensitivity of SIF CFRP thickness

Fig. 2.29. Cracked steel members reinforced by prestressed CFRP patch (Colombi et al. 2003)

Although the SIF approach has been utilized to evaluate the effectiveness of CFRP repair for cracked steel plates, and despite the fact that a number of studies proposed SIF solutions for cracked I-beams (Dunn et al. 1997; Albrecht et al. 2008; Ghafouri and Motavalli 2011), no research has been conducted to estimate the SIF for cracked steel I-beams reinforced with CFRP composites. Dunn et al. (1997) proposed closed-form expressions for SIFs for cracked I-beams under pure-bending load. Estimation of the SIF expressions was based on the elementary

strength theory for defective beams along with finite element calibration and dimensional considerations. Albrecht et al. (2008) implemented a numerical approach based on the finite element method to develop SIF solutions for structural cracked steel I-beams (cracked W Shapes) that were subjected to two types of loading: tension and bending. SIF solutions were introduced for two types of I-beams cracks: a two-tip web crack as well as a symmetric, three-tip crack with one crack tip in the web and the other two located symmetrically in the flange. Expressions for the proposed solutions showed that the SIF is affected by a number of parameters: crack length, crack eccentricity, flange-to-web area ratio, and the applied stress. Ghafoori and Motavalli (2011) presented an analytical procedure to estimate the SIF for structural steel I-beams subjected to two types of loading: pure bending and axial tension. The proposed analytical method was based on both the conservation laws as well as the energy release rate for crack-mouth widening concept.

2.8. Finite Element Analysis (FEA)

2.8.1. Background

Several numerical methods have been applied to solid mechanics problems, including the boundary integral equation, finite difference, and finite element methods. The area of finite element analysis (FEA), of particular interest, is now a standard tool and frequently imperative part of engineering analysis and design. The finite element (FE) computer programs and software packages are now widely used in diverse areas of engineering such as heat transfer, fluid dynamics, and solid mechanics.

In both design and analysis, the finite element method (FEM) is employed to solve physical engineering problems. It is exceptionally powerful when dealing with complicated geometries and boundary conditions that are common in practical applications. Typically,

physical problems include a structural element subjected to loads and boundary conditions. The mathematical model in FE idealizes the actual physical problem. This idealization includes number of assumptions where differential equations are developed and govern the mathematical model. Thus, the FEA solve this model. The numerical solution (i.e., the solution collected from FE) needs to be evaluated for accuracy against a certain criteria. The process of FEA is summarized in Fig. 2.30.

Choosing an effective and reliable mathematical model is very crucial in engineering analysis. This step is important because all assumptions in the mathematical model will be reflected in the anticipated response. For examples, the three-dimensional (3-D) FE model that also takes the material nonlinearity into account is, in general, a comprehensive mathematical model. Because the FE only solves the generated mathematical mode, care should be taken in selecting the appropriate mathematical model in FEA. It is crucial that the user have good understanding of structural modeling, the boundary conditions, and the limitations of the procedure when solving engineering problems with the FEM. Therefore, selecting the mathematical model, solving the model by the proper FE procedures as well as evaluating and judging the results are all fundamental elements of an engineering analysis using the FEM (Bathe 1996).

2.8.2. Finite Element Method (FEM) Procedure

2.8.2.1. General

The FEM overcomes the difficulties of the complicated geometries and boundary conditions of engineering problems by introducing two fundamental concepts (Bhatti 2006):

- *Discrediting the solution domain into elements.* In the FEM, the solid body of interest is divided into discrete shapes called *elements*. Hence, the solution domain is subdivided

into several simpler subdomains (i.e., elements). The geometry for each element is simple, therefore, appropriate assumed solutions for each element can easily be determined. Also, each element only covers a small part of the solution domain which leads to using simpler polynomials that describe the solution for each element. Then, the differential equations are transformed into equivalent integral form called the *weak form*. Finally, and for each individual element, the weak is evaluated and then assembled (added) together to represent the entire model.

- *Coefficients in the assumed solution over an element represent the solution and its appropriate derivatives at nodes.* Unlike the assumed solutions in classical methods where the unknown coefficients have no physical meaning, the polynomial coefficients in the FEM are defined in terms of unknown solutions at the selected locations in an element. These points (locations) are called *nodes*. Typically, the nodal locations are the corners and ends of elements and the solution at these nodes are called the *nodal degrees of freedom*.

The basic steps involved in applying the FEM to a given problem can be summarized as follow:

1. Discretization the solution domain into finite elements, that is the solid body is subdivided into elements and nodes.
2. Development of equations for an element, including the assumption of the appropriate shape functions (also called interpolation functions) that represent the physical behavior of the element.
3. Arrangement and assembly of the element equations to represent the entire system.
4. Application of boundary conditions and loads.

5. Solution for linear or nonlinear equations for nodal unknowns.
6. Computational of solutions and obtaining required quantities.

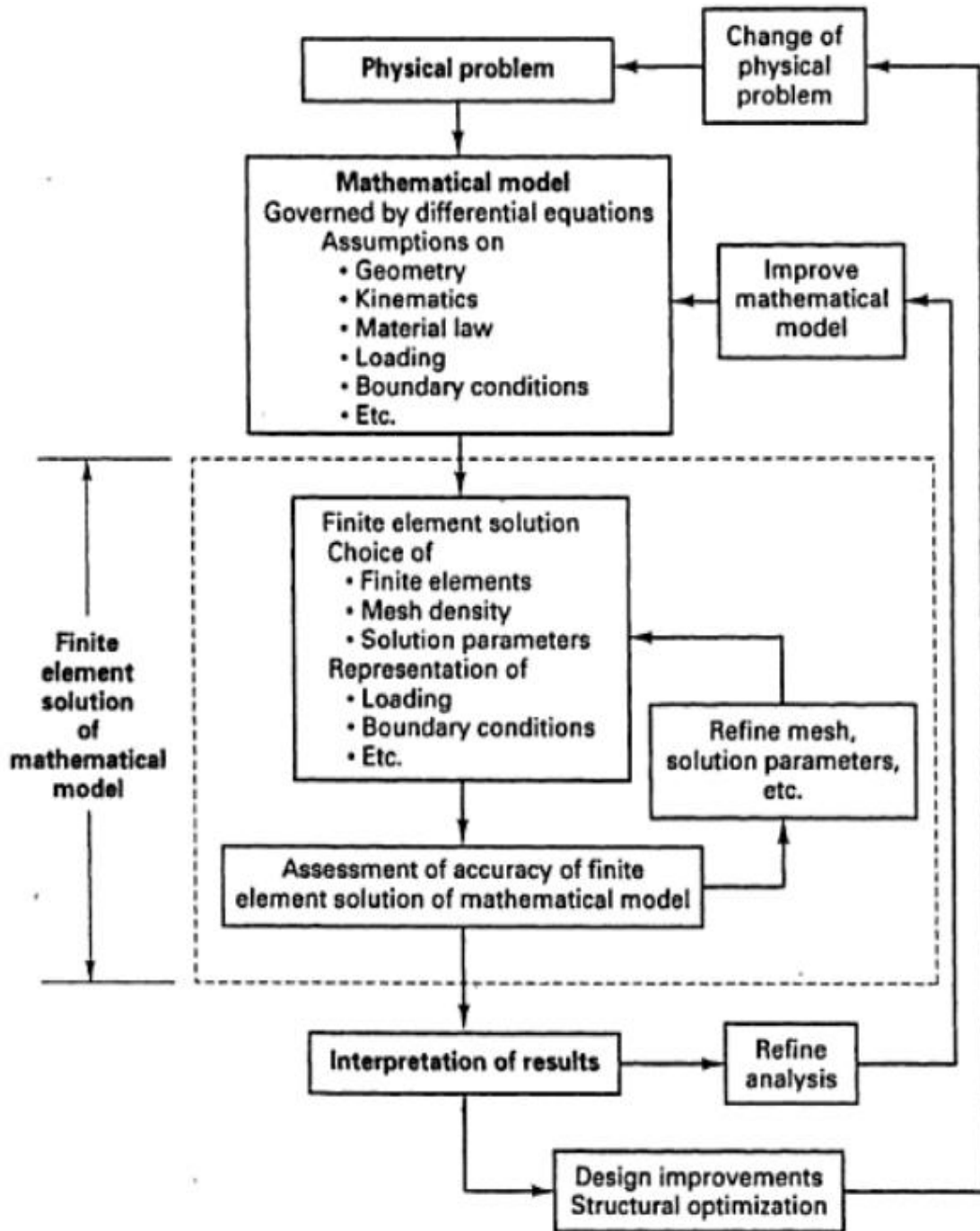


Fig. 2.30. The process of FEA (Bathe 1996)

2.8.2.2. Appropriate element selection

In all FEA, the real structure is idealized to a finite number of discrete shapes called finite elements, or elements, for short. In structural analysis for example, equations for the stiffness matrix are formed and solved to provide equilibrium between the elements, applied loads, and the structural supports. Strain can be computed once the resulting displacement matrix is determined, and then stresses can be evaluated based on the material response.

In all FEA, the type of the elements used is important and will have influence on the results. Typical elements are shown in Fig. 2.31. Beam, shell, and solid elements are the three most common elements used to solve engineering problems in FEA. The appropriate use of each elements type depends highly on the nature of the real structure. Therefore, as indicated earlier, it is crucial that the user have good understanding of structural modeling when solving engineering problems with the FEM.

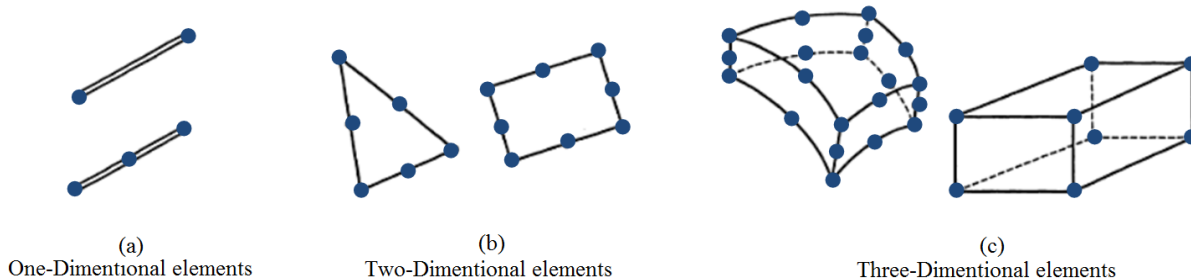


Fig. 2.31. Some typical elements used in FEA

2.8.2.3. Linear and nonlinear response

When a structure is expected to behave linearly, where stress is proportional to strain (i.e. obeys Hook's Law), a linear FEA is initiated. However, nonlinearity is natural in physical problems [Fig. 2.32(a)]. In FEA, a nonlinear analysis is usually required when the structure undergoes considerable change in stiffness under certain loads. There are three types of nonlinearity in FEA:

- *Geometric nonlinearity.* As in the case of a structure experiencing large deformations and/or rotations.
- *Material nonlinearity.* It occurs when the stress-strain response is not linear (strains beyond the elastic limit).
- *Contact nonlinearities.* Such as nonlinearity due to contact between two bodies

In FEA, all nonlinearities require an iteration approach for the numerical solution. For example, in the general-purpose FEA program ANSYS, Newton-Raphson approach is used to solve nonlinear problems, where the load is applied gradually through load increments. At each load step, ANSYS executes equilibrium iterations to bring the incremental solution to convergence by solving the following equation:

$$\{P^e\} - \{P^i\} = [K] \{\Delta u\} \quad (2.19)$$

where $\{P^e\}$ is vector of the external loads, $\{P^i\}$ is vector of the internal forces, $[K]$ is the tangent stiffness matrix, and $\{\Delta u\}$ is the displacement increments [Fig. 2. 32(b)]. When the difference between the external loads and internal forces ($\{P^e\} - \{P^i\}$) reaches a defined tolerance, the equilibrium iterations will be terminated. Due to the iterative nature of nonlinear FEA analysis, it is considered computationally expensive. However, it reflects the physical engineering phenomenon more accurately than linear analyses.

2.8.2.4. Mesh design

The appropriate design for the mesh in FEA is as much an art as it is a science. How small the mesh should be to obtain the most accurate results is usually a very common question when modeling with FEA. Although many FEA programs have automatic refinement capabilities, the answer for such question virtually cannot be provided without a mesh convergence study. Mesh refinement is performed in an iterative procedure by making a series of

FEA runs with gradual decrease in element size and comparing the difference in results. This procedure is repeated until the desired accuracy is obtained.

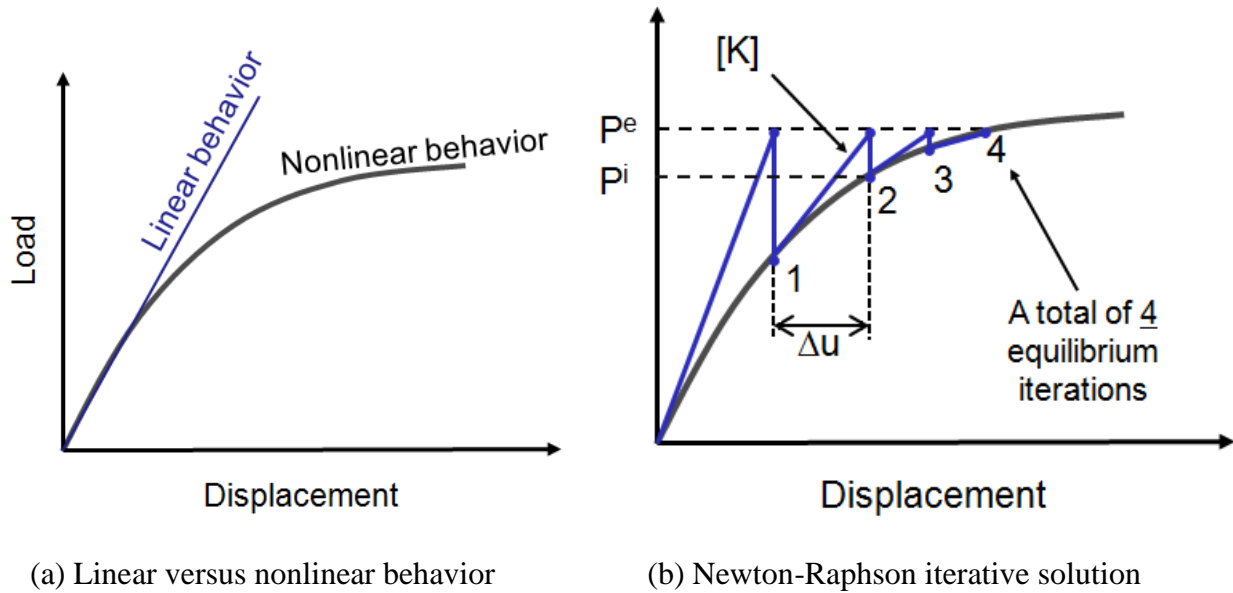


Fig. 2.32. Typical linear and nonlinear material responses and iteration approach for the numerical solution

In the field of fracture mechanics, usually mesh refinement needs certain amount of attention near the crack where error in the approximate solution is the largest. Typically, the degree of refinement of the element mesh near the crack tip must be the smallest. The appropriate level of mesh refinement requires a mesh convergence study, and also judgment on the part of the user will be necessary.

Quadrilateral and brick elements having mid-side nodes are typically used for 2-D and 3-D crack analysis problems, respectively. Quadrilateral elements, for example, collapsed down to triangular-shaped elements by defining the same node number for nodes 6, 7, and 8 as shown in Fig. 2.33. Then, the singularity in the element, which enhances the accuracy of the numerical analysis and cut the need for a very fine mesh near the crack tip, is achieved by forcing the mid-side nodes (nodes 4 and 5) to move to the 1/4-points [Fig. 2.33].

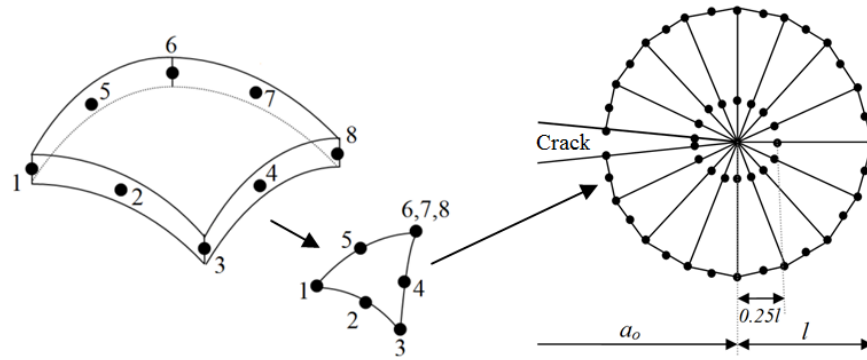


Fig. 2.33. Element degeneration at the crack tip

2.9. Field Applications of CFRP Reinforcement

A number of field applications of CFRP to steel bridges and structural members have been conducted, demonstrating that the application of such material under real field conditions is indeed possible. The following discussion presents examples of field applications where CFRP composites were used as retrofitting material to existing steel bridges.

In an effort to evaluate the effectiveness of using CFRP as retrofit material to existing steel bridges, Miller et al. (2001) transferred this rehabilitation technology from the laboratory level to the real field application. Delaware Department of Transportation selected Christina Creek bridge (1-704) to be used by the University of Delaware to evaluate the CFRP rehabilitation technique. Only a single girder (W610x 150) with a span length of 7500 mm was selected to demonstrate the repair process using CFRP. To mask the full 23-mm wide tension flange, six CFRP plates (elastic modulus of 112 GPa) were adhesively bonded side-by-side. The CFRP extended to cover the entire span length by using four overlapped CFRP sections. It is worth noting that the in-service maximum strains for the steel girder were monitored and recorded for two weeks before the application of the CFRP plates. By comparing the behavior before and after the installation of the CFRP, it was indicated that the presence of CFRP decreased the measured girder stiffness and strain by 12% and 10%, respectively. The study

indicated that future monitoring to the CFRP-strengthened steel girder will add valuable data regarding the long-term durability for this repair technique. Also, Chacon et al. (2004) conducted a similar work where bridge 1-119, also known as the Ashland Bridge over Red Clay Creek in Delaware, was strengthened by using CFRP composites. The comparison between the pre- and post-rehabilitation tests indicated that CFRP plates improved the stiffness and load distribution of the retrofitted beams.

In Iowa, the effectiveness of rehabilitation using CFRP was evaluated by applying CFRP plates to a three-span continuous I-beam bridge located in Pottawattamie County, on State Highway 92 (Phares et al. 2003). The CFRP laminates (elastic modulus of 138 GPa) were applied on all six beams; two W27x84, two W27x91, and two W27x98. The bridge has a total length of 45.7 m with a 9.1 m roadway width, carrying a two-lane head-to-head traffic. The CFRP plates were applied on beams exterior as well as interior side of the tension flange in the positive moment region. After surface treatment of the steel girders, the CFRP plates were installed with the number of CFRP layers varied between one and three layers to evaluate the effect of amount of CFRP. Figure 2.34 shows the bridge and CFRP installation procedure. Analysis of the results by Wipf et al. (2005) indicated that the stiffness of the steel girders increased by 1.2% for each CFRP layer. Insignificant difference in the measured strain on the tension flange was reported when comparing the strain before and after installing the CFRP laminates. The study reported that this inconsequential difference in the behavior may be related to the low CFRP modulus that was used and also due to the small amount of CFRP used. Table 2.1 summarizes different bridges around the world where strengthening technique using CFRP composites have been used.



(a) Side view of bridge



(b) Surface preparation



(c) Cleaning and epoxy application on CFRP



(d) Epoxy application on beam



(e) Installation of CFRP plate on beam



(f) Installed CFRP plate

Fig. 2.34. Installation procedure of CFRP to steel-girder bridges (Phares et al. 2003)

Table 2.1. Bridges around the world strengthened using CFRP composites

Year	Location	Bridge Name	FRP Composite used
2008	Tokyo (Japan)	Takiguchi Bridge	High modulus CFRP plate (Modulus 450 GPa)
2003	Pottawattamie county,Iowa U.S.A	On State Highway 92	CFRP plates (Modulus 138 GPa)
2002	Delaware U.S.A	Ashland Bridge	CFRP plate (Modulus 112 GPa)
2000	Newark, Delaware (U.S.A)	1-704 Bridge	CFRP plate (Modulus 112 GPa)
2000	London Underground (U.K)	Acton Bridge	High modulus CFRP plates (Modulus 310 GPa)
2000	Flintshire (U.K)	King Street Bridge	High modulus CFRP + GFRP plates (Modulus 360 GPa)
2000	Rochdale (U.K)	Slattocks Canal Bridge	CFRP plates (Unknown Modulus)
1999	Oxfordshire (U.K)	Hythe Bridge	CFRP plates (Modulus 160 GPa)

CHAPTER 3. CRACK-DEPENDENT RESPONSE OF STEEL ELEMENTS STRENGTHENED WITH CFRP SHEETS*

3.1. Abstract

This study presents the crack-dependent response of steel members strengthened with carbon fiber reinforced polymer (CFRP) composite sheets subjected to axial tension. A modeling approach is proposed to represent debonding of the CFRP and crack propagation across the steel section. Such an approach is incorporated to a three-dimensional finite element analysis (FEA) model and validated with experimental data. A total of nine specimens are constructed to study the effect of CFRP-strengthening on the behavior of strengthened steel members having various crack properties. Investigation parameters include the level of damage in the members represented by a_o/h ratios (a_o = notch size and h = specimen height) and CFRP-reinforcement ratios (ρ_{CFRP}). The strengthening effect is noticeable when the a_o/h ratio increases. The crack propagation rate of the strengthened members is dependent upon the debonding characteristics of the CFRP and the size of the a_o/h ratio. CFRP-strengthening results in significant improvement in energy release rate, including moderate increases in J integral. Overall, the interaction between the a_o/h ratio and ρ_{CFRP} is substantial for the strengthened members.

3.2. Research Significance

As previously discussed, CFRP-strengthening is a promising method for improving the flexural behavior of damaged steel members. Notched sections are a widely used method to simulate structural damage of steel members. To better understand the effect of such a damage-simulation technique, small-scale experiments with notched tension coupons have been

*: This chapter has been previously published [*Hmidan, A., Kim, Y.J., and Yazdani, S. 2013. Crack-dependent response of steel elements strengthened with CFRP sheets, Construction and Building Materials, Elsevier, 49, 110-120*].

conducted (Hollstein et al. 1983). Of interest are the bond behavior and fracture characteristics of the CFRP sheets bonded to steel surface. Although such an investigation is crucial to understand the failure mechanism of a CFRP strengthening system for damaged steel members (e.g., fatigue cracks in bridge girders), limited information is available on the interaction between CFRP sheets and notched steel elements. It is, therefore, necessary to study the local response of CFRP sheets when associated with various crack properties. Such an investigation will eventually be used for understanding the global behavior of damaged flexural steel members strengthened with CFRP sheets. Contrary to reinforced/prestressed concrete applications that have design standards and guidelines (ACI 2007), globally-accepted design guidelines are not available for steel applications of CFRP composites. Significant research effort is thus required to warrant adequate usage of CFRP materials for the rehabilitation of steel structures.

3.3. Computational Modeling

This section summarizes a proposed modeling approach to predict the response of single-edge notched steel elements strengthened with CFRP sheets when subjected to monotonic axial tension. A three-dimensional nonlinear model was developed using the general-purpose FEA software ANSYS.

3.3.1. Specimen Details

A tension steel element having dimensions of 80 mm high \times 10 mm thick \times 710 mm long was used for the present numerical investigation, based on the test specimen of Hollstein (Hollstein et al. 1983). Figure 3.1 shows the details of the specimens studied. Three different initial crack depth-to-height ratios (a_0/h) of 0.1, 0.3, and 0.6 were taken into consideration at mid-length of the specimen, as shown in Table 1. A total of nine specimens were used (Table 1), including three unstrengthened and six strengthened steel strips to examine the effect of CFRP-

strengthening on the crack-dependent behavior of steel members loaded in axial tension. The CFRP sheet had dimensions of 80 mm wide \times 0.165 mm thick \times 600 mm long per layer, as shown in Fig. 1. CFRP-reinforcement ratios (ρ_{CFRP} = a ratio of CFRP to steel cross-sectional area) varied from 0% to 25%.

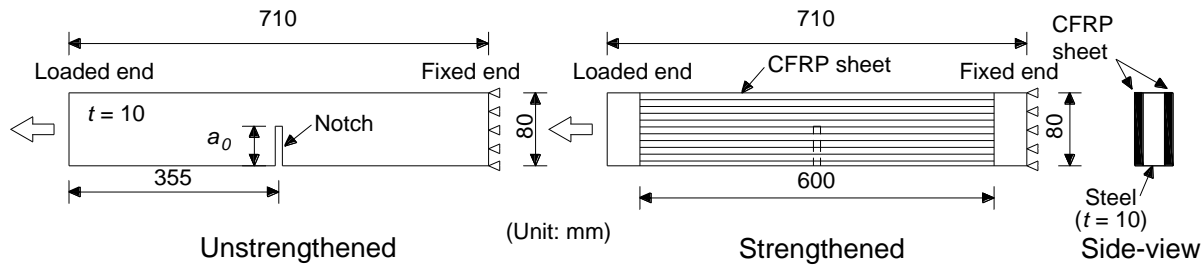


Fig. 3.1. Specimen details

The identification code of the numerical specimens (Table 3.1) represented the a_0/h ratio and the number of CFRP layers per side. For example, T01-0 means the specimen included an a_0/h ratio of 0.1 with no CFRP layer, whereas T06-3 indicates the specimen had an a_0/h ratio of 0.6 with three layers of CFRP sheet per side (i.e., total six layers of CFRP as shown in Fig. 3.1). For the convenience of notation, the number of CFRP layers listed in Table 1 (i.e., CFRP layer per side) was consistently used for this study.

Table 3.1. Specimen details

Specimen ID	CFRP sheet		a_0/h^a	Stiffness per thickness ^b (kN/mm ²)	Yield load (kN/mm)	Ultimate load (kN/mm)	Failure mode ^c
	Layer per side	ρ_{CFRP} (%)					
T01-0	0	0	0.1	22.0	30.8	31.7	Y
T01-1	1	3.7	0.1	23.1	32.3	33.8	Y
T01-3	3	11.0	0.1	23.9	33.5	34.3	Y
T03-0	0	0	0.3	20.8	25.0	26.7	Y
T03-1	1	4.7	0.3	22.0	29.2	32.3	D
T03-3	3	14.1	0.3	23.1	32.3	34.3	D
T06-0	0	0	0.6	18.2	14.6	15.3	Y
T06-1	1	8.3	0.6	20.6	21.2	25.2	R
T06-3	3	24.8	0.6	22.3	26.8	34.3	D

^a: initial crack depth (a_0) to specimen height (h) ratio

^b: apparent stiffness up to yield load

^c: Y = yielding of steel; D = debonding of CFRP after steel-yielding; R = rupture of CFRP

3.3.2. Constitutive Material Modeling

Table 3.2 provides the nominal material properties of the specimens, based on the manufacturers' data sheet. The behavior of structural steel was modeled using a bilinear stress-strain relationship with yield strength of 413 MPa and an elastic modulus of 200 GPa [Fig. 3.2(a)]. Given a crack growth across the specimen was represented by interface elements (discussed below), strain-hardening was not accounted for. In other words, the failure of the specimen would occur within the notch region prior to the initiation of strain-hardening in other regions. The constitutive behavior of CFRP was adopted from the manufacturer's data sheet (BASF 2007), as shown in Fig. 3.2(b), which is basically linear until CFRP-rupture takes place.

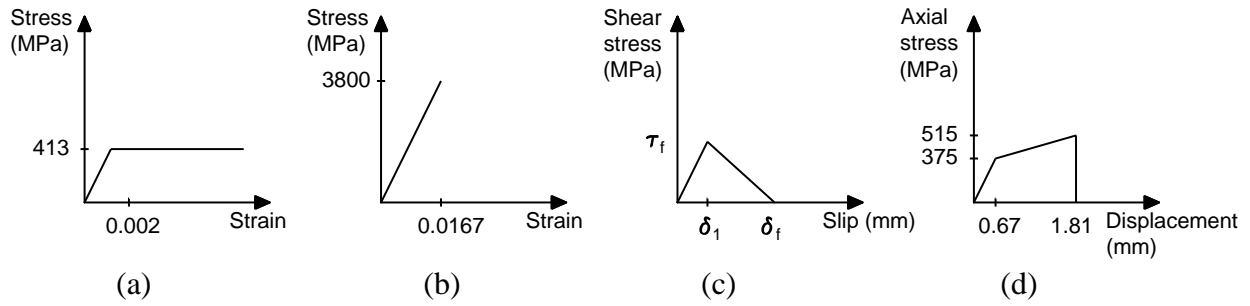


Fig. 3.2. Constitutive behavior: (a) steel; (b) CFRP sheet; (c) CFRP-steel interface; (d) crack opening of steel

The interfacial behavior between the steel and CFRP was modeled using an equation proposed by Xia and Teng (Xia and Teng 2005):

$$\delta_f = 62 \left(\frac{f_{ta}}{G_a} \right)^{0.56} \frac{t_a^{0.27}}{\tau_f} \quad \text{and} \quad \delta_1 = \frac{\tau_f t_a}{G_a} \quad \text{in N and mm} \quad (3.1)$$

where δ_1 and δ_f are the slip values at the peak stress and at zero stress after complete softening of the bond stress, respectively; f_{ta} is the tensile strength of the adhesive; G_a is the shear modulus of the adhesive; t_a is the thickness of the adhesive; and τ_f is the local bond strength that is $0.8f_{ta}$. The bilinear constitutive behavior shown in Eqn. 3.1 and Fig. 3.2(c) represented the local bond-slip

response of CFRP bonded to a steel substrate. Although the interface model is an approximation of the complex fracture mechanism at a material-level, such an approach is well accepted by the research community as in the case of the bilinear CFRP-concrete interface model (Dai et al. 2005; Lu et al. 2005). It should be noted that Eq. 3.1 has empirically been developed using various epoxy adhesives (e.g., tensile moduli from 4.0 GPa to 10.8 GPa) while it may allow reasonable extrapolation because the contribution of adhesives to the global behavior of CFRP-strengthened steel members is negligible (Kim and Harries 2012). Crack opening characteristics of the structural steel were modeled based on an experimentally measured axial stress-displacement response (Hollstein et al. 1983), as shown in Fig. 3.2(d). There may be other alternative models with advanced failure criteria for the crack-growth prediction of the steel substrate, whereas the proposed modeling technique is convenient to use and is further compatible to the CFRP-debonding model.

Table 3.2. Material properties from manufacturer

	Steel ^a	CFRP	Adhesive
Tensile strength (MPa)	413	3800	54
Tensile modulus (GPa)	200	227	3
Ultimate strain	0.002	0.0167	0.035
Poisson's ratio	0.3	0.27	0.4

^a: properties at yielding

3.3.3. Elements and Boundary Conditions

A typical FEA model constructed is shown in Fig. 3.3. Over 3,400 elements were used, including 94 interface elements across the midsection of the model where a refined mesh formulation was required near the notch to address stress concentrations. The size of elements varied from 0.5 mm to 35 mm (i.e., 0.07% to 4.9% of the specimen length). The steel member was modeled using three-dimensional structural solid elements (SOLID45). The eight-node

element had three translational degrees of freedom per node. This element can be used to model structural members showing large plasticity (ANSYS 2010). Homogeneous and rate-independent material characteristics were assumed.

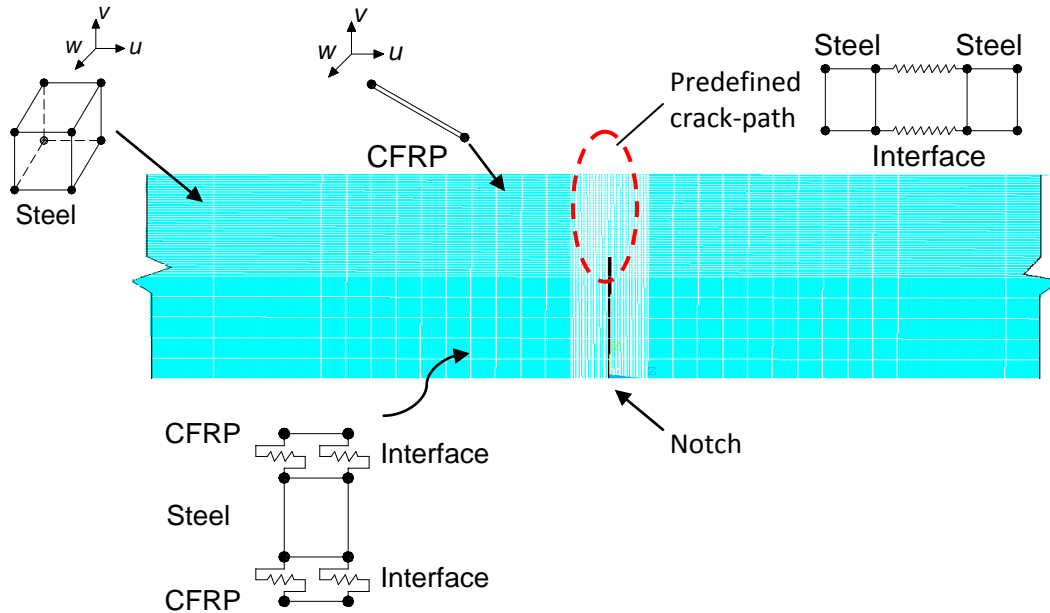


Fig. 3.3. FEA model constructed

The unidirectional CFRP sheet was represented by three-dimensional spar elements (LINK8) that had two nodes per element. The spar element included three degrees of freedom per node as is the case for the solid element and hence additional considerations on the connectivity such as constraint equations to resolve an incompatibility issue in the degrees of freedom between the two elements were not necessary. It should be noted that the transverse directional properties of the wet-lay-up CFRP composite were not modeled because the contribution of such properties to the load-bearing mechanism was negligible. The interface between the CFRP and steel was modeled using nonlinear spring elements (COMBIN39). This element had unidirectional load-displacement responses with two nodes per element that included an initial distance of zero between the two nodes. The spring element can be used for an analysis that requires large displacement (ANSYS 2010). The interfacial constitutive relationship

shown in Eq. 3.1 was incorporated into the spring elements to simulate debonding of the CFRP [Fig. 3.3]. The crack opening of the steel section was predefined across mid-length of the specimen [Fig. 3.3] and was modeled using COMBIN39 elements with the constitutive behavior shown in Fig. 3.2(d).

3.3.4. Validation of the Proposed Modeling Approach

Prior to conducting a parametric study, the proposed modeling approach was validated with published experimental data. The validation phases are as follows: i) an interface element to predict the local load (or stress)-slip response of the interface, (ii) an unstrengthened steel member with a notch subjected to axial tension, and iii) a tension steel member strengthened with CFRP sheets.

3.3.4.1. Interfacial response

Figure 3.4(a) demonstrates how the bond-slip relationship defined was implemented in the model at an interface element level. Necessary parameters for Eq. 3.1 were calculated based on the properties shown in Table 3.2.

3.3.4.2. Unstrengthened steel member in axial tension

Hollstein et al. (1983) tested a steel strip (710 mm long in grip-to-grip \times 10 mm thick \times 80 mm wide) subjected to axial tension. The specimen included a 48 mm notch at mid-length ($a_0/h = 0.6$) and was monotonically loaded until failure occurred. The focus of the experiment was on the fracture behavior of notched steel members, including load-displacement responses and elastic compliance. A three-dimensional FEA model was developed to predict test results, based on the proposed modeling approach [Figs. 3.2 and 3.3]. It should be noted that the geometric configuration and corresponding test scheme of Hollstein et al. (1983) were aligned with the need of the present study (i.e., a single-notched steel strip in monotonic tension). The

model prediction agreed well with the experimental data with an error of 7.6% in the ultimate load, as shown in Fig. 3.4(b). The test specimen exhibited a gradual decrease in axial stiffness near the yield load, whereas the model showed an ideal yield response. This discrepancy is attributed to the bilinear constitutive relationship of the steel, as shown in Fig. 3.2(a).

3.3.4.3. Strengthened steel member in axial tension

Fawzia et al. (2006) examined the behavior of steel elements bonded with CFRP sheets. A double-lap joint specimen, consisting of two steel strips (210 mm long \times 5 mm thick \times 50 mm wide, each) bonded with CFRP sheets ($L_{CFRP} = 160$ mm), was monotonically loaded in axial tension until failure took place. The CFRP sheet had a thickness of 0.176 mm with a tensile modulus of 215 GPa, while the adhesive included a tensile strength of 32 MPa and a modulus of 1.9 GPa with a layer thickness of 0.224 mm. A numerical model was developed to predict experimental data. Figure 3.4(c) compares the measured load-displacement response with the FEA prediction. Good agreement was observed with an error of 11.1% in the ultimate load. Such a discrepancy may be attributed to the experimental randomness of CFRP application; for example, the composite properties (CFRP + resin) could not be uniform along the test specimen given that the CFRP bonding was wet-lay-up. Fawzia et al. (2006) also reported an analogous trend of the prediction (i.e., over-estimation of ultimate loads), which justified the adequacy of the proposed modeling approach. Strain profiles along the CFRP sheets are shown in Fig. 3.4(d). Two load levels (25% and 75% of the ultimate load) were arbitrarily selected for a comparison purpose. The prediction agreed well with the measured strain values, while the predicted peak strains were a bit higher than the measured ones.

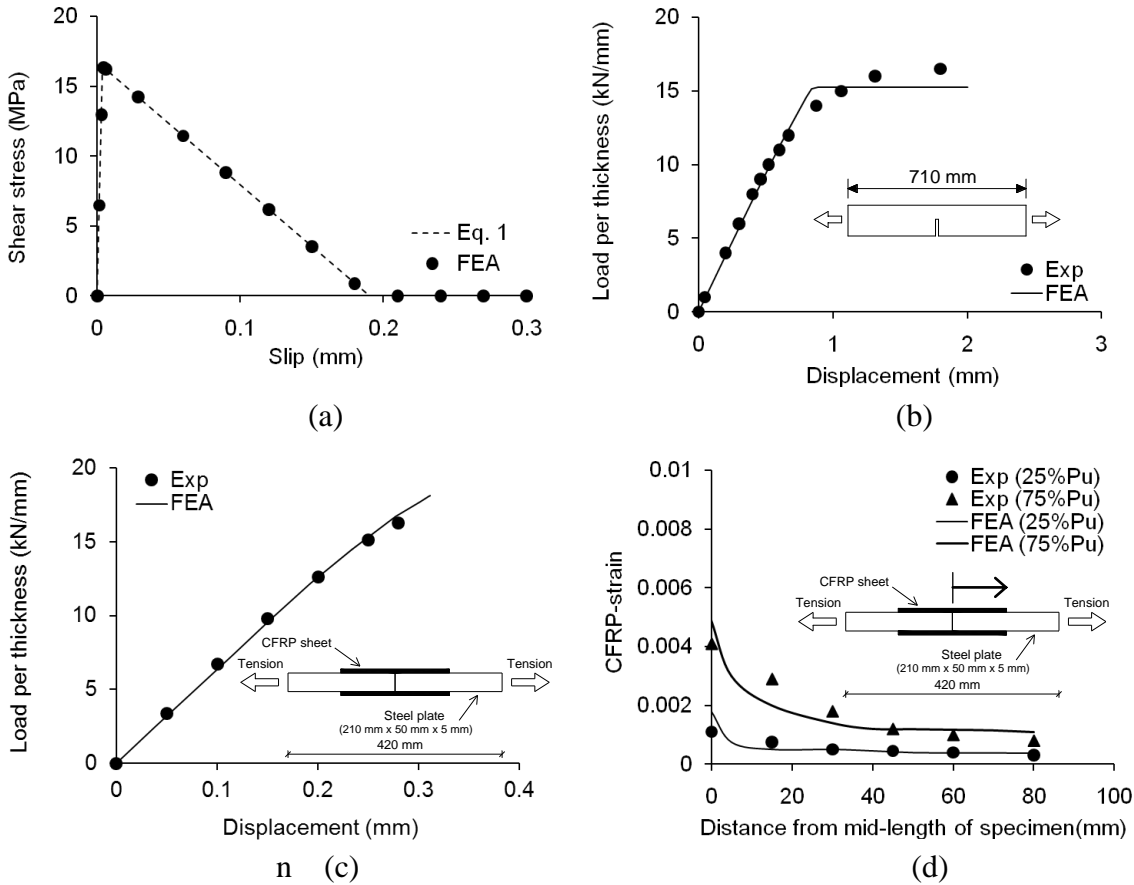


Fig. 3.4. Validation of the proposed modeling approach: (a) interfacial response; (b) unstrengthened steel member (Specimen D25 in Hollstein et al. 1983); (c) strengthened steel member (Specimen SN80 in Fawzia et al. 2006); (d) strain distribution along Specimen SN80 in Fawzia et al. (2006)

3.3.5. Summary of the Validation

The proposed modeling approach showed reasonable agreement in comparison to experimental data, even though some discrepancy was observed in the ultimate load. It was also found that the present mesh formulation was adequate and an additional sensitivity analysis was not necessary. Provided the predictive method was validated in terms of displacement, predictions on other displacement-based parameters (e.g., crack opening displacement) would be reliable. The validated modeling approach was used to predict the behavior of notched steel elements strengthened with multiple-layers of CFRP sheet.

3.4. Analysis of the Results

3.4.1. Load-Carrying Capacity and Failure Mode

The axial behavior of the predictive models is summarized in Table 3.1 and Fig. 3.5, including load-carrying capacity, axial stiffness, and failure modes. The effect of initial crack depth (a_0) was significant on the load-carrying capacity of the unstrengthened members. For example, a drop of 51.7% in the ultimate load was observed when an a_0/h ratio increased from 0.1 (T01-0) to 0.6 (T06-0), as shown in Fig. 3.5(a). It should be noted that the ultimate load of the specimens was determined based on the maximum load when an axial displacement reached 2 mm after yielding of the steel occurred and almost complete crack propagation was done across the steel section (to be discussed). Such a failure criterion was adopted from the experiment conducted by Hollstein et al. (1983) that provided geometric properties of the steel members used for this study. The difference between the ultimate and yield loads of the unstrengthened members was 4.6%, on average. The response of the specimens strengthened with the CFRP sheets was substantially improved, as shown in Fig. 3.5(b) and (c). The level of improvement in load-carrying capacity was proportional to a CFRP reinforcement ratio [Fig. 3.5d], in particular noticeable when the a_0/h ratio increased (i.e., increase in damage levels). An increase of 55.4% in ultimate load was observed when T06-0 was compared to T06-3, whereas the increase in the ultimate load from T01-0 to T01-3 was only 7.6%. For the specimens strengthened with three layers of CFRP sheet, the response was essentially independent of crack properties, as shown in Fig. 3.5(c). This observation indicates that adequate CFRP-strengthening for damaged steel members (e.g., fatigue cracks) can effectively minimize the effects of cracks. All specimens failed by yielding of the steel, followed by debonding of the CFRP sheets for the

strengthened specimens, as shown in Table 1. Specimen T06-1 ($\rho_{CFRP} = 8.3\%$ with $a_0/h = 0.6$) exhibited rupture of the sheets.

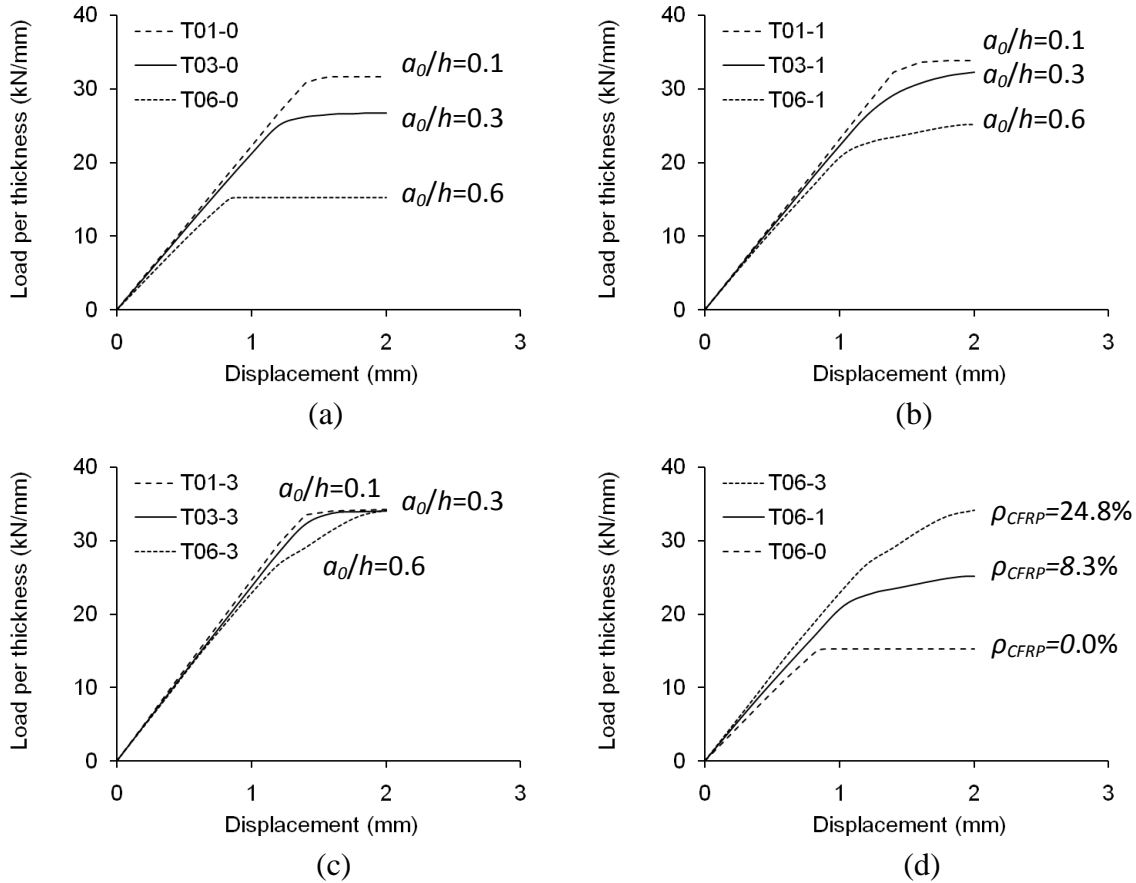


Fig. 3.5. Load-displacement response: (a) unstrengthened specimens; (b) strengthened specimens with one layer of CFRP; (c) strengthened specimens with three layers of CFRP; (d) comparison of various CFRP reinforcement ratios for specimens with $a_0/h = 0.6$

3.4.2. Crack Mouth Opening Displacement

The crack mouth opening displacement (CMOD) of the members is shown in Fig. 3.6, depending upon crack properties a_0/h . The unstrengthened specimens exhibited a long yield plateau [Fig. 3.6a]. The variation of the CMOD-stiffness for such specimens was considerable when an a_0/h ratio changed: a decrease of 76.0% in stiffness was observed when a_0/h ratios increased from 0.1 (T01-0) to 0.6 (T06-0), as shown in Fig. 3.6(a). The decreased stiffness affected the CMOD of the members. After yielding of the member, the CMOD dramatically

increased until failure occurred. A similar trend was observed for the strengthened specimens; however, the contribution of the initial damage (or a_0/h ratio) became reduced when the number of CFRP layer increased [Fig. 3.6(b) and (c)]. This can be explained by the active interaction between the CFRP and CMOD until debonding of the CFRP occurred. A change in CMOD-compliance is shown in Fig. 3.6(d) with respect to CFRP-reinforcement ratios. The CMOD-compliance was found to be a function of the initial damage level (i.e., a_0/h ratio). The specimens with $a_0/h = 0.1$ and 0.3 showed almost constant CMOD-compliance regardless of CFRP-reinforcement ratios. This observation indicates that the steel section was the primary component resisting the crack opening of lightly damaged steel specimens (e.g., a low a_0/h ratio up to 0.3), even though the specimens were strengthened. However, the compliance of the specimens with $a_0/h = 0.6$ exhibited a gradual decrease up to about $\rho_{CFRP} = 10\%$ and tended to be constant. It is, therefore, concluded that CFRP-strengthening is more effective for controlling the crack opening of damaged steel members when the level of damage increases.

3.4.3. Crack Propagation

Figure 3.7 shows the crack propagation of the members. The propagation was vertically measured from the notched end to the other end across the steel section until failure occurred. The crack propagation in all specimens exhibited a noticeable difference after CFRP-strengthening, depending upon a_0/h ratios as shown in Fig. 3.7(a) and (b). The maximum crack propagation values were dominated by the failure mode of the specimens (Table 3.1), while the crack propagation rate of the specimens having $a_0/h = 0.1$ was not influenced by the level of CFRP-strengthening [Fig. 3.7(c)]. This is attributed to the fact that the cross-section of the steel in the specimen with $a_0/h = 0.1$ was large enough to absorb the applied energy so that the crack propagation was primarily reliant upon the steel section area, rather than the external

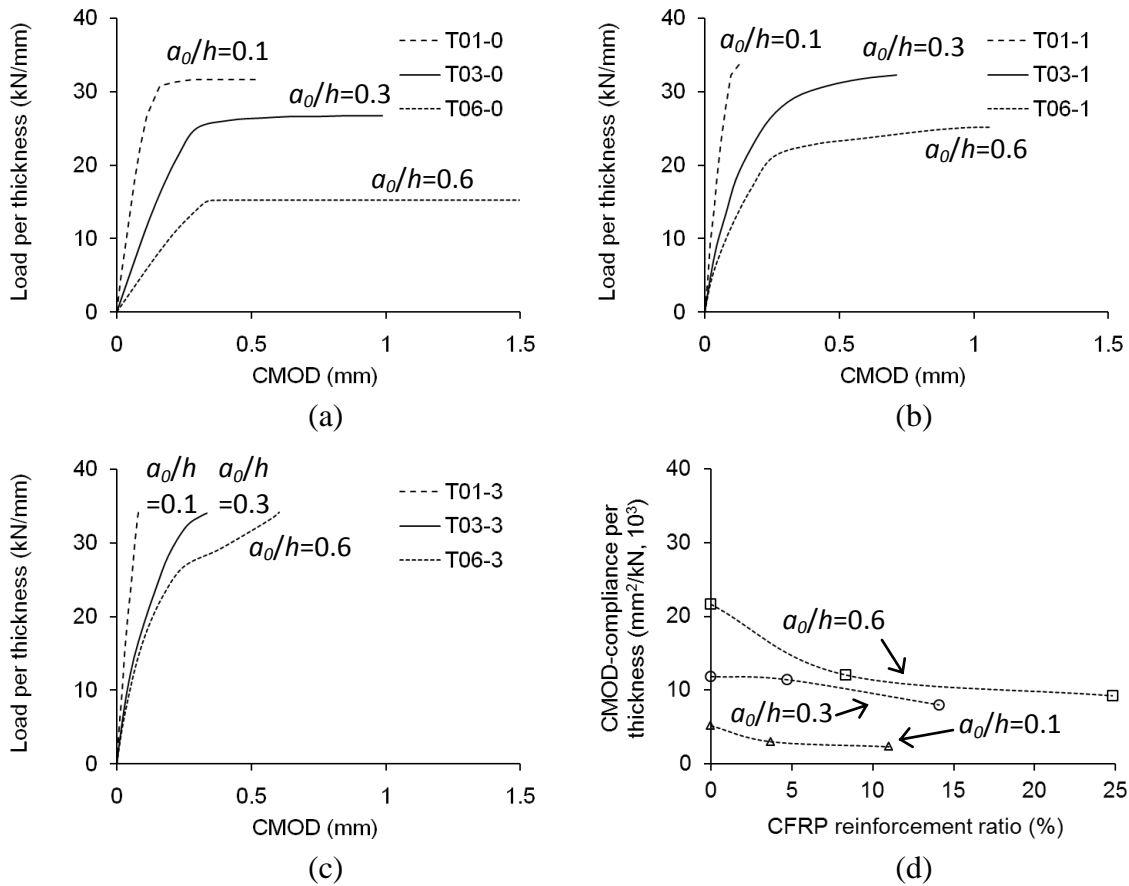


Fig. 3.6. Crack mouth opening displacement: (a) unstrengthened specimens; (b) strengthened specimens with one layer of CFRP; (c) strengthened specimens with three layers of CFRP; (d) comparison of CMOD-compliance per specimen thickness

reinforcement (CFRP sheets). The crack propagation of the members with $a_0/h = 0.6$, on the other hand, was significantly influenced by the level of CFRP-strengthening [Fig. 3.7(d)]. The unstrengthened specimen (T06-0) showed a very rapid propagation rate (almost flat slope) after yielding of the member, whereas the rate was noticeably improved when the CFRP-reinforcement ratio increased. The level of improvement was independent of CFRP-reinforcement ratios (i.e., similar slopes between Specimens T06-1 and T06-3), as shown in Fig. 3.7(d). This observation can be explained by the debonding failure of the CFRP.

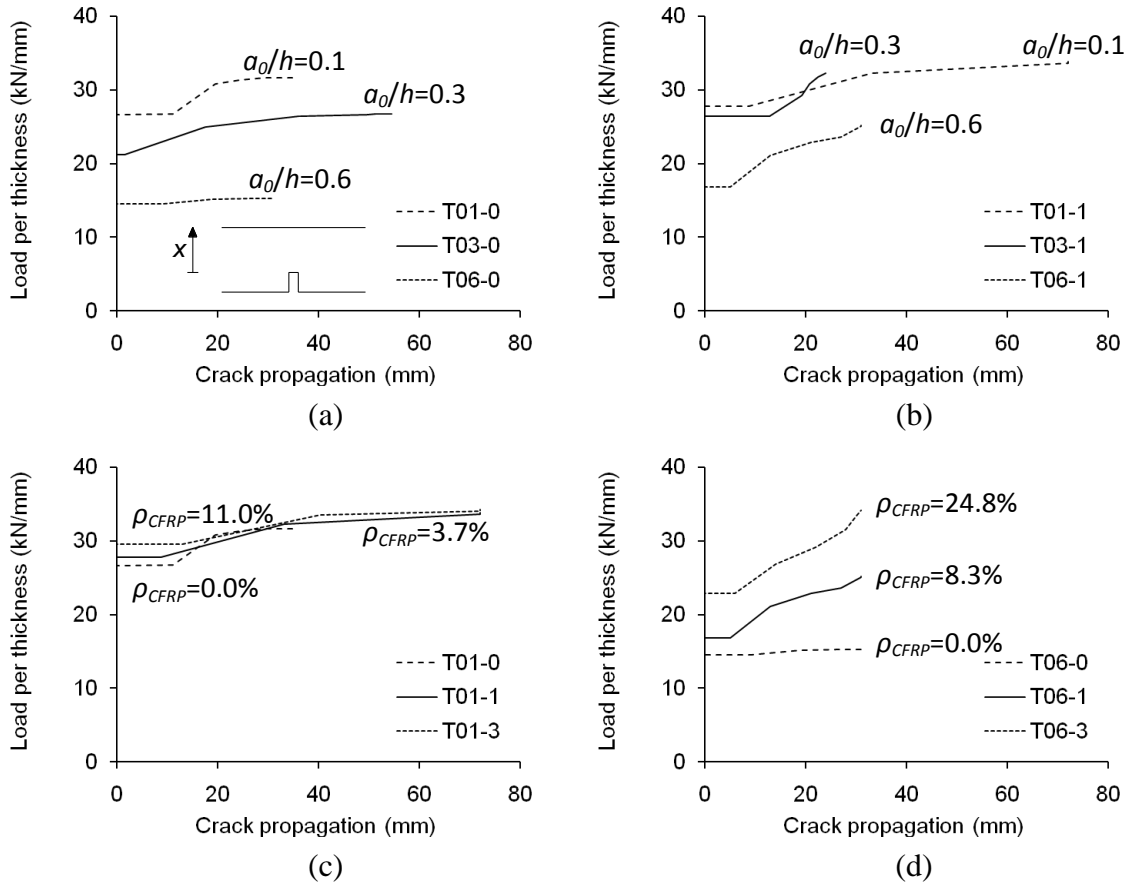


Fig. 3.7. Crack propagation: (a) unstrengthened specimens; (b) strengthened specimens with one layer of CFRP; (c) effect of CFRP strengthening for specimens with $a_0/h = 0.1$; (d) effect of CFRP strengthening for specimens with $a_0/h = 0.6$

3.4.4. Strain Profile

Strain development along the CFRP sheets is shown in Fig. 3.8. The strains were obtained along the notch-end side where CFRP-debonding was critical. For the specimen having $a_0/h = 0.1$ [Fig. 3.8(a)], a gradually increasing strain profile was observed with strain concentrations at the notch when a tension load increased. The strain at the notch was over 350% higher than the adjacent strains at failure of T01-1 (100% P_u in Fig. 3.8(a)) and some debonding of the CFRP was observed near the notch. The sudden increase in strain at 100% P_u near the very left end of T01-1 was due to the local yielding of the steel section that was located outside the CFRP-strengthened region. The specimen with $a_0/h = 0.3$ (T03-1) showed noticeable debonding

of the CFRP after $75\%P_u$, evidenced by the constant strain near the notch (Fig. 3.8b). The left side of the notch was more susceptible to debonding, which was close to the loaded end (i.e., the right side of the model was fixed using the area-constraint option, while the left side was loaded with a point load). In spite of debonding, CFRP strains kept increasing when the applied load increased, as shown in Fig. 3.8(b). The strengthened specimen having $a_0/h = 0.6$ did not exhibit any debonding of the CFRP until a load reached $75\%P_u$ [Fig. 3.8(c)]; however, a sudden increase in strain was observed at $100\%P_u$ up to the level of CFRP-rupture ($\varepsilon_{fu} = 0.0167$). This observation implies that an excessive load level for a steel member having noticeable damage (e.g., fatigue cracks) may cause an abrupt failure of the member even though it is strengthened with CFRP sheets. It should, however, be noted that this technical interpretation is only valid when the level of CFRP-strengthening is moderate (e.g., $\rho_{CFRP} = 8.3\%$ for the case shown in Fig. 3.8(c)). Figure 3.8(d) compares the effect of various a_0/h ratios on the strain profile of the specimens strengthened with one layer of CFRP sheet per side. It is interesting to note that the debonded area of T03-1 was 43.1% wider than that of T06-1. This phenomenon may be attributed to the fact that the steel cross-section of T03-1 was 175.0% larger than that of T06-1 and thus T03-1 resisted more load (i.e., P_u per specimen thickness = 32.3 kN/mm and 25.2 kN/mm for T03-1 and T06-1, respectively, as shown in Table 3.1), which allowed more debonding of the sheets until failure occurred. The maximum strain of T03-1 was, however, 44.3% lower than that of T06-1 [Fig. 3.8(d)]. The predefined failure criterion with a maximum displacement of 2 mm did not affect the behavior of CFRP because i) the steel substrate was not able to carry more load after yielding, ii) crack propagation across the steel was done, and iii) CFRP sufficiently debonded near the damage. It is, therefore, concluded that the level of damage

in the strengthened steel members (e.g., initial crack depth) can influence the debonding behavior of the CFRP and the level of strain development.

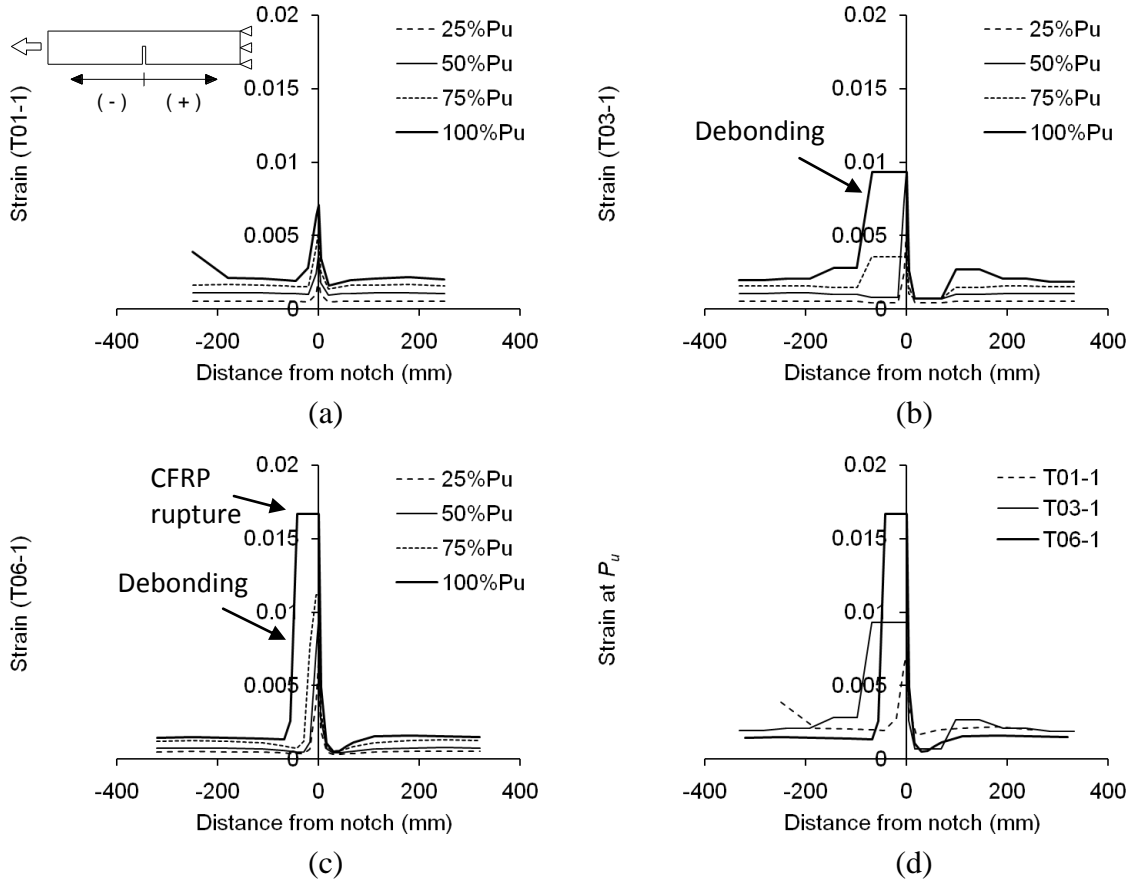


Fig. 3.8. Strain profile along the specimen: (a) $a_0/h = 0.1$ with one layer of CFRP; (b) $a_0/h = 0.3$ with one layer of CFRP; (c) $a_0/h = 0.6$ with one layer of CFRP; (d) comparison of various a_0/h ratios

Figure 3.9 shows CFRP-strain profiles (longitudinal-direction strains) across the steel section at the notch location. The strain increment rate was, in general, almost constant irrespective of load levels except near the notch tip, as shown in Fig. 3.9(a). Such an observation is due to the accumulated plastic damage of the steel near the notch tip where strain concentrations took place, including large local-displacement. Local debonding of the CFRP caused a so-called *strain lag* effect; in other words, the strains at the bottom of the specimen where the notch initiated were lower than the strain at the notch tip. The effect of a_0/h ratios on

strain development across the strengthened specimens is shown in Fig. 3.9(b). The level of initial damage represented by an a_0/h ratio significantly influenced strain development across the CFRP sheets. For example, the peak strain of T01-3 was only 34.9% of that of T06-3. When the initial notch size increased, the location of the peak CFRP strain tended to shift down from the notch tip, as shown in Fig. 3.9(b). It is interesting to note that the location of the peak strain was observed at approximately 1/3 of the notch depth (i.e., distance from the notch tip to the peak strain location = 2/3 of notch depth). This phenomenon implies that there may be a triangular force-distribution zone in the CFRP sheets across the notch. More research is recommended to confirm this hypothesis.

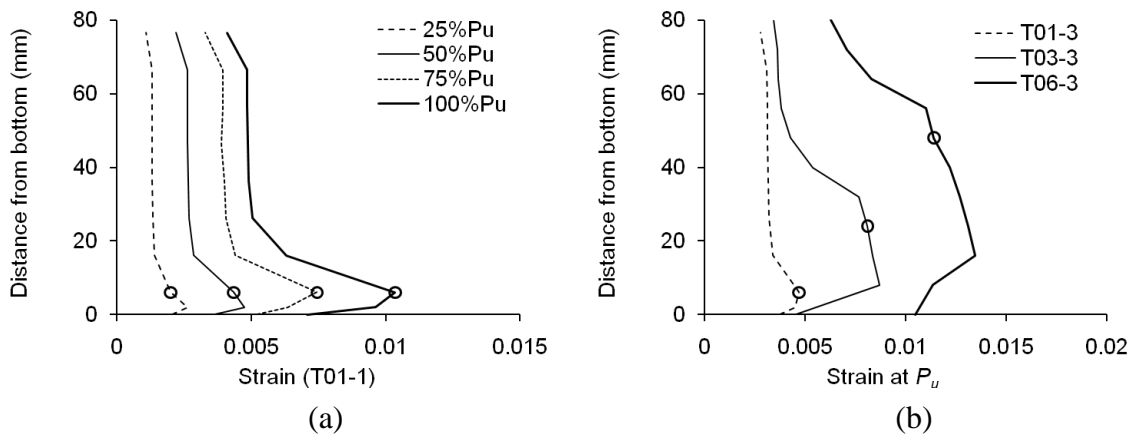


Fig. 3.9. CFRP-strain profiles across the specimen at notched location (circle = tip of notch): (a) specimen having $a_0/h = 0.1$ strengthened with one layer of CFRP; (b) comparison of specimens having various a_0/h ratios strengthened with three layers of CFRP

3.4.5. Fracture Properties

Figure 3.10 shows the work done per specimen thickness. The amount of work was obtained from the area under the load-displacement curve of each specimen at arbitrarily selected displacements from 0.5 mm to 2.0 mm. A trend line was added to represent the work characteristics of the three different a_0/h ratios. For the unstrengthened specimens [Fig. 3.10(a)], the work done per thickness tended to decrease with an increasing a_0/h ratio. Such a trend

became more obvious when a longitudinal displacement increased. This observation can be explained by crack propagation at the notched location; in other words, the area of the uncracked steel section decreased as the longitudinal displacement increased and thus the energy absorption capability of the section was reduced. The specimen strengthened with one layer of CFRP sheet (Fig. 3.10b) showed a similar trend in comparison to the unstrengthened counterparts (Fig. 3.10a). The strengthened specimens with three layers of CFRP exhibited considerable improvement in energy absorption capacity (or the work done per thickness) as shown in Fig. 3.10(c), particularly noticeable for the case of $a_0/h = 0.6$. For example, a drop of 6.7% in the work done per thickness was observed for the specimens with $a_0/h = 0.6$ when compared to that of the specimen with $a_0/h = 0.1$ (Fig. 3.10c), whereas a drop of 39.9% was noticed for the unstrengthened specimens from $a_0/h = 0.1$ to 0.6 [Fig. 10(a)]. Figure 3.10(d) compares the decreasing rate of the work per thickness with respect to the a_0/h ratio of the three categories, namely, unstrengthened, strengthened with one layer, and strengthened with three layers of CFRP sheet. Such an observation clearly indicates the effectiveness of CFRP-strengthening for damaged steel members in terms of absorbing applied energy that is equivalent to the work done by external load.

Figure 3.11 shows the variation of *J integral* values, depending upon strengthening schemes. The *J integral* is an expression to quantify the fracture characteristics of cracked members. This crack-path independent approach is particularly suitable for structural members demonstrating noticeable plasticity (Farahmand 2001). The *J integral* is defined as Eq. 3.2 (Rice 1968; Farahmand 2001):

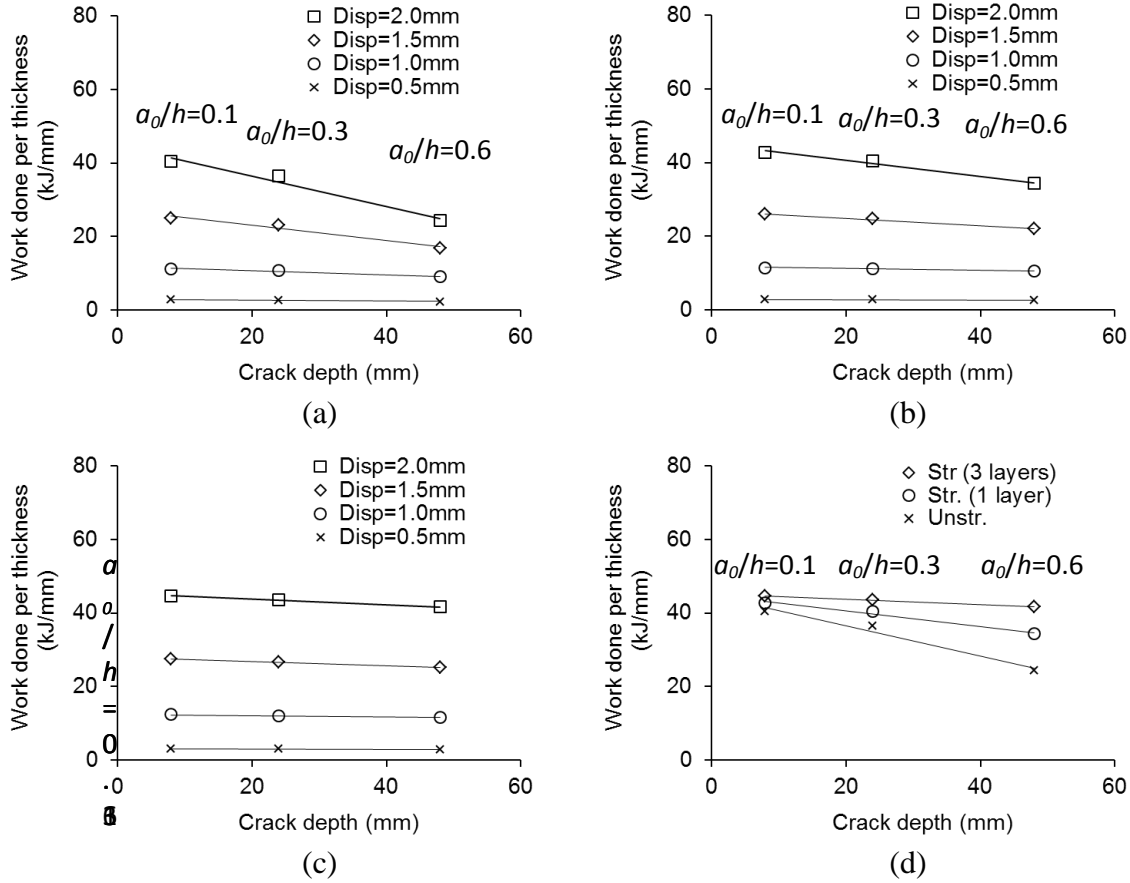


Fig. 3.10. Work done per specimen thickness: (a) unstrengthened; (b) strengthened with 1 layer of CFRP; (c) strengthened with 3 layers of CFRP; (d) comparison at a displacement of 2.0 mm

$$J = \int_{\Gamma} \left(w dy - t \frac{\partial u}{\partial x} ds \right) = -1/B (dU/da) \quad (3.2)$$

where Γ is a curve surrounding the notch tip; w is the strain energy density; x and y are the Cartesian coordinates; t is the traction vector defined as per the outward normal along Γ ; B is the specimen thickness; U is the absorbed energy; and a is the crack depth. The variation of the absorbed energy with respect to the crack propagation (dU/da) per unit thickness of the specimen may conveniently be obtained from the trend-lines shown in Fig. 3.10(a) to (c). The unstrengthened specimen showed an abrupt increase in J integral when its displacement exceeded 1 mm, as shown in Fig. 3.11; however, the increase rate of the J integral was reduced

for the strengthened specimens. This observation illustrates that the energy release rate of the strengthened specimens was much lower than that of the unstrengthened specimens and therefore CFRP-strengthening had contributed to delaying the fracture failure of the cracked steel members.

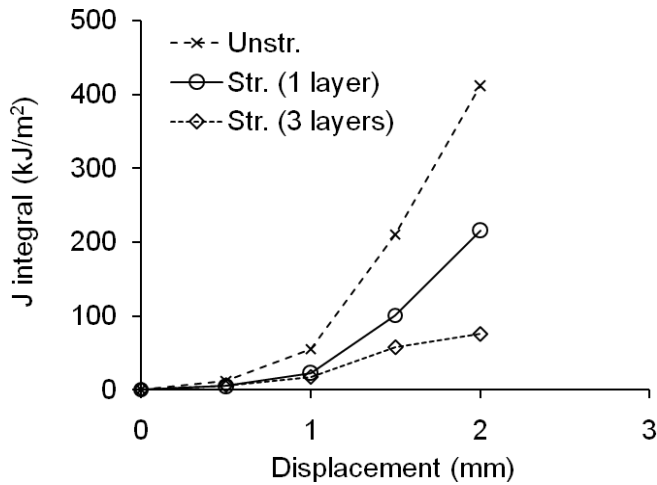


Fig. 3.11. J integral of the specimens

3.5. Summary and Conclusions

This study has presented the crack-dependent behavior of steel elements strengthened with CFRP sheets when loaded in axial tension. A modeling approach to simulate debonding of the sheets and crack propagation of the steel was proposed. Such an approach was experimentally validated and incorporated to three-dimensional FEA models to examine the effect of initial damage (i.e., various notch sizes) on the behavior of CFRP-strengthened steel elements. Further experimental research may help generalize the findings reported here, including experimental uncertainty. Conclusions from this study are presented as follows.

- CFRP-strengthening improved the load-carrying capacity and axial stiffness of the elements, while the level of initial damage represented by a_0/h ratios substantially influenced those responses of the unstrengthened counterparts. Strengthening effects

were noticeable when the initial damage increased (i.e., high a_0/h ratio). This finding indicates that CFRP-repair in design and practice of damaged steel members is an alternative to conventional repair methods. CFRP-reinforcement ratio (ρ_{CFRP}) was an important factor for governing the crack-dependent behavior of the strengthened elements. The yielding of steel sections was the dominant failure mode of the specimens, followed by CFRP-debonding. Such an observation should be taken into account when a repair design is conducted.

- The CMOD and corresponding compliance significantly increased when the level of initial damage (a_0/h ratio) increased, whereas such effects tended to be reduced with an increasing CFRP-reinforcement ratio. The crack propagation rate of the strengthened specimens was dominated by debonding characteristics of the CFRP. The maximum crack propagation values across the steel section were dependent upon the failure mode.
- CFRP-strains along the sheets gradually increased for the specimens with $a_0/h = 0.1$ when a tensile load increased, including strain concentrations near the notch. Abrupt increases in strain were, however, observed for the specimens with $a_0/h = 0.3$ and 0.6 . Debonding of the CFRP sheets influenced strain development. The rate of debonding propagation was primarily governed by the level of initial damage (a_0/h). Peak CFRP-strains were observed at about $1/3$ of the notch depth, rather than the notch tip. A triangular force-distribution zone in the CFRP sheets may exist across the notch.
- The work done per thickness of the strengthened specimens decreased with an increasing a_0/h ratio, particularly noticeable when a longitudinal displacement increased. The decreasing rate was improved because of the energy absorbing characteristics of the CFRP. For the unstrengthened specimens, the J integral abruptly increased when the

displacement increased (i.e., a sudden release of the internal energy); however, a much reduced energy release rate was observed for the strengthened specimens. The interaction between the CFRP reinforcement ratio and J integral was substantial.

CHAPTER 4. CFRP-REPAIR OF STEEL BEAMS HAVING VARIOUS INITIAL CRACK CONFIGURATIONS[†]

4.1. Abstract

This study presents an experimental program to study the behavior of notched steel beams repaired with carbon fiber reinforced polymer (CFRP) sheets. Particular attention is paid to examine the interaction between the level of initial damage (i.e., notch depth) and CFRP-repair. Multiple stages of fatigue crack propagation in a steel beam are simulated by various notch sizes, including a_0/h ratios = 0.1, 0.3, and 0.5 where a_0 is the notch depth and h is the beam height. A modeling approach is proposed to simultaneously take into account crack propagation across the steel section and debonding of the CFRP. The efficacy of the CFRP-repair is more pronounced when the damage level increases. The CFRP sheet stabilizes the crack mouth opening displacement (CMOD) of repaired beams until significant debonding takes place. The level of initial damage affects the behavior of a plastic region above the notch-tip, the rate of web-fracture, and the initiation of CFRP-debonding. The damage, however, does not influence the failure mode of the repaired beams. A crack-path independent fracture mechanics method is used to evaluate the energy release rate of the repaired beams.

4.2. Research Significance

Fatigue fracture of steel girder bridges is a critical consideration. Hysteretic loads can initiate cracks near the lower flange of a member that propagate up the web. The load-carrying capacity of such a member is, therefore, significantly dependent upon the level of damage. CFRP

[†]: This chapter has been previously published [Hmidan, A., Kim, Y.J., Yazdani, S. 2011. CFRP-repair of steel beams having various crack configurations, *Journal of Composites for Construction, American Society of Civil Engineers (ASCE)*, 15(6), 952-962].

is a promising material for repairing damaged steel members. The non-metallic reinforcement provides a number of structural benefits when compared to traditional repair methods (e.g., steel-plating) for deteriorated steel girders. Although the application of CFRP for steel members has recently attracted the rehabilitation community, their contribution to the behavior of repaired members is not fully understood yet. Very limited information is available on the interaction between the level of initial damage in steel girders and CFRP-repair. The present research addresses this identified research gap, based on an experimental program including CFRP-repaired steel beams having various levels of initial damage (representing multiple stages of fatigue crack propagation). A novel modeling approach is proposed by simultaneously taking into account crack propagation across the damaged steel section and debonding of the CFRP-steel interface. The foci of the present study are the crack-dependent response, failure mode, and fracture characteristics of damaged steel beams repaired with CFRP sheets.

4.3. Experimental Program

An experimental program was carried out to examine the behavior of steel beams having various damage properties repaired with CFRP sheets. Of interest was the interaction between the damage level and CFRP-repair (i.e., influence of initial damage such as crack-depth on the behavior of a CFRP-repaired beam), rather than the strength-recovery of damaged beams. The following presents the details of materials, test specimens, and instrumentation.

4.3.1. Beam Details

W4×13 (W100×19 in metric designation) A992 hot-rolled steel sections were used for this study. Table 4.1 summarizes the properties of all materials, including steel, CFRP, and epoxy adhesive. Six beams were tested as summarized in Table 4.2. Damage of the beams was simulated by notching the web using a 0.63 mm-thick blade saw in addition to a cut of 38 mm on

both sides of the tensile flange, as shown in Fig. 4.1. The flange cut was done to initiate stress concentrations at the CFRP-steel interface and also to conveniently observe the cracking behavior of the beams.

Table 4.1. Material properties from manufacturer

	Steel	CFRP	Adhesive
Tensile strength (MPa)	413 ^a	3800	54
Tensile modulus (GPa)	200	227	3
Ultimate strain	0.002 ^a	0.0167	0.035
Poisson's ratio	0.3	0.27	0.4

^a: property at yielding

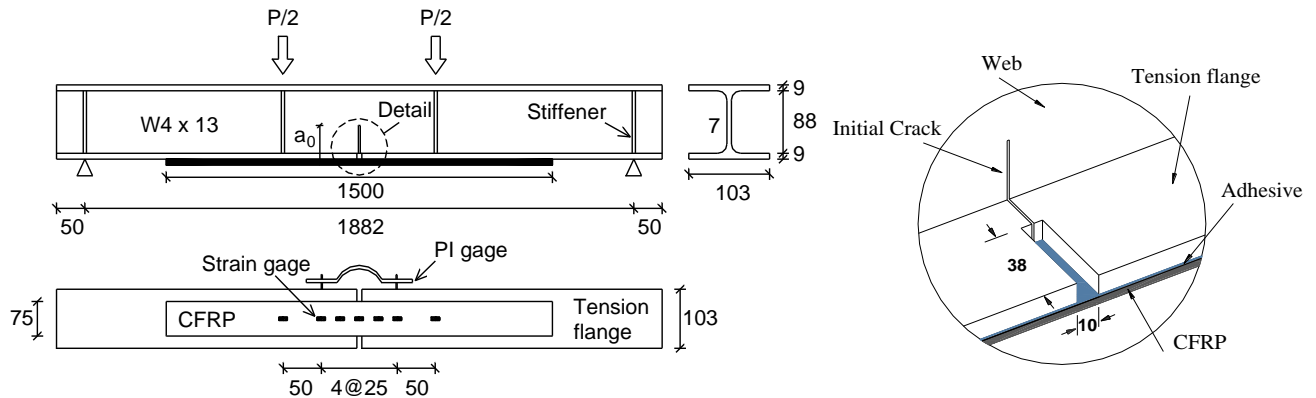


Fig. 4.1. Beam details and test set-up (unit: mm)

The beams had three different notch depths to represent various stages of fatigue-crack propagation (i.e., initial damage prior to repair work being conducted): 10.6 mm ($a_0/h = 0.1$), 31.8 mm ($a_0/h = 0.3$), and 53.0 mm ($a_0/h = 0.5$) where a_0 is the notch depth and h is the beam height [Fig. 4.1]. Three of the six beams were repaired using one layer of CFRP sheet (75 mm wide \times 0.165 mm thick \times 1,500 mm long). The CFRP was bonded to the tensile soffit of the notched beams with an epoxy adhesive ($t = 1.2$ mm on average). The repaired beams were cured for a minimum of seven days at room temperature before a load test was conducted. As shown in Table 4.2, the identification code of the specimens represents the a_0/h ratio and the presence of

the CFRP (0 = unrepaired and 1 = repaired). For example, B01-0 denotes an unrepaired beam with $a_0/h = 0.1$, whereas B05-1 designates a repaired beam with $a_0/h = 0.5$. To preclude the local and flexural torsional buckling of the beams, four pairs of hollow steel sections (50 mm×25 mm ×3 mm) were welded to the web at all loading points [Fig. 4.1].

Table 4.2. Test matrix

Beam	a_0/h	Repair	Method	Load response (kN) ^a			Elastic stiffness (kN/mm)	Failure mode ^b
				P_y	P_{ci}	P_u		
B01-0	0.1	No	Exp	38.4	46.2	46.2	3.5	Y → C
			FEA	36.0	39.1	42.2	3.4	Y → C
B01-1	0.1	Yes	Exp	47.1	51.9	51.9	5.5	D → Y → R → C
			FEA	45.8	52.4	54.0	4.8	D → Y → R → C
B03-0	0.3	No	Exp	23.1	27.2	27.2	2.3	Y → C
			FEA	19.8	24.0	25.2	2.1	Y → C
B03-1	0.3	Yes	Exp	25.0	31.6	33.2	4.9	D → Y → CD → C
			FEA	27.7	32.2	33.6	4.3	D → Y → R → C
B05-0	0.5	No	Exp	10.4	14.8	14.8	1.2	Y → C
			FEA	10.1	12.0	13.2	1.0	Y → C
B05-1	0.5	Yes	Exp	16.4	18.8	19.9	2.9	D → Y → R → C
			FEA	17.8	18.0	22.0	2.5	D → Y → R → C

^a: P_y = yield load; P_{ci} = crack-initiation load across the web; P_u = ultimate load

^b: Y = yielding of steel; C = crack propagation up the web; D = partial debonding of CFRP; R = rupture of CFRP; CD = complete debonding of CFRP

4.3.2. Surface Preparation and Micro-Topography

The tension flange of all repaired beams was grit-blasted [Fig. 4.2(a)] and cleansed with an air compressor and acetone. Although surface preparation is commonly accepted for such a bond-critical application of CFRP to improve bond between the CFRP and substrate (Shaah and Fam 2008), specific requirements have not been developed yet. An instantaneous laser scanner, based on optical triangulation theory, was employed to measure the surface preparation of the steel beams [Fig. 4.2(b)]. The laser scanner projected a laser beam on the steel surface. A charge-coupled device camera mounted to a carriage [Fig. 4.2(c)] captured the reflected light to generate a digital elevation model for the scanned surface. A post-processing was conducted using the

Surfer 8 program for digital-mapping of the scanned data (Golden Software 2010). Further details of the laser scanning are available in Darboux and Huang (2003) and Kim et al. (2011).

The effect of the grit-blasting was obviously observed in Figs. 4.2(d) and (e) which compared the scanned surface before and after the preparation, respectively (only selected portions are shown for clarity).

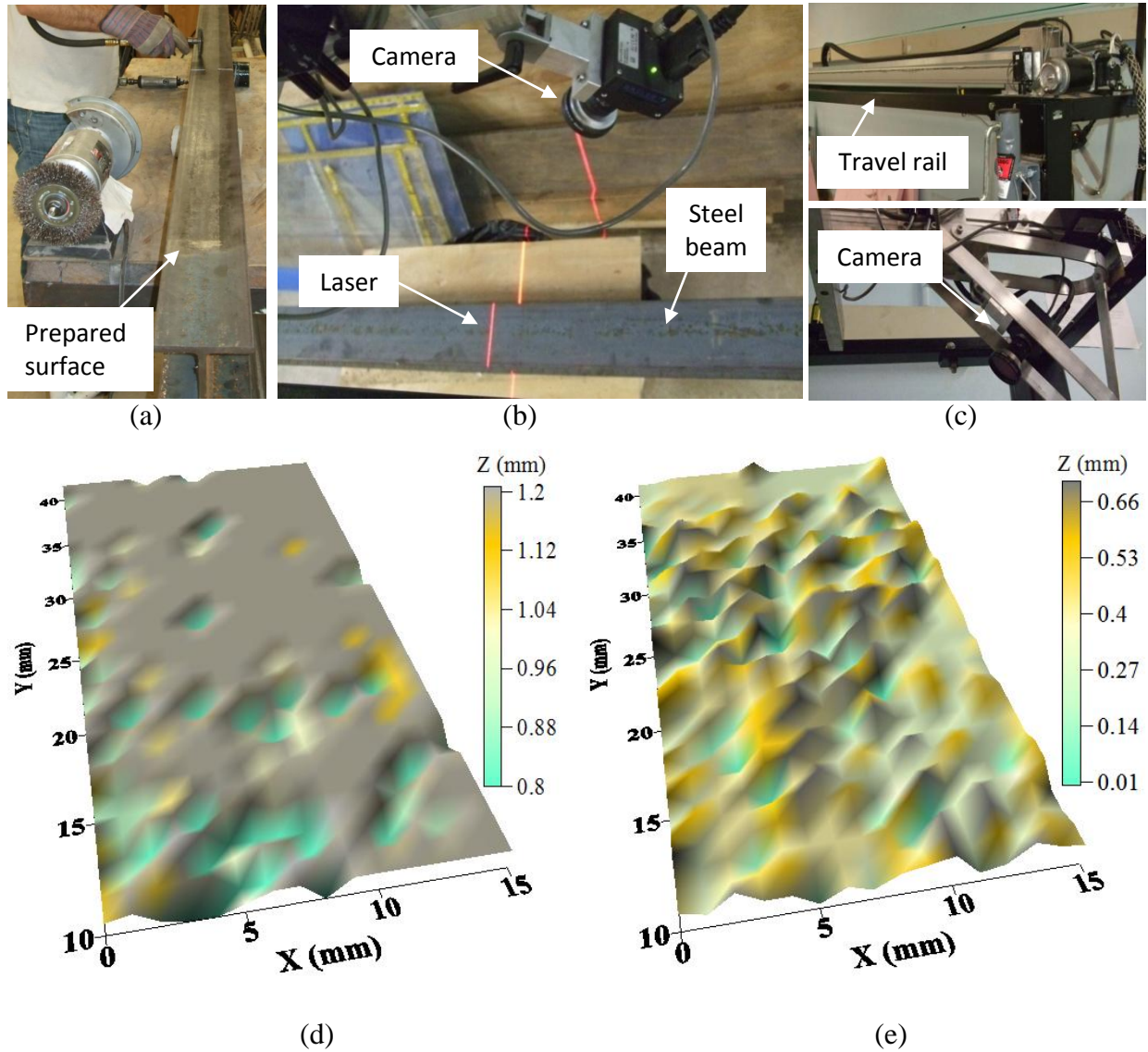


Fig. 4.2. Micro-topography of steel surface: (a) surface preparation; (b) laser scanning; (c) details of laser scanner; (d) unprepared surface; (e) prepared surface

4.3.3. Test Set-up and Instrumentation

All beams were simply supported and loaded in four-point bending. The loading span was 1,882 mm and the constant moment zone was 444 mm, as shown in Fig. 4.1. The flexural behavior at midspan of the test beams was measured using a load cell, a linear potentiometer, and two displacement-type strain transducers (so-called PI gages) with a gage length of 100 mm. Strain gages were bonded to the CFRP to study debonding propagation [Fig. 4.1]. All data were recorded by a data acquisition system.

4.4. Proposed Model

A three-dimensional FE model was constructed to predict the behavior of experimental beams using the general-purpose FEA program ANSYS. The proposed modeling approach is unique because it simultaneously takes into account crack propagation across the critical section of a steel beam repaired with CFRP and debonding progression of the CFRP.

4.4.1. Constitutive Modeling

The behavior of steel was modeled using a bilinear stress-strain relationship with a yield strength of 413 MPa and elastic modulus of 200 GPa [Fig. 4.3(a)]. Strain hardening was not accounted for because the full plastic capacity of steel sections studied here was expected before hardening occurred. The behavior of CFRP was represented by a linear constitutive response with an ultimate tensile strength of 3,800 MPa and corresponding rupture strain of 1.67% [Fig. 4.3(b)]. The crack opening property of the steel section was modeled using an axial stress-displacement response measured from a single-edge notched tension specimen (Hollstein et al. 1983), as shown in Fig. 4.3(c).

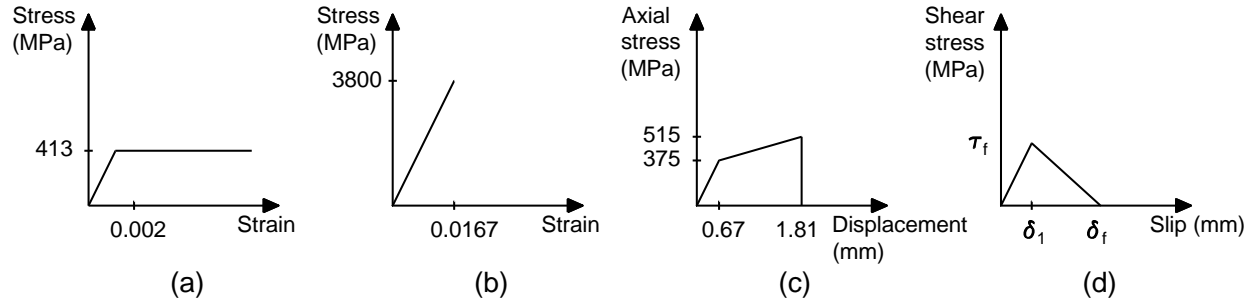


Fig. 4.3. Constitutive modeling: (a) steel beam; (b) CFRP sheet; (c) crack-opening displacement of steel section; (d) CFRP-steel interface

To model the interfacial behavior between the CFRP and steel, a bilinear bond-slip relationship proposed by Xia and Teng (2005) was adopted [Eq. 4.1. and Fig. 4.3(d)]. Such a constitutive model can represent the local response of the CFRP bonded to a steel substrate.

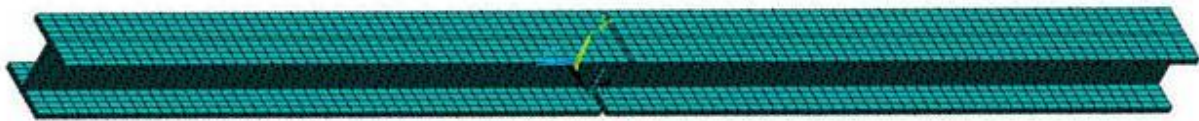
$$\delta_f = 62 \left(\frac{f_{ta}}{G_a} \right)^{0.56} \frac{t_a^{0.27}}{\tau_f} \quad \text{and} \quad \delta_1 = \frac{\tau_f t_a}{G_a} \quad (4.1)$$

where δ_1 and δ_f are the slips at the peak average shear stress and at zero stress after complete softening of the bond stress, respectively; f_{ta} is the tensile strength of the adhesive; G_a is the shear modulus of the adhesive; t_a is the thickness of the adhesive; and τ_f is the local bond strength that is $0.8f_{ta}$. The units used are in N and mm. The applicability of Eq. 4.1 to the present study is reasonable because it has been developed using three types of adhesives that can cover the material properties of the adhesive used here.

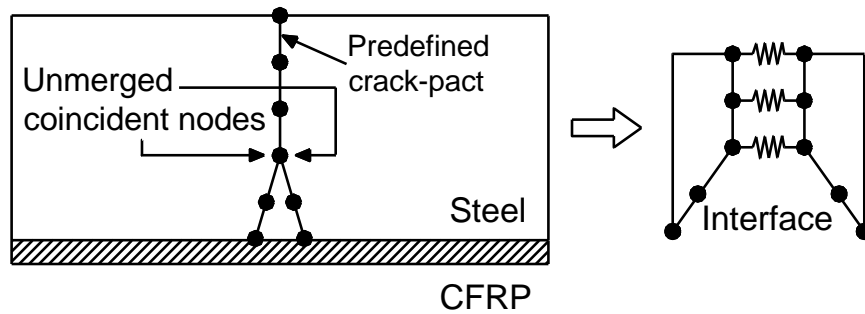
4.4.2. Element Description and Boundary Condition

Figure 4.4(a) shows an FE model developed. Eight-node structural solid elements (SOLID45) that can simulate large plasticity were used to represent the behavior of a steel beam. The CFRP sheet was modeled using three-dimensional spar elements (LINK8). The two-node CFRP element has the same degrees of freedom (three translational) per node as the steel element and thus these elements can be adequately connected using an interface element. Crack

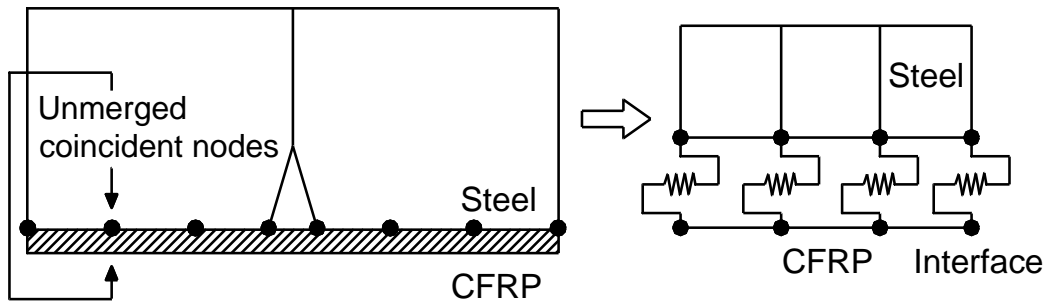
propagation of the steel section was predefined at midspan of the beam where notched, and was represented by interface elements (COMIN39) [Fig. 4.4(b)]. The two-node nonlinear spring element shows a unidirectional displacement when subjected to a load. The distance between the two nodes was initially zero and a stretch (i.e., bond-slip) took place depending upon the level of load, as depicted in Fig. 4.4(c).



(a)



(b)



(c)

Fig. 4.4. Proposed modeling approach: (a) constructed model; (b) crack propagation model across steel section; (c) debonding propagation model along CFRP-steel interface

The interfacial behavior between the CFRP and steel was modeled using COMBIN39 [Fig. 4.4(c)]. The constitutive behavior based on Eq. 4.1 was adopted to represent the interfacial bond-slip between the CFRP and steel substrate. Rate-independent and homogenous material

characteristics were assumed for all the properties described above. A simply-supported boundary condition was provided by constraining necessary nodes in translation as in the case of the experiment [Fig. 4.1].

4.4.3. Validation of Interface Modeling Approach

The proposed interface modeling approach using COMBIN39 was experimentally validated prior to constructing a beam model. Experimental programs conducted by Hollstein et al. (1983) and Fawzia et al. (2006) were used.

4.4.3.1. Single-edge notched specimen in axial tension

The modeling approach described above was used to model a single-edge notched steel coupon (710 mm long×80 mm wide×10 mm thick) conducted by Hollstein et al. (1983). The specimen had a notch length of 48 mm and was monotonically loaded in axial tension until failure occurred. The model accounted for crack propagation across the critical section (i.e., notch location). The predicted response agreed well with that measured experimentally, including an error of 7.6% in the ultimate load, as shown in Fig. 4.5(a).

4.4.3.2. Double-lap steel joint bonded with CFRP sheets

A double-lap joint (Fawzia et al. 2006) was utilized to validate the CFRP-steel interface model. The specimen consisted of two plates (210 mm long×5 mm thick×50 mm wide, each) bonded with three layers of CFRP sheets on both sides. Each layer of CFRP had a thickness of 0.176 mm with a tensile modulus of 215 GPa. The epoxy adhesive ($t = 0.224$ mm) used had a tensile strength of 32 MPa and corresponding modulus of 1.9 GPa. Figure 4.5(b) shows the response of an interface element in comparison to that obtained using Eq. 1. The double-lap joint model predicted well the load-displacement behavior of the experiment, as shown in Fig. 4.5(c), with an error of 11.1% in the ultimate capacity. Figure 4.5(d) compares the predicted CFRP

strains to those measured. Experimental uncertainty could have contributed to the discrepancy, such as adhesive thickness and bond quality in a wet-lay-up application.

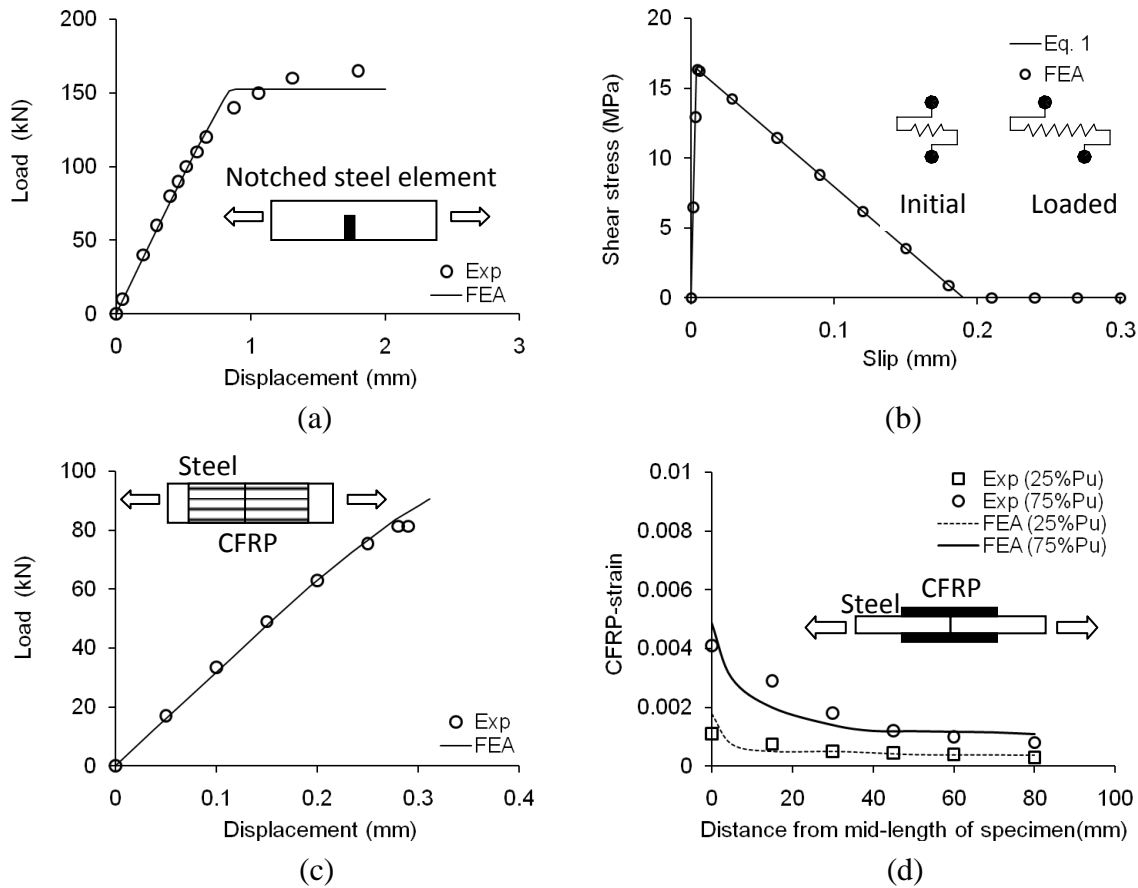


Fig. 4.5. Validation of interface modeling: (a) single-edge notched steel coupon; (b) element response of CFRP-steel interface; (c) steel coupon bonded with CFRP; (d) strain distribution along CFRP bonded to steel substrate

4.5. Test Results and Analysis

This section summarizes all test results and predicted behavior of the beams, including crack-depth-dependent response, failure mode, strain development, and fracture characteristics.

4.5.1. Failure Mode

The failure mode of the experimental and predicted beams is summarized in Table 4.2. The unrepaired beams showed a typical crack-fracture failure. Significant plasticity took place at the tip of the notch, followed by yielding of the web with increased load. Crack propagation was

then observed, as shown in Fig. 4.6(a). The predicted failure agreed well with the experimental counterpart [Fig. 4.6(b)].

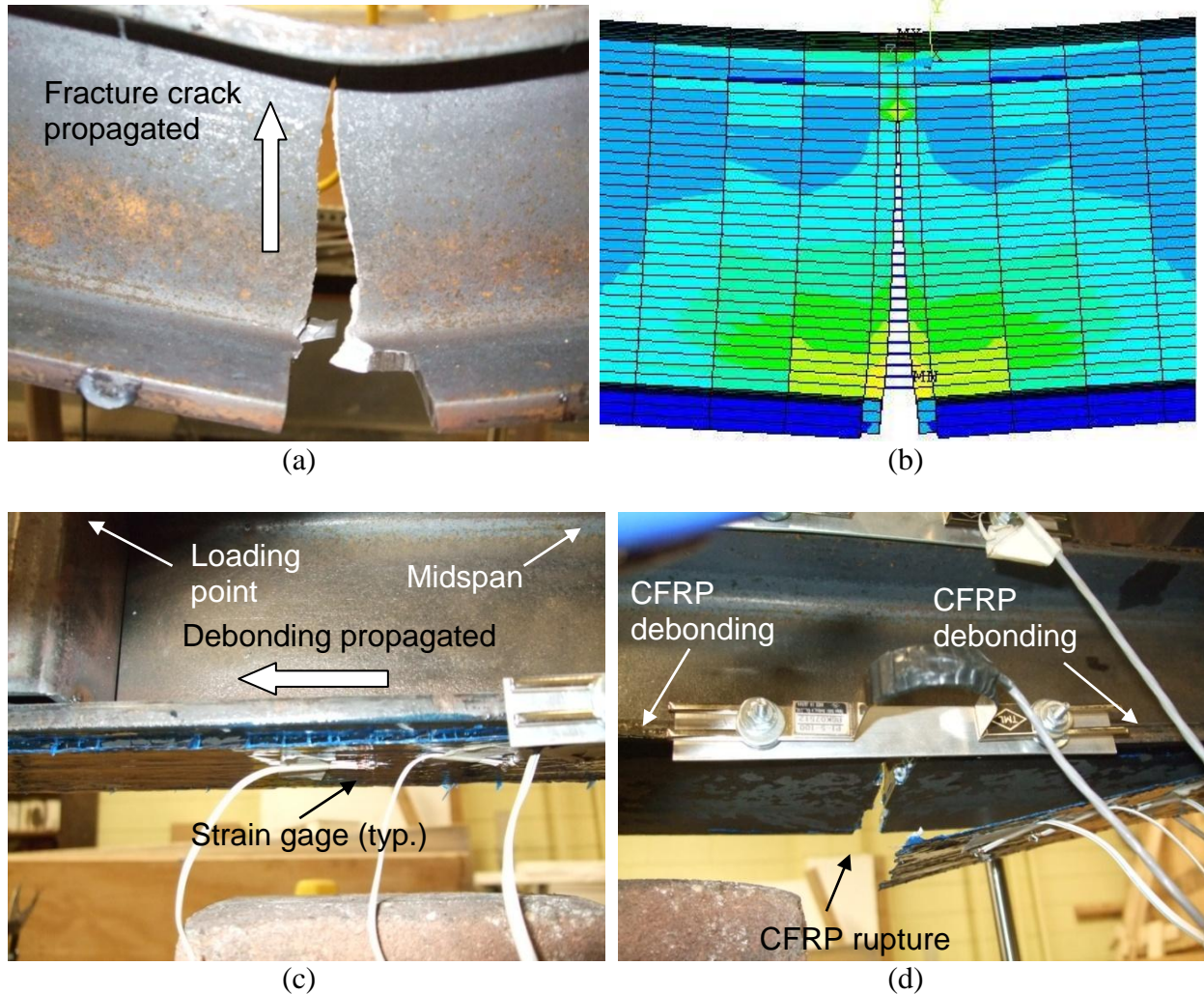


Fig. 4.6. Failure mode: (a) unrepaired experimental beam; (b) unrepaired predicted beam; (c) CFRP-debonding propagated along the interface; (d) CFRP-rupture at notch location

The rate of web-fracture was influenced by the level of initial damage (i.e., a_0/h ratio); for instance, Beam B01-0 demonstrated much rapider crack propagation than did Beam B05-0 because of the sudden energy release (to be discussed). The repaired beams exhibited a consistent failure mode regardless of the notch size: i) partial debonding of the CFRP (interfacial debonding) was initiated at the notch location due to stress concentrations and

propagated along the bond line with increased loads [Fig. 4.6(c)]; ii) rupture of the CFRP occurred when its strain reached the ultimate strain [Fig. 4.6(d)]; and iii) a fracture-crack rapidly developed toward the upper flange as in the case of the unrepaired beam [Fig. 4.6(a)]. It should be noted that the inconsistent failure of the experimental beam B03-1 (failed by CFRP-debonding, rather than rupture, as shown in Table 4.2) is attributed to inadequate bond between the steel substrate and CFRP, which could happen in a wet-lay-up application (further details are discussed in the *Debonding Behavior* section).

4.5.2. Load-Deflection

Figure 4.7 shows the load-deflection response at midspan of the beams. The load-carrying capacity of the beams was significantly influenced by the level of initial damage (i.e., notch size). For example, the measured ultimate loads of the unrepaired beams having $a_0/h = 0.3$ (B03-0) and 0.5 (B05-0) were 41.1% and 56.9% lower than that of the beam with $a_0/h = 0.1$ (B01-0), respectively, as shown in Table 4.2 and Fig. 4.7(d). A similar trend was observed for the repaired beams. The predicted ultimate loads agreed well with those measured experimentally, including average errors (experimental vs. FEA) of 8.9% and 5.3% for the unrepaired and repaired beams, respectively [Fig. 4.7(d)]. The yield capacity of the damaged beams was improved due to the CFRP-repair, particularly noticeable when the level of damage increased, as shown in Table 4.2. The insignificant increase in the experimental yield load of Beam03-1 was due to the premature debonding of the CFRP (to be discussed). Such improvement in the yield capacity is attributed to load-sharing between the CFRP and steel. The bonded CFRP sheet provided a crack-bridging force at the notch location even though partial debonding took place. This effect, however, was not noticeable after significant debonding of the CFRP occurred.

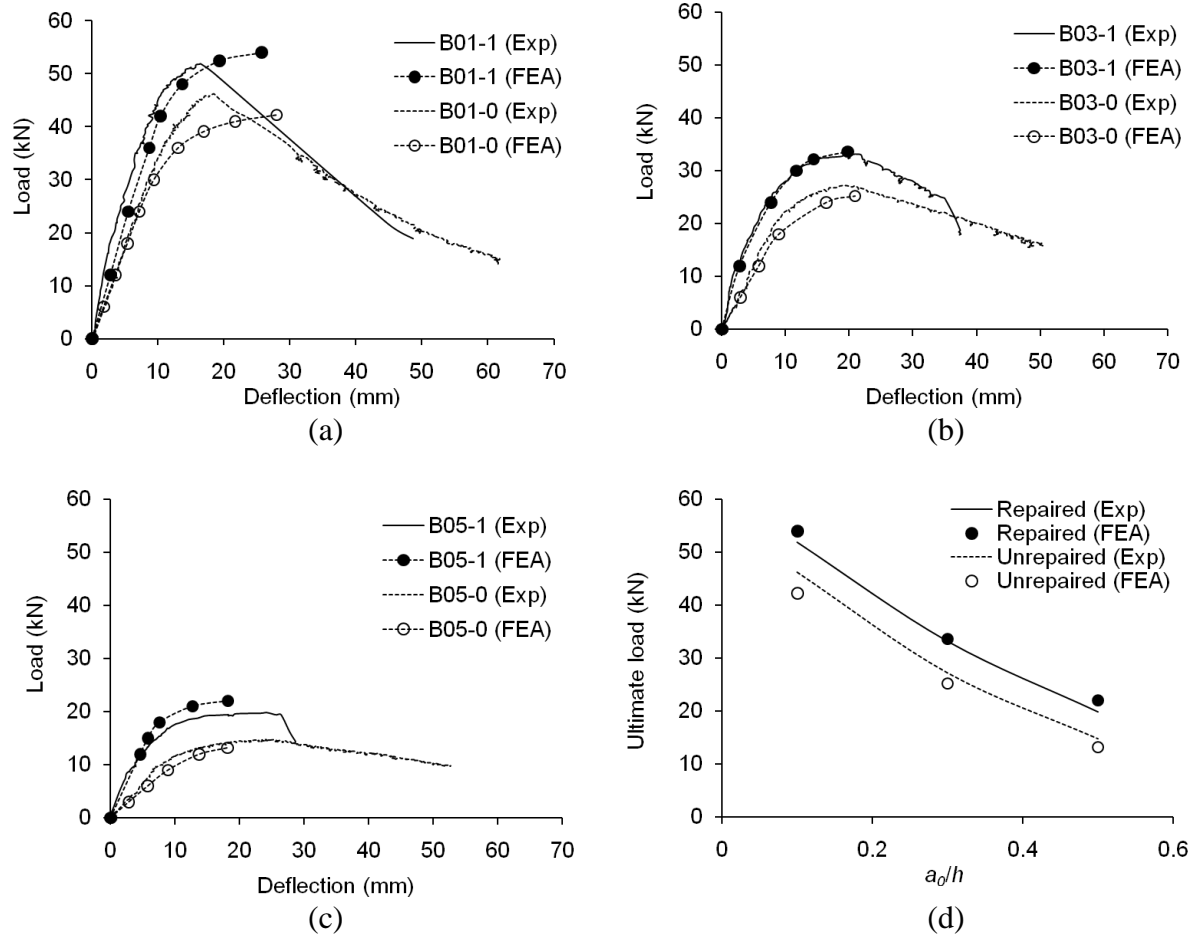


Fig. 4.7. Load-deflection of beams: (a) beams with $a_0/h = 0.1$; (b) beams with $a_0/h = 0.3$; (c) beams with $a_0/h = 0.5$; (d) comparison of ultimate load

The ultimate load of the repaired beams benefitted more when the damage level increased, as shown in Fig. 4.8(a). The flexural stiffness of the repaired beams noticeably increased in comparison to that of the unrepaired beams. The stiffness was obtained from the initial slope of the load-deflection responses shown in Fig. 4.7(a) through (c). The increases in measured stiffness induced by the repair were 57.1%, 113.0%, and 141.7% for the beams having $a_0/h = 0.1, 0.3,$ and $0.5,$ respectively, as shown in Fig. 4.8(b). The predicted stiffness demonstrated similar increments. These observations indicate that CFRP-repair becomes more effective when the level of initial damage (i.e., damage prior to repair work being conducted) increases, including enhanced serviceability and load capacity.

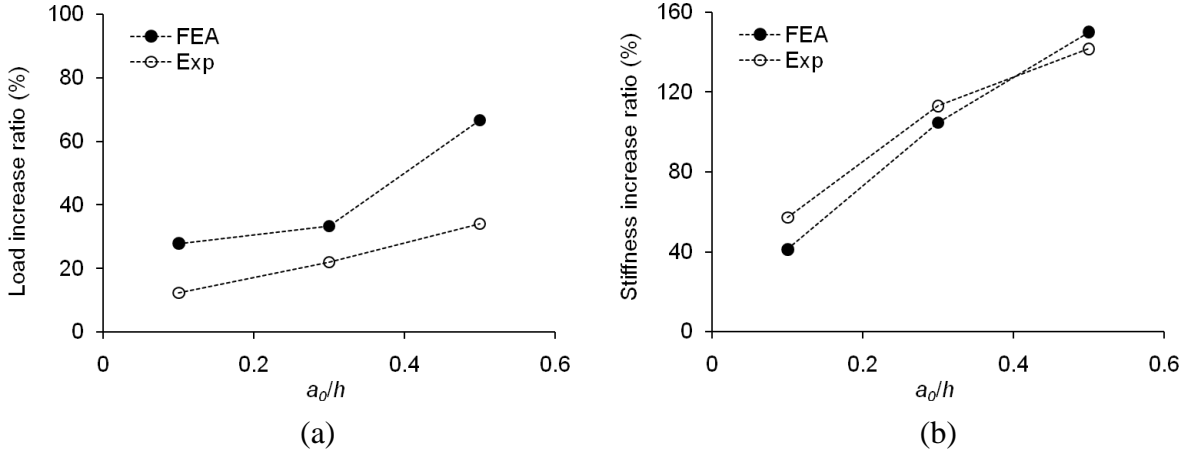


Fig. 4.8. Effect of initial damage: (a) increase of ultimate load after repair; (b) increase of elastic stiffness after repair

4.5.3. Crack Mouth Opening Displacement

Figure 4.9 shows the effect of initial damage on the behavior of crack mouth opening displacement (CMOD) of the beams. The complete descending branch of the experimental CMOD was not predicted because of the ideal failure nature of the model as described in the *Failure Mode* section. The CMOD linearly increased with load prior to yielding of the beams, as shown in Figs. 4.9(a) through (c). The linearity of the measured load-CMOD was maintained up to 62.8% and 72.7% of the ultimate load, on average, for the unrepaired and repaired beams, respectively. The model predicted a similar trend. This observation illustrates that the externally bonded CFRP sheet tended to stabilize the CMOD until noticeable debonding took place. Significant stiffness-softening (i.e., reduced slope of the load-CMOD curve) was noticed when the beams yielded. The CMOD measured at the peak load of the unrepaired beams varied from 1.65 mm to 3.85 mm, whereas that of the repaired beams was from 1.53 to 3.43 mm, as shown in Fig. 4.9(d). The predicted CMOD values at the peak were within these ranges.

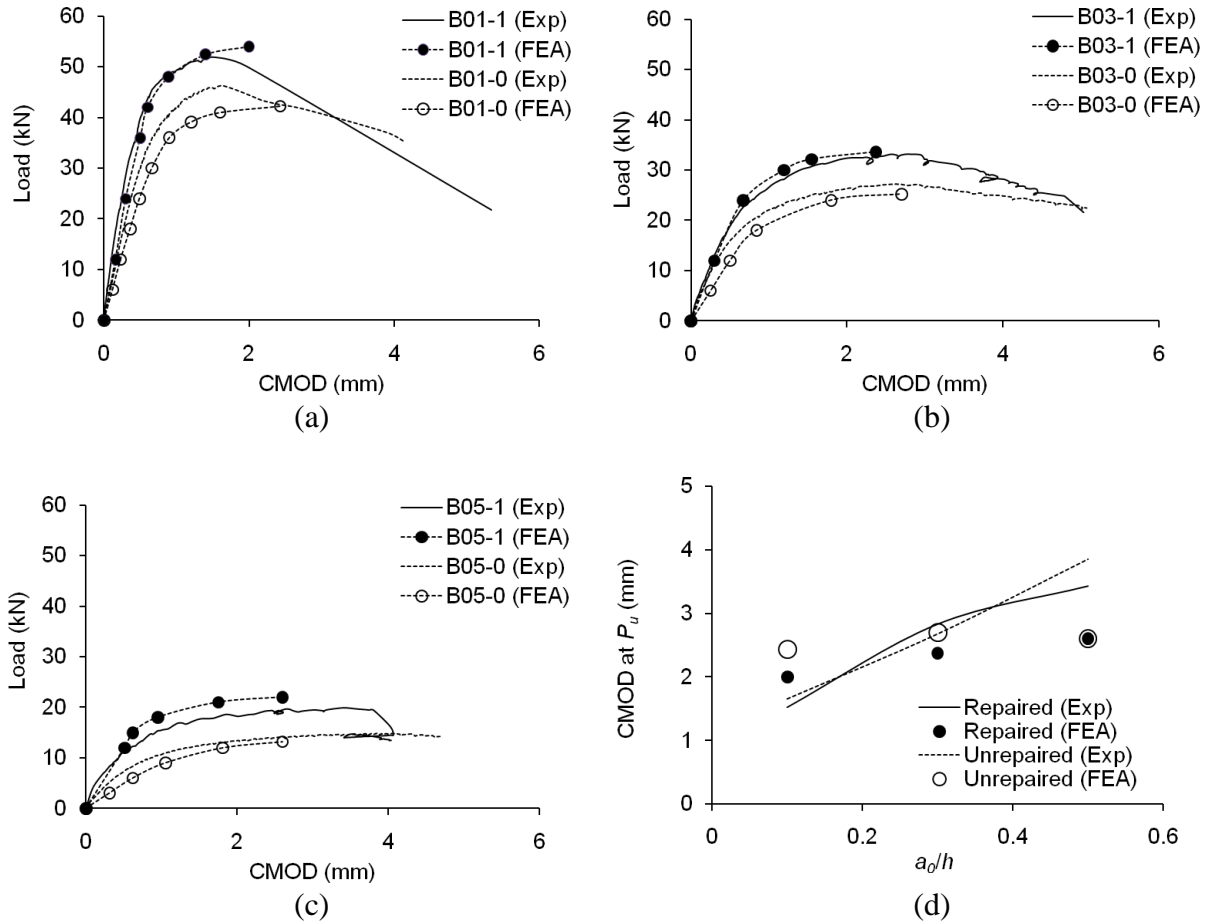


Fig. 4.9. Load-crack mouth opening displacement: (a) beams with $a_0/h = 0.1$; (b) beams with $a_0/h = 0.3$; (c) beams with $a_0/h = 0.5$; (d) effect of CFRP-repair on crack control

The post-peak behavior of the CMOD was significantly influenced by the notch depth, as shown in Fig. 4.9: the lower the a_0/h ratio, the greater the stiffness-softening. This observation can be explained by the fact that the energy absorbed in the beam with a low a_0/h ratio was greater than that with a high a_0/h ratio (primarily due to the high load-carrying capacity) and thus the internally-stored energy of the former tended to be abruptly released when the beam failed. For instance, Beam B05-01 exhibited more gradual load-softening than Beam B01-01 because the absorbed energies of these beams up to the peak load were 384.3 kNmm and 578.4 kNmm (area under the measured load-deflection curve in Fig. 4.7), respectively.

4.5.4. Crack Propagation Up the Web

The crack propagation up the web of each beam is shown in Fig. 4.10. The experimental crack growth toward the upper flange was measured manually from the notch tip. Although all beams (either repaired or not) exhibited noticeable crack propagation beyond their ultimate load, a plastic region had formed above the crack tip prior to the ultimate as supported by the plateau in the load-crack propagation response [Fig. 4.10]. Such an observation implies that accumulated plastic damage above the crack tip influenced crack-tip stability and initiated the fracture-failure of the beams. Sudden and abrupt crack propagation was accompanied as soon as the local plastic capacity reached its critical limit. The predicted propagation showed a similar trend, even though the model was not able to provide the complete post-peak responses due to its ideal failure characteristic. The length of the plateau [Fig. 4.10] was influenced by the notch size. Beam B01-0 showed a 14.4 mm long plateau, while Beams B03-0 and B05-0 demonstrated 8.6 mm and 5.5 mm, respectively. These results indicate that a beam with a low level of initial damage (low a_0/h ratio) tends to show a longer plastic region above its crack tip (i.e., reduced stress-concentrating zone with distributed stresses) and this trend is maintained after the repair. The crack propagation rates of the unrepaired and repaired beams were merged when the CFRP was significantly debonded from the steel, as shown in Fig. 4.10(b) and (c). A complete observation beyond the plateau of Beam B01-1 was not achieved [Fig. 4.10(a)] because of the sudden fracture-failure of the experimental beam.

4.5.5. Debonding Behavior

Figure 4.11 shows the CFRP-strain distribution within a distance of ± 100 mm from the notch. Debonding of the CFRP can be identified by a sudden increase in measured strains. All

beams exhibited strain concentrations at the notch location ($x = 0$ mm) because of insufficient load-sharing between the tensile flange and CFRP.

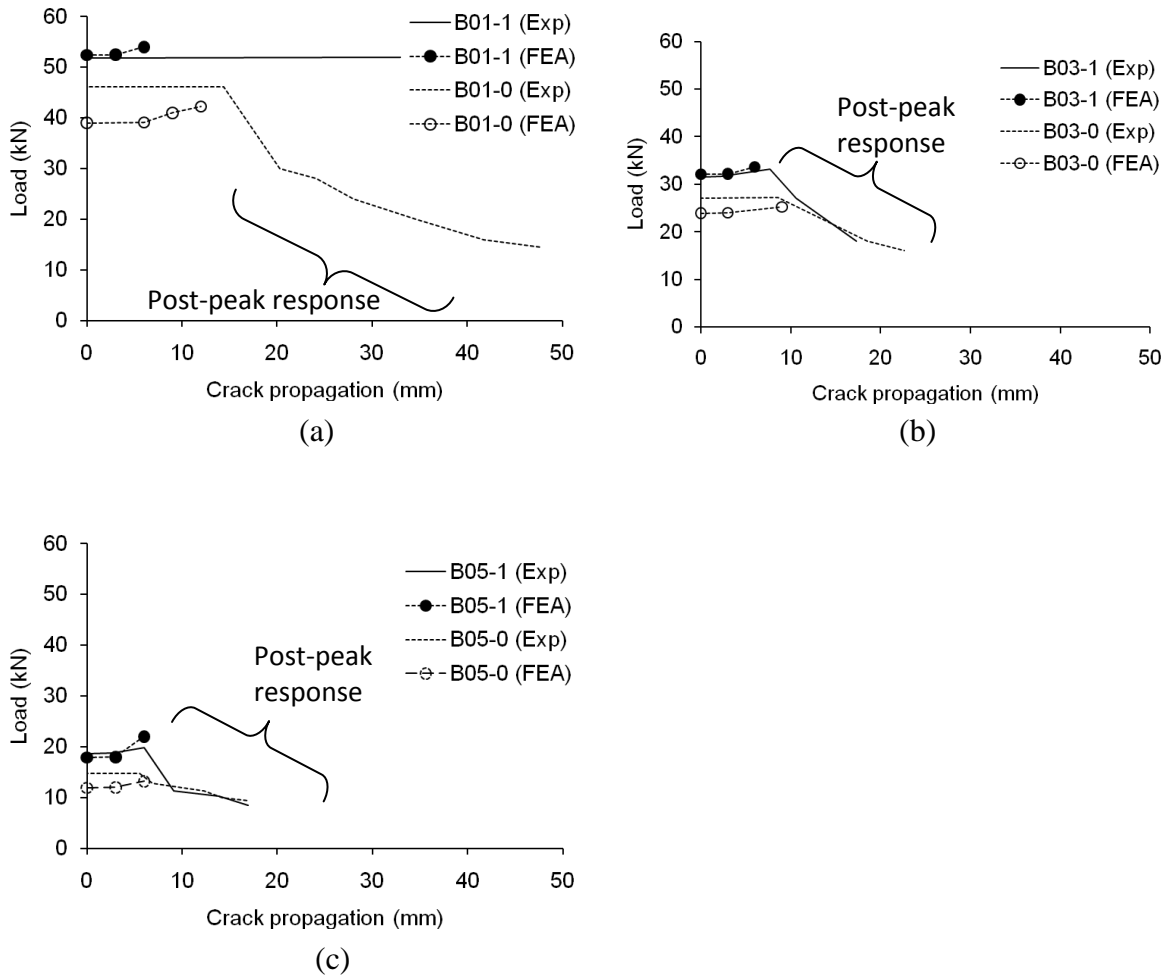


Fig. 4.10. Load-crack propagation measured from top of the notch (distance above notch): (a) beams with $a_0/h = 0.1$; (b) beams with $a_0/h = 0.3$; (c) beams with $a_0/h = 0.5$

For the repaired beam having $a_0/h = 0.1$ (B01-1), CFRP-debonding was not measured within a service load range (up to 50% of the ultimate load) as shown in Fig. 4.11(a). Other beams having $a_0/h = 0.3$ and 0.5 (B03-1 and B05-1, respectively), however, exhibited obvious CFRP-debonding at 50%Pu [Fig. 4.11(b),(c)]. Beyond the service state, gradual strain increases were noticed. Beams B01-1 and B05-1 showed partial debonding of the CFRP within a range of ± 100 mm from the notch until the applied load reached 75%Pu [Fig. 4.11(a),(c)]; however, Beam

B03-1 demonstrated significant debonding over $x = -100$ mm [Fig. 4.11(b)]. This illustrates that bond of Beam B03-1 was not adequate; in fact, premature debonding ($x = -25$ mm) had been already noticed at 25%Pu [Fig. 4.11(b)]. When the load reached 75%Pu, the strain profile of the beams tended to be very similar to each other regardless of the notch size. These observations indicate that the initiation of CFRP-debonding is dominated by the level of initial damage (a_0/h ratio), whereas the debonding behavior is not influenced by the damage level once the CFRP has been completely debonded in the vicinity of the notch. With further increased load, the CFRP strains of Beam B01-1 and B05-1 reached the rupture strain; however, the strain of Beam B03-1 was much lower because it failed by sudden debonding of the CFRP (the strains at 100%Pu in Fig. 4.11(b) were those recorded immediately before the debonding failure, denoting the full tensile capacity of the sheet was not achieved). The strain profiles at 100%Pu in Fig. 4.11 confirm these failure characteristics of the CFRP: Beam B03-1 showed an almost constant strain profile at around $\epsilon_{\text{CFRP}} = 0.008$ (48% of the rupture strain) that evidently meant complete debonding of the sheet had occurred along the tension flange; on the other hand, Beams B01-1 and B05-1 demonstrated apparent strain gradients when the rupture took place at the notch location ($x = 0$ mm), which implies that the CFRP was still bonded to the steel substrate outside the ± 100 mm zone.

The model reasonably predicted the debonding behavior of the CFRP, as shown in Fig. 4.12 (only Beam B01-1 is shown here for brevity). Some discrepancies between the measured and predicted strains were, however, observed when the applied load exceeded a service state [i.e., over 75%Pu in Fig. 4.12(b)]. The bond-slip model based on Eq. 4.1 did not predict the significant debonding of the CFRP at failure of the beam [Fig. 4.12(b)]. This observation may be attributed to the fact that the bond-slip model used for the present study has been developed by a

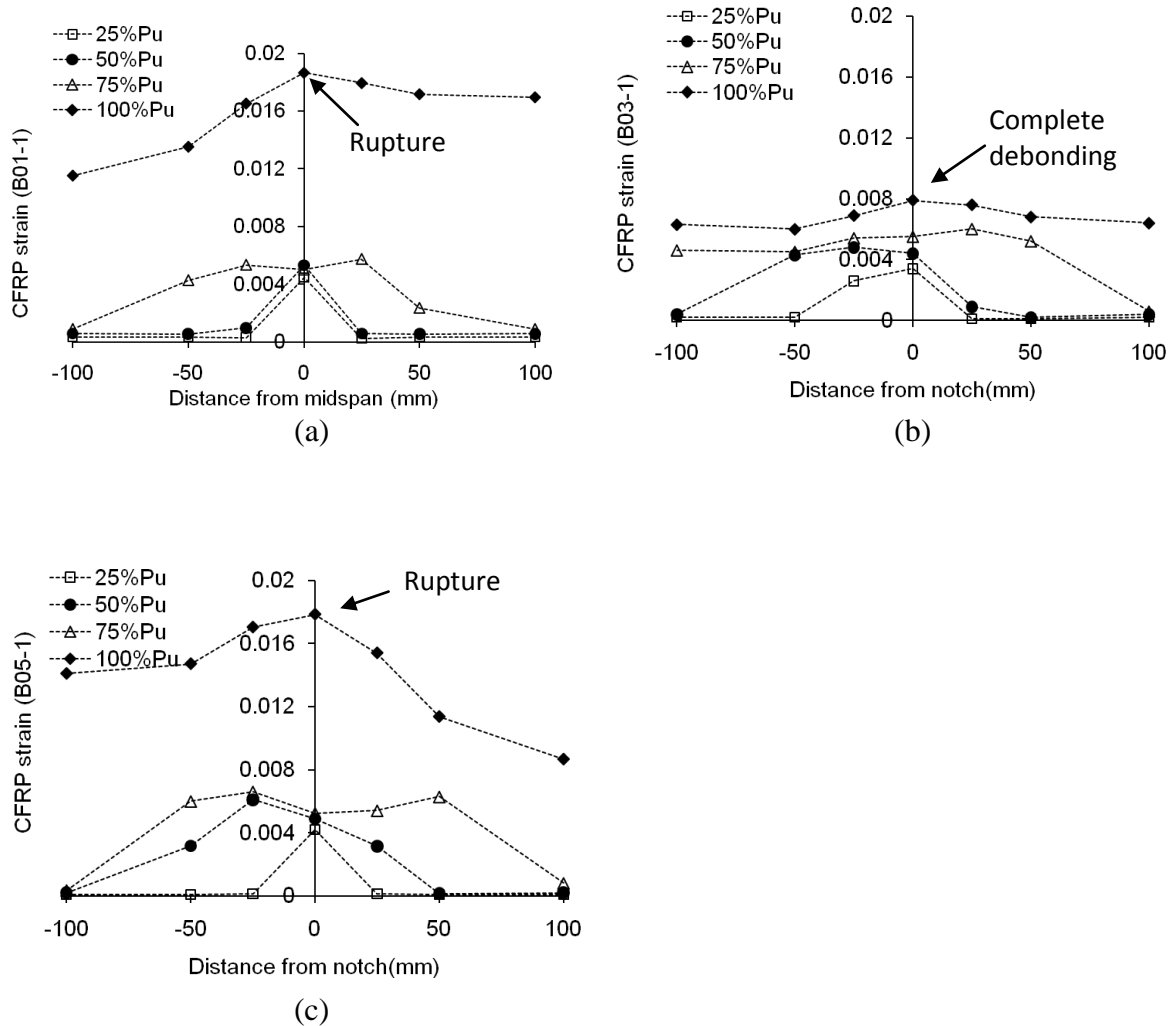


Fig. 4.11. Measured strains along the CFRP: (a) beam with $a_0/h = 0.1$; (b) beam with $a_0/h = 0.3$; (c) beam with $a_0/h = 0.5$

simple pull-out test (Xia and Teng 2005) and thus it cannot account for a bending effect in a beam application, consisting of a combination of shear and normal stresses along the CFRP-steel interface. The experimental strains (i.e., debonding progression of the CFRP) were, therefore, greater than the predictive strains when a large curvature of the beam was associated [Fig. 4.12(b)]. It is recommended that an improved bond-slip model be developed based on a beam test that can take into account bending effects, namely, shear and normal stresses along the interface layer.

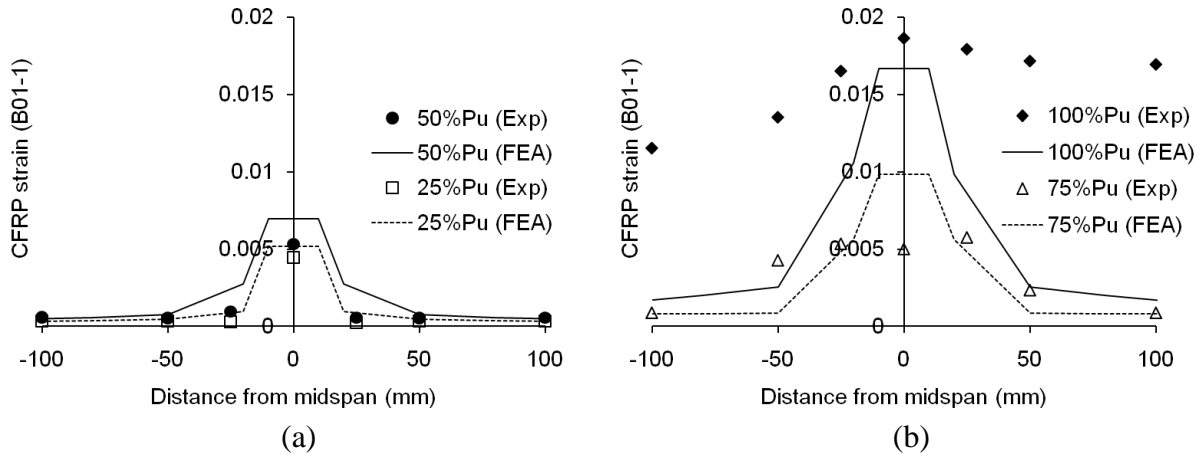


Fig. 4.12. Predicted CFRP strains of beam with $a_0/h = 0.1$: (a) within service range; (b) beyond service range

4.5.6. Fracture Characteristics

Figure 4.13 shows the variation of fracture energy of each beam obtained using Eq. 4.2.

$$G_f = \frac{W_u}{(h - a_0)t_w} \quad (4.2)$$

where G_f is the fracture energy; W_u is the energy dissipated up to peak load; and t_w is the web thickness. After CFRP-repair, the fracture energy of the notched beams was improved with average increases of 14.3% and 20.7% for the experiment and prediction, respectively, as shown in Fig. 4.13. Such increases in fracture energy illustrate that the crack-tip plasticity of the beams at the critical location where most of the energy was released was enhanced because of the repair. The measured fracture energy tended to be constant irrespective of the notch size; however, the predicted energy showed some variation [Fig. 4.13]. Such a discrepancy is due to the abrupt failure of the experimental beams having $a_0/h = 0.1$, as shown in Fig. 4.7(a). This observation implies that the fracture energy of the repaired steel beams is dominated by their failure characteristics. Further research is recommended to develop a ductile system to preclude the abrupt failure of CFRP-repaired steel beams.

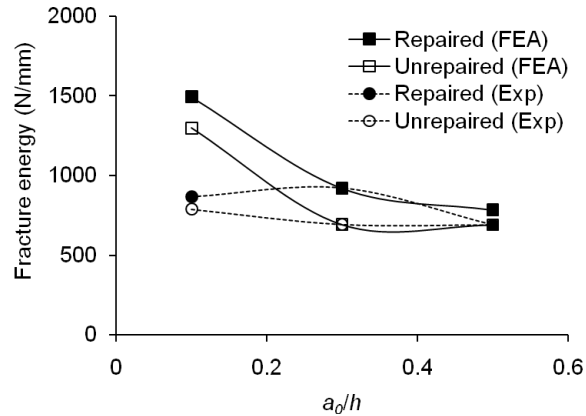


Fig. 4.13. Variation of fracture energy up to peak load

Figure 4.14 shows the energy dissipation rate of the beams, depending upon the size of notch. The energy was obtained from the area of the moment-rotation curve of each beam at midspan. The angular displacement (i.e., rotation of the section), Ω , in radian was arbitrarily selected to draw a trend line [Fig. 4.14]. All beams exhibited a common response such that the energy dissipated was reduced with the increased notch depth. This trend became more obvious when the angular displacement increased. Such behavior agreed with the response of the crack-tip plasticity mentioned previously. The variation of the energy dissipated was improved after the repair [i.e, less stiff slope of the trend lines in Fig. 4.14(b)]. This observation illustrates that the stress intensity at the critical section of the repaired beams was relieved due to the presence of the external reinforcement; in other words, applied stresses at the notch-tip were reduced because of a stress-sharing mechanism with the CFRP.

The variation of *J-integral* with angular displacements of the unrepaired and repaired beams is shown in Fig. 4.15. *J-integral* represents an energy release rate and is independent of a crack path (Rice 1968). Such a method is, therefore, an effective means to evaluate the efficacy of CFRP-repair for cracked steel beams. The concept of *J-integral* is expressed as follows (Rice 1968; Farahmand 2001):

$$J = \int_{\Gamma} \left(W dy - t \frac{\partial u}{\partial x} ds \right) = (-1/B) dU / da \quad (4.3)$$

$$U = \int_0^{\Omega} M d\Omega \quad (4.4)$$

where Γ is a curve surrounding the notch tip; W is the strain energy density; x and y are the Cartesian coordinates; t is the traction vector defined as per the outward normal along Γ ; U is the absorbed energy; a is the crack length; and M and Ω are the bending moment and corresponding angular displacement at midspan of the beam, respectively. The value of J-integral was dependent upon the angular displacement and initial crack length (i.e., notch size) of the beams because the slope of the energy curve was influenced by the notch depth [Fig. 4.14]. The J-integral gradually increased with the angular displacement of the beams (i.e., increased external load), as shown in Fig. 4.15.

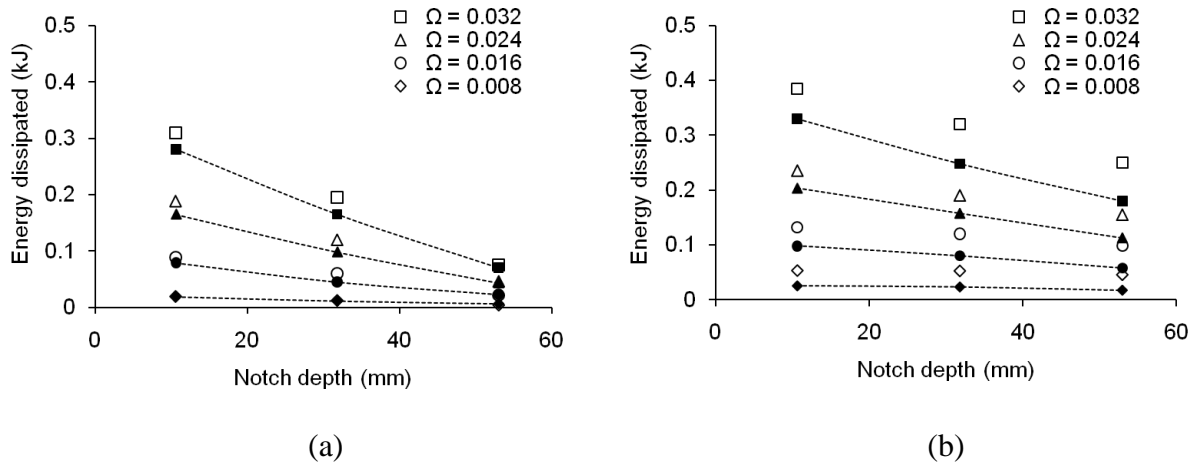


Fig. 4.14. Energy dissipated from steel beams (hollow = experiment; solid = FEA): (a) unrepaired; (b) repaired with CFRP

The repaired beams showed lower J-integral values when compared to the unrepaired beams. For example, the measured J-integral of the repaired beam at an angular displacement of 0.032 radian was 41.8% lower than that of the unrepaired beam. The efficacy of the CFRP-repair

became more obvious when the angular displacement increased, as shown in Fig. 4.15. This observation denotes that the CFRP effectively relieved the energy release rate of the notched steel beams and thus their structural integrity was enhanced (i.e., crack initiation was delayed).

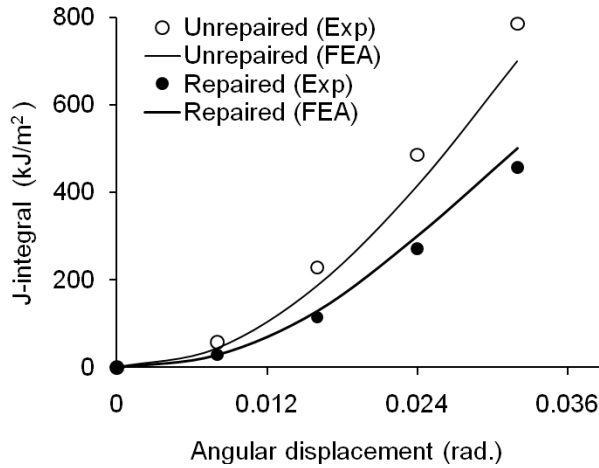


Fig. 4.15. Variation of J-Integral for unrepaired and repaired beams

4.6. Summary and Conclusions

This study has presented an experimental investigation into the behavior of CFRP-repaired steel beams having various notch depths that represent the level of initial damage. A modeling approach was proposed to account for the crack propagation across the beam section and the debonding behavior of the CFRP. The following is concluded.

- The load capacity and serviceability of the repaired beams were significantly affected by the level of initial damage (i.e., notch size). The efficacy of the CFRP-repair was more pronounced when the damage level increased. The load-sharing mechanism between the CFRP and steel substrate improved the yield capacity of the repaired beams, possibly including crack-bridging forces near the notch. Such an effect, however, was not noticeable when significant debonding of the CFRP took place. The proposed modeling approach predicted well the flexure of the experimental beams.

- The CFRP sheet stabilized the CMOD of the repaired steel beams. The linearity of the CMOD was improved until substantial debonding of the CFRP occurred. The level of initial damage in the beams influenced the post-peak behavior of the CMOD that was related to the internally-stored energy and the crack-tip plasticity of the repaired beams.
- The failure mode of the repaired beams was independent of the level of initial damage, whereas the damage level influenced the web-fracture rate of the repaired beams. The plastic region above the crack-tip of the beams was dominated by the damage level. The crack propagation rate across the repaired steel section approached that of the unrepaired counterpart when significant CFRP-debonding occurred.
- The level of initial damage governed the initiation of CFRP-debonding; however, its contribution to the debonding behavior was not significant once the CFRP was completely debonded in the vicinity of the damage location. The bond-slip model based on a simple pull-out test reasonably predicted the experimental debonding behavior within a service state. The need for an improved bond-slip model was addressed to better predict the debonding progression of the CFRP bonded to a steel beam.
- The CFRP-repair improved the fracture energy and the crack-tip plasticity of the damaged beams. The crack-path independent J-integral supported the efficacy of the repair method that relieved the energy release rate of the damaged beams.

**CHAPTER 5. EFFECT OF SUSTAINED LOAD COMBINED WITH COLD
TEMPERATURE ON FLEXURE OF DAMAGED STEEL BEAMS
REPAIRED WITH CFRP SHEETS[‡]**

5.1. Abstract

This study discusses an experimental program to examine the residual behavior of notch-damaged steel beams strengthened with carbon fiber reinforced polymer (CFRP) sheet subjected to typical long-term load configurations in cold regions. Test parameters include two levels of sustained load (40% and 60% of the ultimate capacity of the short-term strengthened beam: $40\%F_u$ and $60\%F_u$, respectively) and cold temperature as low as -30°C . A total of thirteen strengthened beams (W13 \times 4) in addition to one unstrengthened control are monotonically tested in three-point bending after being exposed to the long-term load for 7,000 hours. Experimental results show that the sustained loads significantly influence the load-carrying capacity of the beams due to the presence of creep damage near the crack-tip field above the notch. Cold temperature also affects the capacity and flexural stiffness of the beams. A crack-bridging effect by the bonded CFRP is noted near the crack mouth of the strengthened beams; however, such an effect decreases when the long-term load is applied. CFRP-debonding consistently governs the failure of the strengthened beams, irrespective of the degree of temperature exposure. Local CFRP rupture is observed near the notch location of the beams subjected to $60\%F_u$ due to the combination of stress concentrations and creep damage of the fibers. Interfacial stresses along the CFRP-steel interface are controlled by the sustained loads. Cold temperature results in

[‡]: This chapter has been previously published [Hmidan, A., Kim, Y.J., and Yazdani, S. 2013. *Effect of sustained load combined with cold temperature on flexure of damaged steel beams repaired with CFRP sheets, Engineering Structures, Elsevier 56, 1957-1966*].

reduced interfacial slip of the CFRP, while the temperature effect appears to be insignificant on the magnitude of bond stress. Stress redistribution along the CFRP-steel interface is noticed because of the long-term load.

5.2. Research Significance

Cracking of lower flange in steel girder bridges is a critical consideration because it will influence flexural behavior such as load-carrying capacity. Timely rehabilitation will save long-term repair costs and warrant sustainable performance. Although CFRP-repair has been increasingly accepted by the infrastructure community, limited information is available on the behavior of steel structures strengthened with CFRP. There is a lack of research on the long-term behavior of CFRP-repaired steel beams. To the best knowledge of the author, no research has been conducted as to the creep-induced distress of CFRP-repaired steel structures. Cold region durability of such members is another area to explore. This study presents an experimental study to examine the residual behavior of damaged steel beams strengthened with CFRP sheets subjected to sustained load in conjunction with cold temperature. Emphasis is given to the global response of the test beams, including the performance of CFRP-steel interface, rather than examining the contribution of each parameter separately (e.g., crack-tip plasticity, creep, and temperature).

5.3. Experimental Program

An experimental program was conducted to examine the behavior of damaged steel beams repaired with CFRP sheets subjected to sustained load in conjunction with cold temperature. The following provides a detailed description of materials, test beams, experimental protocol, and instrumentation.

5.3.1. Test Beams and Materials

A total of fourteen W4×13 (W100×19 in metric designation) A992 standard hot-rolled steel beams were employed. Material properties of the steel, unidirectional CFRP composite, and epoxy adhesive used are summarized in Table 5.1. To simulate a severe section loss that may result from corrosion or fatigue cracking, all test beams were intentionally damaged at midspan using a 0.63 mm-thick blade saw: a 31.8 mm deep notch was created into the web, as shown in Fig. 5.1. It is worthwhile to note that such a notch depth was designed based on Kim and Brunell (2011) that had examined the effect of various initial crack configurations on the behavior of CFRP-strengthened steel beams. The tension flange of all beams (except for the control beam) was strengthened with one layer of CFRP sheet (75 mm wide × 635 mm long) with an equivalent fiber thickness of 0.165 mm.

Table 5.1. Material properties from manufacturer

	CFRP	Steel	Adhesive
Tensile strength (MPa)	3800	414 ^a	54
Tensile modulus (GPa)	227	200	3
Ultimate strain	0.0167	0.002 ^a	0.035
Poisson's ratio	0.27	0.3	0.4

^a: property at yielding

Prior to CFRP installation, the steel substrate was grit-blasted, followed by cleaning with an air compressor and acetone. Such a surface preparation process was effective in producing a chemically active steel surface free from contamination that enables the formation of strong bond between the CFRP and steel substrate. A two-part epoxy adhesive was manually mixed at a weight ratio of 3:1 for a resin and a hardener to bond the CFRP. The average measured thickness of the hardened adhesive layer was 1.30 mm. It should be noted that the contribution of adhesive properties to the behavior of CFRP-strengthened steel beams is negligible (Kim and Harries

2012). Premature buckling of the beams was prevented by welding hollow steel sections (50 mm \times 25 mm \times 3 mm) that served as stiffeners at each support [Fig. 5.1].

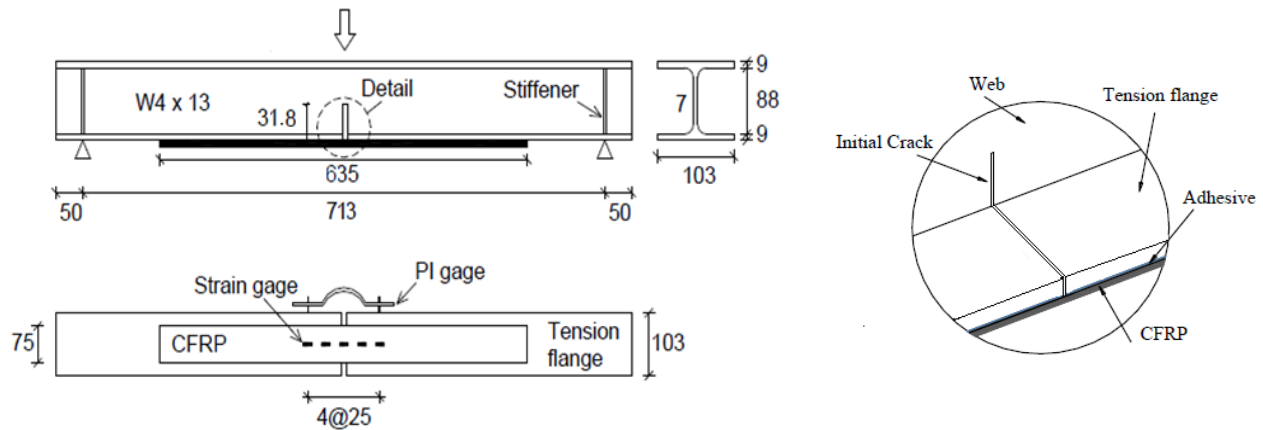


Fig. 5.1. Test beam and notch detail

5.3.2. Sustained Load and Temperature Exposure

After allowing the CFRP-strengthened beams to cure for at least seven days at room temperature, twelve beams were subjected to sustained load in three-point bending, as shown in Fig. 5.2(a). Such a test configuration can accelerate structural damage at the notch location (Kolluru et al. 2000; Wu and Yin 2003). A custom-made loading frame was utilized to apply the sustained load for a pair of beams using perforated steel hollow sections (38.1 mm \times 38.1 mm \times 1.6 mm) and a hydraulic jack [Fig. 5.2(b)]. Two levels of sustained load were designed to represent typical service conditions: 40% and 60% of the ultimate capacity of the strengthened control beam (F_u) that was monotonically tested in three-point bending at room temperature without sustained load. Table 5.2 summarizes beam details. An identification code for each pair (consisting of two specimens: Beams 1 and 2) denotes the presence of CFRP-strengthening (U = unstrengthened and S = strengthened), exposure temperature, and the level of sustained load. For example, S1+25+40 indicates Beam 1 of the strengthened pair subjected to 25°C and 40% F_u , while S2-30+60 designates Beam 2 of the strengthened pair associated with -30°C and 60% F_u . A

load cell was used to monitor the applied load during a jacking operation. Upon achieving the required load level (a 5% more load was applied to compensate for possible setting losses), the beams were clamped in pair using vertical threaded rods (9.5 mm in diameter) with nuts and two transverse steel hollow sections mounted at midspan of each beam. Additional two transverse steel sections were placed between the beams at 50 mm from each end to act as supports [Fig. 5.2(a)]. Selected beams were exposed to cold temperature in an environmental chamber in which the temperature was preset and monitored digitally [Fig. 5.2(c)]. All conditioned beams were kept under the effect of sustained load and temperature exposure for 7,000 hours. The variation of the sustained load and the time-dependent deformation of the beams were not measured due to the limitation of experimental equipment.

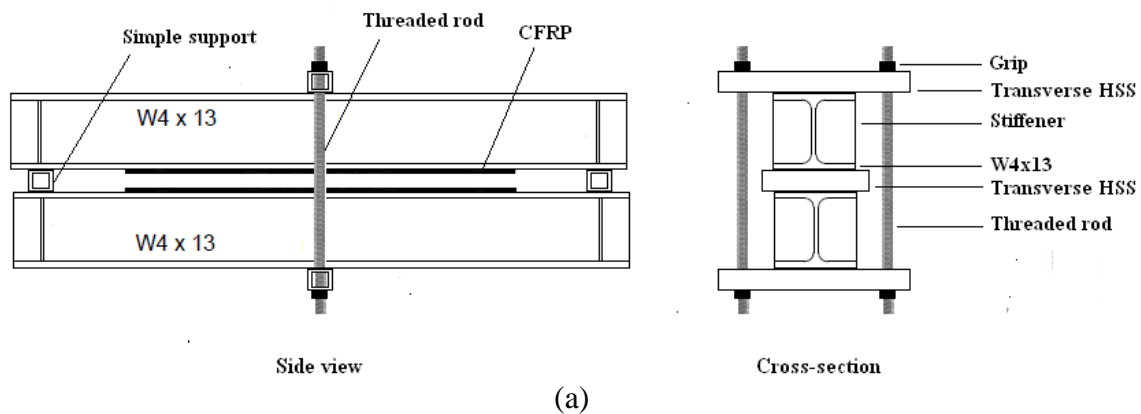


Fig. 5.2. Applying sustained load: (a) schematic view; (b) loading frame; (c) environmental chamber

Table 5.2. Beam details

Beam	Temperature	Sustained load ^a	Ultimate load, P_u (kN)	Elastic Stiffness (kN/mm)	CMOD at P_u (mm)	Failure Mode ^b
U+25+0	+25	0% F_u	68.9	11.8	2.89	WF
S+25+0	+25	0% F_u	84.4	14.9	2.01	CD→WF
S1+25+40	+25	40% F_u	36.9	14.2	1.25	CD→WF
S2+25+40	+25	40% F_u	35.6	14.6	1.13	CD→WF
S1+25+60	+25	60% F_u	35.5	13.8	0.71	CD+PR→WF
S2+25+60	+25	60% F_u	31.1	14.4	0.82	CD+PR→WF
S1-20+40	-20	40% F_u	35.0	12.9	1.01	CD→WF
S2-20+40	-20	40% F_u	30.6	12.5	0.83	CD→WF
S1-20+60	-20	60% F_u	27.8	11.1	1.08	CD+PR→WF
S2-20+60	-20	60% F_u	30.4	12.6	1.10	CD+PR→WF
S1-30+40	-30	40% F_u	30.3	11.5	0.77	CD→WF
S2-30+40	-30	40% F_u	24.4	12.7	1.57	CD→WF
S1-30+60	-30	60% F_u	27.1	12.1	1.54	CD+PR→WF
S2-30+60	-30	60% F_u	23.4	10.4	0.70	CD+PR→WF

^a: F_u = Ultimate load of strengthened beam without sustained load (S+25+0: 84.4kN).

^b: WF = web fracture, CD = CFRP-debonding, PR = partial rupture of CFRP near notch,

5.3.3. Test Set-Up and Instrumentation

To study the residual flexural behavior after completion of the long-term exposure, the clamping system was released and all beams were monotonically loaded to failure in three-point bending at room temperature, similar to the case of the strengthened control beam (S+25+0), as shown in Fig. 5.3. It is important to point out that such a residual test does not necessarily include the time-dependent behavior of the test beams (i.e., real-time creep response and material relaxation). The clear loading span was 713 mm with a 50 mm overhang at each end. The applied load was measured by a load cell positioned at midspan of each beam. Two displacement-type strain transducers (PI gages) having a gage length of 100 mm were installed to measure tension and compression strains at midspan [Fig. 5.3]. The PI gage of the tension flange also measured the crack mouth opening displacement (CMOD) of the notched test beams, including the response of CFRP-steel interface at the damage location. Midspan deflection was recorded by a linear potentiometer. Debonding propagation along the CFRP sheet was monitored

by five electric foil strain gages [Figs. 5.1 and 5.3]. All data were collected and recorded by a data acquisition system.



Fig. 5.3. Set-up for residual test

5.4. Test Results and Discussion

5.4.1. Load-Carrying Capacity

The ultimate load of all test beams is summarized in Table 5.2. The strengthened control beam (S+25+0) showed an increase of 22.5% in flexural capacity compared to the unstrengthened counterpart (U+25+0). The presence of sustained load significantly influenced the residual capacity of the strengthened beams, as shown in Fig. 54(a). The sustained load of 40% of the control capacity (40% F_u : Beams S1+25+40 and S2+25+40) resulted in an average reduction of 57.0% in the capacity relative to that of Beam S+25+0. Such a rate in strength reduction increased to an average of 60.5% for the beams subjected to 60% F_u (Beams S1+25+60 and S2+25+60). These observations are due to the creep deformation of the crack-tip field where significant local plasticity is associated and propagates with time. The local plastic aligned with

a study conducted by Ghafouri and Motavalli (2011), including the irreversible deformation of the beams when the sustained load was released. Accumulated creep damage in the vicinity of the crack-tip may initiate microcracks (Suh et al. 1987), thereby accelerating web-fracture of the long-term beams. Creep deformation of the viscoelastic adhesive could be another factor that has degraded the strengthening effect (i.e., reduced stress transfer from the steel beam to the CFRP), given the polymeric chain of the epoxy molecules became loose due to the sustained load (Epoxy Technology 2009).

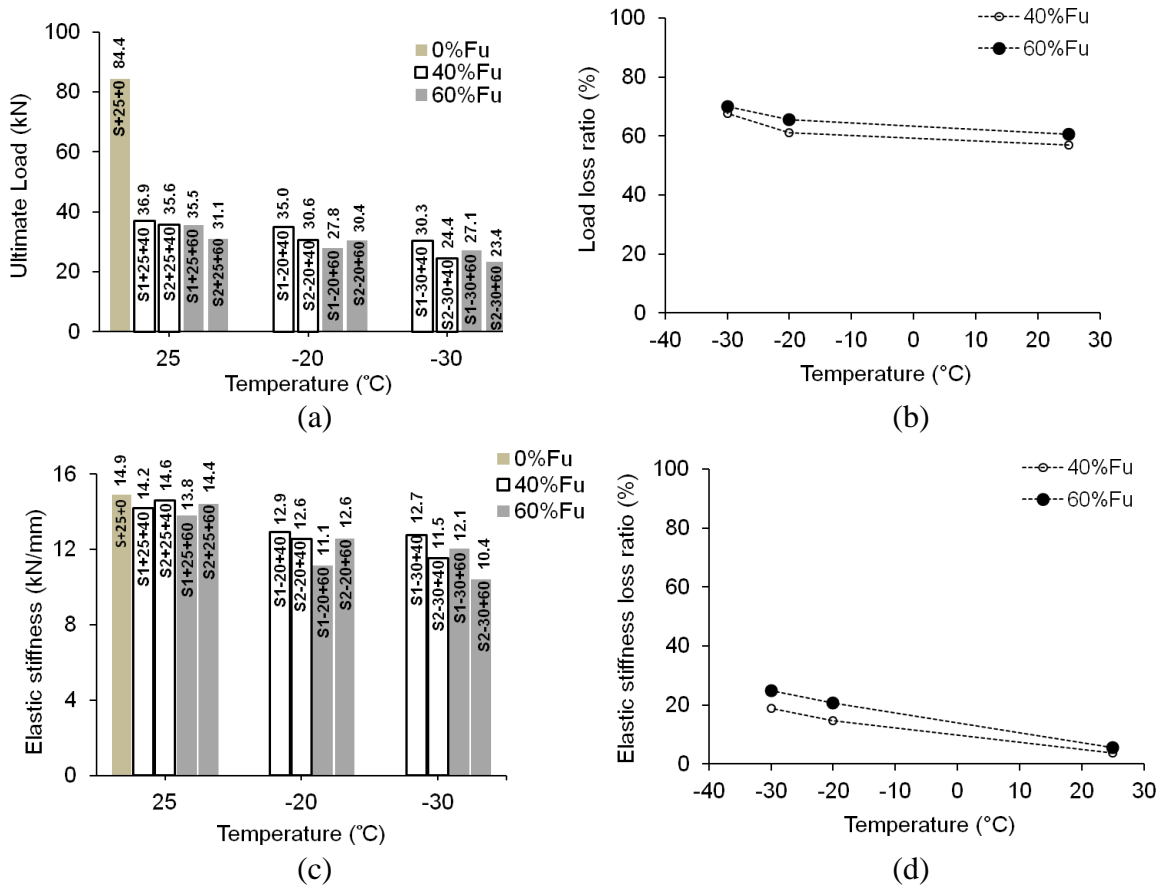


Fig. 5.4. Comparison of flexural behavior with respect to temperature exposure: (a) ultimate load; (b) loss of load-carrying capacity on average; (c) elastic stiffness; (d) loss of elastic stiffness on average

Environmentally assisted reduction in flexural strength was noticeable due to the cold temperature exposure combined with sustained loads, as shown in Table 5.2 and Fig. 5.4(b). The load-carrying capacity of the beams subjected to -20°C and $40\%F_u$ (S1-20+40 and S2-20+40) was reduced by an average of 61.1% when compared to that of the reference beam (S+25+0). A similar average strength reduction of 65.5% was observed for the beams exposed to the same temperature (-20°C) while undergoing a sustained load of $60\%F_u$. Temperature changes from -20°C to -30°C affected elastic stiffness in a similar trend, as shown in Fig. 5.4(c) and (d): average decreases of 67.6% and 70.1% were observed for the beams exposed to -30°C and $40\%F_u$ (S1-30+40 and S2-30+40) and $60\%F_u$ (S1-30+60 and S2-30+60), respectively, in comparison to the reference beam (S+25+0). This may be attributed to the fact that the polymer matrix tended to shrink with a decreasing temperature (Dutta 1988), while the initial moisture inside the adhesive swelled, thereby generating micro-level damage in the adhesive layer. The sustained load then redistributed these effects along the CFRP-steel interface.

5.4.2. Load-Deflection Behavior

The load-deflection behavior of the beams at midspan is shown in Fig. 5.5. The unstrengthened beam (U+25+0) exhibited a linear response up to a load of 58.4 kN beyond which a gradual decrease in tangent stiffness was associated [Fig. 5.5(a)]. The strengthened beam (S+25+0) revealed a similar response until a load of 77.2 kN was attained, while the transition in tangent stiffness after yielding of the steel section was less significant than that of Beam U+25+0 [Fig. 5.5(a)]. Both of these beams showed a sudden load drop immediately after the ultimate load was reached. According to the rate of transition in tangent stiffness between the yield and ultimate loads, the energy release of the unstrengthened beam (U+25+0) was more gradual than that of the strengthened beam (S+25+0) when failure was imminent. Another thing to note is that

the CFRP sheet acted as a crack-bridging medium along the crack mouth and hence a 26.3% increase in flexural stiffness was observed for Beam S+25+0 in comparison to Beam U+25+0 [Fig. 5.5(a)]. The effect of sustained load is given in Fig. 5.5(b). Despite the significant drop in load-carrying capacity due to the sustained load, flexural stiffness of the beams subjected to $40\%F_u$ (S1+25+40) and $60\%F_u$ (S1+25+60) was maintained until yielding of the section took place. Post-peak deflection of the beams with sustained load rapidly increased once the beams failed, as shown in Fig. 5.5(b). This observation confirms the degraded crack-tip field above the notch due to the presence of sustained loads, which was explained in the *load-carrying capacity* section. The behavior of all beams subjected to cold temperature and sustained load was virtually bilinear, as shown in Fig. 5.5(c) to (e). Because of stress redistribution between the paired beams while clamped together, the extent of local plasticity of one beam could be greater than that of the other. This has caused the difference in the peak load of the test beams in the same category. Flexural stiffness of the test beams was influenced by temperature, as briefly mentioned above. When a temperature dropped from -20°C to -30°C , an average reduction of 13.9% and 18.1% in stiffness was recorded for the beams under sustained loads of $40\%F_u$ and $60\%F_u$, respectively, in comparison to the room-temperature beams subjected to the same level of sustained load (Table 2). Such a decrease in flexural stiffness can be explained by the degradation of the CFRP-steel interface due to the cold temperature exposure, in addition to the deterioration of the crack-tip field described previously: internal stresses induced by a mismatch in the coefficient of thermal expansion (CTE) among the CFRP, adhesive, and steel could initiate microcracks along the interface (i.e., CTE of the CFRP, adhesive, and steel = $-0.38 \times 10^{-6}/^{\circ}\text{C}$, $35 \times 10^{-6}/^{\circ}\text{C}$, and $12 \times 10^{-6}/^{\circ}\text{C}$, respectively, according to the manufacturers). The performance of the CFRP-steel interface

subjected to the long-term load is further discussed in the *behavior of CFRP-steel interface* section.

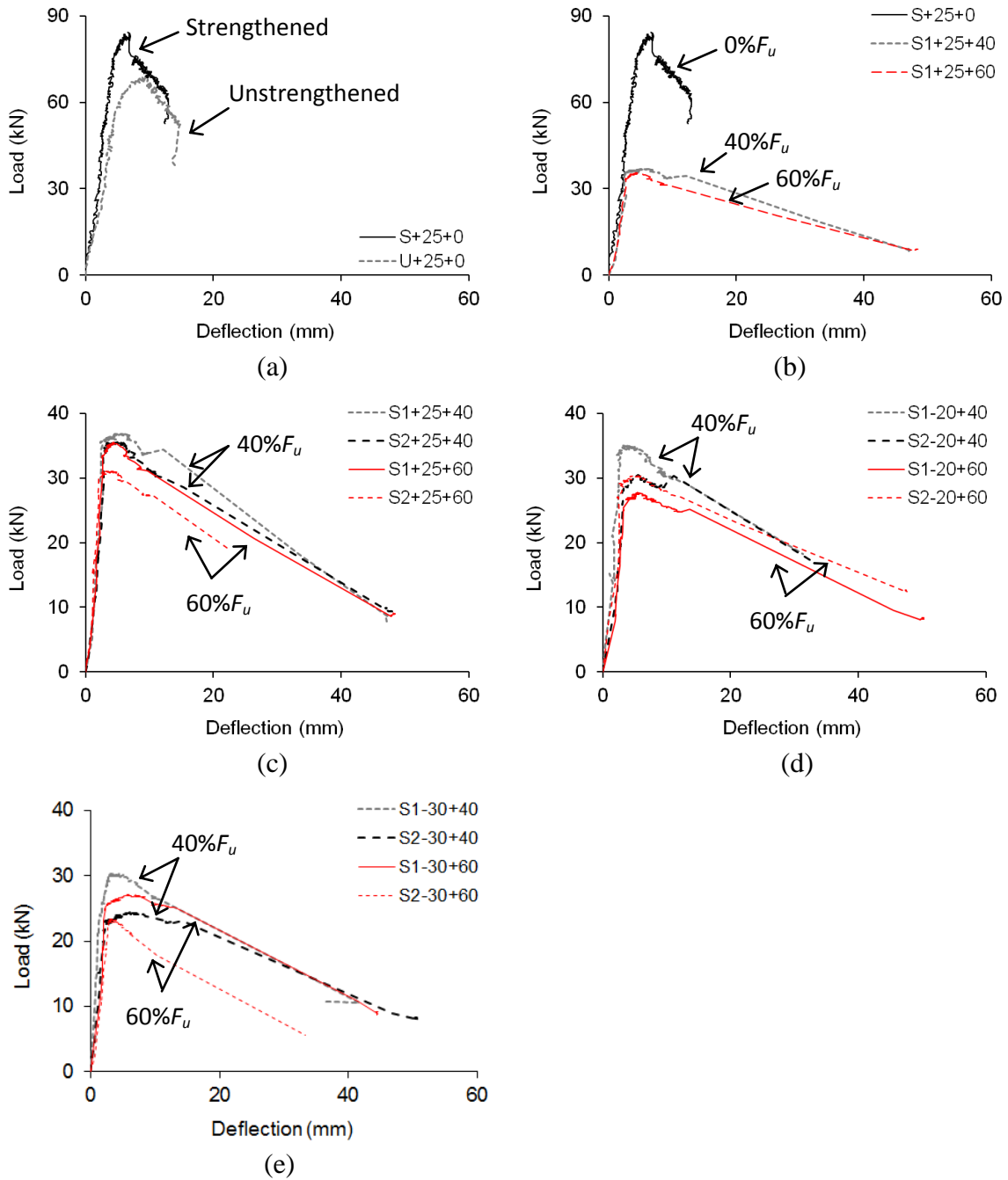


Fig. 5.5. Load-deflection behavior of beams: (a) effect of strengthening; (b) effect of sustained load without cold temperature; (c) subject to +25°C; (d) subject to -20°C; (e) subject to -30°C

5.4.3. Energy Dissipation

Figure 5.6 shows the effect of temperature and sustained load on the energy dissipation of the test beams. The energy (E_d) was quantified by the area under each load-deflection curve up to peak load:

$$E_d = \int_0^{x_p} P dx \quad (5.1)$$

where P is the applied load and x_p is the displacement at the peak load of the specimen. It should be noted that the post-peak energy of the beams has insignificant meaning because the contribution of CFRP-strengthening is none to the flexural behavior after the peak load is attained. Considerable reduction in energy dissipation was observed when the beams were subjected to sustained load, as shown in Fig. 5.6(a). The average energy dissipation of the beams under 40% F_u and 60% F_u at 25°C was 65.3% and 71.2% less than that of the beam without long-term load (S+25+0), respectively. Such an observation corroborates the presence of creep damage that has developed in the crack-tip field of the long-term beams. The contribution of cold temperature to the energy capacity of the strengthened beams is given in Fig. 5.6(b). The energy loss ratio of the beams exposed to -30°C was 10.2% higher than that of the room temperature beams, on average. The loss ratio is defined as $(E_{reference} - E_{long-term})/E_{reference}$ where $E_{reference}$ and $E_{long-term}$ are the energy dissipation of the reference beam (S+25+0) and the beam exposed to long-term load, respectively. The beams subjected to 60% F_u revealed an average of 5.0% higher energy dissipation relative to those under 40% F_u , as shown in Fig. 5.6(b).

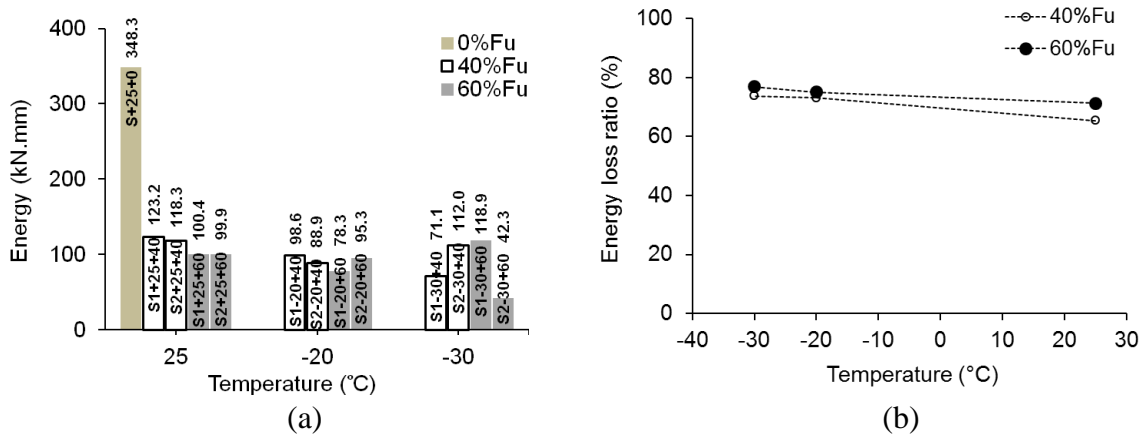


Fig. 5.6. Variation of energy in test beams: (a) energy dissipated up to peak load; (f) loss of energy dissipated

5.4.4. Crack Mouth Opening Displacement

The development of crack mouth opening displacement (CMOD) for all test beams is given in Fig. 5.7. The reference beam (S+25+0) demonstrated nonlinearity when the applied load exceeded a service level (i.e., over 60% of the ultimate load), while such a nonlinear response was not noticed for the long-term beams until failure occurred [Fig. 5.7(a)]. This observation implies that the beams subjected to sustained loads failed prior to the advent of the gradual load-CMOD softening because of the accumulated creep damage in the crack-tip field (i.e., regional plasticity). The reduced slope of the load-CMOD response of the beams with sustained loads [Fig. 5.7(a)] illustrates that the crack-bridging effect of the CFRP was influenced by the long-term load. The load-CMOD behavior of the beams exposed to cold temperature and sustained load was similar to each other, as shown in Fig. 5.7(b) to (d). The post-peak plateau of these beams was continued without demonstrating crack growth up the web until the beams abruptly failed by CFRP-debonding (to be discussed in the *failure mode* section). The effect of cold temperature on the CMOD development was rather inconclusive in this research program because no clear trend of temperature dependency was observed [Fig. 5.7(e) and (f)]. The

CMOD response, however, appears to be more dependent upon the level of sustained load than temperature.

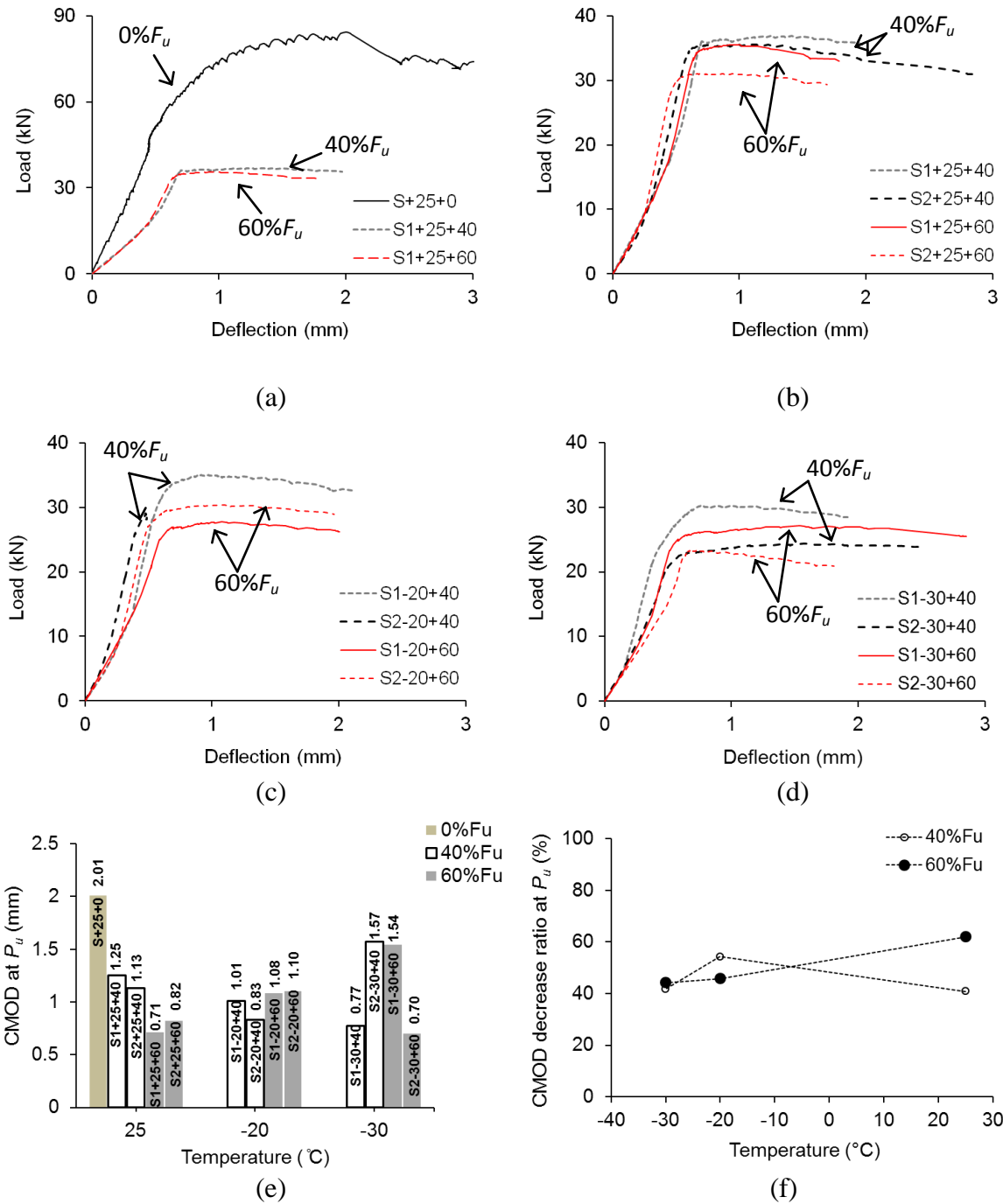


Fig. 5.7. Load-crack mouth opening displacement: (a) effect of sustained load; (b) subject to +25°C; (c) subject to -20°C; (d) subject to -30°C; (e) CMOD at ultimate load; (f) CMOD decrease ratio compared to reference beam

5.4.5. Failure Mode

Figure 5.8 shows the failure mode of the test beam. CFRP-debonding dictated the failure of the reference beam (S+25+0) and the beams subjected to the long-term loads, irrespective of temperature exposure. CFRP-debonding initiated near the notch at midspan due to stress concentrations and rapidly propagated along the CFRP-bond line in a direction of decreasing moment. Web-fracture of the beams was observed as soon as the strengthening effect disappeared (i.e., complete debonding of the CFRP), as shown in the inset of Fig. 5.8. It is of interest to note that the beams subjected to $60\%F_u$ demonstrated partial CFRP-rupture in the vicinity of the notch prior to the initiation of CFRP-debonding. Stress concentrations combined with a high level of sustained load (i.e., $60\%F_u$) appear to have caused time-dependent fiber damage in the CFRP at the notch location. Similar local fiber rupture was reported by Kim et al. (2004) where a geometric discontinuity induced stress concentrations of the CFRP sheets bonded to a steel substrate.



Fig. 5.8. Failure mode

5.4.6. Behavior of CFRP-Steel Interface

5.4.6.1. Strain distribution along CFRP sheet

Development of strain profiles along the CFRP sheet at selected load levels is shown in Fig. 5.9. Overall, consistent strain profiles were observed for each test category even though slight scatter was noticed due to the nature of wet-lay-up. The response of the beams subjected to $40\%F_u$ is given in Fig. 5.9(a), (c), and (e). A gradual increase in strain was recorded with an increasing load up to $75\%P_u$ where P_u is the ultimate load of the beam, while the increase rate of these beams was influenced by the degree of temperature exposure. For example, the midspan strains at $75\%P_u$ were 0.0031, 0.0025, and 0.0017 for the $40\%F_u$ beams exposed to 25°C , -20°C , and -30°C , respectively. The midspan strains at $100\%P_u$ were, however, constant at about 30% of the nominal CFRP-rupture strain ($\varepsilon_{fu} = 1.67\%$), regardless of the temperature exposure (i.e., 0.0049, 0.0048, and 0.0047 for Beams S1+25+40, S1-20+40, and S1-30+40, respectively). These results imply that cold temperature can influence the behavior of the CFRP-steel interface in service, whereas such an environmental effect becomes negligible once mechanical action (i.e., initiation and propagation of CFRP-debonding) controls the interface response. Strain profiles of the beams subjected to $60\%F_u$ are available in Fig. 5.9(b), (d), and (f). As in the case of the $40\%F_u$ beams, a gradual increase in CFRP-strain was observed. The cold temperature effect discussed above, however, was not apparent for the beams exposed to $60\%F_u$. In conjunction with the partial rupture of the CFRP sheet discussed in the *failure mode* section, the beams under $60\%F_u$ tended to demonstrate high strains at midspan [Fig. 5.9(d) and (f)]. The increased damage in the crack-tip field due to a sustained load of $60\%F_u$ is believed to have augmented stress concentrations. Creep damage in the carbon fibers combined with stress concentrations at the

geometric discontinuity (i.e., notch) could also be a synergetic factor for such a strain profile of the beams subjected to $60\%F_u$.

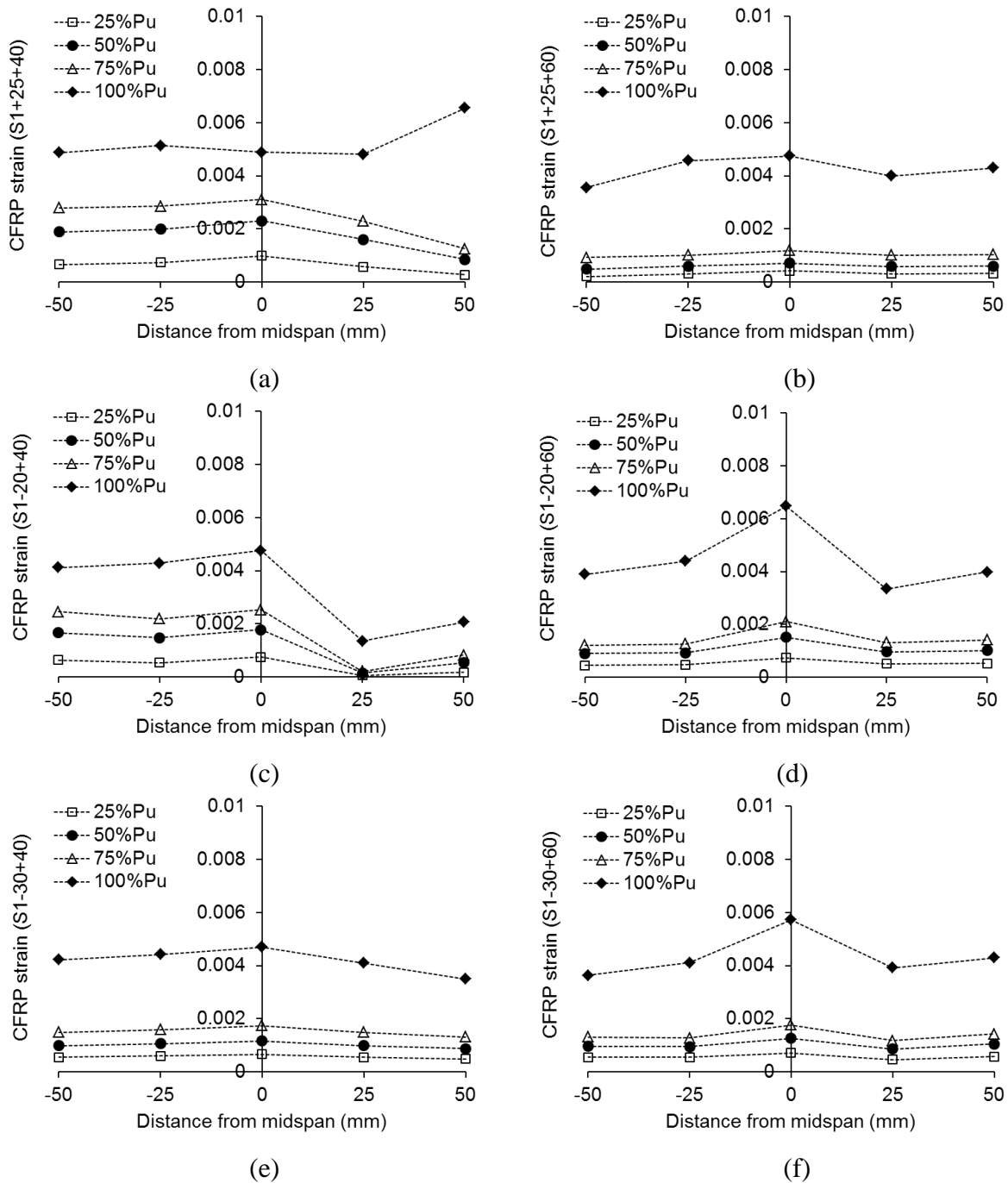


Fig. 5.9. Measured strains along the CFRP: (a) $40\%F_u$ at 25°C ; (b) $60\%F_u$ at 25°C ; (c) $40\%F_u$ at -20°C ; (d) $60\%F_u$ at -20°C ; (e) $40\%F_u$ at -30°C ; (f) $60\%F_u$ at -30°C

Figure 5.10 compares the effect of sustained load and cold temperature at an arbitrary service load level of 21.1 kN (25% of the load-carrying capacity of the reference beam, S+25+0). CFRP strains of the beams subjected to sustained loads without cold temperature (S1+25+40 and S1+25+60) were rather uniform in comparison to that of the reference beam, as shown in Fig. 5.10(a). This illustrates that the long-term creep effect redistributed flexural stresses along the CFRP-steel interface (Choi 2007; Zhang and Wang 2012) and such a trend became more prominent when the level of sustained load increased. The beams subjected to both sustained load and temperature demonstrated similar behavior in stress redistribution; however, such a combined load effect caused a somewhat random trend in strain development [Fig. 5.10(b)]. To fully understand this complicated interaction between the sustained load and cold temperature, a material-level study associated with multi-scale modeling may be conducted in future research.

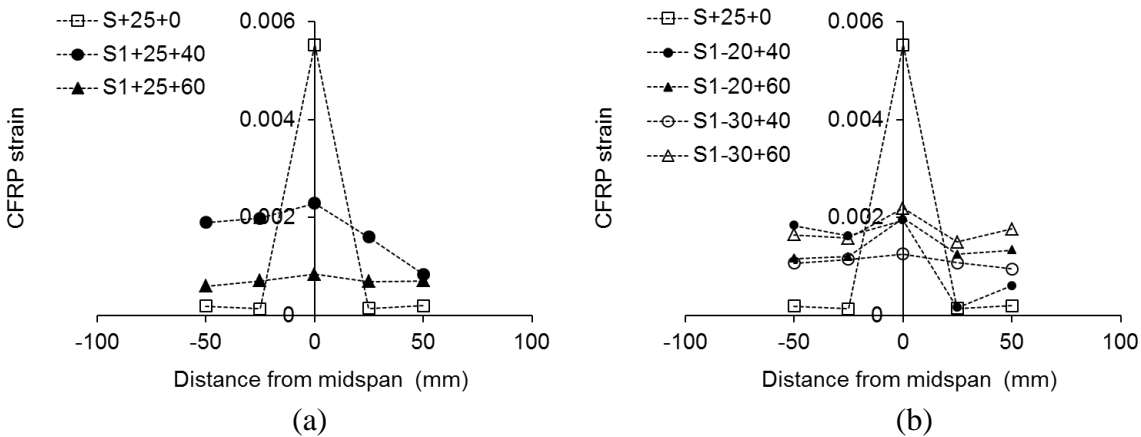


Fig. 5.10. Effect of long-term load on CFRP-strain development at 25% P_u of the reference beam S+25+0: (a) without cold temperature exposure; (b) with cold temperature exposure

5.4.6.2. Bond stress-slip response

Figure 5.11 shows the slip of the CFRP sheet with an increasing load. The slip representing a relative displacement between the CFRP and steel substrate was calculated by integrating strains measured at two adjacent locations x_{i+1} and x_i along the CFRP-steel interface.

It should be noted that the contribution of the steel substrate to the local slip of the CFRP is frequently ignored for technical convenience (Dai et al. 2005; Mazzotti et al. 2008). A steady increase in CFRP-slip was observed for all test specimens within a service load range (only selected cases are shown in Fig. 5.11 for brevity). The slip of the interface subjected to cold temperature tended to be less than that of the case at room temperature, as shown in Fig. 5.11. This observation indicates that the cold temperature exposure has influenced the deformation characteristics of the adhesive layer. Local bond stress-slip response along the CFRP-steel interface, which can characterize a force transfer mechanism between the CFRP and steel substrate, is given in Fig. 5.12.

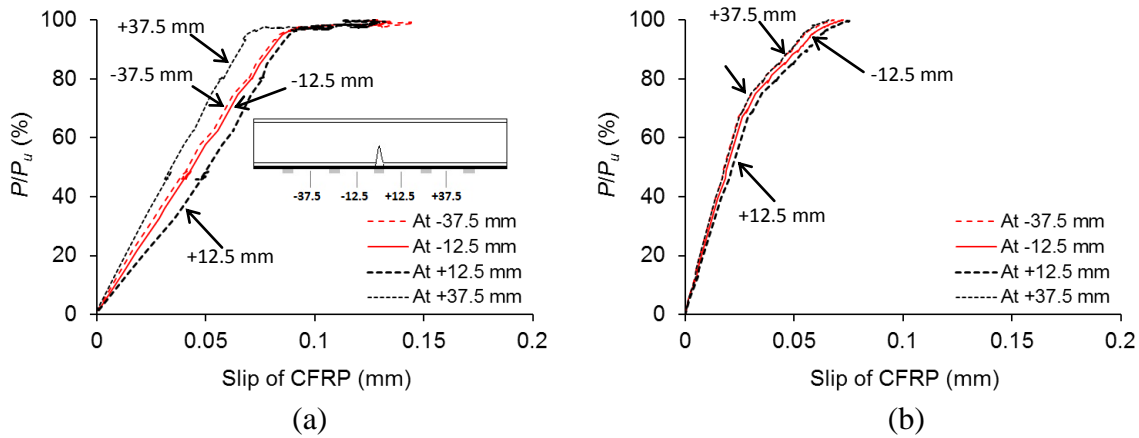


Fig. 5.11. Development of CFRP slip: (a) S1+25+40; (b) S1-30+40

The average local shear stress, τ_a , was obtained from strain readings measured at two neighboring locations using Eq. 5.2:

$$\tau_a = E_c t_c \frac{\varepsilon_{i+1} - \varepsilon_i}{x_{i+1} - x_i} \quad (5.2)$$

where E_c and t_c are the elastic modulus and thickness of the CFRP, respectively; and ε_{i+1} and ε_i are the CFRP strains at x_{i+1} and x_i , respectively. It is important to note that possible variation in

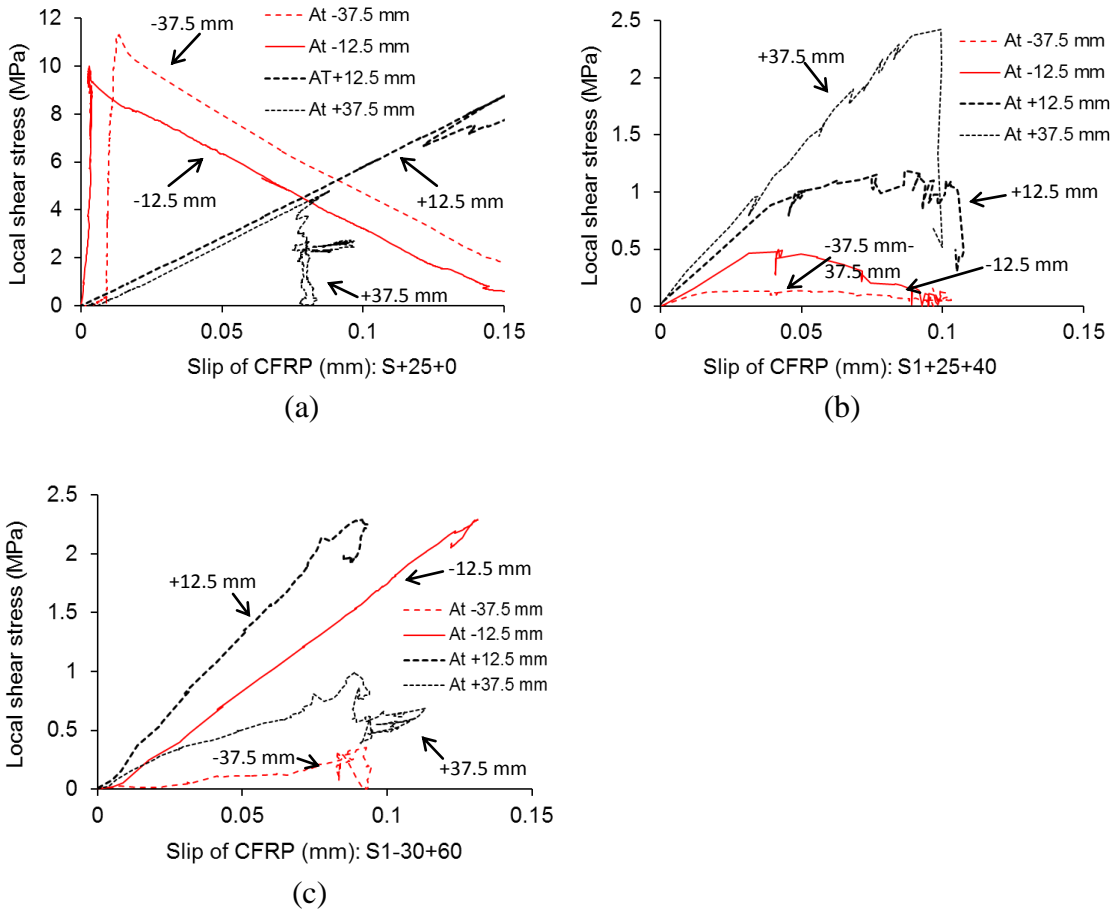


Fig. 5.12. Local shear stress-slip of CFRP-steel interface: (a) reference beam (S+25+0); (b) beam subjected to $40\%F_u$ without cold temperature exposure (S1+25+40); (c) beam subjected to $60\%F_u$ with cold temperature exposure (S1-30+60)

material properties of the constituents due to the long-term exposure was not fully included in Eq. 5.2 due to the limited acquisition of the experimental data. As shown in Fig. 5.12(a), the reference beam without long-term load (S+25+0) exhibited a biased response with two distinct debonded regions consisting of the primary CFRP-debonding (+12.5 mm and +37.5 mm) and the secondary debonding (-12.5 mm and -37.5 mm). The primary debonded region showed a more rapid increase in CFRP-slip than the secondary region when the local interfacial stress increased, indicating that CFRP-debonding initiated within the primary debonded region. Such debonding patterns were not observed in the beams subjected to the long-term load [Fig. 5.12(b) and (c)].

The reason is due to the fact that the sustained loads caused uniform creep damage along the adhesive layer on both sides of the notch. The local shear stress of these long-term beams was less than that of the reference beam. For example, the maximum interfacial shear stress of Beam S+25+0 was 11.3 MPa, while those of Beams S1+25+40 and S1-30+60 were 2.4 MPa and 2.3 MPa, respectively. This observation confirms the creep effect has redistributed shear stresses along the CFRP-steel interface, thereby reducing the maximum stress values. The effect of cold temperature on the local shear stress development of the CFRP-steel interface appeared to be negligible.

5.5. Summary and Conclusions

This study has discussed the residual behavior of notch-damaged steel beams strengthened with CFRP sheet subjected to various levels of sustained load and cold temperature. Emphasis was given to flexural responses such as load-carrying capacity, stiffness variation, energy dissipation, crack mouth opening displacement, and failure mode. The behavior of the CFRP-steel interface was also reported. The present investigation did not compare the behavior of the strengthened beams with that of unstrengthened counterparts, which could have been an interesting study (i.e., crack propagation mechanism). Further research with full creep test data may explain the complex time-dependent mechanism in the crack-tip field and along the CFRP-steel interface. Another potential research topic is the statistical characterization of the behavior of CFRP-strengthened beams subjected to cold region environment, given the response of such beams is intrinsically stochastic. The following conclusions are drawn.

- The sustained loads decreased the flexural capacity of the strengthened beams up to 60% in comparison to the reference beam without long-term load. The occurrence of creep damage associated with significant crack-tip plasticity was the primary contribution to

this observation. Cold temperature exposure influenced the capacity and elastic stiffness of the long-term beams, including the degradation of the CFRP-steel interface. Energy dissipation of the strengthened beams was influenced by the level of sustained load.

- The bonded CFRP sheet functioned as a crack-bridging medium along the crack mouth of the strengthened steel beams. Such a crack-bridging effect was, however, reduced when the long-term load was applied. The response of crack mouth opening displacement was controlled by the sustained loads, irrespective of cold temperature exposure.
- CFRP-debonding was the governing failure mode in all cases, followed by abrupt web-fracture of the beams. Partial rupture of the CFRP was noticed for the beams subjected to a sustained load of $60\%F_u$ because of the synergetic interaction between stress concentrations and time-dependent fiber damage at the geometric discontinuity (i.e., notch). The reference beam without long-term load demonstrated a biased debonding pattern in the vicinity of the notch, whereas such an observation was not made for those subjected to long-term load.
- Cold temperature exposure affected the rate of strain development before mechanical action such as the initiation and propagation of CFRP-debonding controlled the behavior of the CFRP-steel interface. Sustained loads redistributed interfacial stresses and thus uniform strain profiles were observed in the long-term beams in comparison to the case of the reference beam. Further investigations appear to be necessary to extract the creep component of the notched steel beam that could influence the interfacial behavior.
- The beams subjected to cold temperature exhibited less interfacial slip relative to the room-temperature beams. The interfacial shear stress of the long-term beams was less than that of the reference beam because of the stress-redistribution effect.

CHAPTER 6. STRESS INTENSITY FACTORS FOR STRUCTURAL STEEL I-BEAMS STRENGTHENED WITH CFRP SHEETS

6.1. Abstract

Steel girder bridges are vulnerable to fatigue-induced cracks and corrosion damage. Carbon-fiber-reinforced polymer (CFRP) composites have demonstrated significant potential as a repair material for such cracked structures. The stress intensity factor (SIF), which defines the amplitude of the stress field ahead of the crack tip, for the CFRP-strengthened cracked beams cannot be overlooked. The objective of this study is to use the finite element method to develop an accurate SIF of mode I (K_I) solutions for structural steel I-beams strengthened with CFRP under bending. A total of 1,240 cases are analyzed including various combinations of flange-to-web area ratio (eight different W Shapes), crack length, CFRP-to-steel area ratio, CFRP-to-steel stiffness ratio, and CFRP geometry. Such solutions for the SIF are important in the development of static strength prediction for the unstrengthened and strengthened cracked structures. Results show that K_I for the strengthened beams is significantly influenced compared to the unstrengthened counterparts due to the crack-bridging force at the crack location. Efficiency of the CFRP repair is more pronounced when the damage level (i.e. crack depth) increases. The SIF for the strengthened beams is also influenced by the geometry and amount of CFRP as well as the CFRP-to-steel stiffness ratio. The validity of the numerical results and the proposed regression models for SIF are examined through comparison with the experimental results.

6.2. Research Significance

Cracking of the lower tensile flange in steel I-girder bridges has a significant influence on beams' flexural load-carrying capacity and serviceability. Timely rehabilitation will avert long-term repair costs and warrant sustainable performance. Existing research has shown that an

externally bonded CFRP composite is a promising material for strengthening and repairing damaged steel members. Scant research has evaluated the effectiveness of such an emerging strengthening technique using the concept of SIF. To the authors' current knowledge, SIF evaluation for structural cracked steel I-beams repaired with CFRP composites has not been reported in the literature for the CFRP-repair of steel members. This study presents a numerical method to evaluate the SIF for structural single-edge cracked steel I-beams repaired with CFRP composites subjected to bending loads. The study's focus is to investigate the effect of material and geometric properties on the SIF before and after strengthening with CFRP composites. Using a three-dimensional finite element model, a total of 1,240 cases are analyzed, including various combinations of flange-to-web area ratio (eight different W Shapes), crack length, CFRP geometry, CFRP-to-steel area ratio, and CFRP-to-steel stiffness ratio. It is worth noting that the contribution of adhesive properties to the behavior of CFRP-strengthened steel beams is negligible (Kim and Harries 2012) and is not considered in this study. Because complete CFRP failure usually emerges after yielding and crack propagation of the CFRP-repaired cracked steel beams, as previously discussed, and because this study focuses on the static strength, a perfect bond between the CFRP and steel is assumed. In this study, a CFRP composite is applied over the entire span length of the cracked steel beams to minimize the effect of any local debonding of the CFRP that may occur prior to yielding or crack propagation as was observed experimentally. A three-dimensional finite element method is introduced to study the fracture responses of beams by evaluating the SIF at the crack tip. Regression analysis is used to model the numerical results, hence, introducing SIF solutions for structural cracked steel I-beams repaired with CFRP composites. In the design against fracture, and according to the fundamental theory of fracture mechanics, the applied SIF of mode I (K_I) must not exceed the material's fracture toughness (K_{Ic})

to preclude crack propagation. The validity of the numerical results for SIF are examined through a comparison with the experimental results.

In this study, it is postulated that the concept of linear elastic fracture mechanics (LEFM) with small-scale-yielding (SSY) is applicable. As a parameter, K_I , describing the amplitude of the stress field ahead of the crack tip, is used. This assumption is not unreasonable because SIF amplitude affects the crack bridging by CFRP materials, thus, SSY prevails at the crack tip (Baker et al. 2002). In addition, it is observed from Hmidan et al. (2011) that crack initiation loads for most CFRP-strengthened beams are approximately 40% closer to the yield load compared to the unstrengthened counterpart. This observation suggests that CFRP-strengthened beams experience limited yielding before crack propagated into the web, unlike the unstrengthened beams where larger-scale yielding occurs prior to crack growth; therefore, LEFM with SSY is not unreasonably applicable. At low temperatures, steel becomes more brittle, and the fracture of cracked steel girders is likely with limited plastic deformation around the crack tip, making the validity of the LEFM with SSY approach even more acceptable. In this study, it is assumed that crack propagation is governed solely by a critical value for the SIF, the so-called fracture toughness, K_{Ic} . In other words, it is assumed that the failure of CFRP-reinforced beams initiates at a critical load that causes the crack to grow before CFRP failure. Therefore, the static strength of the CFRP-repaired steel beams can easily be determined once the SIF is known.

6.3. Beam Details and Parameters for Cracked I-Beams

A total of eight standard W Shapes with a flange-to-web area ratio (λ) ranging from 0.91 to 2.01, two W Shapes to validate the λ parameter, as well as one W Shape (W4 × 13) that was employed to verify the validity of the proposed approach were used for this study as summarized in Table 6.1 and identified with footnotes 1, 2, and 3, respectively. Beam damage at the midspan

is simulated by a crack through the entire width of the tension flange into the web; introducing single-edge cracked W Shapes, as shown in Fig. 6.1. To represent various stages of fatigue crack propagation (i.e., initial damage before CFRP repair), five different crack lengths (a_o) are considered for each W shape (i.e., five different ζ values ($\zeta = a_o/h$), where h represents the beam depth). For all eight beams and for each crack length, three different geometries are considered and analyzed, Control (unrepaired), Full-Flange (CFRP covering the full width of the tension flange), and Half-Flange (CFRP covering half the width of the tension flange), as shown in Figs. 6.1(b), (c), and (d), respectively, and summarized in Table 6.1 and identified with footnote 1. For each CFRP-repaired beam (Full or Half-Flange geometry), five different CFRP-to-steel area ratios ($\psi = A_c/A_s$, where A_c is the area of CFRP and A_s is the area of steel) are considered. Each case is analyzed under three different CFRP-to-steel stiffness ratios ($\eta = E_c/E_s$, where E_c is the elastic modulus of CFRP and E_s is the elastic modulus of steel). In all cases, and to reduce the influence of the bond length, CFRP is applied to the entire length of the tensile-cracked soffit [Fig. 6.1(a)].

6.4. Equations for the Stress Intensity Factor

The SIF is one of the most important concepts in fracture mechanics. The solutions for such single-parameter descriptions of crack tip conditions (i.e., SIF) for several geometric configurations and loads are reported in several handbooks that are concerned solely with the SIF solutions (Rooke and Catwright 1976; Tada et al. 1985; Murakami 1987). The general form of the SIF solutions at the crack tip for mode I (i.e., opening mode) loading is expressed as follows:

$$K_I = Y\sigma\sqrt{\pi a} \quad (6.1)$$

where K_I is the stress intensity factor for mode I fracture, Y is the correction factor for the SIF, σ is the uncracked body extreme tensile fiber stress, and a is the crack size. In this study, the SIF

for structural single-edge cracked steel I-beams (i.e., single-edge cracked W shapes) that are unrepaired and repaired with CFRP composites subjected to bending loads is proposed to be as follows:

$$K_I = Y(\lambda, \zeta)\sigma\sqrt{\pi a_o} \quad (\text{Unrepaired beams}) \quad (6.2)$$

$$K_I = Y(\lambda, \zeta, \psi, \eta, \text{geometry})\sigma\sqrt{\pi a_o} \quad (\text{CFRP – repaired beams}) \quad (6.3)$$

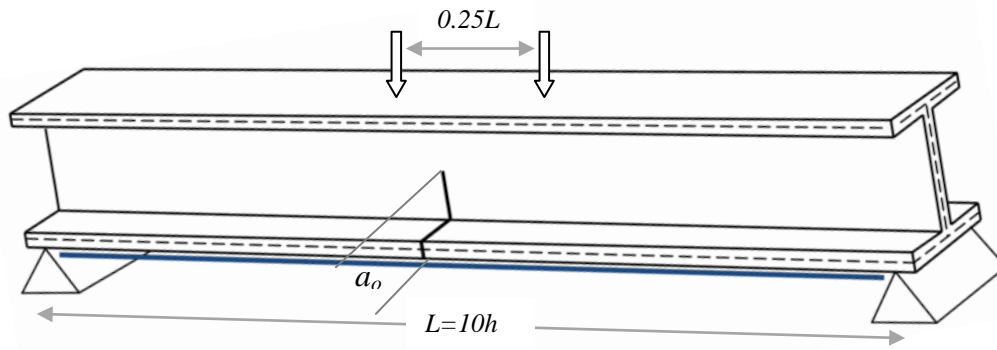
where,

λ = flange-to-web area ratio ($\lambda = 2A_f/A_w$), ranging from 0.91 to 2.01 for eight different W shapes;

ζ = normalized crack length ($\zeta = a_o/h$), where a_o is the crack length and h is the beam depth, with five different ζ values (i.e. five different initial crack lengths) for each W Shape considered: 0.1, 0.3, 0.5, 0.7, and 0.9.

ψ = CFRP-to-steel area ratio ($\psi = A_c/A_s$, where A_c represents the cross-sectional area of CFRP and A_s is the cross-sectional area of steel), for each CFRP-repaired beam (Full or Half-Flange geometry), five different ψ values (i.e., five different CFRP areas) are considered: 0.002, 0.004, 0.006, 0.008, and 0.01 for Full-Flange geometry, and 0.001, 0.002, 0.003, 0.004, and 0.005 for Half-Flange geometry. It should be noted that the CFRP thickness for both geometries remains the same and that only the CFRP width is reduced to Half-Flange width.

η = CFRP-to-steel stiffness ratios ($\eta = E_c/E_s$, where E_c is the elastic modulus of CFRP and E_s is the elastic modulus of steel). The SIF for each CFRP-repaired steel beam is evaluated under three η values (i.e., three different CFRP elastic moduli: 150 GPa, 225 GPa, and 300 GPa) that are considered: 0.75, 0.125, and 1.5. The steel modulus of elasticity is 200 GPa. The Poisson's ratio for CFRP and steel are 0.27 and 0.30, respectively.



(a)

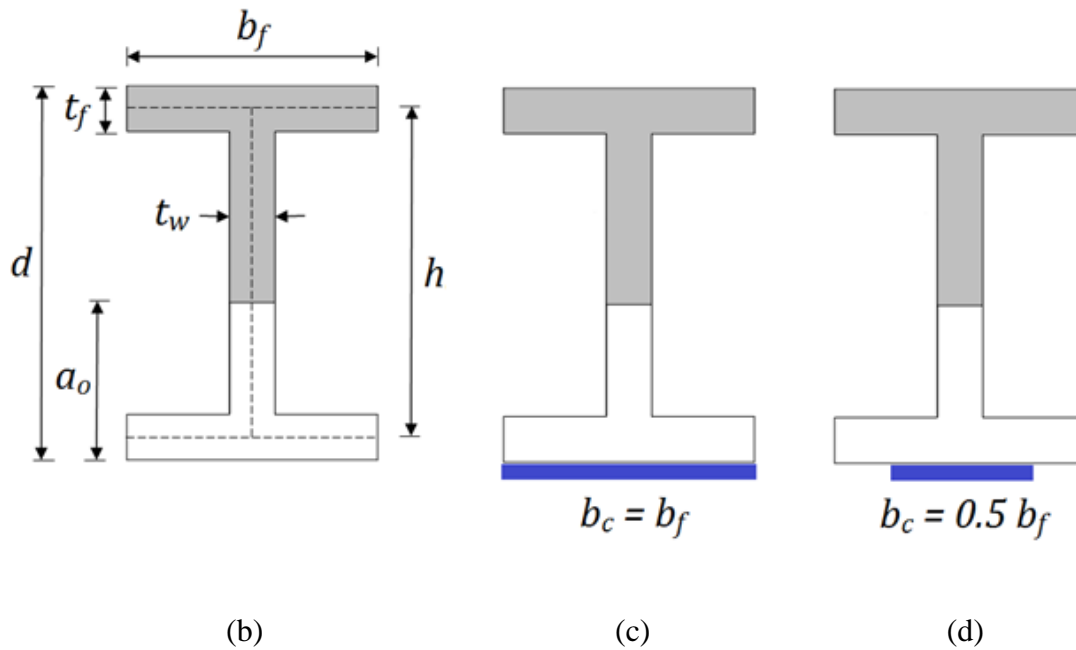


Fig. 6.1. Beam details showing the three geometries: (a) beam geometry; (b) cross-section for Control (unrepaired) beam; (c) cross-section for repaired Full-Flange beam; (d) cross-section for repaired Half-Flange beam

6.4.1. Flange-to-Web Area Ratio Parameter

Parameter λ in correction factor Y in Eqns. 6.2 and 6.3, which is the cross-sectional area ratio between the two flanges and the web for I-beams, is assumed to characterize the W Shapes

Table 6.1. Matrix of W Shapes employed in Finite Element Analysis

<i>W Shapes (Metric)</i>	λ ($2A_f/A_w$)	ϕ (h/b_f)	ζ (a_o/h)	ψ (A_c/A_s)	<i>Geometry</i>	η (E_c/E_s)
W36 × 135 ¹ (W920×201)	0.91	2.90	0.1,0.3, 0.5,0.7, and 0.9	0	Control	0
				0.002,0.004,0.006, 0.008, and 0.010	Full- Flange	0.75,1.125, and 1.5
				0.001,0.002,0.003, 0.004, and 0.005	Half- Flange	0.75,1.125, and 1.5
W33 × 130 ¹ (W840×193)	1.05	2.80	0.1,0.3, 0.5,0.7, and 0.9	0	Control	0
				0.002,0.004,0.006, 0.008, and 0.010	Full- Flange	0.75,1.125, and 1.5
				0.001,0.002,0.003, 0.004, and 0.005	Half- Flange	0.75,1.125, and 1.5
W27 × 102 ¹ (W690×152)	1.23	2.63	0.1,0.3, 0.5,0.7, and 0.9	0	Control	0
				0.002,0.004,0.006, 0.008, and 0.010	Full- Flange	0.75,1.125, and 1.5
				0.001,0.002,0.003, 0.004, and 0.005	Half- Flange	0.75,1.125, and 1.5
W40 × 199 ¹ (W1000×29)	1.38	2.38	0.1,0.3, 0.5,0.7, and 0.9	0 (control)	Control	0
				0.002,0.004,0.006, 0.008, and 0.010	Full- Flange	0.75,1.125, and 1.5
				0.001,0.002,0.003, 0.004, and 0.005	Half- Flange	0.75,1.125, and 1.5
W24 × 103 ² (W1000×29)	1.38	2.61	0.1,0.3, 0.5,0.7, and 0.9	0	Control	0
W33 × 201 ¹ (W840×299)	1.55	2.07	0.1,0.3, 0.5,0.7, and 0.9	0	Control	0
				0.002,0.004,0.006, 0.008, and 0.010	Full- Flange	0.75,1.125, and 1.5
				0.001,0.002,0.003, 0.004, and 0.005	Half- Flange	0.75,1.125, and 1.5
W24 × 117 ¹ (W610×174)	1.69	1.83	0.1,0.3,0. 5,0.7, and 0.9	0	Control	0
				0.002,0.004,0.006, 0.008, and 0.010	Full- Flange	0.75,1.125, and 1.5
				0.001,0.002,0.003, 0.004, and 0.005	Half- Flange	0.75,1.125, and 1.5
W21 × 101 ¹ (W530×150)	1.91	1.68	0.1,0.3, 0.5,0.7, and 0.9	0	control	0
				0.002,0.004,0.006, 0.008, and 0.010	Full- Flange	0.75,1.125, and 1.5
				0.001,0.002,0.003, 0.004, and 0.005	Half- Flange	0.75,1.125, and 1.5

Table 6.1. Matrix of W Shapes employed in Finite Element Analysis (continued)

<i>W Shapes (Metric)</i>	λ ($2A_f/A_w$)	ϕ (h/b_f)	ζ (a_o/h)	ψ (A_c/A_s)	<i>Geometry</i>	η (E_c/E_s)
W27 \times 336 ² (W530 \times 150)	1.91	1.90	0.1,0.3, 0.5,0.7, and 0.9	0	Control	0
W18 \times 76 ¹ (W460 \times 113)	2.01	1.59	0.1,0.3, 0.5,0.7, and 0.9	0	Control	0
				0.002,0.004,0.006, 0.008, and 0.010	Full- Flange	0.75,1.125, and 1.5
W4 \times 13 ³ (W100 \times 19)	2.62	0.94	0.1,0.3, 0.5,0.7, and 0.9	0	Control	0
				0.005,0.010,0.015, 0.020, and 0.025	73% Flange	0.75,1.135, and 1.5

¹: W Shapes included in regression models

²: W Shapes used to validate that λ characterizes W Shapes

³: W Shape for preliminary analysis and validation of proposed method

in the SIF calculations. Chen (1992) and Albrecht et al. (2008) have shown through an extensive numerical computation included a wide range of W shapes that such parameter (λ) can identify W shapes in SIF calculations. For example, Albrecht et al. (2008) suggested that the depth-to-width ratio of I-beams ($\phi=b_f/h$) may influence the SIF results, where b_f is flange width. Under various crack and loading configurations, the correction factors for several pairs of W Shapes that have identical λ values, but are significantly different in geometry (i.e., different ϕ values, such as deeper and narrower W Shapes), were calculated and compared. Results from the study showed, with very limited exceptions, that the maximum SIF difference between the two parameters is not more than 3.5%.

Figure 6.2 shows the correlation between λ (flange-to-web area ratio) and ϕ (depth-to-width ratio) for all 273 W Shapes listed in the Steel Construction Manual (AISC 2005) with each W shape represented by one data point. The figure shows a relatively linear relationship between λ and ϕ . The linearity of such a correlation becomes more pronounced for the W Shapes located

within the bandwidth which represents more than 54% of all W Shapes. The eight W Shapes used in this study (identified with footnote 1 in Table 6.1) are located within the bandwidth and are pinpointed with solid, square symbols. The corresponding smallest and biggest λ for the W Shapes used are 0.91 and 2.01, respectively. To investigate the validity of λ in characterizing the W Shapes, two pairs of W Shapes were randomly selected in this study: λ values of 1.38 and 1.91 (identified with footnote 2 in Table 6.1) where the corresponding W Shapes with similar λ but higher ϕ values are pinpointed with solid, circular symbols as shown in Fig. 6.2.

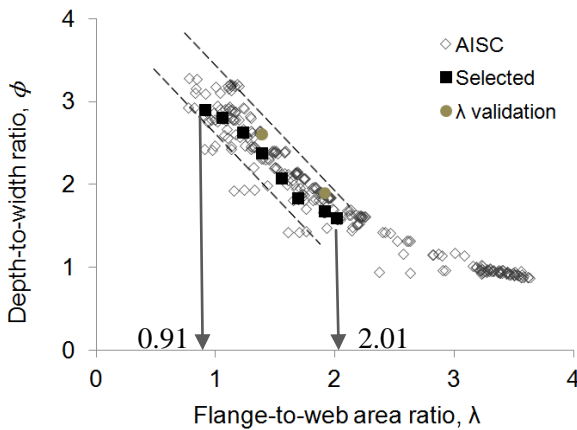


Fig. 6.2. Correlation between λ and ϕ for all W Shapes in AISC

Because previous studies already validated that the ϕ parameter has minimal influence on SIF calculations and that λ can characterize W Shapes (Chen 1992; Albrecht et al. 2008), only two pairs of W Shapes were randomly chosen in this study to verify such validation. The correction factor, Y , for the two pairs of W Shapes was calculated at different crack lengths, and the ratios of Y between the W Shapes with low and high values of ϕ are plotted as shown in Fig. 6.3. The maximum difference between the correction factors for both pairs was 3.7%. Such an inconsequential difference in the SIF results implies that λ can characterize W Shapes without taking ϕ into consideration, which is consistent with Albrecht et al. (2008).

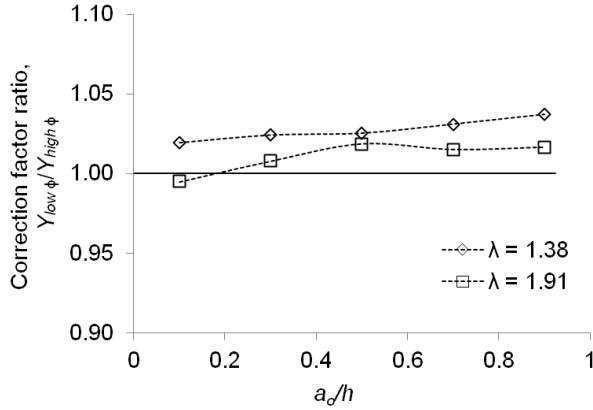


Fig. 6.3. Effect of λ on the correction factor

6.4.2. Remote Stress: the Uncracked Section Extreme Tensile Fiber Stress

Equations 6.2 and 6.3 show that the opening-mode SIF, K_I , is linearly proportional to the applied remote stress, $K_I \propto \sigma$. For I-beams subjected to pure bending moment loading, the following flexure formula defines the normal stress that is linearly distributed over the beam's cross-section:

$$\sigma = \frac{My'}{I'} \quad (6.4)$$

where M is the applied moment, y' is the perpendicular distance from the neutral axes, and I' is the moment of inertia for the cross-sectional area. In this study, the remote stress, σ , for the uncracked I-beam repaired with CFRP is calculated by applying the *transformed-section method* for composite beams as shown in Fig. 6.4. When a bending moment is applied to a beam made of two materials, in this case steel and CFRP, which have the cross-sectional area shown in Fig. 6.4(a), it is assumed that: no slip will occur between the two materials, that the total cross-sectional area will remain plane during bending, and that the materials have linear-elastic behavior. Applying the flexure formula in Eqn. 6.4 requires the material to be homogenous, so the cross-section of the I-beam must be transformed into a single material. In this case, the

CFRP-reinforced steel I-beam is transformed into a beam made from a single material, steel in this case, as shown in Fig. 6.4(b). Here, the original width of CFRP (b_c) has been changed to ηb_c , where $\eta = E_c/E_s$. It should be noted that, in this case, the transformation factor, η , must be more than one assuming $E_c > E_s$. Because the CFRP-reinforced I-beam has been transformed into steel material, Fig. 6.4(b), the normal stress distribution over the transformed section will be linear; consequently, the location of the centroid (neutral axis) and the moment of inertia for the transformed section can be determined using Eqns. 6.5 and 6.6, respectively:

$$\bar{y} = \frac{\sum \tilde{y}A}{\sum A} \quad (6.5)$$

$$I = \sum (\bar{I} + Ad_o^2) \quad (6.6)$$

where \tilde{y} represents the algebraic distances for the centroid of each composite part, $\sum A$ represents the sum of the areas for the composite parts, \bar{I} represents the moment of inertia for each composite part, and d_o is the perpendicular distance between the centroidal axis and the parallel axis. Neglecting the thickness of the CFRP laminate, \bar{y} and I for the transformed section are calculated as follows:

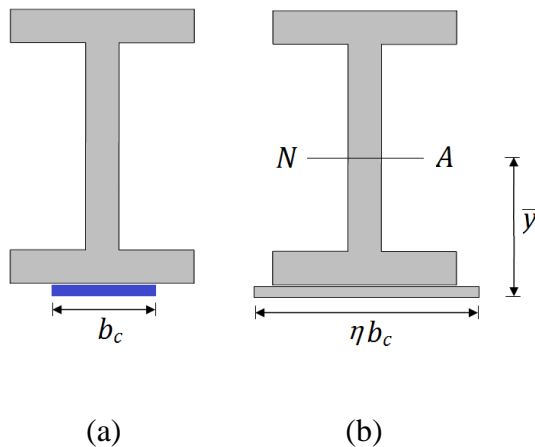


Fig. 6.4. The transformed-section method (uncracked cross-section)

$$\bar{y} = \frac{A_s d}{2(\eta A_c + A_s)} \quad (6.7)$$

$$I = \eta A_c \bar{y}^2 + (0.5d - \bar{y})^2 A_s + I_s \quad (6.8)$$

where I_s is the moment of inertia for the steel. Finally, the remote, extreme tensile fiber stress for the uncracked I-beam repaired with CFRP can be obtained by multiplying the stress calculated in the transformation section by the transformation factor, η , as shown in Eqn. 6.9:

$$\sigma = \frac{\eta M \bar{y}}{I} \quad (6.9)$$

It should be mentioned that Moy et al. (2002) and Colombi and Poggi (2005) also proposed similar assumptions while analyzing the static behavior of CFRP-reinforced steel beams using this approach.

6.5. Finite Element Model Development

To evaluate the effect of CFRP repair on the SIF at the crack tip, a three-dimensional finite element analysis (FEA) for unstrengthened and strengthened cracked W Shapes was conducted using the general-purpose FEA program ANSYS. The following summarizes the proposed modeling approach, including element types and boundary conditions and mesh design for crack tip region.

6.5.1. Element Types and Boundary Conditions

In this study, the steel beams were considered as a combination of three plates representing the two flanges and the web, as shown by the dotted lines in Fig. 6.1. The dimension of each plate was defined by its mid-plane, width, and thickness connected together at the junction line. The constructed FE model is shown in Fig. 6.5(a). The steel beams were modeled with the eight-node structural shell element (SHELL281). Beside the fact that SHELL281 is appropriate for analyzing thin and moderately thick structures and its adequacy for

both linear and non-linear applications, it has the mid-side node capability required to produce the singularity that is needed to determine the SIF at the crack tip (to be discussed). Because perfect connection is assumed between the CFRP and steel, and because SHELL281 element kinematics allow for membrane stiffness (stretching), the SHELL281 element was also used to model the CFRP, hence achieving strain compatibility across the repaired section as well as creating a compatible finite element mesh. A pure bending moment was produced over the midspan section through a four-point bending configuration as shown in Fig. 6.1(a). A simply supported boundary condition was provided by constraining the appropriate nodes in translation. The loading span was selected to be 10 times the beam depth, and the constant moment zone was set to be 25% of the beam span [Fig. 6.1(a)]. It should be noted that neither the beam span nor the length of the constant moment zone affects the calculated SIF when the CFRP is applied to the entire length of the tensile-cracked soffit.

6.5.2. Crack-Tip Quadrilateral Element

The desired singularity of stresses and strains around the crack tip in elastic crack problems can be achieved by using the quarter-point elements at the crack tip. The singularity in the eight-node isoperimetric quadratic element (e.g., SHELL281 element) can be created by moving the mid-side nodes a quarter of the element edge length (1/4-points) towards the crack tip. In this study, and as previously mentioned, the SHELL281 element has the mid-side node capability required to produce the singularity that is needed to determine the SIF at the crack tip. SHELL281 is defined by eight nodes, 1 through 8, as shown in Fig. 6.5(b). At the crack tip, SHELL281 is collapsed down to a triangular-shaped element by defining the same node number for nodes 6, 7, and 8. Then, the singularity in the element is achieved by forcing the mid-side nodes (nodes 4 and 5) to move to the 1/4-points [Fig. 6.5(b)]. Demanding the elements around

the crack tip to exhibit a $1/\sqrt{r_o}$ strain singularity (where r_o is the radial distance from the crack tip) allows the finite element programs, such as ANSYS, to model the crack-tip fields accurately and also reduces the need for very fine mesh around the crack tip (Anderson 2005). It should be noted that, by using the quarter-point element, the strain will be singular only at the node point located at the crack tip, whereas the strain will vary as $1/\sqrt{l}$ over the innermost part of the element, where l is the element length. It is worth noting that the behavior of the quarter-point element was first independently noted by Henshell and Saw (1975) and Barsoum (1976).

6.5.3. Mesh Design for Crack-Tip Region

Figure 6.5(c) illustrates the spider-web mesh design for the region surrounding the crack tip in the constructed FE model shown in Fig. 6.5(a). Such mesh configuration is proven to be favorable for fracture mechanics problems (Anderson 2005). The spider-web configuration consists of concentric circles of quadrilateral elements that are focused at the crack tip. The first row of elements surrounding the crack tip is the degenerated, triangular, quarter-point elements (i.e., singular elements) that are capable of addressing the theoretical singularity as described above.

The appropriate level of mesh refinement for the region surrounding the crack tip is selected by considering the ANSYS-recommended meshing guidelines to solve fracture mechanics problems. The number of elements in the first row surrounding the crack tip in the circumferential direction is selected to be 16 (one element per 22.5°) as shown in Fig. 6.5(c). The ratio between the first row and the second row of elements surrounding the crack tip is set to be 0.67. To study the influence of the mesh density around the crack-tip region on the accuracy of calculating the SIF, the analysis of an edge-cracked plate subjected to pure bending moment loading, for which reliable solutions are found in the literature, is performed using similar

element types and a mesh design to the one used in this study, as shown in Fig. 6.6. At the two crack lengths analyzed ($a/h = 0.1$ and 0.5), it can be clearly seen that the SIF is sensitive to the length of the crack-tip element. The FE values of K_I (K_{FEA}) were within 1.7% of the established values found in the literature (K_{LIT}) when the crack-tip element-to-crack length ratio [l/a_o in Fig. 6.5(b)] is 0.025; hence, this ratio was accepted in this study. It should be mentioned that although a smaller ratio of l/a_o of 0.015 may result in K_{FEA}/K_{LIT} being approximately 1.6%, $l/a_o = 0.025$ was adopted in this study due to the limitation on the maximum number of nodes in the ANSYS license used because the number of nodes becomes an issue when analyzing large W Shapes.

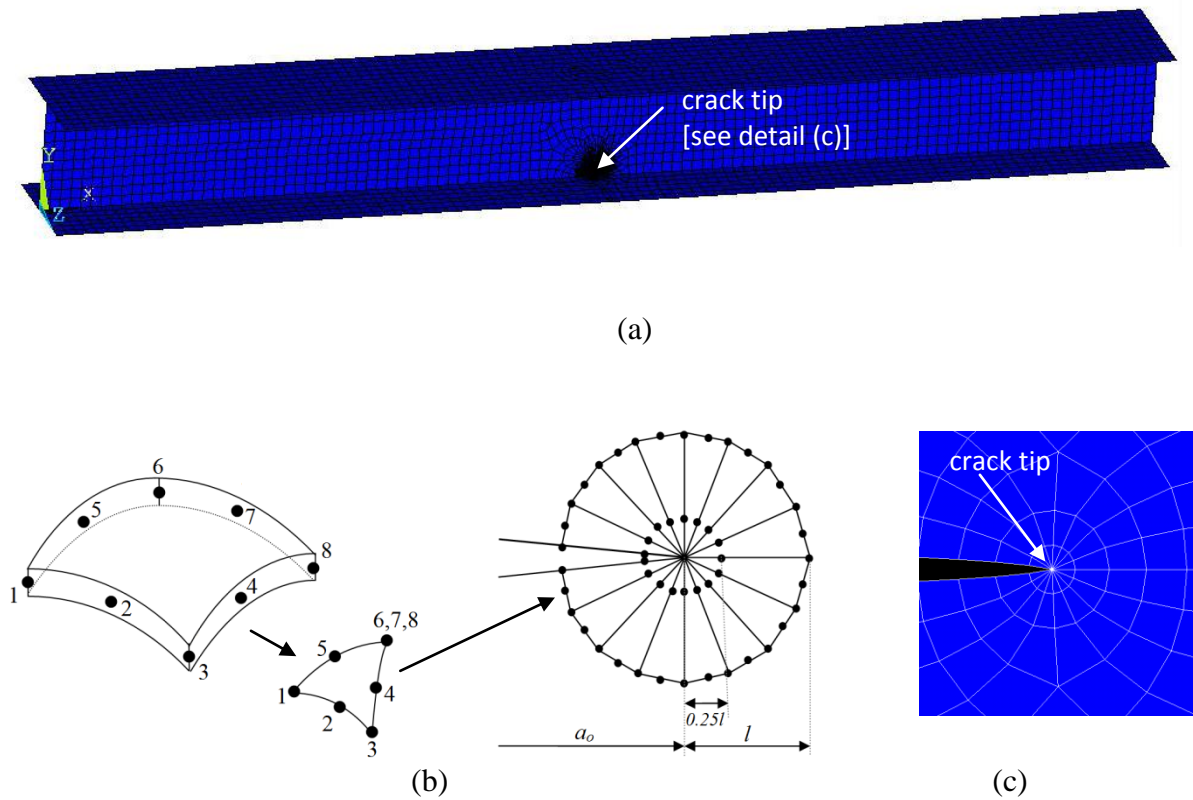


Fig. 6.5. Proposed modeling approach: (a) constructed FEA model; (b) degeneration of the quadrilateral element into a triangle at the crack tip; (c) crack-tip region showing spider-web configuration

The spider-web mesh expedites a smooth transition from a very fine mesh at the tip of the crack to a coarser mesh away from the crack. Such a transition is designed to take place within a square region, X^2 , surrounding the crack (where $X = 2*a_o$ when $a_o/h \leq 0.5$ [Fig. 6.7(a)] or $2*h-a_o$ when $a_o/h > 0.5$ [Fig. 6.7(b)]). The element lengths within this region transition from triangular fine element at the crack tip (with l equal to $0.025*a_o$ when $a_o/h \leq 0.5$ or $0.025*h-a_o$ when $a_o/h > 0.5$) to a relatively coarse, square element along the perimeter of the square region and the rest of the beam with an element length of $0.09h$.

Finally, the mode-I stress intensity factor, K_I , is calculated in a specific post-processing procedure using the displacement extrapolation method supported by ANSYS. Henceforth, the correction factor, Y , is determined by normalizing the calculated K_I with all the other parameters; the applied remote stress, crack length, and CFRP properties and factors in the case of calculating Y for the CFRP-repaired beams.

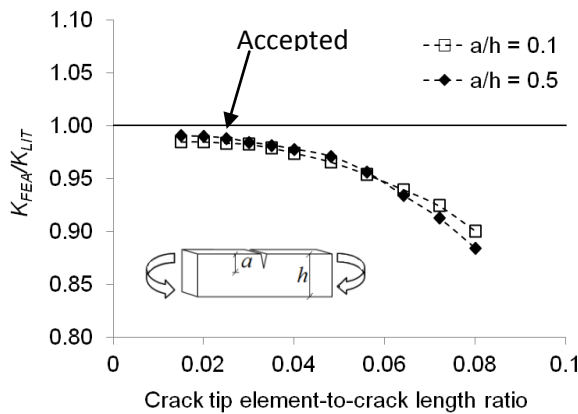


Fig. 6.6. Comparison of SIFs calculated from FEA and handbooks for edge crack in beam in bending

6.6. Results and Discussion

6.6.1. Experimental Evidence and Approach Validation

In this study, reference is made to the CFRP-repaired steel I-beams with various initial crack configurations that were experimentally tested by Hmidan et al. (2011). A summary of the experimental program and the test results are given here to provide a comparison with the predicted results from the proposed SIF approach with an emphasis on the beams' static load carrying-capacity.

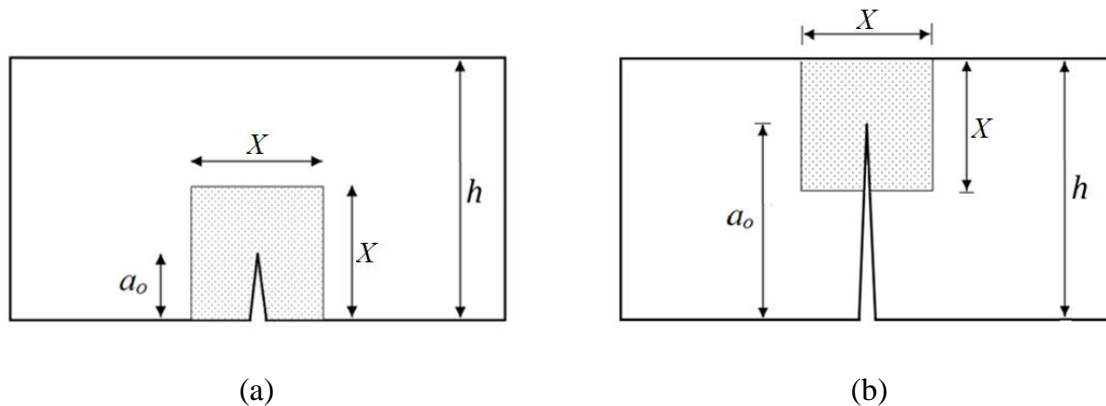


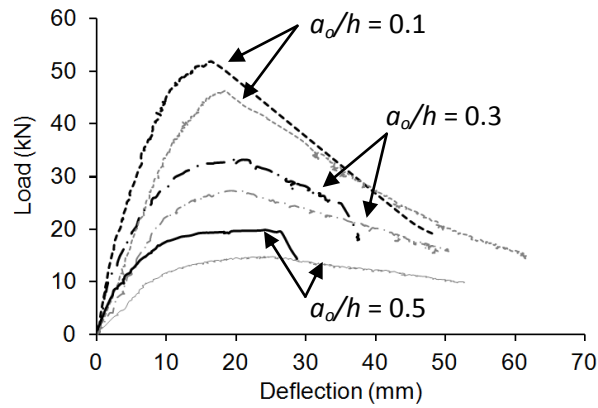
Fig. 6.7. Fine mesh mapping near the crack tip region at different crack lengths: (a) $a_o/h \leq 0.5$; (b) $a_o/h > 0.5$

6.6.1.1. Overview of the experimental program and test results

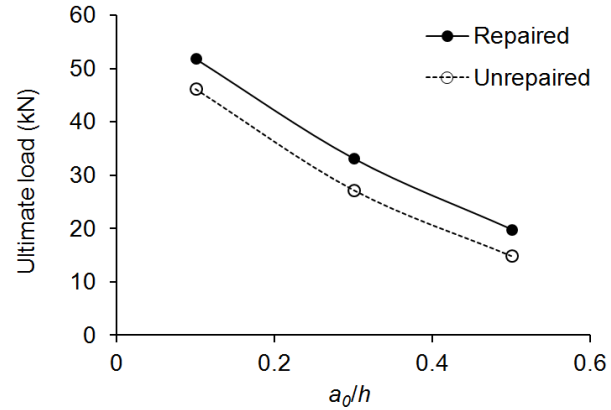
Hmidan et al. (2011) monotonically tested six $W4 \times 13$ A992 hot-rolled steel sections. The beams had three different notch depths to represent various stages of fatigue crack propagation (i.e. initial damage before repair work was conducted) producing three a_o/h ratios: 0.1, 0.3, and 0.5. Three of the six beams were repaired using one layer of a CFRP sheet, and the other three were unrepaired Control beams. The CFRP was bonded to the tensile soffit of the notched beams with an epoxy adhesive. All beams were simply supported and loaded under four-point bending in a test setup similar to the one shown in Fig. 6.1(a) with different lengths for the loading span and the constant moment zone along with the CFRP bonded to only 80% of the

loading span (symmetrical about the midspan) and 73% of the tensile flange width (symmetrical about the web), in other words, with a geometry that falls between the Full and Half-Flange geometries shown in Figs.6.1(c) and (d), respectively.

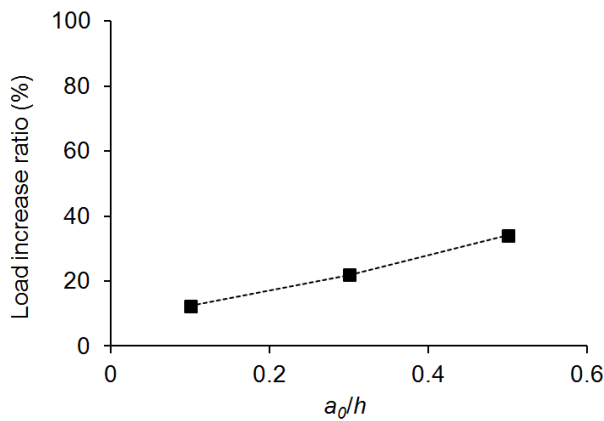
Figure 6.8(a) shows the load-deflection responses at the midspan for all test beams. The load-carrying capacity of the beams was significantly influenced by the level of initial damage (i.e., notch size). For example, the measured ultimate loads of the unrepaired beams having $a_o/h = 0.3$ and 0.5 were 41.1% and 56.9% less than that of the beam with $a_o/h = 0.1$, respectively. A similar trend was observed for the repaired beams, as shown in Fig. 6.8(b). Flexural stiffness, yield capacity, and the ultimate load of the damaged beams improved because of the CFRP repair and were particularly noticeable when the level of initial damage increased [Fig. 6.8(a)]. For example, Fig. 6.8(c) shows that the ultimate load of the repaired beams benefitted more when the damage level increased. Such improvement in the flexural behavior is attributed to load sharing between the CFRP and steel through a crack-bridging force at the notch location. Fig. 6.8(d) shows the CFRP-strain distribution within a distance ± 100 mm from the notch at 75% of the ultimate load (P_u). Strain gauges were bonded to the CFRP to study the debonding propagation. It can be noticed that the strain profile for the beams tended to be very similar regardless of the notch size. The CFRP strain for all beams at the midspan at a load level exceeded the service state (i.e. 75% P_u) was measured to be less than 35% of the CFRP rupture strain ($\epsilon_{\text{rupture}} = 0.0167$). Such experimental results indicate that CFRP rupture is unlikely within the static capacity of the CFRP-strengthened beams. In fact, the failure mode of beams with $a_o/h = 0.1$ and 0.5 was rupture of the CFRP when CFRP strain reached the ultimate strain which took place at 100% P_u , well beyond yielding of the steel. The beam with $a_o/h = 0.3$ failed by CFRP debonding rather than rupture which also took place after yielding and beyond the beam's static



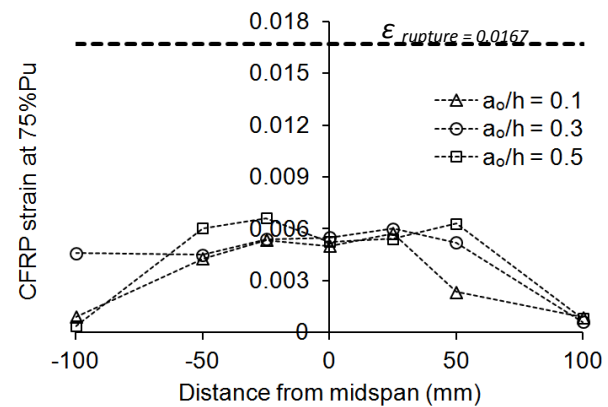
(a)



(b)



(c)



(d)

Fig. 6.8. Experimental behavior of test beams [Hmidan et al. 2011]: (a) load-deflection response at midspan of beams (faint = unrepaired; dark = repaired); (b) comparison of ultimate load; (c) increase of ultimate load after repair; (d) measured strains along the CFRP

capacity. It should be mentioned that such a failure mode was attributed to an inadequate bond between the CFRP and steel which could happen during the wet-layup application. These experimental observations legitimize the assumption that crack propagation is governed solely by a critical value of the SIF. In other words, it is assumed that the failure of CFRP-reinforced beams will initiate at a critical load that causes the crack to grow before the CFRP's failure.

Therefore, the static strength of the CFRP-repaired steel beams can be easily determined once the SIF is known.

6.6.1.2. SIF and approach validation

Using the proposed FE modeling approach described above, including the beam geometry and setup shown in Fig. 6.1(a), SIFs at the crack tip for W4 × 13 (identified by footnote 3 in Table 6.1) were calculated. The material and geometric properties for both the steel and CFRP used in the FE model were similar to the one in the experimental test with the CFRP bonded to 73% of the tensile flange width, $\psi (A_c/A_s) = 0.005$, and $\eta (E_c/E_s) = 1.135$. Fig. 6.9 shows the variations of the calculated SIFs with the three normalized crack lengths (i.e., $a_o/h = 0.1, 0.3, \text{ and } 0.5$) at five different levels of bending moment, M , applied on the constant moment zone. It can be clearly seen that K_I increases as the initial crack length increases for both unrepaired and repaired beams: Figs. 6.9(a) and (b), respectively. However, the rate of K_I increase due to the larger crack length is reduced due to the CFRP repair. For example, at $M = 20$ kN.m, K_I for the unrepaired beams increased by a factor of 3.3 when the normalized crack length increased from 0.1 to 0.5, whereas K_I increased by only a factor of 2.3 for the CFRP-repaired beams. The effect of CFRP repair to reduce the rate of the K_I increase by approximately 30% holds true regardless of the M level. This observation implies that crack bridging by the CFRP sheet stabilized the crack-mouth opening displacement of the repaired beams which resulted in a significant reduction in the amplitude of the SIF ahead of the crack tip, hindering crack growth. The SIF of the repaired beams benefited more when the damage level increased as shown in Fig. 6.9(c). The decrease in the calculated SIF induced by the repair was 18.3%, 18.7%, and 41.8% for the beams having $a_o/h = 0.1, 0.3, \text{ and } 0.5$, respectively. This trend for the interaction between

the initial damage and the CFRP repair is consistent with the one observed experimentally when evaluating the ultimate loads, as shown in Fig. 6.8(c).

To examine the validity of the proposed approach, a comparison between the numerical prediction for the critical load (P_{cr}) using the proposed SIF solutions and other loads determined experimentally by Hmidan et al. (2011) (i.e., yield load, P_y ; and crack-initiation load, P_{ci}) is shown in Fig. 6.10. The critical loads for the unrepaired and CFRP-repaired beams were calculated based on the basic assumption that crack growth takes place when the SIF at the crack tip reaches a critical value that is fracture toughness of the steel, K_{Ic} . The K_{Ic} value for the A992 structural steel (steel used in the experimental program) was estimated using the upper shelf coloration introduced by Rolfe and Novak (1970) and Barsom and Rolfe (1970); this method is known as the Rolfe-Novak-Barsom correlation. The empirical correlation (Eqn. 6.10) between Charpy values and the material's fracture toughness is described as the best-known correlation (Kanninen and Popelar 1985). The K_{Ic} - CVN empirical correlation (i.e., the Rolfe-Novak-Barsom correlation) included 11 steels with a wide range of yield strengths having a fracture toughness ranging from 87 to 246 ksi in^{1/2} (94.5 to 270.3 MPa m^{1/2}) (Blake 1996). The Rolfe-Novak-Barsom correlation is as follows:

$$\left(\frac{K_{Ic}}{\sigma_Y}\right)^2 = 5 \left[\frac{CVN}{\sigma_{YS}} - 0.05 \right] \quad (6.10)$$

where CVN is the upper-shelf Charpy V-Notch impact energy in ft-lbs, σ_{YS} is the yield strength in ksi, and K_{Ic} is the fracture toughness in ksi in^{1/2}. The fracture toughness, K_{Ic} , for the W4 × 13 steel beams was evaluated using Eqn. 6.10 to be approximately 105.4 ksi in^{1/2} (116 MPa m^{1/2}; shown in Figs. 6.9(a) and (b)) using a value of $CVN = 40$ ft-lbs (54.23 Joules) at 70°F for the

A992 structural steel (Brockenbrough and Frederick 2006) and a yield strength of 60 ksi (414 MPa).

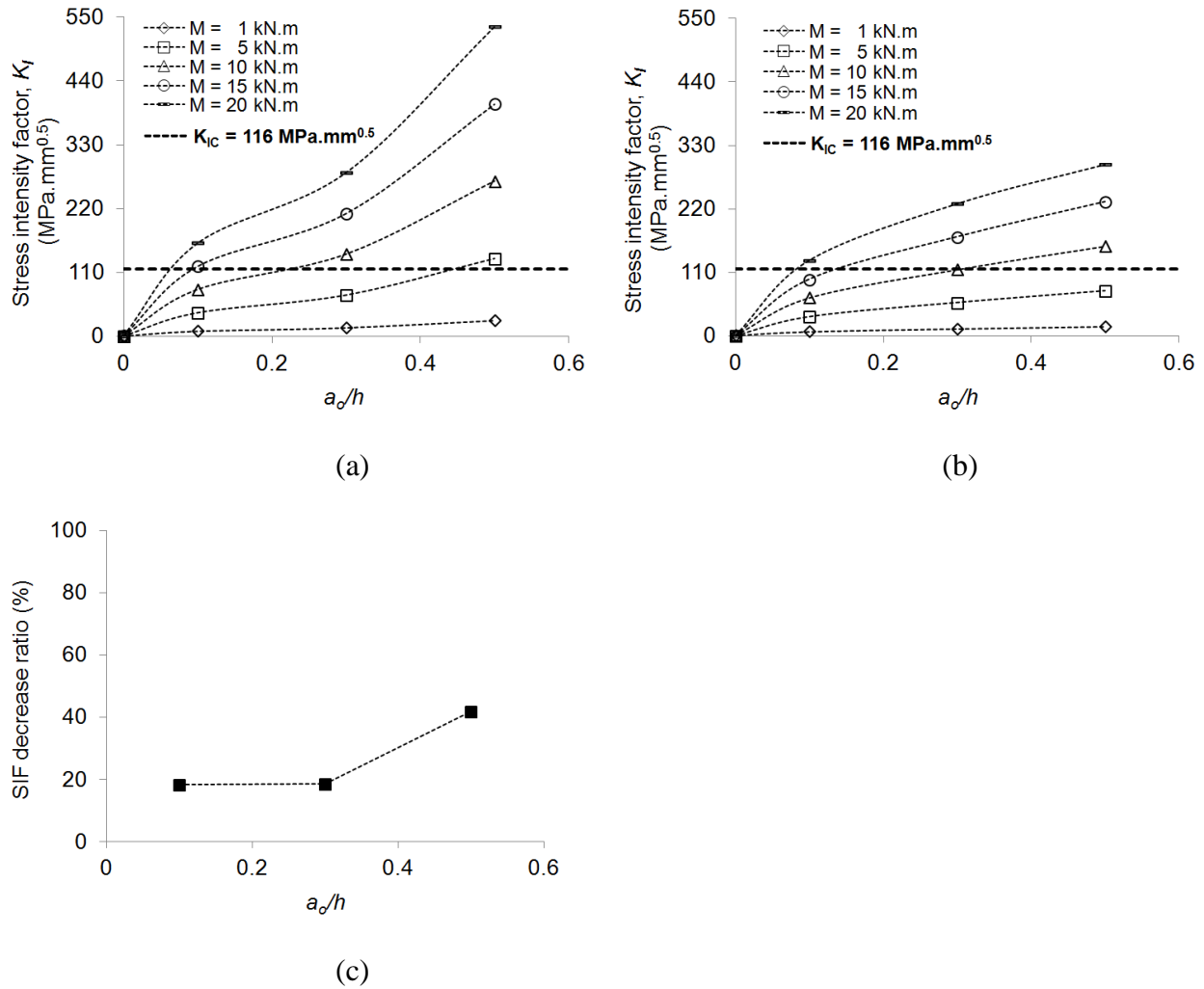


Fig. 6.9. Correlations between SIF and crack length for W4 × 13 beams under different bending moments: (a) unrepaired beams; (b) repaired beams; (c) decrease in SIF after repair

Figure 6.10(a) shows that the predicted, static critical loads, P_{cr} , for the unrepaired beams are within reasonable agreement with those obtained experimentally: P_y and P_{ci} . For example, the calculated critical loads of the unrepaired beams having $a_o/h = 0.1$ and 0.5 were 4.7% and 16.3% higher than the measured yield loads as well as 13.0% and 18.2% less than the measured crack- initiation loads, respectively [Fig. 6.10(c)]. For the unrepaired beam with $a_o/h = 0.3$, the

calculated critical load was 1.8% and 16.6% less than the measured yield load and the crack-initiation load, respectively. It should be noted that, for the test beams, the onset of crack propagation was noticed and recorded after the beams underwent significant yielding and plasticity at the tip of the notch, whereas the proposed modeling approach only focused on static fracture mechanics with small-scale yielding. Thus, the observation that experimentally measured crack initiation loads are up to 18.2% higher than the predicted critical loads was not unreasonable. For the CFRP-repaired beams, a fairly similar trend was observed, as shown in Fig. 6.10(b). The calculated critical loads of the repaired beams having $a_o/h = 0.1$ and 0.3 were 4.7 and 19.6% higher than the measured yield loads and 5.0% and 5.4% less than the measured crack-initiation loads, respectively [Fig. 6.10(d)]. For the repaired beam with $a_o/h = 0.5$, the predicted critical load was calculated to be 31.1% and 17.5% higher than the measured yield and crack-initiation loads, respectively. The experimental results for this beam indicated that the crack-initiation load ($P_{ci} = 18.8$ kN) was 14.6% higher than the yielding load ($P_y = 16.4$ kN), where the predicted load was calculated as 21.5 kN [Fig. 6.10(b)]. In other words, the proposed approach overestimated the critical load compared to the experimental results for a high value of a_o/h with the repaired beam (i.e., $a_o/h = 0.5$), unlike the satisfactory consistency that was observed for the unrepaired beams. This observation can be explained by the fact that the proposed SIF approach assumes a perfect bond between the CFRP and steel with the CFRP bonded to the entire length of the loading span, unlike the test beams where partial debonding was recorded prior to and after yielding of steel with CFRP applied to only 80% of the loading span length, hence, possibly influencing the fracture response. Also, the predicted critical loads were obtained using the fracture toughness of steel that was estimated from a developed numerical

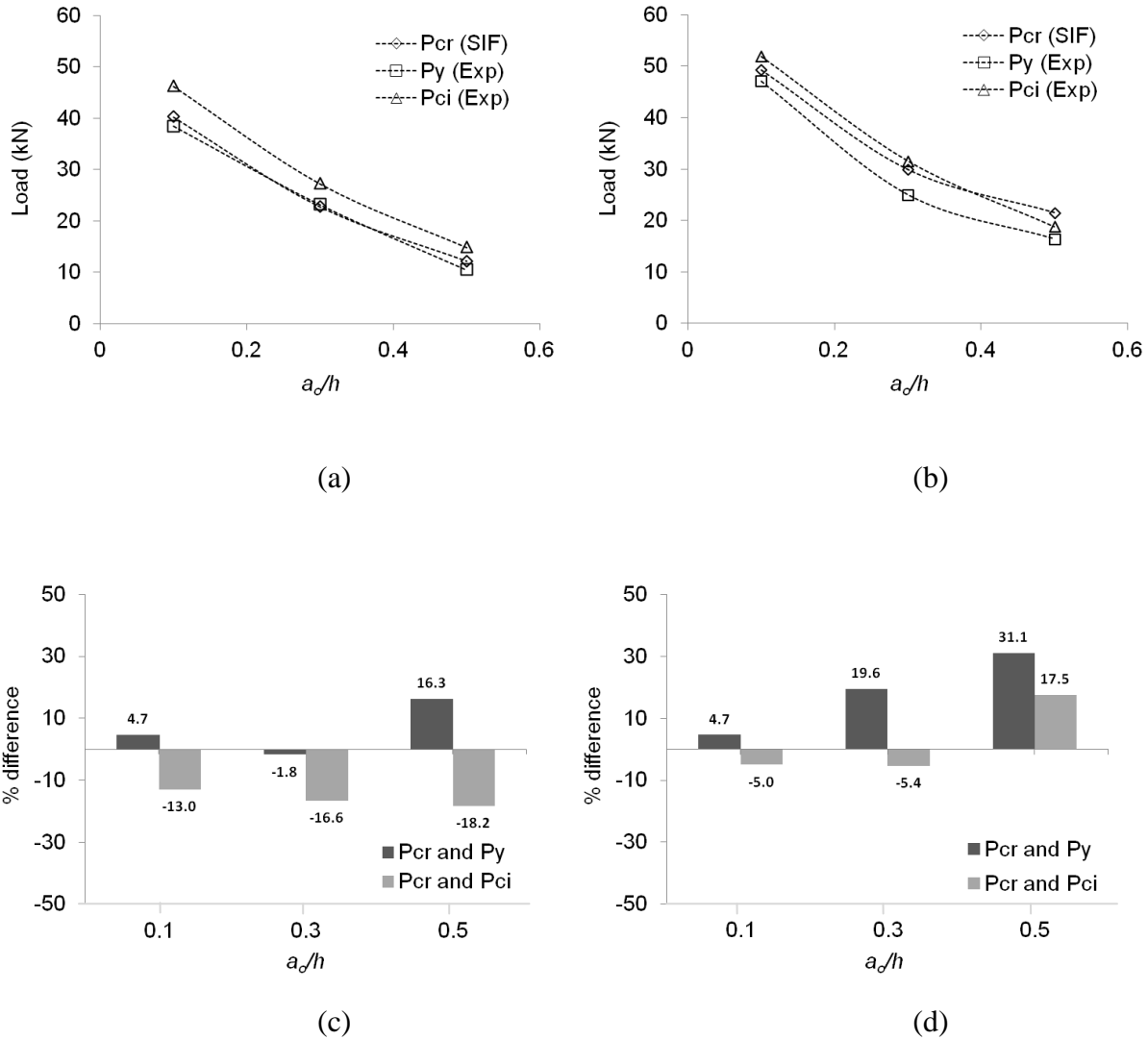


Fig. 6.10. Comparison between the numerical prediction of the critical load (P_{cr}) using the proposed SIF solutions and other loads determined experimentally in Hmidan et al. (2011) : (a) loads for unrepaired beams; (b) loads for repaired beams; (c) % difference in loads for unrepaired beams; (d) % difference in loads for repaired beams

correlation. The experimentally measured value for fracture toughness will unequivocally increase the confidence in the calculated critical loads which result in a more accurate analogy.

The comparison between the experimentally measured results and the numerical prediction using the proposed SIF approach showed a relatively good agreement for both the unrepaired and CFRP-repaired beams. Consequently, the approach was further expanded to evaluate the SIF for the $W4 \times 13$ beams with initial crack lengths beyond what was used in the

experimental testing (i.e., $a_o/h = 0.7$ and 0.9) along with performing parametric analysis (to be discussed in the following section). Further, the same approach was used to develop accurate SIF solutions for mode I (K_I) by analyzing eight different W Shapes (to be discussed).

6.6.1.3. Correction factors including a parametric analysis

Figure 6.11 shows the calculated correction factors for $W4 \times 13$ beams performed on five a_o/h values (0.1 through 0.9, in steps of 0.2). The correction factor, Y , is determined by normalizing the calculated K_I with all other parameters: the applied remote stress and crack length for unrepaired beams as well as the applied remote stress, crack length, and CFRP properties and factors for the repaired beams. All calculated correction factors in this study are also listed in appendix A.

6.6.1.3.1. Effect of the initial crack length

Figure 6.11(a) compares the correction factors between the unrepaired and repaired beams, as described in the previous section (i.e., CFRP bonded to 73% of the tensile flange width, $\psi (A_c/A_s) = 0.005$, and $\eta (E_c/E_s) = 1.135$). For the unrepaired beams, it can be clearly seen that the correction factor dramatically increases as the initial crack depth increases. In contrast, the correction factor for the repaired beams increases slightly as the initial crack depth goes up to $a_o/h = 0.5$ then then decreases considerably with the increased crack length [Fig. 6.11(a)]. This observation is discussed and verified against the experimental findings when the SIF was compared for the first three a_o/h values: 0.1, 0.3, and 0.5. The trend where the efficacy of the CFRP repair is more pronounced when the initial damage increases seems to continue and become even more effective for a_o/h values higher than 0.5 (i.e. $a_o/h = 0.7$ and 0.9) [Fig. 6.11(a)]. For example, the decreases in correction factor arose from the constraining effect of CFRP repair

were 18.3%, 41.8%, and 93.5% for the beams having $a_o/h = 0.1, 0.5,$ and $0.9,$ respectively, as shown in Fig. 6.11(b).

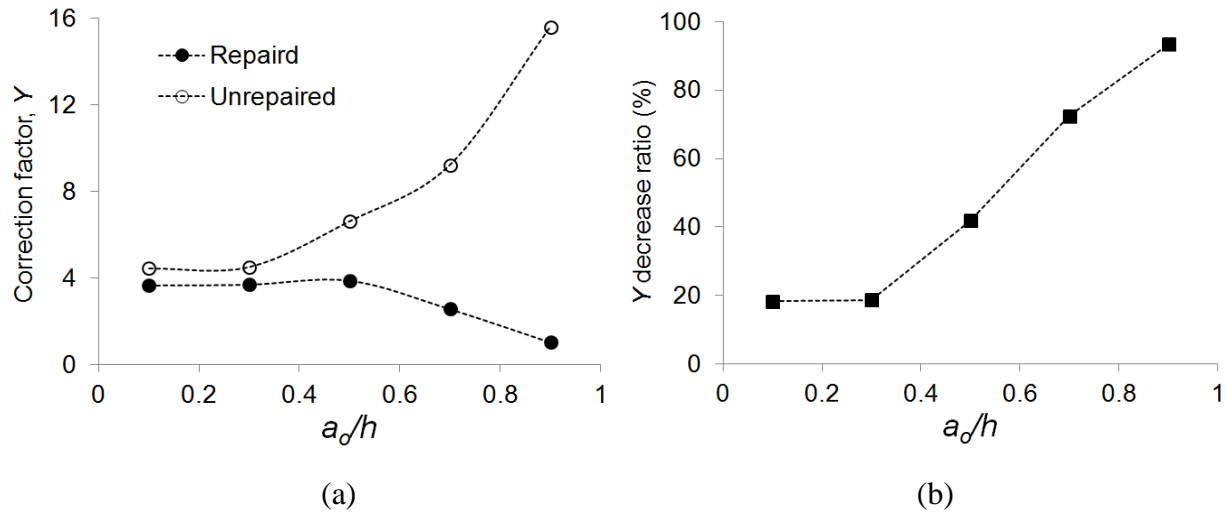


Fig. 6.11. Effect of repair on stress intensity correction factors for $W4 \times 13$ beams ($\psi = 0.005$ and $\eta = 1.135$): (a) comparison between unrepaired and repaired beams; (b) decrease of Y after repair

The noticeable reduction in SIFs (or correction factors) for the repaired beams having an a_o/h ratio higher than 0.5 can be explained by the decreased level of tensile stresses at the vicinity of the crack tip. When repaired, cracked I-beams are loaded in bending, as shown in Fig. 6.12(a), the overall SIF at the crack tip is a combination of two SIFs that have opposite influence: the applied external positive bending moment that tends to open the crack, resulting in increased tensile stresses (i.e., increase in K_I), and the opposite negative moment produced by the reaction load in CFRP laminate (which is a function of the applied external moment) that tends to cause compressive stresses ahead of the crack tip, which tends to close the crack and reduce K_I ahead of the crack tip (Ghafoori et al. 2012). Hence, for lower a_o/h ratios, the negative moment caused by the CFRP load on the uncracked ligament is insignificant, and only high tensile stresses caused by the external positive moment are in effect, causing high SIF values as shown in Fig. 6.12(b). Whereas for deeper cracks (i.e., high a_o/h ratios; [Fig. 6.12(c)]), the influence of the

negative moment introduced by the CFRP becomes more apparent which imposes the compressive stress field on the uncracked ligament opposite to the influence of the external moment, which reduces the tensile stresses ahead of the crack tip, thus lower K_I value. In other words, for repaired beams, the crack tip is located closer to the neutral axes when repairing beams with deeper cracks. It should be noted that a negative SIF suggests the presence of compressive stress ahead of the crack tip and has no physical meaning (Ghafoori et al. 2012). It is worth pointing out that the calculation of the SIF assumes that crack propagation is governed solely by the critical SIF value. In other words, it is assumed that the failure of CFRP-repaired beams will initiate at a critical load that causes the crack to grow before the CFRP failure. This prediction needs to be verified experimentally, for $a_o/h = 0.7$ and 0.9 in particular, which is outside the scope of this study.

6.6.1.3.2. Effect of the CFRP amount and modulus

To investigate the effect of the amount and modulus of CFRP on the SIF for the repaired beams, a parametric study is conducted to compare the results obtained from beams repaired with five different ψ values: 0.005 through 0.025, representing 1 to 5 layers of CFRP with a sheet thickness of 0.165 mm, respectively, that were analyzed at three different η values, 0.75, 1.135, and 1.5, representing three different CFRP moduli, 150, 227, and 300 GPa, respectively, as shown in Fig. 6.13. It can be easily observed that the correction factor decreases as the amount of CFRP increases with such influence becomes more pronounced as the initial damage (i.e., a_o/h) increases. In Fig. 6.13(a), for $\eta = 0.75$, for example, when the amount of CFRP increased from 0.005 to 0.010, the correction factor at $a_o/h = 0.1$ decreased by 10.9%, whereas the reduction in the correction factor increased to 51.2% for $a_o/h = 0.9$. This observation indicates that the increased amount of CFRP (i.e., a higher number of CFRP layers) becomes

more effective when the level of initial damage is high. Also, it is evident that the influence that the amount of CFRP has on the correction factor declines with increased CFRP thickness. For instance, at $a_o/h = 0.7$ [Fig. 6.13(a)], when the amount of CFRP increases from 0.005 to 0.010, the correction factor decreases by 40.7%, whereas the reduction for the correction factor dropped to 18.6% when the amount of CFRP increases from 0.020 to 0.025. Moreover, the increase for the amount of CFRP influenced the interaction between the crack length and the correction factor. This effect is more obvious for small a_o/h ratios ($a_o/h \leq 0.5$). In [Fig. 6.13(a)], for example, the correction factor increases by 19.9% as a_o/h increases from 0.1 to 0.5, whereas it decreases by 29.8% when ψ increases from 0.005 to 0.025, respectively. In other words, the effectiveness of the repair for beams having an initial crack length with $a_o/h \leq 0.5$ becomes more pronounced as the CFRP thickness increases. These observations anent the influence of the amount of CFRP on the correction factor seems to hold true, following a similar trend for repaired beams with higher η values (i.e., higher CFRP modulus) as shown in Figs. 6.13(b) and (c).

Figure 6.13(d) shows the effect of the CFRP modulus on the correction factor for the repaired beams compared to that of the unrepaired counterparts (only beams with $\psi = 0.005$ and 0.025 are shown for brevity). The reduced correction factor induced by the repair increased as the CFRP modulus increased. This effect, however, was influenced by the amount of CFRP where the reduced correction factor due to the increased stiffness was more pronounced for beams with low ψ -values. For beams with $\psi = 0.005$ and as the CFRP modulus increased from 150 to 300 GPa, the reduction in the correction factor increased by 72.2, 65.7, and 5.8% for beams having $a_o/h = 0.1, 0.5,$ and $0.9,$ respectively. Whereas for beams with $\psi = 0.025,$ the reduction in the correction factor increased by 52.7%, 23.4%, and 1.8% for beams having $a_o/h =$

0.1, 0.5, and 0.9, respectively. In addition, it was observed that the reduced correction factor due to the increased CFRP modulus became less significant as the initial crack increased. These observations indicated that the increase for the CFRP modulus was more effective in reducing the SIF at the crack tip as the number of CFRP layers and the level of initial damage decreased.

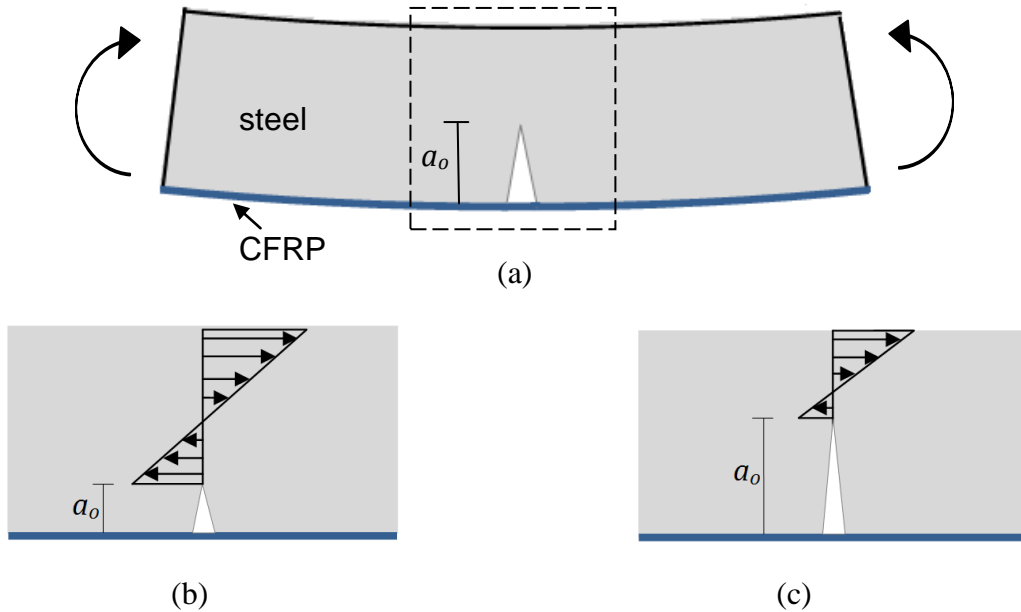


Fig. 6.12. Effect of crack length on strain distribution along the uncracked ligamen: (a) cracked beam repaired with CFRP under bending; (b) strain distribution when $a_o/h \leq 0.5$; (c) strain distribution when $a_o/h > 0.5$

6.6.1.3.3. Equation for correction factor Y

Figure 6.14 shows the correction factors for the CFRP-repaired beams subjected to bending moment with each surface corresponding to one CFRP modulus (also shown in 2-D plots in Figs. 6.13(a) through 6.13(c)). The effects for each of the three factors ($\zeta(a_o/h)$, ψ , and η) on the correction factor were discussed in the previous sections. Analyzing the results for the correction factor, Y , was performed using the response surface-regression analysis procedure (RSREG) of the Statistical Analysis System (SAS Institute, Inc., Cary, NC) and the fit model platform of JMP software (SAS Institute, Inc.). Initially, second and third-order response surface

models were fit and developed separately for all three surfaces in Fig. 6.14, where each surface represented the correction factors for one CFRP modulus. The six preliminary correction factor equations (three second-order and three third-order equations) were a function of two parameters: $Y(a_o/h, \psi)$. The third-order regression functions for the correction factor provided a better fit for curves with higher coefficient of determination (R^2) values and more parsimonious models. This conclusion was also consistent with the results obtained from the second and third-order response surface models for all three surfaces combined, as shown in Fig. 6.14, where the developed models for the correction factor were a function of the three parameters: $Y(a_o/h, \psi, \eta)$. Therefore, the third-order, response surface-regression model was used to generate the 17-term equation that best fitted the calculated correction factor, Y , for the CFRP-repaired $W4 \times 13$ beams, as follows:

$$Y(\zeta, \psi, \eta) = 4.88 + 12.04\zeta - 1.63\eta - 143.96\psi + 33.49\psi\eta - 511.26\zeta\psi - 5.53\zeta\eta + 3932.82\psi^2 + 0.58\eta^2 - 13.45\zeta^2 + 79.96\zeta\psi\eta - 833.9\psi^2\eta + 2667.62\zeta\psi^2 - 9.99\psi\eta^2 + 0.29\zeta\eta^2 + 356.5\zeta^2\psi + 3.9\zeta^2\eta \quad (6.11)$$

where the regression equation (Eqn. 6.11) was developed using a total of 75 data points with the following parameters ranges: five ζ (a_o/h) values (0.1, 0.3, 0.5, 0.7, and 0.9), five ψ (A_o/A_s) values (0.005, 0.010, 0.015, 0.020, and 0.025), and three η (E_o/E_s) values (0.75, 1.135, and 1.5). It should be noted that R^2 for the above regression equation was 0.9844. Montgomery (1984) indicated that R^2 represents the proportion of the variability in the data explained by the model. Hence, Eqn.6.11 can be used to calculate the correction factor Y required to determine the SIF for the repaired $W4 \times 13$ beams as expressed in Eqn. 6.3. Therefore, the static strength of the CFRP-repaired steel beams can be easily determined once the SIF is known. The adequacy of the third-order polynomial model shown in Eqn. 6.11 and all other regression models used in this study is explained through the panel of diagnostics as shown in appendix B.

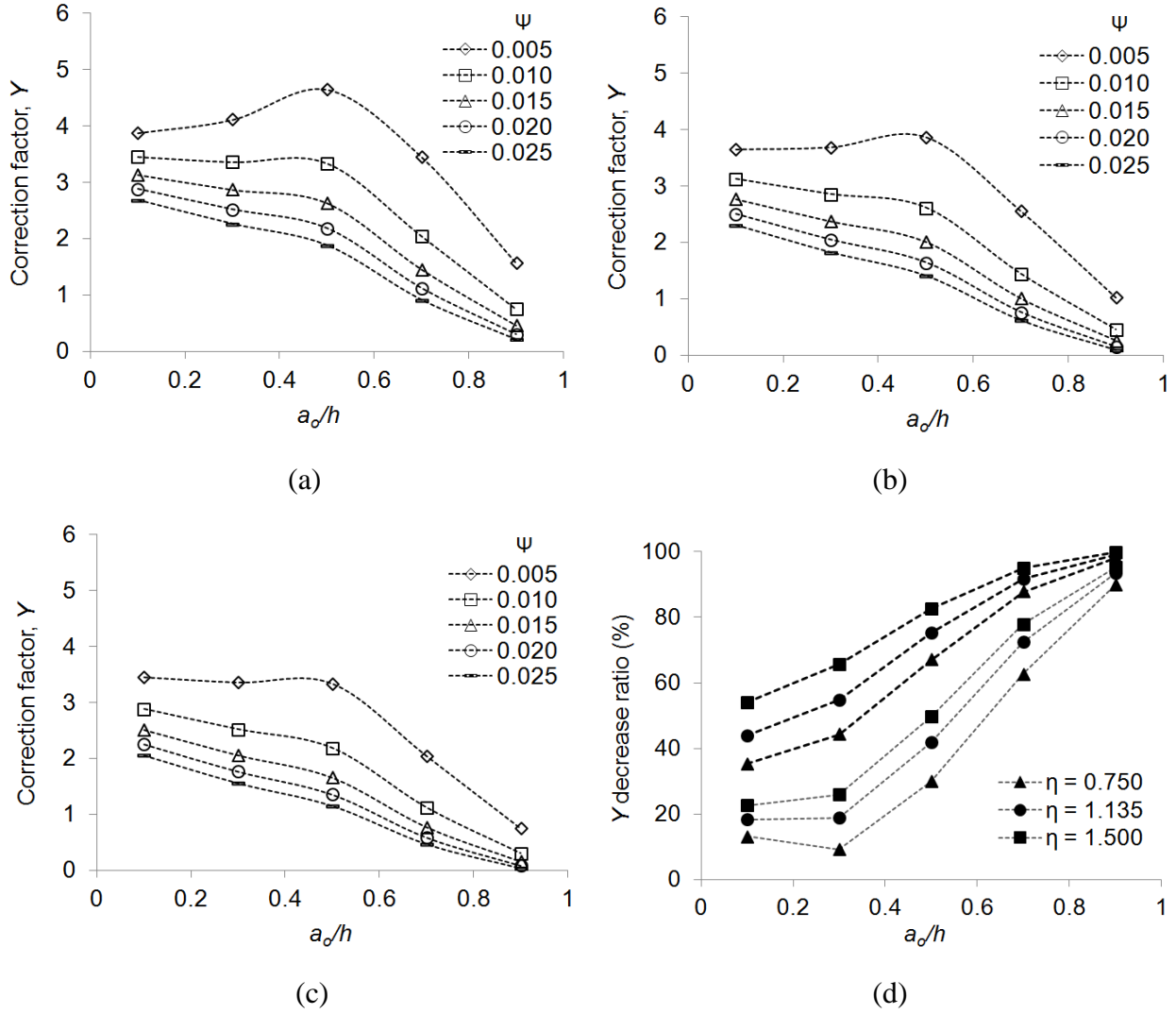


Fig. 6.13. Correction factors for CFRP-repaired W4 × 13 beams at various ψ values: (a) $\eta = 0.75$; (b) $\eta = 1.135$; (c) $\eta = 1.5$; (d) decrease of Y after repair at different η (faint for $\psi = 0.005$; dark for $\psi = 0.025$)

6.6.2. SIF for Cracked W Shapes with λ Ranging from 0.91 to 2.01

This section focuses on developing equations for the correction factor for unrepaired and CFRP-repaired, cracked W Shapes with λ values ranging from 0.91 to 2.01 (W18 to W40; identified by footnote 1 in Table 6.1). The equations for the correction factor are developed in a procedure similar to the one used for the W4 × 13 beams, as previously discussed.

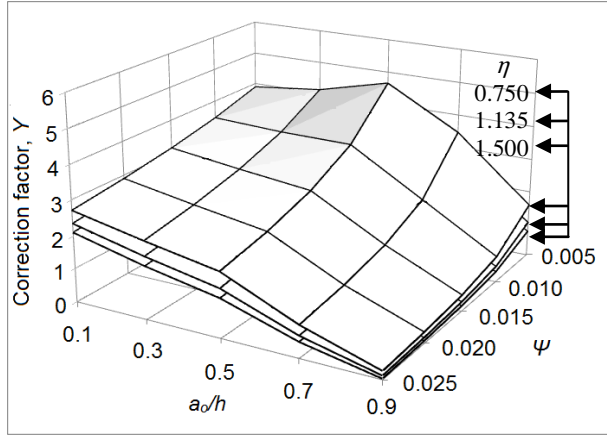


Fig. 6.14. Correction factors for CFRP-repaired W4 × 13 beams

6.6.2.1. Correction factors for unrepaired beams

To investigate the effect of the flange-to-web area ratio (λ) and the crack length ($\zeta = a_o/h$) on the correction factor for the unrepaired (Control) beams [Fig. 6.1(b)], a total of 40 finite element analyses were implemented with combinations of eight W Shapes where λ ranged from 0.91 to 2.01 and five ζ values ranged from 0.1 to 0.9. The results for the correction factors in 2-D and 3-D plots are shown in Figs. 6.15(a) and (b), respectively. The correction factor goes up as λ increases. This observation reveals that the SIF sensitivity increases for beams with a higher flange-to-web area ratio, λ . The greatest increase is observed at $a_o/h = 0.5$ and decreases for $0.5 < a_o/h < 0.9$ [Fig. 6.15(a)]. For example, when λ increases from 0.91 to 2.01, the correction factor increases by 71.8% at $a_o/h = 0.5$ while it only increases by 59.5% and 36.2% for $a_o/h = 0.1$ and 0.9, respectively. The crack length's influence on the correction factor is consistent for all W Shapes where the correction factor increases as the crack length increases [Fig. 6.15]. This increased correction factor becomes more significant for deeper cracks. For $\lambda = 1.38$, for example, the correction factor rises by 3.1% when a_o/h changes from 0.1 to 0.3, whereas the increase for the correction factor is 176.0% when a_o/h goes from 0.7 to 0.9. Therefore, the SIF

becomes more critical as the initial crack length increases, considerably reducing the static strengths of the cracked beam.

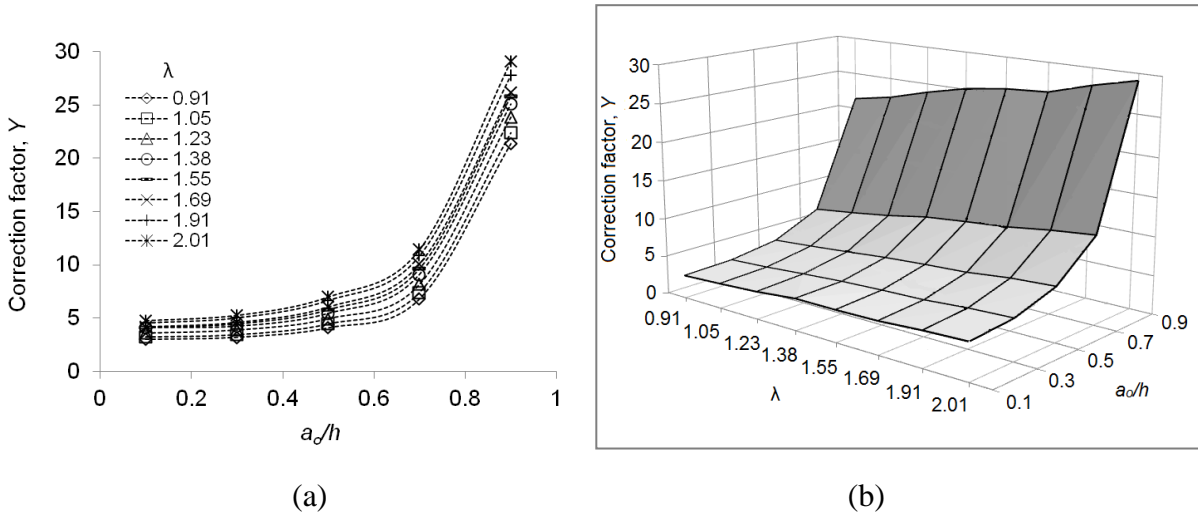


Fig. 6.15. Correction factors for unrepaired beams: (a) 2-D plot; (b) 3-D plot

6.6.2.1.1. Equation for correction factor Y

The following eight-term, third-order regression equation was found to be the best fit for the calculated correction factors:

$$Y(\lambda, \zeta) = 4.69 - 32.55\zeta + 2.83\lambda - 2.63\lambda\zeta - 0.36\lambda^2 + 47.12\zeta^2 - 0.06\lambda^2\zeta + 8.96\zeta^2\lambda \quad (6.12)$$

Eqn. 6.12 was generated using SAS software, as described previously, with R^2 value of 0.957.

Hence, Eqn. 6.12 can be used to calculate the correction factor, Y , required to determine the SIF for the unrepaired W Shapes as expressed in Eqn. 6.2. Therefore, the static strength for the unrepaired W Shapes with λ values ranging from 0.91 to 2.01 can be easily determined once the SIF is known.

6.6.2.2. Correction factors for repaired beams

To evaluate the effect of the flange-to-web area ratio (λ), crack length ($\zeta=a_o/h$), CFRP-to-steel area ratio ($\psi=A_c/A_s$), CFRP-to-steel stiffness ratio ($\eta=E_c/E_s$), and CFRP geometry on the correction factor for the repaired beams, a total of 1,200 cases were analyzed; the analysis

included various combinations of eight λ values (ranging from 0.91 to 2.01), five ζ values (ranging from 0.1 to 0.9), ten ψ values (five values ranging from 0.002 to 0.01 for Full-Flange geometry and five values ranging from 0.001 to 0.005 for Half-Flange geometry [Fig. 6.1(c) and (d)]), and three η values (0.75, 1.125, and 1.5) as summarized in Table 6.1.

6.6.2.2.1. Effect of the CFRP amount and modulus

The amount of CFRP influenced the correction factor in a trend similar to the one observed for the $W4 \times 13$ beam (described previously) where the correction factors decreased as ψ increased (i.e., as the number of CFRP layers increased), as shown in Figs. 6.16 and 6.18 for Full-Flange and Half-Flange geometries, respectively. Each surface corresponds to one CFRP-to-steel area ratio. It should be noted that the very top surface corresponds to the lowest ψ value and that the surface at the very bottom corresponds to the highest ψ value. The correction factors for the three η values (0.75, 1.125, and 1.5) are shown in Figs. 6.16(a), (b), and (c) for the Full-Flange geometry and in Figs. 6.18(a), (b), and (c) for the Half-Flange geometry.

Figure 6.17(a) shows the effect of the CFRP amount and modulus on the correction factors for the Full-Flange geometry of the repaired beams compared to the unrepaired beams (only selected cases are shown for brevity). Both the amount and modulus of the CFRP affected the SIF (or correction factor) for the repaired beams; the latter had a less pronounced influence. For beams with $\lambda = 0.91$ and at $a_o/h=0.5$, for example, the decrease in the correction factor changed from 35.4% to 70.2% when the amount of CFRP (ψ) increased from 0.002 to 0.010. This influence becomes less pronounced, specifically for an a_o/h higher than 0.5 (only changed by 5.1% at $a_o/h = 0.9$) [Fig. 6.17(a)]. The same figure shows the effect of the CFRP modulus on the correction factor where the greatest change in the correction factor was observed at $a_o/h = 0.5$ where the decrease in the correction factor changed from 35.4% to 41.9% as η increased from

1.125 to 1.5 for $\psi = 0.002$. A similar trend was observed for the repaired beams with $\psi = 0.004$. These observations revealed that the SIF sensitivity influenced by the number of CFRP layers more than the CFRP's elastic modulus. The same conclusion can be drawn about the Half-Flange geometry where the effect of the amount and modulus of CFRP on the correction factor followed a similar trend to the one observed for the Full-Flange geometry, as shown in Fig. 6.19(a).

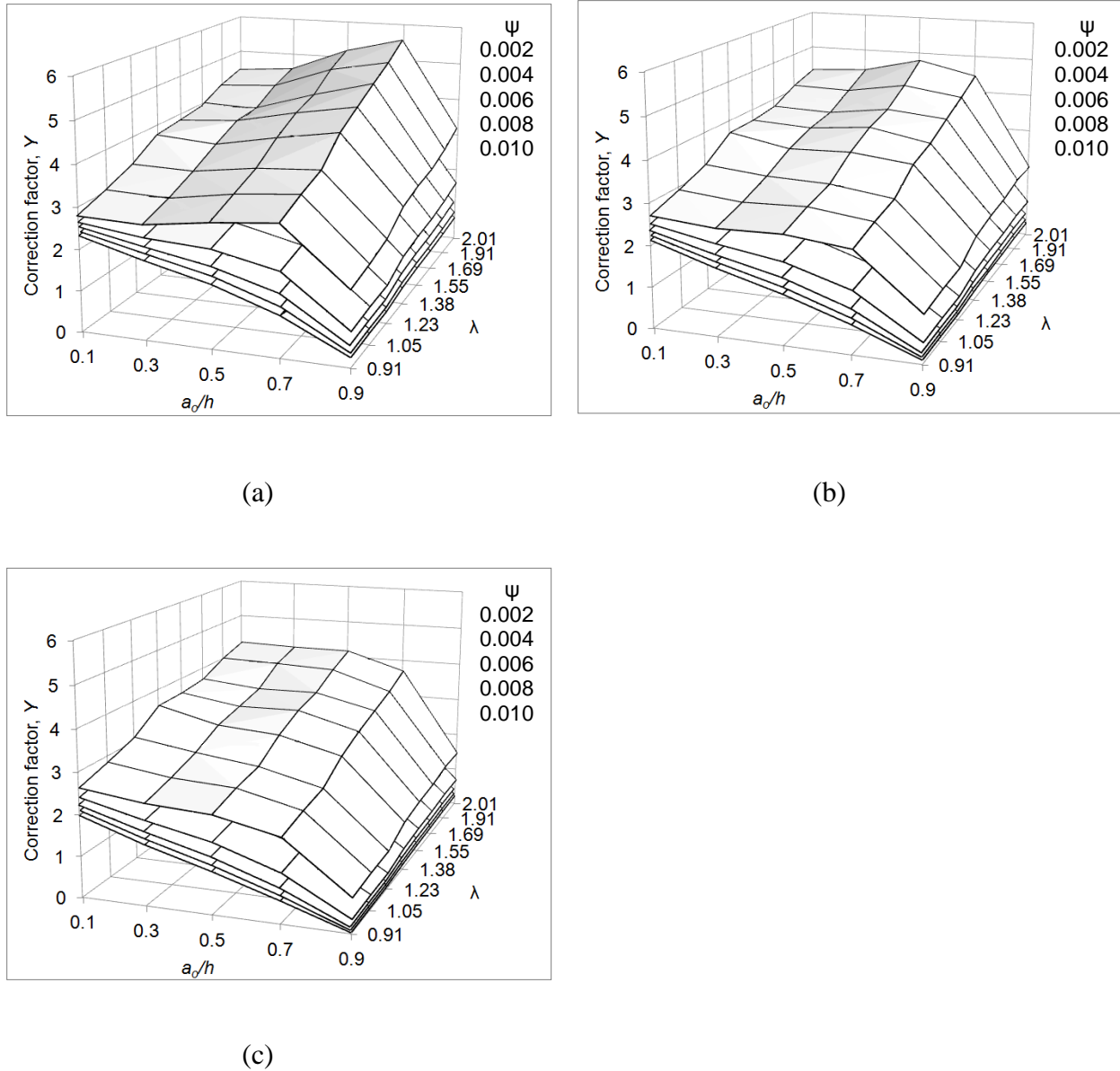


Fig. 6.16. Correction factors for repaired beams under Full-Flange geometry: (a) $\eta = 0.75$; (b) $\eta = 1.125$; (c) $\eta = 1.5$

6.6.2.2.2. Effect of the flange-to-web area ratio

Figure 17(b) compares the effect of the flange-to-web area ratio, λ , on the correction factors of the repaired beams compared to the unrepaired beams for Full-Flange (only selected cases are shown for brevity). The decreased correction factor after the CFRP repair was found to be nearly unaffected by the beams' flange-to-web area ratios, particularly for $0.5 < a_o/h < 0.5$ for beams with a low ψ value, and became negligible for beams with a high ψ value. At $\psi = 0.002$, for example [Fig. 17(b)], the differences for the decreased correction factor induced by the repair between beams with $\lambda = 0.91$ and 2.01 were 0.12%, 4.2%, and 1.3% for beams having $a_o/h = 0.1$, 0.5, and 0.9, respectively, where the differences dropped to 0.23%, 0.75%, and 0.64% for beams with $\psi = 0.010$. This negligible influence for the flange-to-web area ratio on the SIF becomes even more pronounced for beams under Half-Flange geometry as shown in Fig. 19(b). These observations indicated that the influence of CFRP repair on the SIF is consistent for all beams regardless of their flange-to-web area ratios.

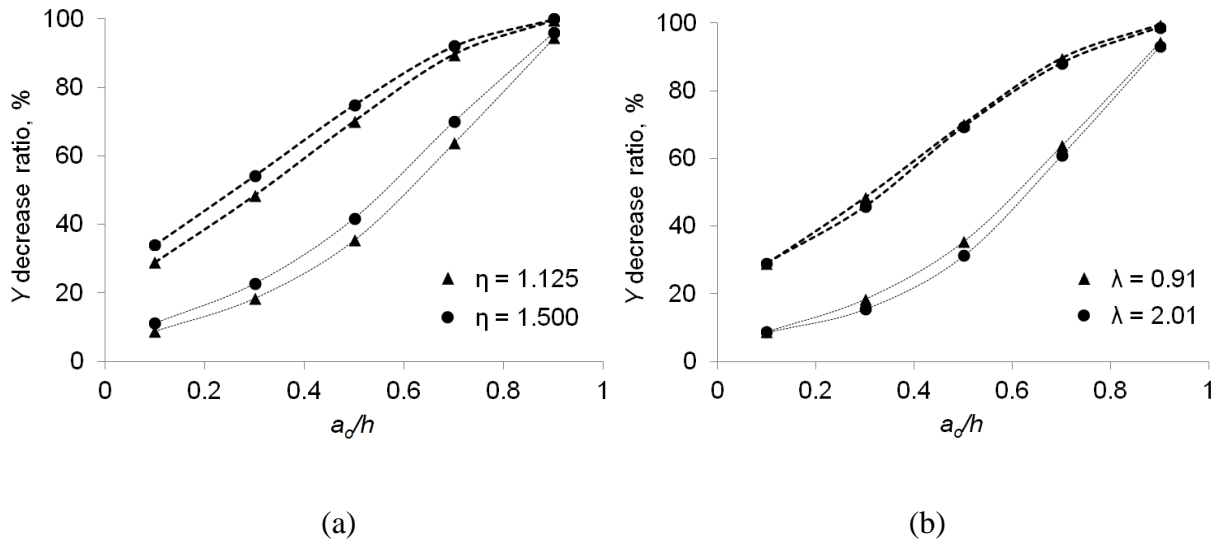


Fig. 6.17. Comparison for decrease of Y after repair under Full-Flange geometry (faint for $\psi = 0.002$; dark for $\psi = 0.010$): (a) effect of elastic modulus of CFRP ($\lambda = 0.91$); (b) effect of flange-to-web area ratio ($\eta = 1.125$)

6.6.2.2.3. Effect of geometry

Figure 6.20 shows a comparison between the Full and Half-Flange geometries at $\eta = 1.125$ (only selected cases are shown for brevity). The figure compares the effect of the geometry for two scenarios: the two geometries having the same CFRP thickness (i.e., same number of CFRP layers) and another case with the two geometries having the same ψ value. For the case of beams repaired with a similar number of CFRP layers (two layers of CFRP sheet thickness that are 0.165 mm), beams under Full-Flange geometry showed lower correction factors than the one under Half-Flange geometry as shown in Fig. 6.20(a). The decrease for the correction factors of the repaired beams under both geometries compared to the unrepaired beams with $\lambda = 0.91$ is shown in Fig. 6.20(b). Although an insignificant difference was observed, it can easily be seen that beams repaired under the Half-Flange geometry decreased the correction factor at a lower rate than of beams under the Full-Flange geometry. This observation is not unpredictable because the beams repaired under the Full-Flange geometry provide a crack-bridging force along the full width of the tensile flange, whereas crack-closure force is only concentrated at the middle half of the tensile flange for the Half-Flange geometry. Hence, for strengthened beams having similar CFRP thicknesses, and although an insignificant difference was observed, the efficiency of the CFRP repairs under the Full-Flange geometry is more pronounced through reducing the SIF than the beams under Half-Flange geometry. On the other hand, the efficiency of the CFRP repair under the Half-Flange geometry is more pronounced than the beams repaired under the Full-Flange geometry for beams having similar ψ values ($\psi = 0.004$ in this case; two layers of CFRP sheet thickness that are 0.165 mm for Full-Flange geometry and 4 layers for Half-Flange geometry) as shown in Fig. 6.20. For beams with $\lambda = 0.91$ [Fig. 6.20(b)], for example, the decrease in the correction factors after the repair under Half-Flange geometry at

$a_o/h = 0.1$ is 62.5% in comparison to that of the unrepaired beams, whereas it is 51.2% for repaired beams under Full-Flange geometry. This finding indicates that the concentration of CFRP material along and closer to the center of the cracked tensile flange shows more influence in reducing the SIF than spreading the repair material further away, covering the full width of the flange.

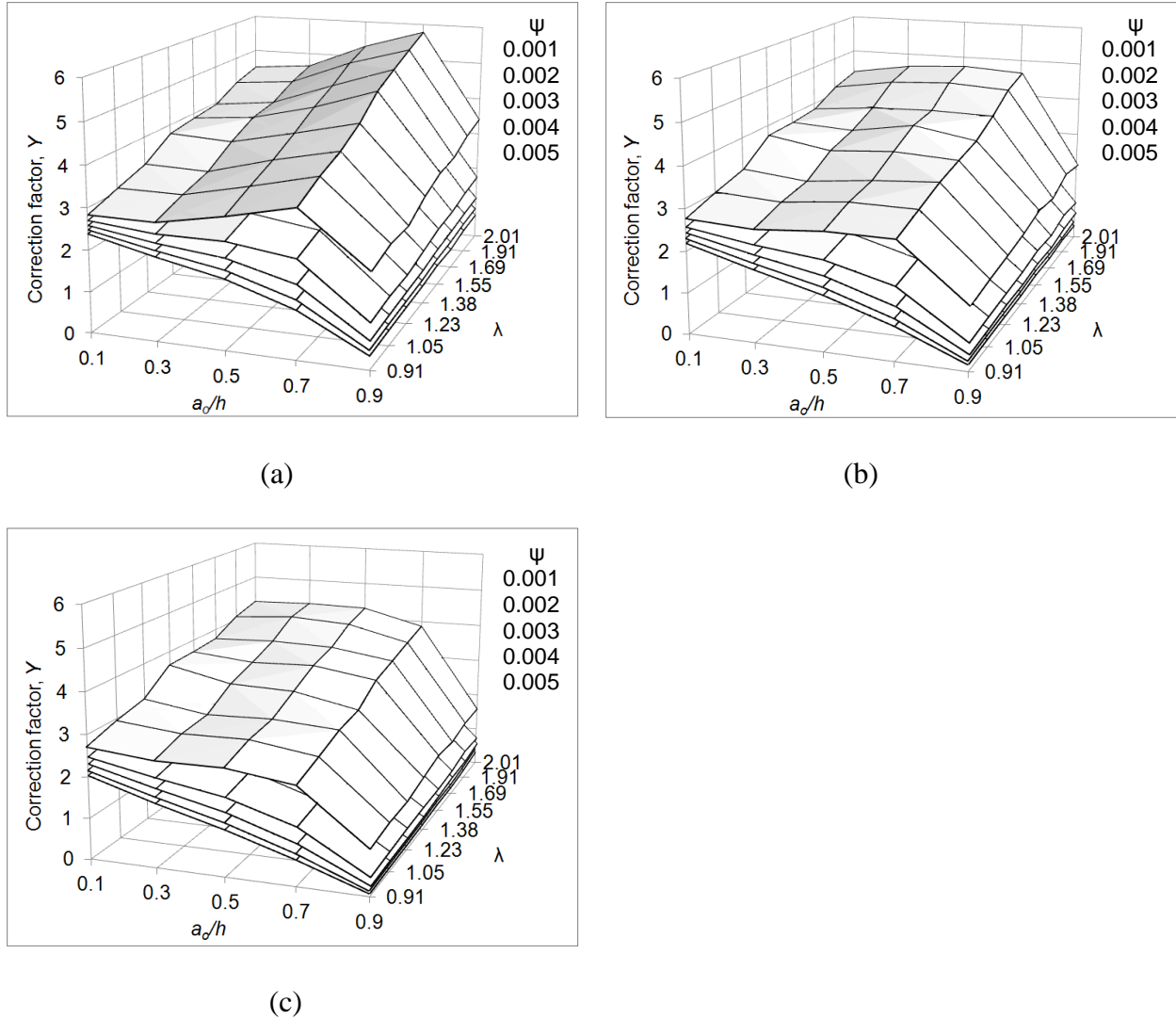


Fig. 6.18. Correction factors for repaired beams under Half-Flange geometry: (a) $\eta = 0.75$; (b) $\eta = 1.125$; (c) $\eta = 1.5$

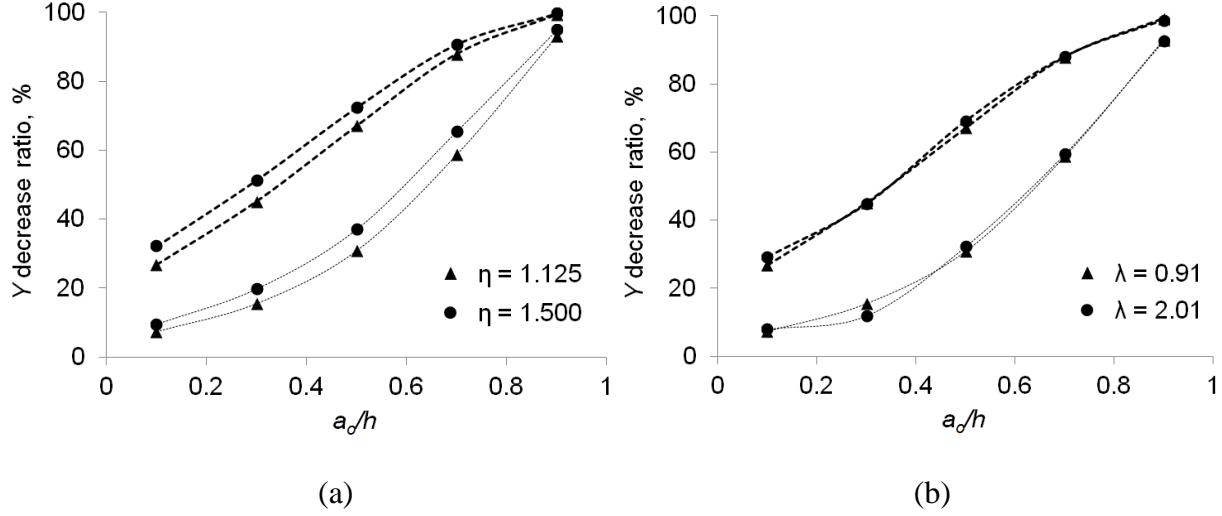


Fig. 6.19. Comparison for decrease of Y after repair under Half-Flange geometry (faint for $\psi = 0.001$; dark for $\psi = 0.005$): (a) effect of elastic modulus of CFRP ($\lambda = 0.91$); (b) effect of flange-to-web area ratio ($\eta = 1.125$)

6.6.2.2.4. Equation for correction factor Y

Equations for the correction factor for repaired beams were developed for both geometries; Full and Half-Flange. Analyzing the results for correction factor Y was performed using the response surface-regression analysis procedure of SAS (as previously discussed). The 17-term third-order regression equation for the correction factor of the repaired beams is as follows:

$$\begin{aligned}
 Y(\zeta, \lambda, \psi) = & c_1 + c_2\zeta + c_3\lambda + c_4\psi + c_5\psi\lambda + c_6\zeta\psi + c_7\zeta\lambda + c_8\psi^2 + c_9\lambda^2 + c_{10}\zeta^2 + \\
 & c_{11}\zeta\lambda\psi + c_{12}\psi^2\lambda + c_{13}\zeta\psi^2 + c_{14}\psi\lambda^2 + c_{15}\zeta\lambda^2 + c_{16}\zeta^2\psi + c_{17}\zeta^2\lambda
 \end{aligned} \quad (6.13)$$

where the regression equation [Eqn. 6.13] was developed using a total of 200 data points for each η value of each geometry (a total of 1,200 data points) with the following parameters ranges: eight λ values (ranging from 0.91 to 2.01), five ζ values (ranging from 0.1 to 0.9), ten ψ values (five values ranged from 0.002 to 0.01 for the Full-Flange geometry and five values ranged from 0.001 to 0.005 for the Half-Flange geometry), and three η values (0.75, 1.125, and 1.5). The

curve-fitting coefficients (c_1 through c_{17}) in Eqn. 6.13 and the R^2 for each case are listed in Table 6.2. Hence, Eqn.6.13 can be used to calculate the correction factor, Y , required to determine the SIF for the repaired beams as expressed in Eqn. 6.3. Therefore, the static strength of the CFRP-repaired steel beams can easily be determined once the SIF is known.

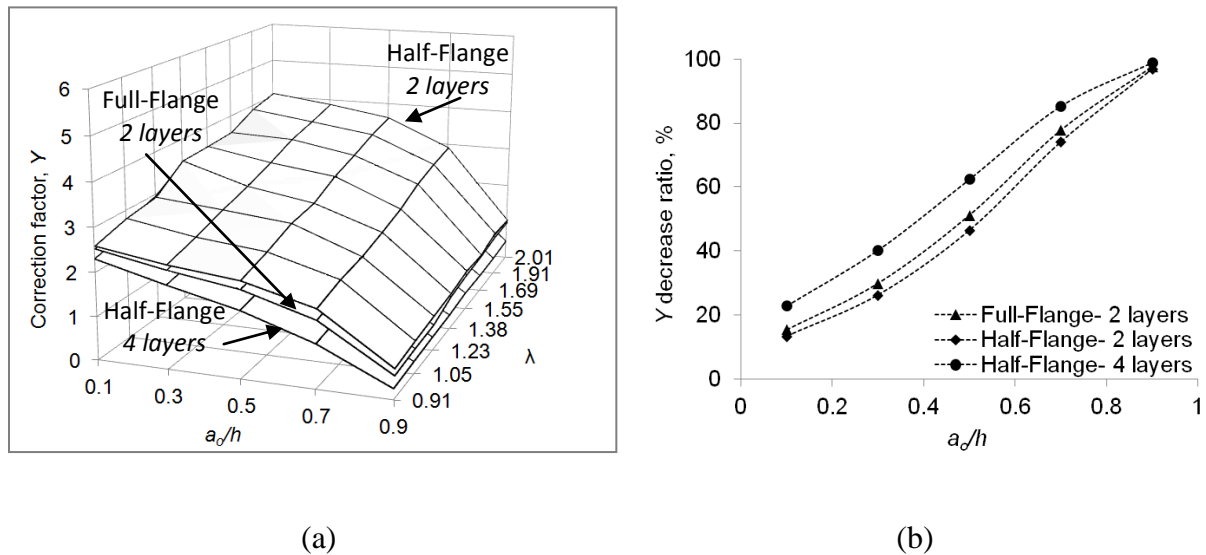


Fig. 6.20. Comparison of correction factors for repaired beams under Full and Half-Flange geometries for $\eta = 1.125$: (a) correction factors for Full-Flange at $\psi = 0.004$ (2 layers) and Half-Flange at $\psi = 0.002$ (2 layers) and 0.004 (4 layers) (b) decrease of Y after repair for beams with $\lambda = 0.91$

6.7. Summary and Conclusions

This study has presented the fracture response of unrepaired and CFRP-repaired cracked steel I-beams subjected to pure bending by evaluating the stress intensity factors (SIFs) of mode I (K_I) at the crack tip. SIF solutions were proposed for both unrepaired and CFRP-repaired beams by analyzing a total of 1,240 cases, including various combinations of the flange-to-web area ratio (eight different W Shapes), crack length, CFRP-to-steel area ratio, and CFRP-to-steel stiffness ratio as well as CFRP geometry. The following is concluded:

Table 6.2. Coefficients for regression equations for correction factor for beams with λ ranging from 0.91 to 2.01

Coefficient	Full-Flange			Half-Flange		
	η			η		
	0.75	1.125	1.5	0.75	1.125	1.5
c_1	0.26	0.65	0.87	0.16	0.84	0.69
c_2	4.37	3.21	2.48	5.72	4.48	3.65
c_3	2.18	2.01	1.95	2.07	1.52	2.14
c_4	211.78	138.27	59.03	272.72	111.82	85.09
c_5	-53.98	-94.37	-107.88	-88.74	-25.46	-148.50
c_6	-1393.84	-1218.76	-1042.38	-1516.15	-1352.67	-1161.49
c_7	2.32	1.69	1.00	1.96	1.52	0.67
c_8	-18930.00	-12166.00	-3757.25	-20518.00	-10746.00	-903.73
c_9	-0.29	-0.17	-0.13	-0.21	0.02	-0.20
c_{10}	-3.01	-2.88	-2.71	-3.41	-3.28	-2.97
c_{11}	-163.31	-104.23	-60.94	-140.74	-53.41	-0.79
c_{12}	8999.36	10289.00	7704.27	8445.87	7856.95	6121.60
c_{13}	62279.00	42164.00	29930.00	70234.00	46901.00	30528.00
c_{14}	-19.91	-18.29	-10.49	-10.14	-38.34	4.04
c_{15}	0.47	0.37	0.29	0.40	0.28	0.37
c_{16}	637.47	749.62	731.56	583.85	716.72	726.77
c_{17}	-3.48	-3.18	-2.59	-3.19	-3.16	-2.84
R^2	0.9641	0.9791	0.9859	0.9562	0.9772	0.9813

- The SIFs of the unrepaired beams were significantly affected by the level of initial damage (i.e., initial crack length). The crack length's influence on the SIF was consistent for all W Shapes where the SIF increased as the crack length increased and became significantly critical for very deep cracks, indicating a considerable reduction in the static strengths of the cracked beams.
- The SIF sensitivity for unrepaired beams increased as the flange-to-web area ratio of beams increased with the greatest increase observed at $a_o/h = 0.5$ and decreased for $0.5 < a_o/h < 0.5$.

- The SIFs for the CFRP-repaired beams were significantly decreased compared to the unrepaired counterparts due to the crack-bridging force at the crack location. Efficiency of the CFRP repair was more pronounced when the damage level increased.
- The SIFs for the repaired beams were affected by the amount (i.e., number of CFRP layers) and elastic modulus of the CFRP. The amount of CFRP had the greatest influence in reducing the SIF for repaired beams. However, the rate of SIF reduction for the repaired beams decreased as the CFRP thickness increased. Also, the SIFs were reduced as the CFRP modulus increased. This effect, however, was influenced by the amount of CFRP where the SIF reduction due to the increased CFRP modulus was more pronounced as the CFRP thickness decreased. In addition, it was observed that the reduction for the correction factor due to the increased CFRP modulus became less significant as the initial crack increased. These observations indicated that the increased CFRP modulus was more effective in reducing SIF at the crack tip as the number of CFRP layers and the level of initial damage decreased.
- An insignificant influence of the CFRP geometry on the SIF of repaired beams was observed when similar CFRP thicknesses were used for Full and Half-Flange geometries. However, the efficiency of the CFRP repair under the Half-Flange geometry was more pronounced compared to beams repaired under the Full-Flange geometry when the CFRP-to-steel area ratio was similar in both geometries. In other words, the concentration of CFRP material along and closer to the center of the cracked tensile flange (as in the case of the Half-Flange geometry) showed more influence in reducing the SIF than spreading the repair material further away, covering the full width of the flange (as in the case of the Full-Flange geometry).

- The influence of CFRP repair on the SIF was found to be consistent for all eight W Shapes and was nearly unaffected by the flange-to-web area ratio.
- The proposed SIF equations are applicable to commercially available standard steel W Shapes used in civil engineering applications ranging from W18 to W40 subjected to bending load.
- The analysis of the CFRP-repaired cracked steel beams assumed perfect bond between the CFRP and steel and that the failure of the repaired beams initiate at a critical load that causes the crack to grow before the CFRP failure. Therefore, the static strength of the CFRP-repaired steel beams can easily be determined once the SIF is known.

CHAPTER 7. CONCLUSIONS AND RECOMMENDATIONS

7.1. Introduction

This study presented a modern strengthening application using carbon-fiber-reinforced polymer (CFRP) sheets for the rehabilitation of damaged steel members, including the strengthening of single-edge notched steel specimens and structural steel I-beams. In this research, both experimental and computational investigations were carried out. Generally, the study undeniably demonstrated the significant potential of this retrofitting technique as an alternative to conventional repair materials. The study's conclusions and the recommendations for current research needs are presented in the following sections.

7.2. Summary and Conclusions

7.2.1. Steel Elements Strengthened with CFRP

Chapter 3 presented a computational method to study the response of cracked steel members strengthened with carbon-fiber-reinforced polymer (CFRP) composite sheets that were subjected to axial tension. Of interest were the bond behavior and fracture characteristics of the CFRP sheets bonded to the steel surface as well as the interaction between the local response of CFRP sheets and the cracked steel elements with various crack properties. Such an investigation will eventually be used to understand the global behavior of damaged flexural steel members strengthened with CFRP sheets. A modeling approach to simulate debonding of the CFRP sheets and crack propagation of the steel was proposed. This approach was incorporated in a three-dimensional finite element analysis (FEA) model and was validated with experimental data. Investigation parameters included the level of initial damage to the members (i.e., notch size) and the amount of CFRP reinforcement. The strengthening effect was noticeable when the level of initial damage increased. The crack-propagation rate of the strengthened members was

dependent upon the debonding characteristics of the CFRP and the size of the initial damage. CFRP-strengthening resulted in significant improvement in energy release rate, including moderate increases in the J integral as a fracture parameter. Overall, the interaction between the level of initial damage and the amount of CFRP was substantial for the strengthened members.

7.2.2. CFRP-Repair of Steel Beams

Fatigue fracture of steel-girder bridges is a critical consideration. Hysteretic loads can initiate cracks near the lower flange of a member that propagate up the web. The load-carrying capacity of such a member is, therefore, significantly dependent upon the level of damage.

Chapter 4 presented an experimental and numerical investigation to study the behavior of CFRP-repaired steel beams having various notch depths that represent the level of initial damage. Particular attention was paid to the interaction between the level of initial damage (i.e., notch depth) and CFRP repair. A novel modeling approach using FEA was proposed; it simultaneously accounted for crack propagation across the steel section and debonding of the CFRP. The serviceability and load capacity of the repaired beams were significantly affected by the level of initial damage (i.e., notch size). The efficacy of the CFRP repair was more pronounced when the damage level increased. The CFRP sheet stabilized the crack mouth opening displacement (CMOD) of repaired beams, and the linearity of the CMOD was improved until significant debonding took place. The level of the initial damage affected the behavior of a plastic region above the notch tip, the rate of web fracture, and the initiation of CFRP debonding. The initiation of CFRP debonding was affected by the level of initial damage, however, its contribution to the debonding behavior was not significant once the CFRP was completely debonded in the vicinity of the damage location. The failure mode of CFRP-strengthened beams was found to be independent of the degree of initial damage. A crack-path independent fracture

mechanics method was used to evaluate the energy release rate of the repaired beams. The results from this fracture-based approach supported the efficacy of this repair method. The proposed modeling approach predicted well the flexure of the experimental beams.

7.2.3. Durability of the CFRP-Repair for Steel Beams

In addition to the applied loads, bridges are usually exposed to various weathering conditions, such as water, temperature, humidity, and other corrosive environments. It is important to investigate the durability of the bonded FRP-steel system to ensure adequate long-term performance. Inconclusive predictions regarding the long-term durability and performance aspects of the FRP-steel system is a concern and an obstacle to the rapid expansion of utilizing FRP materials to retrofit steel structures.

Chapter 5 presented an experimental program to examine the residual behavior of notch-damaged steel beams strengthened with CFRP sheets that were subjected to typical long-term load configurations for 7,000 hours in cold regions. Test parameters included different levels of sustained load and cold temperatures as low as -30°C . Emphasis was given to flexural responses such as load-carrying capacity, stiffness variation, energy dissipation, crack mouth opening displacement, failure mode as well as the behavior of the CFRP-steel interface. Test results showed that the sustained loads significantly influence the load-carrying capacity of the beams due to the presence of creep damage near the crack-tip field above the notch. Cold temperature also affected the capacity and flexural stiffness of the beams. A crack-bridging effect by the bonded CFRP was noted near the crack mouth of the strengthened beams; however, this effect decreased when the long-term load was applied. CFRP debonding consistently governed the failure of the strengthened beams, irrespective of the degree of temperature exposure. Local CFRP rupture was observed near the notch location for beams subjected to a high level of

sustained loads due to the combination of stress concentrations and the fibers' creep damage. Interfacial stresses along the CFRP-steel interface were controlled by the sustained loads. Cold temperatures resulted in a reduced interfacial slip of the CFRP while the temperature effect appeared to be insignificant for the magnitude of bond stress. Stress redistribution along the CFRP-steel interface was noticed because of the long-term load.

7.2.4. SIF for Structural Steel I-Beams Strengthened with CFRP

Research showed that damaged steel beams that were repaired with CFRP sheets illustrated the need for a failure criterion to predict critical loads and to ensure the safety of the repaired members. Because the failure of such beams ultimately involves crack propagation assisted by local stress intensities, some researchers examined the fracture mechanics path to the problem by utilizing the elastic and fracture-material properties.

Chapter 6 presented a numerical method to evaluate the stress intensity factor (SIF) for structural single-edge cracked steel I-beams repaired with CFRP composites and subjected to bending loads. The static strength of the CFRP-repaired steel beams can easily be determined once the SIF is known. The objective of the study was to use the finite element method to develop an accurate SIF for mode I (K_I) solutions for the unstrengthened and CFRP-strengthened beams. The study's focus was to investigate the effect of material and geometric properties on the SIF. A total of 1,240 cases were analyzed, including various combinations of the flange-to-web area ratio (eight different W Shapes), crack length, CFRP geometry, CFRP-to-steel area ratio, and CFRP-to-steel stiffness ratio. Results showed that the K_I for the strengthened beams was significantly influenced compared to the unstrengthened counterparts due to the crack-bridging force at the crack location. Efficiency for the CFRP repair was more pronounced when the damage level (i.e., crack depth) increased. The SIF for the strengthened beams was influenced by

the geometry and amount of CFRP as well as the CFRP-to-steel stiffness ratio. The validity of the numerical results and the proposed regression models for SIF were examined with comparison to the experimental results.

7.3. Recommendations for Future Research

While the present dissertation investigated the crack-dependent response of steel beams strengthened with CFRP composite materials, additional research work is needed to cover a number of topics that were identified during this study:

- The proposed fracture-mechanics-based approach (the stress intensity factor (SIF) equations for W Shapes) only focused on predicting the static strength of the CFRP-strengthened beams. More general predictive equation for the ultimate flexural loads should be proposed based on the elastic-plastic fracture mechanics (EPFM), such as the J integral concept.
- The proposed SIF predictive equations, based on linear-elastic fracture mechanics (LEFM), assumed a perfect bond between the CFRP and steel. When EPFM is used, the FEA model that is needed to develop such predictive equations should be improved by considering crack propagation across the critical section of the steel beams repaired with CFRP and also the debonding progression of the CFRP sheet.
- The current FEA models and the proposed predictive equations focused on studying beams containing cracks in the constant moment region where shear forces are zero. However, in many cases, beams are subjected to a combination of bending moment, shear forces, and axial forces. Therefore, additional research is needed to address these gaps.
- The proposed FEA model predicted the load-deflection responses of beams up to their ultimate load-carrying capacity. A more complete FEA model should be developed to

predict the full load-deflection responses of the CFRP-strengthened steel beams including the descending branch (post-peak region).

- The bilinear bond-slip relationship used to model the interfacial behavior between CFRP and steel in the constructed FEA model was developed based on a simple pull-out test that was found in the literature. This bond-slip relationship is not very accurate because it cannot account for the bending effect in a beam application that consists of a combination of shear and normal stresses along the CFRP-steel interface. Therefore, further research is needed to develop a more accurate bond-slip response to better understand and model the interfacial behavior (i.e., debonding progression) between the CFRP and steel in bending.
- The effect of a sustained load combined with cold temperatures on the damaged steel beams that were strengthened with CFRP sheets was experimentally investigated in this study. The residual strengths of beams underwent cold temperature exposure were obtained by testing the beams at room temperature. However, testing when the beams are subjected to the cold temperatures may result in a different response. Also, an analytical and/or numerical model should be developed to predict the behavior of these beams.
- The experimental results obtained from this study were used to validate the accuracy of the proposed SIF equations to predict the static strength of CFRP-repaired beams. Because only one W Shape was considered for the experimental program while the proposed equations cover a wide range of W Shapes, additional experimental work should be conducted on a broad range of W shapes to verify the applicability of these predictive equations.

- Further research is needed to evaluate the effect of other environmental loads, such as wet-dry cycles, and other physical loads, such as fatigue, on the long-term performance of a CFRP-steel strengthening system.

REFERENCES

- Al-Saidy, A.H., Klaiber, F.W., and Wipf, T.J. 2004. Repair of steel composite beams with carbon fiber-reinforced polymer plates, *Journal of Composites for Construction*, 8(2), 163-172.
- Albrecht, P., Lenwari, A., and Feng, D. 2008. Stress intensity factors for structural steel I-beams. *Journal of Structural Engineering*, ASCE, Vol. 134, No. 3, 421-429.
- Al-Emrani, M., Linghoff, D., and Kliger, R. 2005. Bonding strength and fracture mechanisms in composite steel-CFRP elements. *Proceedings of the International Symposium on Bond Behavior of FRP in Structures*. Hong Kong, China, December 7-9: 433-441.
- Andresen, H.W., and Echtermeyer, A.T. 2006. Critical energy release rate for a CSM reinforced carbon fiber composite/steel bonding. *Composites: Part A*, 37, 742-751.
- Anderson, T. L. 2005. *Fracture mechanics – fundamentals and Applications*, third edition, CRC, Taylor & Francis Group, New York, USA.
- ASCE. 2009. Report card for America's infrastructure, American Society of Civil Engineers, Reston, VA.
- ASCE. 2013. Report card for America's infrastructure, American Society of Civil Engineers, Reston, VA.
- American Concrete Institute (ACI). 2007. Report on fiber reinforced polymer (FRP).
- ANSYS. 2010. ANSYS online manual, Canonsburg, PA, USA.
- Bakis, C.E., Bank, L.C., Brown, V.L., Cosenza, E., Davalos, J.F., Lesko, J.J., Machida, A., Rizkalla, S.H., and Triantafillou, T.C. 2002. Fiber-reinforced polymer composites for construction-state-of-the-art review, *Journal of Composites for Construction*, 6(2), 73-87.

- Bank, L.C., and Gentry, T.R. 1995. Accelerated test methods to determine the long-term behavior of FRP composite structures: environmental effects, *Journal of Reinforced Plastics and Composites*, 14, 559-587.
- Baker, A.A., Rose, L.R.F., and Jones, R. 2002. *Advances in the bonded composite repair of metallic aircraft structure*. Elsevier Ltd.; Amsterdam, the Netherlands.
- Bakht, B., Sweeney, R. A. P., Saunders, W. W., Yule, R. B., Byers, W. G., Mosese, F., McKeel, W. T., Higgins, M., Kahn, L., and Heins, C. P. 1979. *Repair and strengthening of old steel truss bridges*. American Society of Civil Engineers, New York.
- Barsom, J.M., and Rolfe, S.T., 1970. Correlations between K_{IC} and Charpy V-Notch test results in the transition-temperature range. *Impact Testing of Metals*, ASTM STP 466, American Society for Testing and Materials, Philadelphia, pp 281-302.
- Barsoum, R.S. 1976. On the use of isoparametric finite elements in linear fracture mechanics. *International Journal for Numerical Methods in Engineering*, Vol. 10, 25-37.
- BASF. (2007) MBrace[®] CF130 Unidirectional high strength carbon fiber fabric for the MBrace composite strengthening system, BASF Construction Chemicals, Shakopee, MN, USA.
- Bathe, K.J. 1996. *Finite element procedures*. Prentice Hall, New Jersey 07632.
- Belingardi, G., Goglio, L. and Tarditi, A. 2002. Investigating the effect of spew and chamfer size on the stresses in metal/plastics adhesive joints. *International Journal of Adhesion & Adhesives*, 22, 273-282.
- Bhatti, A. M. 2006. *Advanced topics in finite element analysis of structures*. Hoboken, NJ: John Wiley and Sons.
- Blake, A. 1996. *Practical Fracture Mechanics in Design*, Marcel Dekker, Inc., USA.

- Bocciarelli, M., Colombi, P., Fava, G., Poggi, C. 2009. Fatigue performance of tensile members strengthened with CFRP plates. *Composite Structures*; 87:334–43.
- Boresi, A. P. and Schmidt, R. J., 2003. *Advanced mechanics of materials* (6th Edition), John Wiley & Sons, Inc., Hoboken, NJ.
- Bourban P. E., Mcknight S. H., Shulley S. B., Karbhari V. M. and Gillespie J. W. 1994. Durability of steel/composites bonds for rehabilitation of structural components. *Infrastructure: New Materials and Methods of Repair: Proceedings of the 3rd Materials Engineering Conference*, San Diego, CA, USA, 29.
- Brockenbrough, R.L., and Frederick, S.M. 2006. *Structural steel designer's handbook: AISC, AASHTO, AISI, ASTM, AREMA, and ASCE-07 design standards*. McGraw-Hill construction series, University of Michigan.
- Cadei, J.M.C., Stratford, T.J., Hollaway, L.C., and Duckett, W.G. 2004. Strengthening metallic structures using externally bonded fibre- reinforced polymers CIRIA C595, CIRIA, London, UK.
- Chacon, A., Chajes, M., Swinehart, M., Richardson, D. and Wenczel, G. 2004. Application of advanced composites to steel bridges: a case study on the ashland bridge (Delaware-USA). *Proceedings, Advanced Composite Materials in Bridges and Structures*, Calgary.
- Chen, X.G. 1992. Application of fracture mechanics to highway bridges. Ph.D. Dissertation, Department of Civil Engineering, University of Maryland, College Park, MD.
- Choi, K.K., MESHGIN, P., and Taha, M.M.R. 2007. Shear creep of epoxy at the concrete-FRP interfaces, *Composites Part B*, 38, 772-780.

- Colombi, P., Bassetti, A., and Nussbaumer, A. 2003. Analysis of cracked steel members reinforced by pre-stressed composite patch. *Fatigue and Fracture of Engineering Materials and Structures*, 26(1):59-67.
- Colombi, P., and Poggi, C. 2006. An experimental, analytical and numerical study of the static behavior of steel beams reinforced by pultruded CFRP strips, *Composites Part B*, 37, 64-73.
- Crasto, A.S. and Kim, R.Y. 1996. Environmental durability of a composite-to-composite adhesive bond in infrastructure applications. 28th international SAMPE technical conference, November, 4-7, 1996, 837-849.
- Cui, H. 2013. Glass fiber reinforced bio-renewable polymer composites and the fabrication with pultrusion process. *Graduate Theses and Dissertations*. Paper 13567.
- Dai, J., Ueda, T., and Sato, Y. 2005. Development of the nonlinear bond stress-slip model of fiber reinforced plastics sheet-concrete interfaces with a simple method, *Journal of Composites for Construction*, 9(1), 52-62.
- Darboux, F. and Huang, C. 2003. An instantaneous-profile laser scanner to measure soil surface microtopography, *Soil Science Society of America Journal*, 67, 92-99.
- Davis, G. D. 1991. *Surface Interface Analysis*. 17: 439.
- Dawood, M., and Rizkalla, S. 2010. Environmental durability of a CFRP system for strengthening steel structures, *Construction and Building Materials*, 24, 1682-1689.
- Deng, J., and Lee, M.M.K. 2007. Fatigue performance of metallic beam strengthened with a bonded CFRP plate. *Composite Structures*; 78: 777-231.
- Deng, J., and Lee, M.M.K., 2009. Adhesive bonding in steel beams strengthened with CFRP, *Structures and Buildings*, 162, 241-249.

- Diaz, A.D., Hadj-Ahmed, R., Foret, G., and Ehrlacher, A. 2008. Stress analysis in a classical double lap, adhesively bonded joint with a layer wise model. *International Journal of Adhesion & Adhesives*.
- Dunn, M.L., Suwito, W., and Hunter, B. 1997. Stress intensity factor for cracked I-beams. *Engineering Fracture Mechanics*; 57(6):609–15.
- Dutta, P.K. 1988. Structural fiber composite materials for cold regions, *Journal of Cold Regions Engineering*, 2(3), 124-134.
- Epoxy Technology. 2009. Epoxy adhesive application guide, Epoxy Technology Inc., Billerica, MA.
- Fam, A., MacDougall, C., and Shaat, A. 2009. Upgrading steel-concrete composite girders and repair of damaged steel beams using CFRP laminates, *Thin-walled Structures*, 47, 1122-1135.
- Farahmand, B. 2001. Fracture mechanics of metals, composites, welds, and bolted joints, Kluwer Academic.
- Fawzia S, Al-Mahaidi R, Zhao X.-L. 2006. Experimental and finite element analysis of a double strap joint between steel plates and normal modulus CFRP, *Composite Structures*, 75 (1-4), 156-62.
- FHWA. 2009. Bridge technology, Federal Highway Administration, Washington, D.C.
- FHWA. 2013. Bridge technology, Federal Highway Administration, Washington, D.C.
- Ghafoori E. and Motavalli M. 2011. Analytical calculation of stress intensity factor of cracked steel I-beams with experimental analysis and 3D digital image correlation measurements, *Engineering Fracture Mechanics*, 78(18), 3226-3242.

- Ghafoori, E., Motavalli, M., Botsis, J., Herwig, A., and Galli, M. 2012. Fatigue strengthening of damaged metallic beams using prestressed unbonded and bonded CFRP plates. *International Journal of Fatigue*, 44: 303-315.
- Gillespie, J.W., Mertz, D.R., Kasai, K., Edberg, W.M., Demitz, J.R., and Hodgson, I. 1996. Rehabilitation of steel bridge girders: large scale testing. *Proceeding of the American Society for Composites 11th Technical Conference on Composite Materials*, pp. 231-240.
- Golden Software, 2010. <http://www.goldensoftware.com/products/surfer/surfer.shtml> [accessed May 17, 2010]
- Great Planes Model Distributors and Tower Hobbies, subsidiaries of Hobbico, Inc. © 2014. [Used with Permission]
- Haider, A., Riadh, A., and Xiao-Ling, Z. 2012. Experimental investigation of bond characteristics between cfrp fabrics and steel plate joints under impact tensile loads. *Composite Structures*, 94, 510-518.
- Haedir, J., Bambach, M.R., Zhao, X.-L., and Grzebieta, R.H. 2009. Strength of circular hollow sections (CHS) tubular beams externally reinforced by carbon FRP sheets in pure bending, *Thin-walled Structures*, 47, 1136-1147.
- Haedir, J., Zhao, X.-L., Bambach, M.R., and Grzebieta, R.H. 2010. Analysis of CFRP externally-reinforced steel CHS tubular beams, *Composite Structures*, 92, 2992-3001.
- Harries, K.A. and El-Tawil, S. 2008. Review of Steel-FRP Composite structural systems proceedings of the 5th international conference on composite construction, Colorado.
- Harries, K.A., Peck, A.J., and Abraham, E.J. 2009. Enhancing stability of structural steel sections using FRP, *Thin-walled Structures*, 47(10), 1092-1101.

- Harries, K.A. and Webb, P. 2009. Experimental assessment of bonded FRP-to-steel interfaces, *Structures and Buildings*, 584, 233-240.
- Henshell, R.D. and Shaw, K.G. 1975. Crack tip finite elements are unnecessary. *International Journal for Numerical Methods in Engineering*, Vol. 9, 495-507.
- Hollaway, L.C. and Cadei, J. 2002. Progress in the technique of upgrading metallic structures with advanced polymer composites, *Progress in Structural Engineering and Materials*, 4, 131-148.
- Hmidan, A., Kim, Y.J., Yazdani, S. 2011. CFRP-repair of steel beams having various crack configurations, *Journal of Composites for Construction*, 15(6), 952-962.
- Hmidan, A., Kim, Y.J., and Yazdani, S. 2013. Effect of sustained load combined with cold temperature on flexure of damaged steel beams repaired with CFRP sheets, *Engineering Structures*, Elsevier 56, 1957-1966.
- Hollstein, T., Schmitt, W., and Bluel, J.G. 1983. Numerical analysis of ductile fracture experiments using single-edge notched tension specimens, *Journal of Testing and Evaluation*, 11, 174-181.
- Hutchinson, J.W. 1968. Singular behavior at end of tensile crack in hardening material, *Journal of the Mechanics and Physics of Solids*, 16, 1, 13-31.
- Jiao, H. and Zhao, X.-L. 2004. CFRP strengthening butt-welded very high strength circular steel tubes, *Thin-Walled Structures*, 42(7), 963-978.
- Jones, S.C. and Civjan, S.A. 2003. Application of fiber reinforced polymer overlays to extend steel fatigue life, *Journal of Composites for Construction*, 7(4), 331-338.
- Kanninen, M.F., and Popelar, C.H. 1985. *Advanced fracture mechanics*. Oxford University Press.

- Kim, Y.J., Bizindavyi, and Green, M.F. 2004. Applicability of steel anchor plates for prestressing multilayered CFRP sheets, 4th International Conference on Advanced Composite Materials in Bridges and Structures (ACMBS-IV), Calgary, AB, Canada (CD-ROM).
- Kim, Y.J. and Brunell, G. 2011. Interaction between CFRP-repair and initial damage of wide-flange steel beams subjected to three-point bending, *Composite Structures*, 93(8), 1986-1996.
- Kim, Y.J. and Heffernan, P.J., 2008. Fatigue behavior of structures strengthened with fiber reinforced polymers: state-of-the-art, *Journal of Composites for Construction*, 12(3), 246-256.
- Kim, Y.J., Green, M.F., and Wight, R.G., 2007. Flexural behaviour of reinforced or prestressed concrete beams strengthened with prestressed CFRP sheets: application of a fracture mechanics approach, *Canadian Journal of Civil Engineering*, 34(5), 664-677.
- Kim, Y.J., Fam, A., and Green, M.F. 2010a. Application of SRP composite sheets for retrofitting reinforced concrete beams: cracking and tension stiffening, *Journal of Reinforced Plastics and Composites*, 29(17), 2647-2662.
- Kim, Y.J., Longworth, J.M., Wight, R.G., and Green, M.F. 2010b. Punching shear of two-way slabs retrofit with prestressed or non-prestressed CFRP sheets, *Journal of Reinforced Plastics and Composites*, 29(8), 1206-1223.
- Kim, Y.J. and Harries, K.A. 2011. Fatigue behavior of damaged steel beams repaired with CFRP strips, *Engineering Structures*, 33(5), 1491-1502.

- Kim, Y.J. and Harries, K.A. 2012. Predicted response of notched steel beams repaired with CFRP strips including bond-slip behavior, *International Journal of Structural Stability and Dynamics*, 12(1), 23-51.
- Kim, Y.J., Hossain, M., and Chi, Y. 2011. Characteristics of CFRP-concrete interface subjected to cold regions environments including three-dimensional topography, *Cold Regions Science and Technology*, (submission number-CRST-D10-00109: available online).
- Kolluru, S.V., O'Neil, E.F., Popvics, J.S., and Shah, S.P. 2000. Crack propagation in flexural fatigue of concrete, *Journal of Engineering Mechanics*, 126(9), 891-898.
- Kulak, G.L., and Grondin, G.Y. 2002. Limit states design in structural steel, Canadian Institute of Steel Construction. Alliston, Ontario, Canada 63. Lam, C.C.A.
- Lam, C.C.A., Cheng, J.J.R. and Yam, C.H.M. 2004. Study of the tensile strength of CFRP/steel double lap joint. 4th International Conference on Advanced Composite Materials in Bridges and Structures, July 20-23, Calgary, Alberta.
- Lam, C.C.A., Michael, C.H.Y., Cheng, J.J.R, and Gaylene, D.K. 2010. Study of stress intensity factor of a cracked steel plate with a single-side CFRP composite patching. *Journal of Composites for Construction*, ASCE, 14(6), 791-803.
- Lau, D. and Buyukozturk, O. 2010. Fracture characterization of concrete/epoxy interface affected by moisture, *Mechanics of Materials*, 42(12), 1031-1042.
- Lenwari, A., and Thepchatri, T. 2002. Predictin of premature separation of bonded CFRP plates from strengthened steel beams using a fracture criterion. *Structural Engineering and Mechanics*, 14(5), 565-574.
- Lenwari, A., Thepchatri, T., and Albrecht, P. 2006. Debonding strength of steel beams strengthened with CFRP plates, *Journal of Composites for Construction*, 10(1), 69-78.

- Linghoff, D., Haghani, R., and Al-Emrani, M. 2009. Carbon-fibre composites for strengthening steel structures, *Thin-Walled Structures*, 47, 1048-1058.
- Liu, H.B., Zhao, X.L., Al-Mahaidi, R., and Rizkalla, S. 2005. Analytical bond models between steel and normal modulus CFRP. In: 4th international conference on advances in steel structures. 1545-52.
- Liu, X., Silva, P. F., and Nanni, A. 2001. rehabilitation of steel bridge members with FRP composite materials. 1st International Conference on Composites in Construction, Porto, Portugal, 613-617.
- Lopez, A. and Nanni, A. 2006. Composite technology evaluation, *Concrete International*, 28(1), 74-80.
- Lu, X.Z., Ye, L.P., Teng, J.G., and Jiang, J.J. 2005. Meso-scale finite element model for FRP sheets/plates bonded to concrete, *Engineering Structures*, 27, 564-575.
- Manteghi, S., Maddox, S.J. 2006. Methods for fatigue life improvement of welded joints in medium and high strength steels. IIW Document No. XIII-2006-04.
- Mazzotti, C. Savoia, M., and Ferracuti, B. 2008. An experimental study on delamination of FRP plates bonded to concrete, *Construction and Building Materials*, 22, 1409-1421.
- Messick, S.C. 1996. Adhesive selection and evaluation for strengthening steel stringer bridges using CFRP. MS thesis, Dept. of Mechanical Engineering, West Virginia University, Morgantown, W.V.
- Miller, T.C., Chajes, M.J., Mertz, D.R., and Hastings, J.N. 2001. strengthening of a steel bridge girder using CFRP plates. *Journal of Bridge Engineering*, ASCE, 6(6):514-522.
- Murakami, Y., 1987. Stress intensity factors handbook. Pergamon Press, New York.

- Naderi, M. and Hajinasri, S.A. 2013. Using twist-off method for measuring CFRP/concrete adhesion when exposed to cyclic temperature changes, wet-dry and freeze-thaw, *Journal of Adhesion*, 89(7), 559-577.
- Nozaka, K., Shield, C.K., and Hajjar, J. 2005. Effective bond length of carbon-fiber-reinforced polymer strips bonded to fatigued steel bridge I-girders, *Journal of Bridge Engineering*, 10(2), 195-205.
- Phares, B. M., Wipf T.J., Klaiber F.W., Abu-Hawash A., Lee Y-S. 2003. Strengthening of steel girder bridges using FRP. *Proceedings of the 2003 Mid-Continent Transportation Research Symposium*, Ames, Iowa, August.
- Pellegrino, C., Maiorana, E., and Modena, C. 2009. FRP strengthening of steel and steel-concrete composite structures: an analytical approach, *Materials and Structures*, 42, 353-363.
- Photiou, N.K., Hollaway, L.C., and Chryssanthopoulos, M.K. 2006. Strengthening of an artificially degraded steel beam utilizing a carbon/glass composite system, *Construction and Building Materials*, 20, 11-21.
- Reinforcement for concrete structures (ACI-440R-07), ACI Committee 440 (Fiber Reinforced Polymer Reinforcement), Farmington Hills, MI.
- Rice, J.R. 1968. A path independent integral and the approximate analysis of strain concentration by notches and cracks, *Journal of Applied Mechanics*, 35, 379-386.
- Rice, J.R. and Rosengren G.F., 1968. Plane strain deformation near crack tip in power-law hardening material, *Journal of the Mechanics and Physics of Solids*, 16, 1, 1-12.
- Rizkalla, S., Dawood, M., and Schnerch, D. 2008. Development of a carbon fiber reinforced polymer system for strengthening steel structures, *Composites Part A*, 39, 388-397.

- Rolfe, S.T., and Novak, S.T., 1970. Slow bend K_{IC} testing of medium strength high toughness steels. ASTM STP 463, American Society for Testing and Materials, Philadelphia, pp 124-159.
- Rooke, D.P. and Cartwright, D. J. 1776. Compendium of stress intensity factors, Her Majesty's Stationery Office, London.
- Schnerch, D. 2005. Strengthening of steel structures with high modulus carbon fiber reinforced polymer (CFRP) Materials. Ph.D. dissertation, North Carolina State University, Raleigh, NC.
- Sciolti, M.S., Aiello, M.A., and Frigione, M. 2012. Influence of water on bond behavior between CFRP sheet and natural calcareous stones, Composites Part B, 43(8), 3239-3250.
- Sebastian, W.M. 2006. Performance implications of imperfectly plastic material in metallic structures with nonmetallic reinforcement. Journal of Structural Engineering, 132(2), 37-243.
- Sen, R., Liby, L., and Mullins, G. 2001. Strengthening steel bridge sections using CFRP laminates, Composites Part B, 32, 309-322.
- Shaat, A.A. 2007. Structural behaviour of steel columns and steel-concrete composite girders retrofitted using CFRP. Doctoral dissertation. Kingston, Ontario: Queen's University.
- Shaat, A. and Fam, A. 2008. Repair of cracked steel girders connected to concrete slabs using carbon-fiber-reinforced polymer sheets, Journal of Composites for Construction, 12(6), 650-659.

- Shaat, A., Schnerch, D., Fam, A., Rizkalla, S. 2004. Retrofit of steel structures using fiber-reinforced polymer (FRP): state-of-the-art, Transportation Research Board (TRB) annual meeting, Washington, D.C. (CD-ROM).
- Shulley, S.B., Huang, X., Karbhari, V. M., and Gillespie, J.W. 1994. Fundamental consideration of design and durability in composite rehabilitation schemes for steel girders with web distress. Proceedings of the Third Materials Engineering Conference, San Diego, California, November 13-16, pp. 1187-1194.
- Smith, S.T., and Teng, J.G. 2001. Interfacial stresses in plated beams. *Engineering Structures*, 23, No. 7, 857–871.
- Smith, S.T. and Teng, J.G. 2002. FRP-strengthened RC beams I: review of debonding strength models, *Engineering Structures*, 24, 385-395.
- SpecialChem. S. A. 2013. Raw material database, <http://www.specialchem4adhesives.com/resources/adhesionguide/index.aspx?id=theory2> [Accessed: December 2013]
- Suh, C.-M., Kang, Y.-G., Suh, D.-Y., and Hwang, B.-W. 1987. Basic characteristics of surface microcracks in type 304 stainless steel at 538°C, *KSME Journal*, 1(2), 115-120.
- Tada, H., Paris, P.C., and Irwin, G.R. 1973. *The stress analysis of cracks handbook*. 2nd edition, Paris Productions Inc., St. Louis, Mo.
- Tavakkolizadeh, M., Saadatmanesh, H. 2003b. Fatigue strength of steel girders strengthened with carbon fiber reinforced polymer patch, *Journal of Structural Engineering*, 129(1), 186-196.
- Tavakkolizadeh, M. and Saadatmanesh, H. 2003. Repair of damaged steel-concrete composite girders using carbon fiber-reinforced polymer sheets, *Journal of Composites for Construction*, ASCE, 7(4), 311-322.

- Teng, J.G., Chen, J.F., Smith, T., and Lam, L. 2002. FRP-strengthened RC Structures, John Wiley & Sons Ltd, West Sussex, UK.
- Teng, J.G., Chen, J.F., Smith, S.T., and Lam, L. 2003. Behavior and strength of FRP-strengthened RC structures: a state-of-the-art review, Structures and Buildings, ICE, 156(1), 51-62.
- Tien-Cuong, N., Yu, B., Riadh, A., and Xiao-Ling, Z. 2012. Time-dependent behavior of steel/CFRP double strap joints subjected to combined thermal and mechanical loading. Composite Structures.
- Tilly, G.P., Matthews, S.J., Deacon, D., De Voy, J., and Jackson, P.A. 2008. Iron and steel bridges: condition appraisal and remedial treatment. CIRIA, London.
- USDOT. 2008. Transportation statistics annual report, United States Department of Transportation, Washington, D.C.
- Wipf, T.J., Phares, B.M., Klaiber, F.W., Al-Saidy, A.H., and Lee, Y. 2005. Strengthening steel girder bridges with carbon fiber-reinforced polymer plates. Transportation Research Board – 6th International Bridge Engineering Conference: Reliability, Security and Sustainability in Bridge Engineering, 435-447.
- Wu, C., Zhao, X.L., Al-Mahaidi, R. and Duan, W.H. 2013. Effects of CFRP bond locations on the Mode I stress intensity factor of centre-cracked tensile steel plates. Fatigue & Fracture of Engineering Materials & Structures, 36(2), 154-167.
- Wu, H. C. 2006. Advanced civil infrastructure materials-Mechanics, science, and applications, H. C. Wu, ed., Woodhead Publishing, Cambridge, U.K.
- Wu, Z. and Yin, J. 2003. Fracturing behaviors of FRP-strengthened concrete structures, Engineering Fracture Mechanics, 70, 1339-1355.

- Xia, S.H. and Teng, J.G. 2005. Behaviour of FRP-to-steel bonded joints, Proceedings of the International Symposium on Bond Behaviour of FRP in Structures, Hong Kong, China, 411-418.
- Yu, Q.Q., Xiao, Z.G., Zhao, X.L., Chen, T., and Gu, X.L. 2012. Numerical analysis of stress intensity factor in cracked steel plates strengthened with CFRP plate, 6th International Composites Conference (ACUN6) Composite & Nanocomposites in Civil, Offshore and Mining Infrastructure, Melbourne, 14-16 December, 187-192.
- Yu, W., Xing-Sheng, X., Jia-Bin, S., and Cheng, J. 2012. Analytical Solution for the Bond Strength of Externally Bonded Reinforcement, Composite Structures, and Nov., 94 (11): 3232-3239.
- Zhang, C. and Wang, J. 2012. Interface stress redistribution in FRP-strengthened reinforced concrete beams using a three-parameter viscoelastic foundation model, Composites Part B, 43, 3009-3019.
- Zhao, X.-L. and Al-Mahaidi, R. 2009. Web buckling of light steel beams strengthened with CFRP subjected to end-bearing forces, Thin-walled Structures, 47(10), 1019-1148.
- Zhao, X.L. and Zhang, L. 2007. State-of-the-art review on FRP strengthened steel structures, Engineering Structures, 29(8), 1808-1823.

APPENDIX A. CALCULATED CORRECTION FACTORS

Table A.1. Correction factors for repaired W4 × 13 beams

η		ζ	ψ				
			0.005	0.010	0.015	0.020	0.025
0.750	0.1	3.877	3.455	3.136	2.885	2.682	
	0.3	4.110	3.363	2.871	2.523	2.262	
	0.5	4.648	3.341	2.633	2.188	1.882	
	0.7	3.450	2.047	1.454	1.126	0.917	
	0.9	1.566	0.750	0.459	0.309	0.218	
1.135	0.1	3.645	3.128	2.770	2.506	2.302	
	0.3	3.684	2.859	2.374	2.050	1.817	
	0.5	3.863	2.618	2.010	1.647	1.405	
	0.7	2.552	1.443	1.003	0.765	0.615	
	0.9	1.021	0.454	0.255	0.152	0.090	
1.500	0.1	3.455	2.885	2.514	2.252	2.054	
	0.3	3.363	2.523	2.059	1.762	1.555	
	0.5	3.341	2.188	1.657	1.349	1.146	
	0.7	2.047	1.126	0.771	0.581	0.462	
	0.9	0.750	0.309	0.155	0.076	0.027	

Table A.2. Correction factors for unrepaired (control) beams

ζ	λ							
	0.91	1.05	1.23	1.38	1.55	1.69	1.91	2.01
0.1	2.990	3.252	3.569	4.092	4.093	4.201	4.553	4.770
0.3	3.181	3.465	3.863	4.218	4.452	4.615	5.029	5.266
0.5	4.068	4.472	4.924	5.418	5.779	6.068	6.670	6.990
0.7	6.789	7.421	8.151	9.094	9.625	10.100	10.856	11.432
0.9	21.381	22.373	23.848	25.100	25.836	26.182	27.790	29.115

Table A.3. Correction factors for repaired Full-Flange beams ($\eta = 0.75$)

ψ		ζ	λ						
			0.91	1.05	1.23	1.38	1.55	1.69	1.91
0.002	0.1	2.807	3.049	3.332	3.759	3.846	3.947	4.274	4.485
	0.3	2.759	2.992	3.293	3.641	3.952	4.013	4.365	4.597
	0.5	2.967	3.236	3.500	3.930	4.270	4.477	4.907	5.208
	0.7	3.117	3.382	3.596	4.181	4.529	4.870	5.192	5.590
	0.9	1.804	1.926	2.089	2.480	2.638	2.721	2.920	3.204
0.004	0.1	2.657	2.879	3.135	3.523	3.640	3.731	4.037	4.246
	0.3	2.456	2.653	2.894	3.223	3.482	3.570	3.882	4.101
	0.5	2.364	2.565	2.749	3.117	3.419	3.583	3.921	4.186
	0.7	2.031	2.197	2.316	2.727	3.014	3.258	3.435	3.720
	0.9	0.858	0.925	0.955	1.221	1.321	1.371	1.482	1.634
0.006	0.1	2.530	2.736	2.967	3.356	3.462	3.546	3.837	4.038
	0.3	2.227	2.397	2.597	2.908	3.157	3.233	3.511	3.719
	0.5	1.948	2.143	2.283	2.602	2.873	3.008	3.288	3.523
	0.7	1.510	1.630	1.711	2.025	2.412	2.503	2.577	2.796
	0.9	0.522	0.569	0.590	0.770	0.849	0.886	0.963	1.068
0.008	0.1	2.413	2.609	2.825	3.213	3.311	3.387	3.666	3.858
	0.3	2.063	2.198	2.368	2.664	2.812	2.968	3.221	3.415
	0.5	1.721	1.853	1.965	2.250	2.492	2.609	2.848	3.056
	0.7	1.203	1.297	1.358	1.619	1.896	1.989	2.067	2.246
	0.9	0.348	0.386	0.403	0.540	0.604	0.636	0.696	0.775
0.010	0.1	2.320	2.501	2.701	3.099	3.174	3.249	3.513	3.700
	0.3	1.902	2.036	2.184	2.464	2.632	2.751	2.983	3.167
	0.5	1.529	1.641	1.734	1.990	2.210	2.312	2.523	2.710
	0.7	0.999	1.077	1.126	1.348	1.571	1.612	1.730	1.879
	0.9	0.242	0.273	0.288	0.400	0.455	0.482	0.532	0.595

Table A.4. Correction factors for repaired Full-Flange beams ($\eta = 1.125$)

ψ		ζ	λ						
			0.91	1.05	1.23	1.38	1.55	1.69	1.91
0.002	0.1	2.729	2.960	3.227	3.720	3.741	3.833	4.151	4.359
	0.3	2.596	2.810	3.078	3.427	3.656	3.774	4.111	4.450
	0.5	2.628	2.858	3.026	3.471	3.792	3.973	4.353	4.810
	0.7	2.458	2.663	2.816	3.299	3.500	3.826	4.130	4.464
	0.9	1.183	1.270	1.308	1.655	1.776	1.837	1.979	1.991
0.004	0.1	2.527	2.736	2.967	3.429	3.462	3.544	3.837	4.038
	0.3	2.227	2.397	2.597	2.910	3.120	3.233	3.550	3.699
	0.5	1.984	2.143	2.220	2.603	2.873	3.007	3.288	3.523
	0.7	1.510	1.630	1.711	2.029	2.300	2.413	2.577	2.796
	0.9	0.522	0.569	0.590	0.771	0.849	0.886	0.963	0.975
0.006	0.1	2.367	2.555	2.760	3.201	3.237	3.313	3.585	3.776
	0.3	1.972	2.113	2.272	2.559	2.760	2.853	3.121	3.330
	0.5	1.618	1.740	1.773	2.112	2.341	2.449	2.674	2.871
	0.7	1.092	1.177	1.232	1.471	1.700	1.812	1.884	2.046
	0.9	0.290	0.323	0.339	0.463	0.523	0.550	0.606	0.617
0.008	0.1	2.235	2.404	2.592	3.013	3.102	3.123	3.378	3.562
	0.3	1.784	1.903	2.034	2.301	2.489	2.572	2.900	3.150
	0.5	1.380	1.478	1.488	1.792	1.958	2.084	2.272	2.442
	0.7	0.856	0.921	0.962	1.154	1.256	1.370	1.489	1.618
	0.9	0.171	0.198	0.211	0.305	0.311	0.378	0.421	0.433
0.010	0.1	2.124	2.280	2.451	2.854	2.899	2.962	3.205	3.377
	0.3	1.638	1.743	1.855	2.104	2.220	2.353	2.710	2.850
	0.5	1.213	1.295	1.322	1.567	1.746	1.824	1.989	2.137
	0.7	0.703	0.756	0.789	0.952	1.193	1.200	1.234	1.340
	0.9	0.099	0.121	0.133	0.207	0.253	0.272	0.309	0.321

Table A.5. Correction factors for repaired Full-Flange beams ($\eta = 1.5$)

ψ		ζ	λ						
			0.91	1.05	1.23	1.38	1.55	1.69	1.91
0.002	0.1	2.654	2.879	3.135	3.613	3.640	3.728	4.037	4.246
	0.3	2.456	2.653	2.894	3.235	3.399	3.570	3.989	4.199
	0.5	2.364	2.565	2.694	3.117	3.419	3.582	3.921	4.186
	0.7	2.031	2.197	2.316	2.727	3.002	3.220	3.435	3.720
	0.9	0.858	0.925	0.955	1.221	1.321	1.371	1.482	1.494
0.004	0.1	2.419	2.609	2.825	3.274	3.311	3.386	3.666	3.858
	0.3	2.048	2.198	2.368	2.664	2.800	2.967	3.360	3.612
	0.5	1.721	1.853	1.898	2.250	2.492	2.607	2.848	3.056
	0.7	1.203	1.297	1.358	1.619	1.800	2.001	2.067	2.246
	0.9	0.348	0.386	0.403	0.540	0.604	0.635	0.696	0.707
0.006	0.1	2.235	2.404	2.592	3.013	3.055	3.123	3.378	3.562
	0.3	1.784	1.903	2.034	2.301	2.500	2.572	2.899	3.111
	0.5	1.380	1.478	1.488	1.792	1.993	2.084	2.272	2.442
	0.7	0.856	0.921	0.962	1.154	1.300	1.385	1.489	1.618
	0.9	0.171	0.198	0.211	0.305	0.355	0.378	0.421	0.433
0.008	0.1	2.091	2.242	2.410	2.805	2.854	2.915	3.151	3.322
	0.3	1.597	1.698	1.804	2.047	2.200	2.291	2.566	2.787
	0.5	1.168	1.245	1.238	1.506	1.680	1.754	1.912	2.053
	0.7	0.664	0.713	0.744	0.899	1.001	1.050	1.167	1.267
	0.9	0.080	0.102	0.113	0.184	0.227	0.247	0.281	0.292
0.010	0.1	1.975	2.111	2.262	2.638	2.690	2.744	2.966	3.128
	0.3	1.458	1.543	1.633	1.858	2.000	2.080	2.315	2.514
	0.5	1.022	1.085	1.101	1.311	1.462	1.527	1.663	1.786
	0.7	0.541	0.580	0.606	0.735	0.801	0.899	0.961	1.043
	0.9	0.025	0.043	0.053	0.109	0.148	0.166	0.195	0.207

Table A.6. Correction factors for repaired Half-Flange beams ($\eta = 0.75$)

ψ		ζ	λ						
			0.91	1.05	1.23	1.38	1.55	1.69	1.91
0.001	0.1	2.840	3.087	3.319	3.772	3.873	3.959	4.304	4.504
	0.3	2.829	3.078	3.273	3.685	4.011	4.126	4.430	4.635
	0.5	3.130	3.429	3.699	4.032	4.397	4.689	5.053	5.295
	0.7	3.492	3.813	4.048	4.404	4.921	5.222	5.509	5.779
	0.9	2.241	2.417	2.405	2.729	2.948	3.001	3.256	3.405
0.002	0.1	2.707	2.940	3.108	3.644	3.680	3.747	4.084	4.271
	0.3	2.560	2.777	2.952	3.286	3.452	3.690	3.969	4.151
	0.5	2.561	2.796	2.963	3.230	3.392	3.639	4.087	4.279
	0.7	2.344	2.558	2.652	2.900	3.128	3.429	3.688	3.862
	0.9	1.091	1.188	1.208	1.345	1.482	1.528	1.654	1.732
0.003	0.1	2.590	2.810	2.929	3.339	3.505	3.557	3.891	4.065
	0.3	2.345	2.538	2.651	2.972	3.222	3.339	3.605	3.761
	0.5	2.177	2.370	2.448	2.703	2.900	3.053	3.441	3.600
	0.7	1.760	1.921	2.055	2.155	2.477	2.600	2.769	2.897
	0.9	0.676	0.744	0.800	0.848	0.950	1.000	1.072	1.124
0.004	0.1	2.486	2.693	2.825	3.229	3.354	3.440	3.717	3.882
	0.3	2.170	2.342	2.444	2.723	2.856	3.101	3.309	3.455
	0.5	1.899	2.064	2.160	2.336	2.501	2.704	2.981	3.119
	0.7	1.407	1.535	1.615	1.715	2.012	2.122	2.215	2.317
	0.9	0.462	0.515	0.555	0.593	0.676	0.701	0.771	0.811
0.005	0.1	2.390	2.587	2.712	3.061	3.211	3.265	3.560	3.718
	0.3	2.022	2.180	2.300	2.518	2.698	2.856	3.063	3.197
	0.5	1.691	1.833	1.926	2.063	2.199	2.408	2.635	2.756
	0.7	1.169	1.276	1.324	1.422	1.602	1.741	1.844	1.927
	0.9	0.331	0.374	0.408	0.438	0.507	0.490	0.587	0.619

Table A.7. Correction factors for repaired Half-Flange beams ($\eta = 1.125$)

ψ		ζ	λ						
			0.91	1.05	1.23	1.38	1.55	1.69	1.91
0.001	0.1	2.772	3.011	3.211	3.743	3.772	3.847	4.189	4.385
	0.3	2.689	2.919	3.049	3.474	3.679	3.990	4.430	4.635
	0.5	2.815	3.078	3.215	3.584	3.935	4.033	4.516	4.731
	0.7	2.806	3.063	3.320	3.498	3.660	3.998	4.419	4.632
	0.9	1.489	1.614	1.711	1.823	1.991	1.921	2.210	2.114
0.002	0.1	2.590	2.810	2.929	3.464	3.505	3.558	3.891	4.065
	0.3	2.345	2.538	2.776	2.975	3.220	3.498	3.669	3.860
	0.5	2.177	2.370	2.613	2.707	3.007	3.210	3.441	3.603
	0.7	1.760	1.921	2.001	2.158	2.336	2.601	2.769	2.897
	0.9	0.676	0.744	0.799	0.849	0.950	0.917	1.072	1.028
0.003	0.1	2.436	2.639	2.701	3.230	3.280	3.316	3.636	3.798
	0.3	2.093	2.257	2.420	2.616	2.890	3.110	3.329	3.559
	0.5	1.788	1.940	2.001	2.191	2.450	2.560	2.796	2.925
	0.7	1.278	1.394	1.490	1.555	1.870	1.910	2.013	2.104
	0.9	0.389	0.437	0.499	0.507	0.582	0.562	0.669	0.710
0.004	0.1	2.304	2.492	2.610	3.029	3.087	3.220	3.419	3.569
	0.3	1.898	2.041	2.201	2.347	2.549	2.699	3.010	3.190
	0.5	1.527	1.652	1.722	1.851	2.077	2.290	2.404	2.590
	0.7	1.000	1.090	1.190	1.213	1.498	1.619	1.800	1.900
	0.9	0.243	0.280	0.311	0.333	0.394	0.382	0.399	0.447
0.005	0.1	2.189	2.365	2.490	2.860	2.922	3.092	3.233	3.371
	0.3	1.744	1.872	2.000	2.136	2.399	2.590	2.811	2.900
	0.5	1.339	1.446	1.550	1.610	1.811	1.990	2.058	2.150
	0.7	0.819	0.892	0.950	0.992	1.200	1.356	1.296	1.354
	0.9	0.153	0.185	0.209	0.227	0.279	0.271	0.337	0.327

Table A.8. Correction factors for repaired Half-Flange beams ($\eta = 1.5$)

ψ		ζ	λ						
			0.91	1.05	1.23	1.38	1.55	1.69	1.91
0.001	0.1	2.707	2.940	3.108	3.644	3.680	3.742	4.084	4.271
	0.3	2.553	2.777	2.858	3.286	3.519	3.790	4.190	4.310
	0.5	2.561	2.796	2.898	3.230	3.564	3.740	4.087	4.279
	0.7	2.344	2.558	2.788	2.900	3.310	3.493	3.688	3.862
	0.9	1.091	1.188	1.203	1.345	1.482	1.430	1.559	1.583
0.002	0.1	2.486	2.693	2.772	3.304	3.354	3.500	3.717	3.882
	0.3	2.170	2.342	2.460	2.723	3.099	3.229	3.454	3.619
	0.5	1.899	2.064	2.220	2.336	2.500	2.636	2.981	3.119
	0.7	1.407	1.535	1.662	1.715	2.001	2.116	2.215	2.317
	0.9	0.462	0.515	0.563	0.593	0.603	0.652	0.771	0.741
0.003	0.1	2.304	2.492	2.610	3.029	3.087	3.112	3.419	3.569
	0.3	1.898	2.041	2.230	2.347	2.559	2.669	2.983	3.209
	0.5	1.527	1.652	1.745	1.851	2.077	2.222	2.419	2.631
	0.7	1.000	1.090	1.188	1.213	1.592	1.752	1.859	2.077
	0.9	0.243	0.280	0.300	0.333	0.394	0.455	0.463	0.559
0.004	0.1	2.148	2.324	2.511	2.807	2.871	2.883	3.175	3.312
	0.3	1.699	1.821	1.996	2.076	2.328	2.459	2.612	2.887
	0.5	1.288	1.389	1.452	1.546	1.739	1.885	1.974	2.219
	0.7	0.771	0.841	0.888	0.934	1.088	1.211	1.300	1.466
	0.9	0.131	0.161	0.177	0.200	0.251	0.243	0.306	0.399
0.005	0.1	2.028	2.183	2.337	2.622	2.688	2.879	2.971	3.096
	0.3	1.547	1.653	1.771	1.872	2.099	2.429	2.552	2.618
	0.5	1.121	1.206	1.299	1.336	1.529	1.663	1.822	1.999
	0.7	0.625	0.681	0.711	0.757	0.897	1.011	1.099	1.210
	0.9	0.063	0.088	0.101	0.123	0.163	0.160	0.210	0.299

APPENDIX B. REGRESSION DIAGNOSTICS FOR THE CORRECTION FACTORS

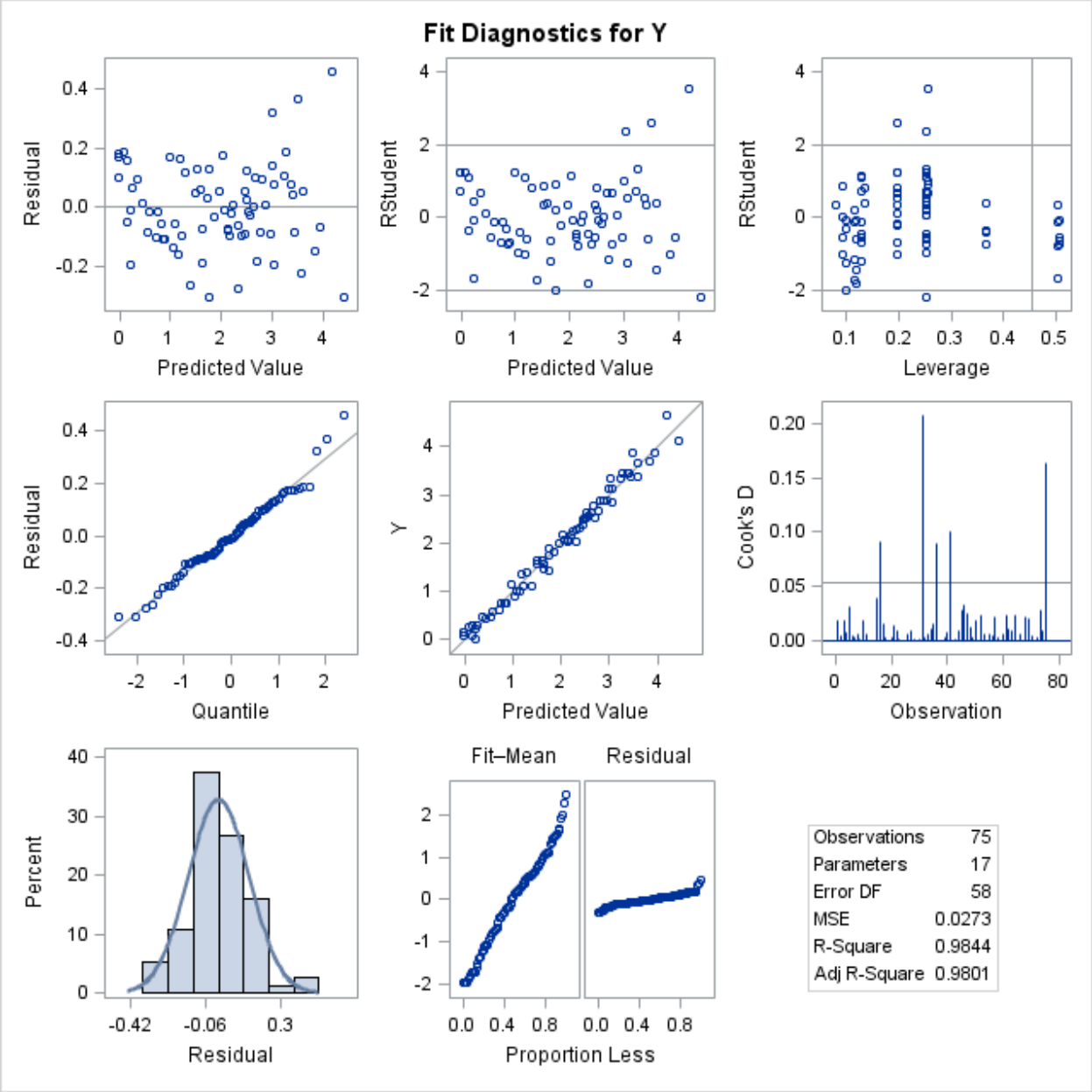


Fig. B.1. Fit diagnostics panel of the correction factor for repaired W4 × 13 beams

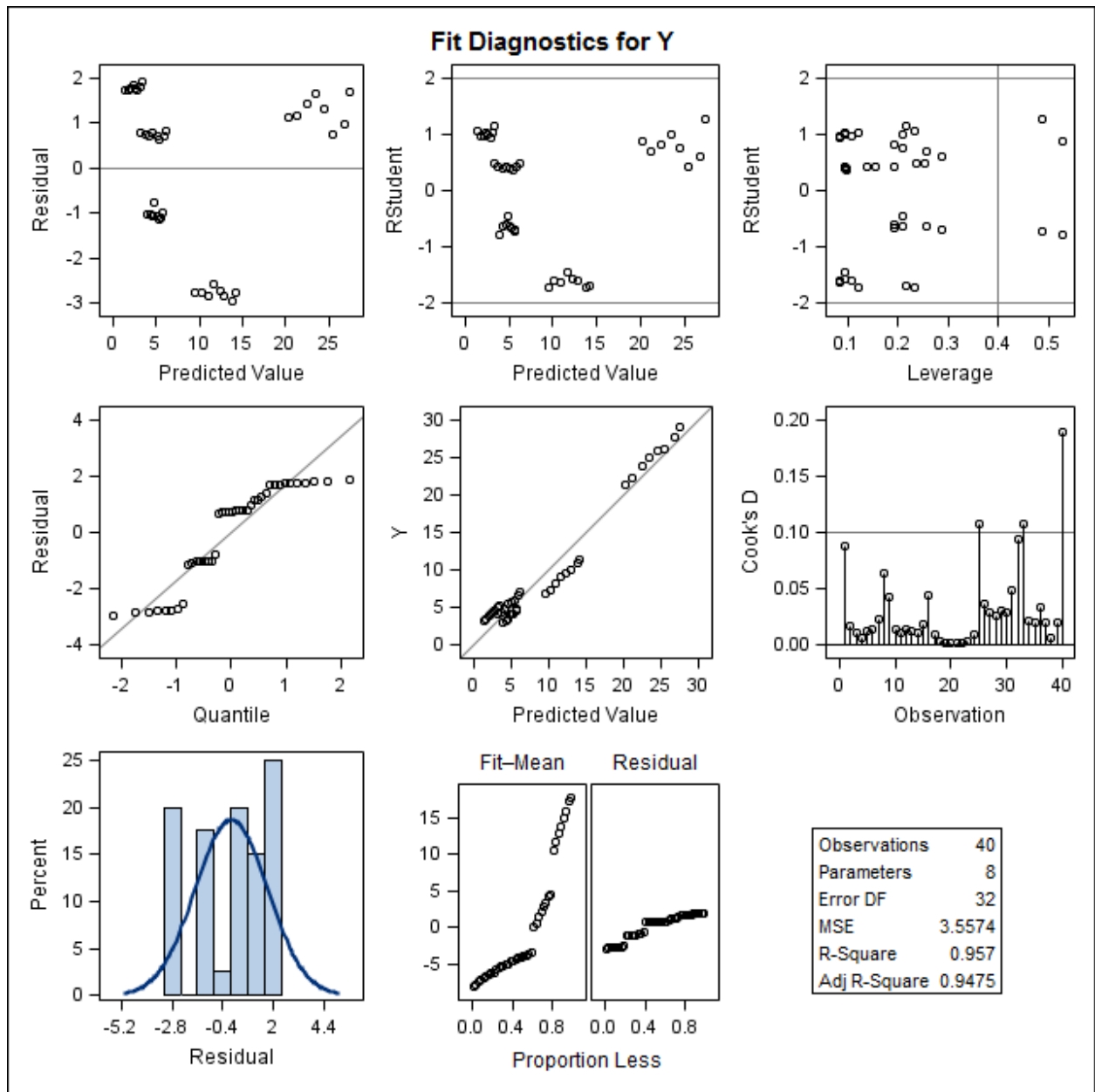


Fig. B.2. Fit diagnostics panel of the correction factor for unrepaired (control) beams

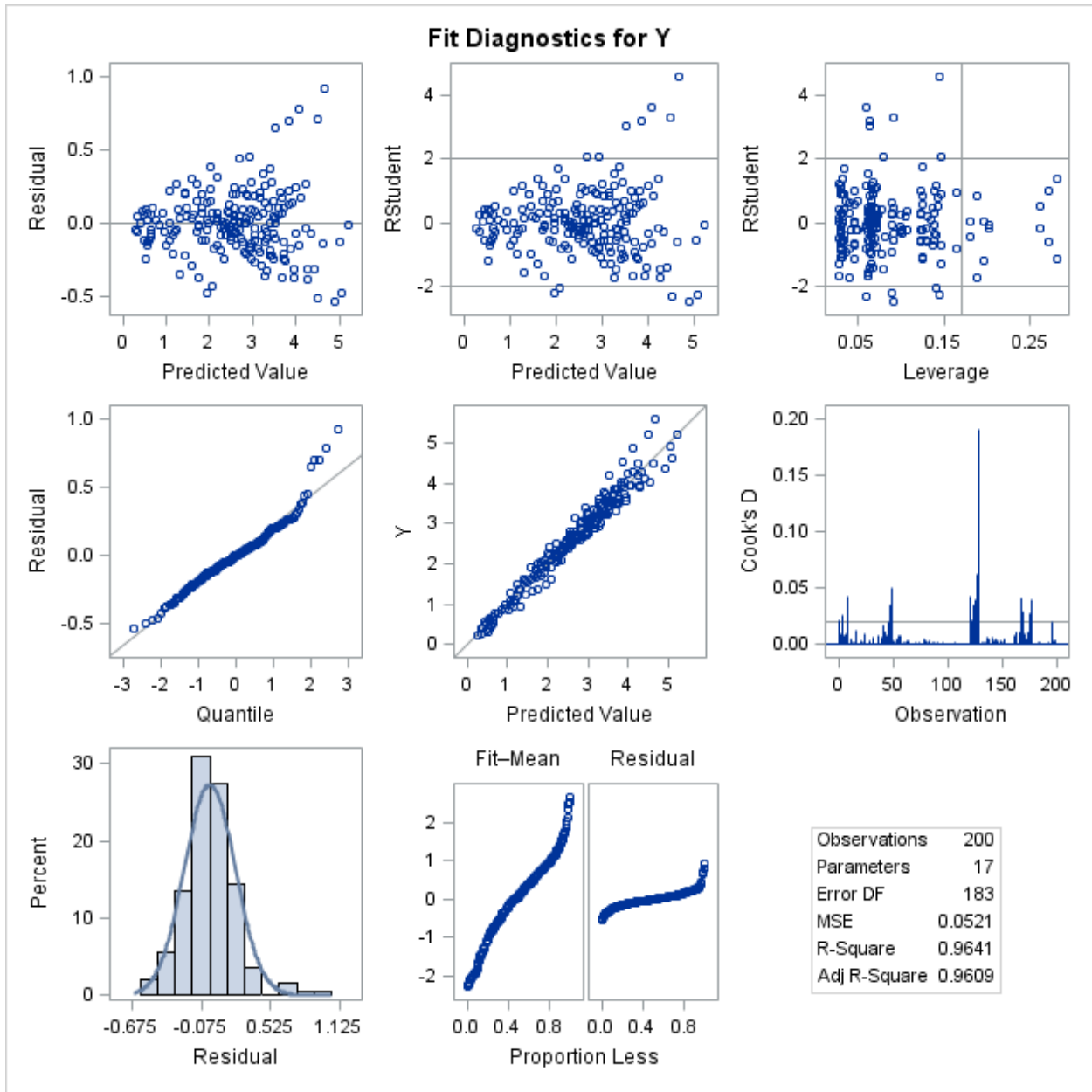


Fig. B.3. Fit diagnostics panel of the correction factor for Full-Flange geometry ($\eta = 0.75$)

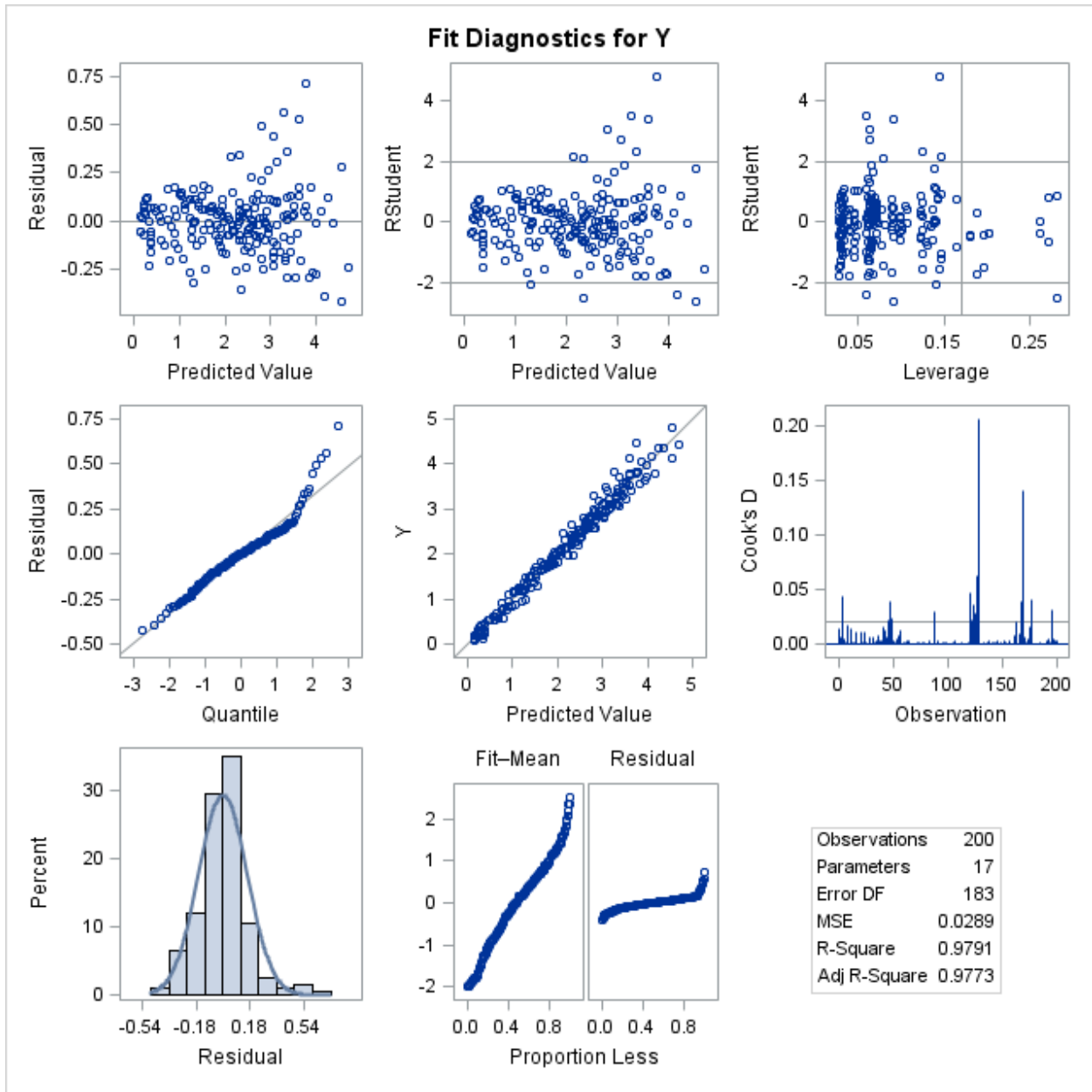


Fig. B.4. Fit diagnostics panel of the correction factor for Full-Flange geometry ($\eta = 1.125$)

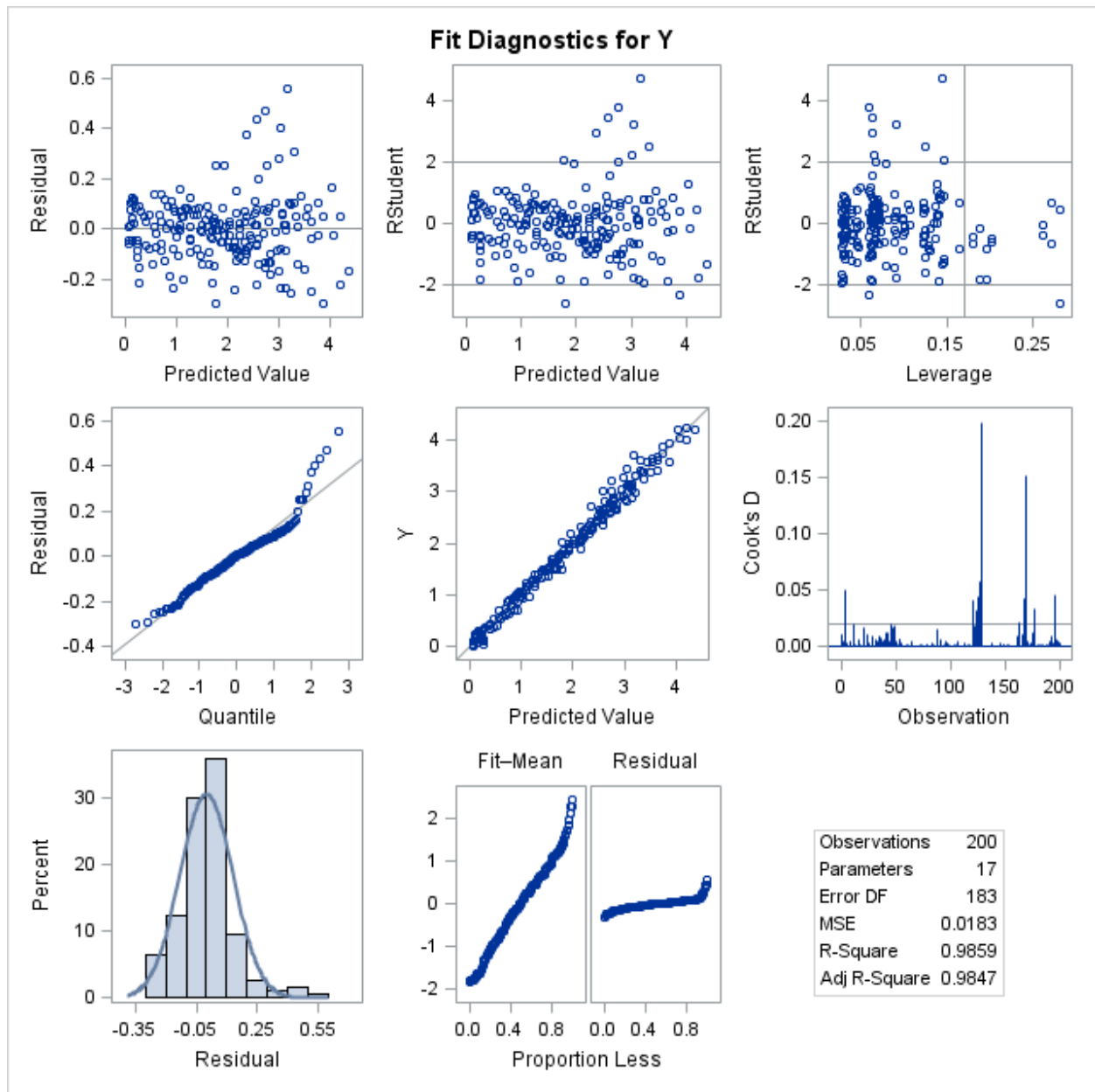


Fig. B.5. Fit diagnostics panel of the correction factor for Full-Flange geometry ($\eta = 1.5$)

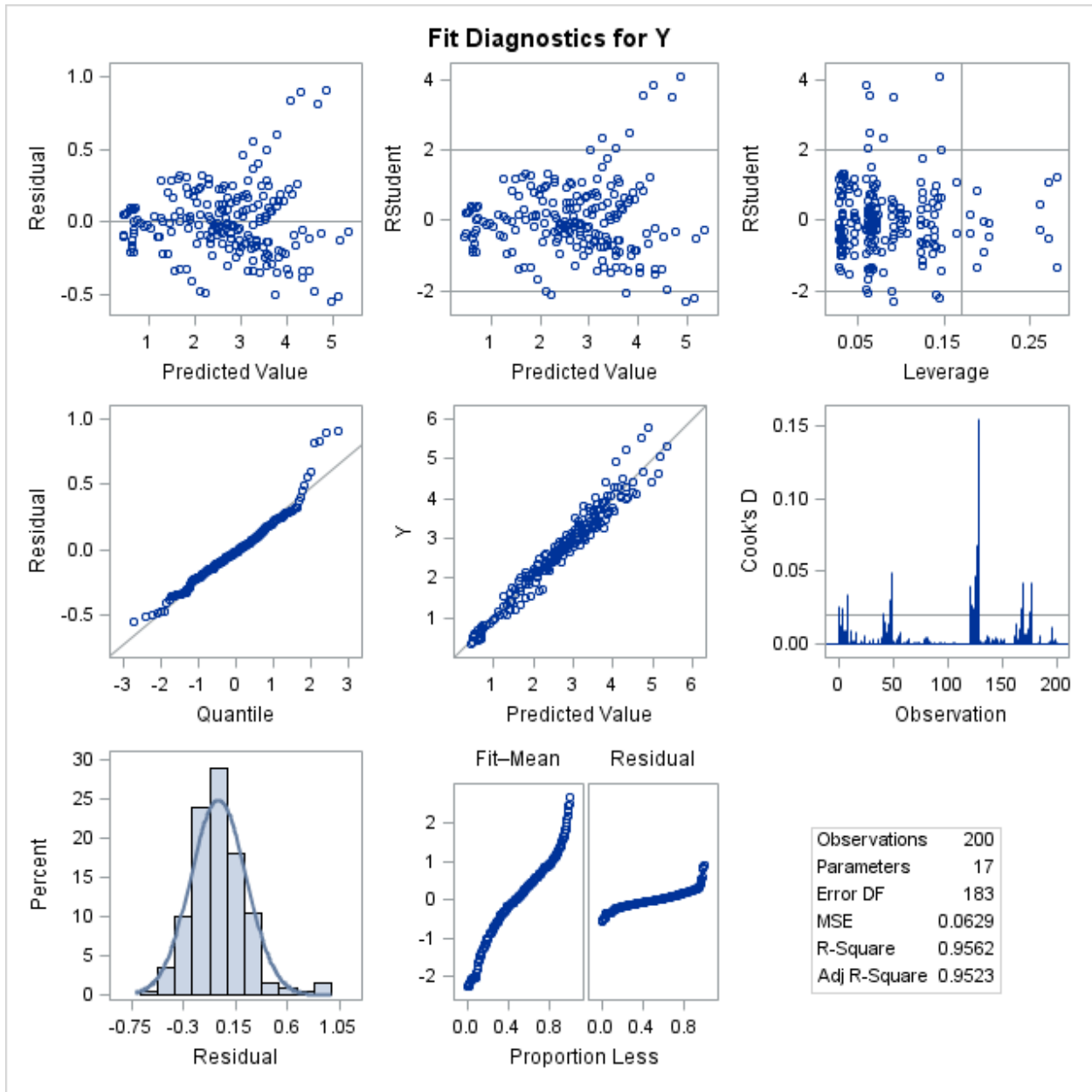


Fig. B.6. Fit diagnostics panel of the correction factor for Half-Flange geometry ($\eta = 0.75$)

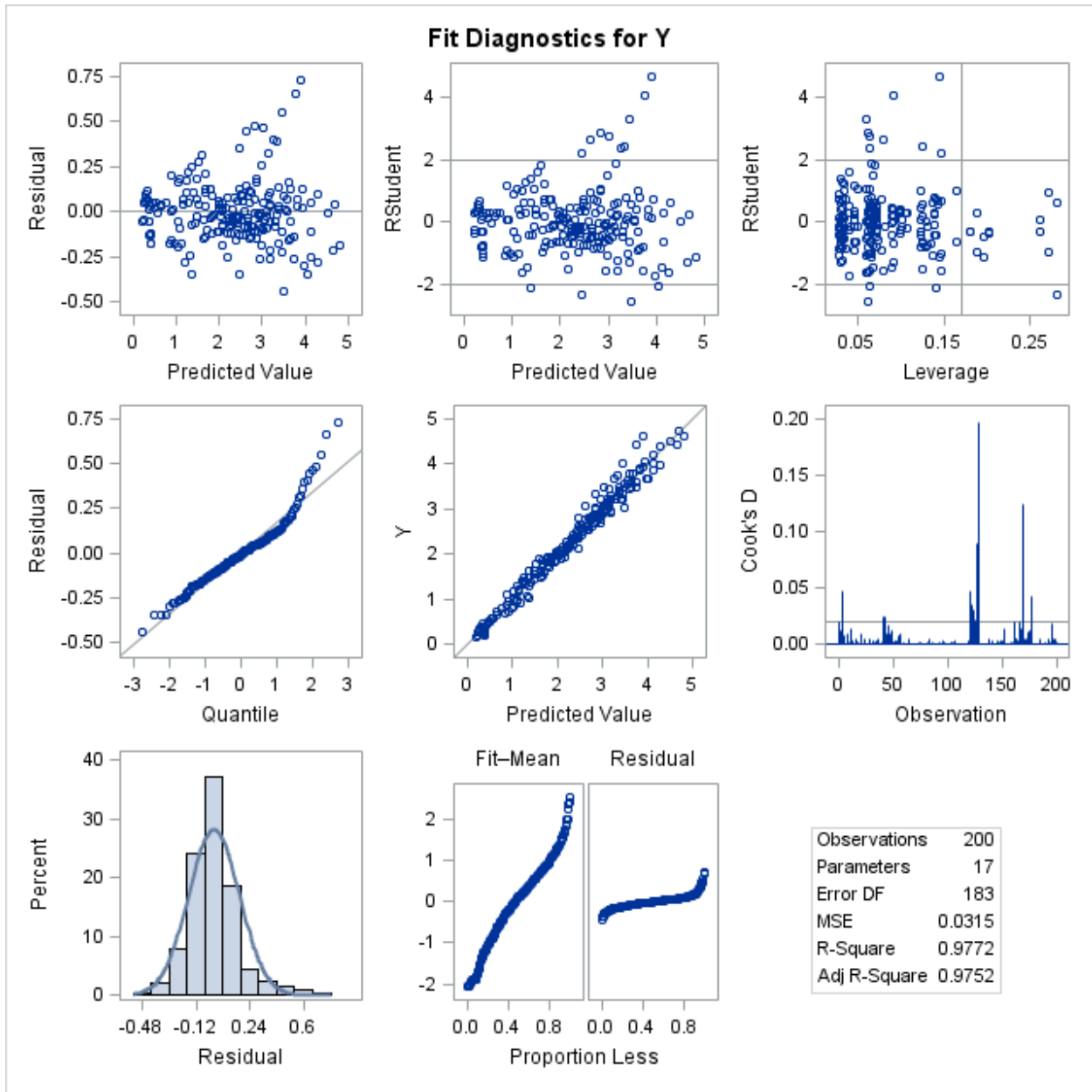


Fig. B.7. Fit diagnostics panel of the correction factor for Half-Flange geometry ($\eta = 1.125$)

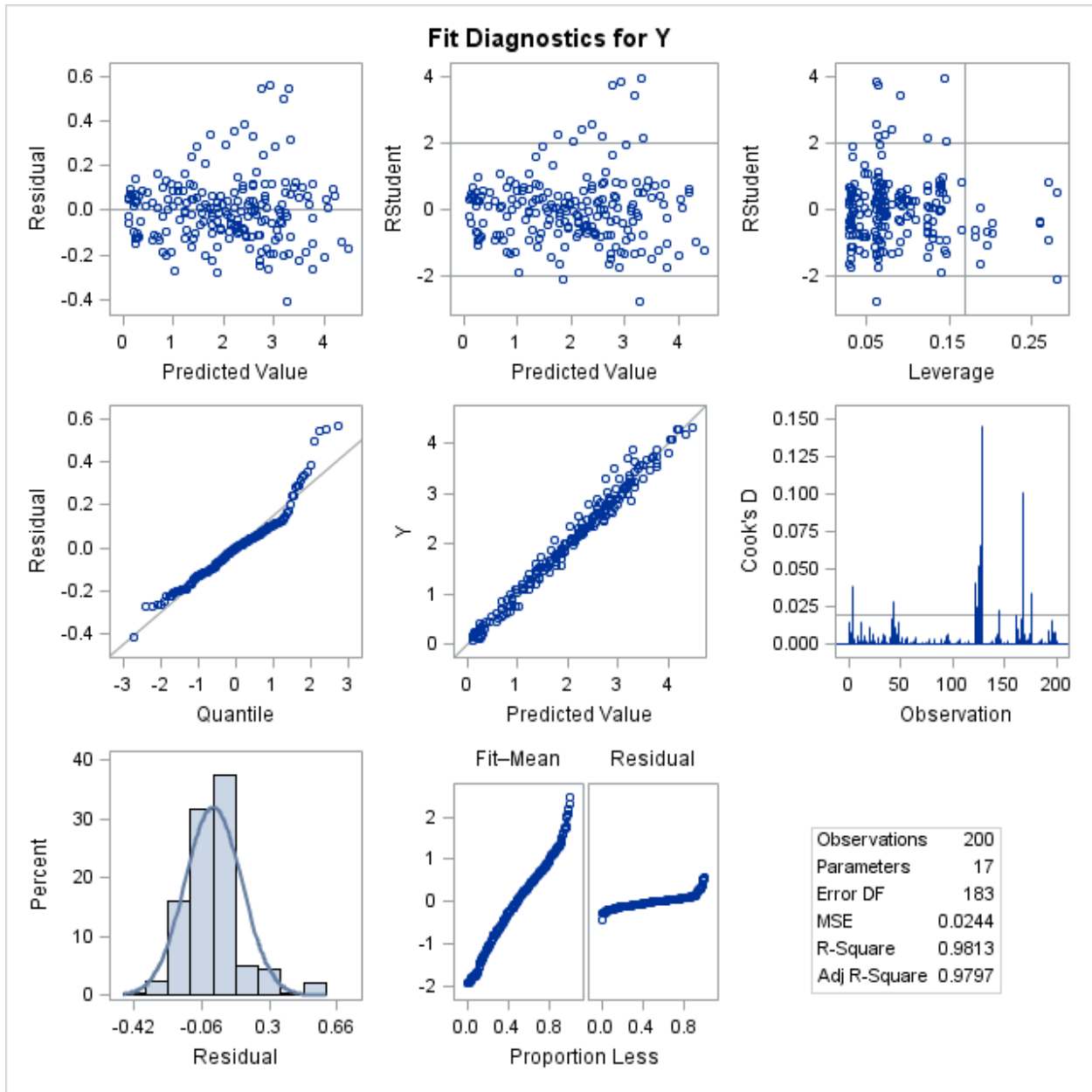


Fig. B.8. Fit diagnostics panel of the correction factor for Half-Flange geometry ($\eta = 1.5$)